

# Magnetostrophic analysis of Earth's internal magnetic field

Colin Michael Hardy

SUBMITTED IN ACCORDANCE WITH THE REQUIREMENTS FOR THE DEGREE OF  
DOCTOR OF PHILOSOPHY

THE UNIVERSITY OF LEEDS

EPSRC CENTRE FOR DOCTORAL TRAINING IN FLUID DYNAMICS

OCTOBER 2020

# Declaration

The candidate confirms that the work submitted is his own, except where work which has formed part of jointly authored publications has been included. The contribution of the candidate and the other authors to this work has been explicitly indicated below. The candidate confirms that appropriate credit has been given within the thesis where reference has been made to the work of others.

Chapter 3 contains material from the publication [Hardy et al. \(2018\)](#):

Hardy, C., Livermore, P., Niesen, J., Luo, J. and Li, K. 2018. Determination of the instantaneous geostrophic flow within the three-dimensional magnetostrophic regime. *Proc. R. Soc. A*. 474(2218), pp. 20180412.

Chapter 5 contains material from the publication [Hardy and Wong \(2019\)](#):

Hardy, C. and Wong, J. 2019. Stably stratified layers within Earth's core. *Astronomy & Geophysics*. 60(3), pp. 3–30.

Chapter 6 contains material from the publication [Hardy et al. \(2020\)](#):

Hardy, C., Livermore, P., Niesen, J. 2020. Enhanced magnetic fields within a stratified layer. *Geophysical Journal International*, 222(3) pp. 1686–1703

This copy has been supplied on the understanding that it is copyright material and that no quotation from the thesis may be published without proper acknowledgment.

The right of Colin M Hardy to be identified as Author of this work has been asserted by Colin M Hardy in accordance with the Copyright, Designs and Patents Act 1988.

# Acknowledgements

I would like to thank all the people who have either directly or indirectly assisted me during my studies. Firstly, I am indebted to my supervisors Phil Livermore and Jitse Niesen for their unwaveringly excellent and supportive supervision. It has been a privilege to work with them at the University of Leeds, where the Centre for Doctoral Training for Fluid Dynamics, the Deep Earth Research group, and the Astrophysical and Geophysical fluid dynamics group comprised my diverse and enriching tripartite research home. I thank many of my colleagues, both at Leeds and beyond, who have aided the progression of my work, specifically, Kuan Li, Chris Jones, Jérémie Vidal, Emmanuel Dormy and Julien Aubert for stimulating conversations that helped develop research ideas.

I am grateful to the Geodynamo group at ISTERre, Université Grenoble Alpes for hosting me for a 6 week academic research placement. This was a very enjoyable and productive experience. During my time there I had many fruitful discussions with the whole group, I particularly thank Dominique Jault and Nathanaël Schaeffer for their regular availability and keen interest shown during my visit, it was a pleasure to work closely with them and draw on their expertise during this time.

I'm much obliged to my fellow PhD students and friends at Leeds, including Rob, Tom, Andy and Eva, with whom the many discussions and healthy scientific debates were both enjoyable and occasionally enlightening. I also appreciate the hospitality and affability shown by my peers during visits to Université Grenoble Alpes and ETH Zürich, particular thanks goes to Felix, Fabian, Daria and Sylvie.

This work was financially supported by the Engineering and Physical Sciences Research Council (EPSRC) Centre for Doctoral Training in Fluid Dynamics at the University of Leeds under Grant No. EP/L01615X/1. Some numerical work was undertaken on ARC2 and ARC3, part of the High Performance Computing facilities at the University of Leeds

# Abstract

Throughout this thesis we build on the central tenet of the seminal work by Taylor (1963), which argued that the geophysically relevant limit for dynamo action within the Earth’s outer core is one of negligibly small inertia and viscosity in the magnetohydrodynamic equations. Within this ‘magnetostrophic’ limit, he showed the existence of a necessary condition, now well known as Taylor’s constraint, which requires that the cylindrically-averaged Lorentz torque must everywhere vanish; magnetic fields that satisfy this condition are termed ‘Taylor states’.

We extend the use of this condition, to analyse the geomagnetic field and investigate the underlying geodynamo process within Earth’s core, through several key strands of work.

Firstly, we detail a general method that is the first to enable correct evaluation of the instantaneous geostrophic flow for any 3D Taylor state, fully incorporating all necessary boundary conditions.

Secondly, we explore the subsequent dynamics of Taylor state magnetic fields, calculating the field induced by these flows and hence the rate of change of magnetic field. Importantly, we note the similarities and differences that arise between these magnetostrophic dynamo models and observationally derived geomagnetic field models. We show that Taylor state magnetic fields that remain stable over geophysical time scales are very rare.

Thirdly, we consider the prospect of the fluid in the outermost part of Earth’s core being stratified. This leads to a necessary adaptation to the Taylor constraint, resulting in the analogous condition within a stratified fluid, termed the ‘Malkus constraint’. Implementing this additional constraint allows us to construct a model for the entirety of Earth’s outer core, matching observational geomagnetic field models at the core surface, obeying the Malkus constraint in the stratified layer and satisfying the Taylor constraint in the bulk of the core. The results from this model suggest that the dynamics within the stratified layer may be distinct from the inner convective part of the core, characterised not only by suppressed radial flow but by a strong magnetic field. The present-day toroidal field strength immediately beneath the CMB is estimated to be significantly stronger than that within the convective region of the outer core.

# Contents

<b>List of Figures</b>	<b>xiii</b>
<b>1 Introduction</b>	<b>1</b>
1.1 Earth's interior . . . . .	1
1.2 Earth's magnetic field . . . . .	3
1.2.1 Origin of Earth's magnetic field . . . . .	3
1.2.2 Core convection . . . . .	5
1.2.3 Paleomagnetism . . . . .	6
1.2.4 Magnetic field observations . . . . .	7
1.2.5 Archeomagnetic models . . . . .	10
1.3 Dynamo theory . . . . .	11
1.3.1 Electromagnetism . . . . .	11
1.3.2 Fluid dynamical equations . . . . .	13
1.3.3 Numerical Dynamo models . . . . .	15
1.4 Data assimilation models . . . . .	17
1.5 Thesis outline . . . . .	18
<b>2 Magnetostrophy</b>	<b>21</b>
2.1 The Magnetostrophic approximation . . . . .	21
2.2 Derivation of Taylor's constraint . . . . .	22
2.3 Magnetostrophic Dynamo simulations . . . . .	24
2.4 The magnetostrophic limit . . . . .	26
2.5 Mean field theory . . . . .	27
2.6 The segregation of time scales . . . . .	29
2.7 Torsional oscillations . . . . .	31
<b>3 Determination of the instantaneous geostrophic flow within the three-dimensional magnetostrophic regime</b>	<b>33</b>
3.1 Introduction . . . . .	33
3.2 Magnetic field and fluid velocity representations . . . . .	34
3.2.1 A Galerkin representation . . . . .	35
3.3 Solving for the ageostrophic flow . . . . .	36

---

3.4	The initial state . . . . .	37
3.5	Overview of time evolution and the geostrophic flow . . . . .	38
3.6	Braginsky’s formulation . . . . .	40
3.7	Existing methods to determine the geostrophic flow . . . . .	41
	3.7.1 An axisymmetric first-order implicit method . . . . .	41
	3.7.2 A 3D fully implicit scheme . . . . .	42
	3.7.3 An instantaneous axisymmetric method . . . . .	44
	3.7.4 Taylor’s 3D instantaneous method . . . . .	45
3.8	Technical aside: higher order boundary conditions . . . . .	46
	3.8.1 Higher order boundary conditions in the heat equation . . . . .	46
	3.8.2 The relevance for Taylor’s equation . . . . .	47
	3.8.3 Schemes in which the boundary information is included . . . . .	49
3.9	An appraisal of Taylor’s method . . . . .	49
	3.9.1 An illustration of when Taylor’s method fails . . . . .	49
	3.9.2 Specific cases when Taylor’s method succeeds . . . . .	53
3.10	A generalisation of Taylor’s analysis . . . . .	55
	3.10.1 A potential-based spherical transform method . . . . .	56
	3.10.2 A potential-based Green’s function method . . . . .	58
	3.10.3 A modal projection . . . . .	58
3.11	Examples of the geostrophic flow in 3D . . . . .	60
3.12	Analytic approximation for an Earth-like field . . . . .	62
3.13	Singularities of $u_g$ . . . . .	64
	3.13.1 Singularities at $s = 0$ . . . . .	65
	3.13.2 Singularities at $s = 1$ . . . . .	66
	3.13.3 Singularities off the $s$ -axis . . . . .	67
3.14	Discussion . . . . .	68
<b>4</b>	<b>Stable steady Taylor states</b>	<b>71</b>
4.1	Introduction . . . . .	71
4.2	Methodology . . . . .	73
	4.2.1 Method for calculating instantaneous $u_g$ and magnetic induction	75
	4.2.2 Time-dependent, implicit method for dynamically evolving $\mathbf{B}$ . . . . .	78
	4.2.3 Symmetry . . . . .	78
4.3	Searching for steady Taylor states . . . . .	79
4.4	Dynamical magnetostrophic simulations in search of stable Taylor states . . . . .	81
	4.4.1 Simulations with single mode initial conditions . . . . .	82
	4.4.2 Simulations with random mixed symmetry initial conditions . . . . .	84

4.4.3	The evolution from a quasi-steady Taylor state . . . . .	85
4.4.4	The strength of the known symmetric solutions as attractors . . . . .	88
4.4.5	The dependence on the choice of $\alpha$ -effect . . . . .	89
4.5	Comparison to observational models . . . . .	92
4.5.1	Comparison to other numerical dynamo simulations . . . . .	93
4.6	Discussion . . . . .	94
<b>5</b>	<b>Stratified layer at the top of Earth's core</b>	<b>99</b>
5.1	Stratification in outermost part of core . . . . .	99
5.1.1	Formation . . . . .	101
5.2	The effect of a stratified layer on the observed geomagnetic field . . . . .	102
5.2.1	Compatibility of a stratified layer with geomagnetic simulations and observations . . . . .	103
<b>6</b>	<b>Constraints on the magnetic field within a stratified outer core</b>	<b>107</b>
6.1	Introduction . . . . .	107
6.2	Derivation of Malkus' constraint . . . . .	109
6.3	Geometry and representation of a stratified magnetostrophic model . . . . .	111
6.4	Discretisation of the constraints . . . . .	113
6.4.1	The Taylor constraints . . . . .	113
6.4.2	The Malkus constraints . . . . .	114
6.5	Existence of Malkus states . . . . .	118
6.5.1	Simple analytic states . . . . .	118
6.5.2	General Malkus states . . . . .	119
6.6	Earth-like Malkus states . . . . .	124
6.6.1	Magnetic field at 2015 . . . . .	124
6.6.2	Time averaged field over the past ten millenia . . . . .	127
6.7	Discussion . . . . .	128
6.7.1	Do Malkus states exist? . . . . .	129
6.7.2	Can we tell from a snapshot of the geomagnetic field if a stratified layer exists? . . . . .	129
6.7.3	What might be the present-day internal structure of the geomagnetic field inside a stratified layer? . . . . .	130
6.7.4	Limitations and robustness . . . . .	131
6.7.5	Ohmic dissipation . . . . .	132
6.8	Conclusion . . . . .	133
<b>7</b>	<b>Conclusions and future work</b>	<b>135</b>
7.1	Summary . . . . .	135
7.2	Further extensions . . . . .	136

---

<b>A</b>	<b>Derivation of an alternative form of the Taylor constraint</b>	<b>143</b>
<b>B</b>	<b>Solution of a full sphere low-resolution Malkus state</b>	<b>147</b>
<b>C</b>	<b>Basic theory</b>	<b>149</b>
C.1	Toroidal and poloidal functions . . . . .	149
C.2	Solving Laplace's equation . . . . .	151
C.3	Spherical Harmonics . . . . .	152
C.3.1	Equatorial symmetry . . . . .	153
C.3.2	Rotational symmetry . . . . .	153
C.4	Boundary conditions . . . . .	154
C.5	Angular momentum . . . . .	156
C.6	Vector calculus . . . . .	157
	<b>References</b>	<b>174</b>

# List of Figures

1.1	The interior structure of Earth. . . . .	2
1.2	The phase PKiKP reflected at the inner core boundary (ray 5) is observed in the shadow zone of the core (between rays 2 and 3), a zone where no P-wave is supposed to arrive <a href="#">Souriau (2007)</a> . . . . .	3
1.3	Schematic of the fluid motions within convecting and stratified regions. . . . .	6
1.4	Vertical (downward) component of the magnetic field (in microtesla) at the surface of the Earth in 1835 according to the Gauss model. Figure from <a href="#">Kono (2015)</a> . . . . .	8
1.5	Radial (outward) component of the magnetic field at the surface of the Earth in 2015 according to the CHAOS-6 model ( <a href="#">Finlay et al., 2016</a> ). Visualised using the Mollweide projection and centred on the Greenwich meridian . . . . .	8
1.6	Vertical (downward) component of the magnetic field (in microtesla) at the core mantle boundary of the Earth based on Gauss model (1835). Figure from <a href="#">Kono (2015)</a> . . . . .	9
1.7	Radial (outward) component of the magnetic field at the CMB in 2015 according to the CHAOS-6 model ( <a href="#">Finlay et al., 2016</a> ). . . . .	10
1.8	Ekman - Magnetic Prandtl and Alfvén - Magnetic Prandtl regime diagrams showing the currently possible range of simulation parameters. The Earth’s core lies far away beyond the bottom left corner at $E = 10^{-15}$ , $P_m = 10^{-6}$ , $A = 10^{-2}$ . Figure from <a href="#">Schaeffer et al. (2017)</a> (to which the ‘this paper’ points refer.) . . . . .	16
2.1	A schematic diagram illustrating the cylindrical surface within a spherical domain and the closure this surface using the spherical caps (dashed lines). . . . .	23
2.2	Reynolds–Ekman regime diagram showing the different capabilities of various methods of studying rotating convection and dynamo physics. The regions of parameter space occupied by Earth and magnetostrophic models are also indicated. Figure modified from <a href="#">Aurnou et al. (2015)</a> . . . . .	25
2.3	An illustration of some of the geostrophic cylinders over which Taylor’s constraint is defined <a href="#">Livermore et al. (2008)</a> . . . . .	32

- 
- 3.1 A comparison of the cases where Taylor’s method fails and where it succeeds. (a) Compares the solutions for the geostrophic flow for an axisymmetric dipolar poloidal initial field. Red is the analytic solution of the first order BWR equation (3.21), dotted blue is a numerical solution of Taylor’s second order ODE (see text) and dashed black is the solution using the implicit time step method with  $h = 10^{-9}$ . (b) Shows the geostrophic flow corresponding to a non-axisymmetric  $l = 1, m = 1$  purely-toroidal Taylor state, on which all methods agree. 52
- 3.2 A comparison of the absolute value of the polynomial spectral coefficients  $A_i$ , defined in equation (3.20), against degree for numerical solutions using the Braginsky-Wu-Roberts and Taylor formulations. . . . . 53
- 3.3 The geostrophic flow for the non-axisymmetric  $l = 2, m = 2$  poloidal Taylor state of equation (3.46). Solutions using the spherical transform method, the implicit timestep method with  $h = 10^{-9}$  and Taylor’s ODE are compared. . . . . 61
- 3.4 The geostrophic flow for the  $l = 2, m = 1$  non-axisymmetric mixed Taylor state of equation (3.47). Solutions using the spherical transform method, the implicit timestep method with  $h = 10^{-9}$  and Taylor’s ODE are compared. Solutions for solely either the poloidal and toroidal components of the Taylor state using the spherical transform method are also shown. . . . . 62
- 3.5 The geostrophic flow for a non-axisymmetric Earth-like Taylor state. Numerical solution using the spherical transform method (red) is compared to the analytic solution neglecting the boundary term (blue). . . . . 64
- 3.6 Contour plots of (a) the total azimuthal flow  $u_\phi$  driven by the axisymmetric poloidal field in §3.9.1, (b) the axisymmetric part of the total azimuthal flow driven by the Earth-like field of (3.49). The azimuthal flow is shown to be approximately 50 times stronger in (b) and similar to values expected in Earth’s core (Holme, 2015). . . . . 64
- 3.7 A plot of  $\partial_s(u_g/s)$  for solutions to a mixed axisymmetric Taylor state consisting of the poloidal field of the example of §3.9.1 with a  $l = 1, m = 0, n = 1$  toroidal Galerkin mode, using the BWR and Taylor equations. (a) Shows the whole domain, a singularity of the form  $s^{-1}$  is visible for both solutions at  $s = 0$  and for Taylor’s solution only, a weaker singularity also occurs at  $s = 1$ . (b) Zoomed-in plot of the  $s = 1$  singularity to show clearly that it only occurs when solving Taylor’s equation; it has the form  $(1 - s^2)^{-\frac{1}{2}}$ . . . . . 68

4.1	Surface plot of the normalised instantaneous rate of change of magnetic field on the core surface, $I_S$ , as a function of the $L = 1, N = 1$ and $L = 1, N = 2$ coefficients values. The vertical red line corresponds to the coefficient values of the known stable steady solution of <a href="#">Li et al. (2018)</a> . The $\alpha$ -effect form (4.2) is used, with an above critical magnitude of $\alpha_0 = 18$ . (a) and (b) show the same 3D plot viewed from a different angle. . . . .	81
4.2	The path taken as this single poloidal $L = N = 1$ mode Taylor state evolves toward a stable steady state with vanishingly small $I_V$ , the red data points are plotted a frequency of every one hundredth of a magnetic diffusion time (500 yrs). . . . .	82
4.3	Graph showing the evolution of $I_S$ with time for the suite of single poloidal mode initial conditions . . . . .	83
4.4	Graph showing the evolution of $I_S$ with time for the suite of mixed symmetry, with (a) all 1000 different random initial conditions shown, (b) just 4 models with initial conditions plotted for clarity. . . . .	85
4.5	The paths taken from two initial magnetic fields (coloured red and blue) that are quasi-steady Taylor states. The fields diverge from the initial states (green circles) before finally converging to the same stable steady Taylor state. (a) and (b) show the same 3D plot viewed from a different angle. . . . .	88
4.6	Surface plot of $I_S$ as a function of the $L = 1, N = 1$ and $L = 1, N = 2$ coefficients values. The vertical red line corresponds to the coefficient values of the known stable steady solution of <a href="#">Li et al. (2018)</a> . The $\alpha$ -effect form (4.2) is used, with an above critical magnitude of $\alpha_0 = 16$ . (a) and (b) show the same 3D plot viewed from a different angle. . . . .	90
4.7	Normalised instantaneous rate of change of magnetic field on the core surface, $I_S$ , with $\alpha_0 = 16$ , for 60 different random initial conditions of mixed symmetry. . . . .	91
4.8	Plot of $I_S$ over the last 100,000 years for CMB field data from the GGF100k model ( <a href="#">Panovska et al., 2018</a> ). . . . .	93
4.9	Plot of $I_S$ for core surface field data from Aubert's simulation (a) at $\epsilon = 1$ ( $E = 3 \times 10^{-5}$ ), (b) at $\epsilon = 1 \times 10^{-5}$ ( $E = 3 \times 10^{-10}$ ). . . . .	94
4.10	Plot of $I_S$ for the core surface field (a) comparing the axisymmetric, degree 10 truncated data from Aubert's simulation at $\epsilon = 1$ (black) with the GGF100k data (blue) and in (b) with our simulation results (§4.4.2) too. . . . .	94

5.1	(a) Ray paths for SmKS ( $2 \leq m \leq 6$ ) for a source (star) 550 km deep to a station (triangle) at 155. (b) Core legs of ray path. As multiples in core increase, bottoming depth in core decreases. S6KS bottoms at 60km below the CMB, whereas S2KS bottoms 700 km below the CMB (Helfrich and Kaneshima, 2013) . . . . .	100
6.1	(a) Earth-like spherical shell with radius $r_{SL} = 0.9R$ . A Malkus state defined in a stratified layer surrounds an interior Taylor state. (b) Geometry of constraint surfaces. . . . .	111
6.2	This graph compares the number of constraints to degrees of freedom (DOF) as a function of toroidal field spherical harmonic resolution with $L_{max} = N_{max}$ , given a fixed poloidal field of $L_{max} = 13$ . This illustrates that for the non-axisymmetric linear system, the number of degrees of freedom (blue circles) exceeds the number of independent constraints (red triangles) for a toroidal field of resolution $L_{max} = N_{max} \geq 10$ . . . . .	123
6.3	Magnetic field at the CMB based on the poloidal field fit to CHAOS-6 at epoch 2015. Visualised using the Mollweide projection and centred on the Greenwich meridian. . . . .	125
6.4	The root mean squared azimuthal field strength (defined over solid angle) $B_{\phi}^{rms} = \sqrt{\int_0^{2\pi} \int_0^{\pi} B_{\phi}^2 \sin \theta \, d\theta \, d\phi}$ , as a function of radius, comparing the strengths of the poloidal field (red) and toroidal field (blue, green, magenta and cyan) for toroidal fields with maximum spherical harmonic degree, order and radial resolution, 13–16 respectively. The poloidal field is the degree 13 field of minimum Ohmic dissipation compatible with the CHAOS-6 model at epoch 2015 (Finlay et al., 2016). . . . .	126
6.5	Minimal toroidal-energy solution (a,c) shown by the azimuthal component, of a Malkus state ( $0.9R < r \leq R$ ) and Taylor state $r \leq 0.9R$ , compared with the total azimuthal component (b,d). Figures (a,b) show the field at a radius of $r = 0.98R$ , close to where the maximum rms azimuthal toroidal field occurs, while (c,d) show the inner region at $r = 0.7R$ . . . . .	127
6.6	Azimuthal field for an unstratified comparative case, for which the magnetic field satisfies only Taylor’s constraint. . . . .	128
6.7	Magnetic field at the CMB based on the 10000-year time average field from CALS10k.2 . . . . .	128

---

6.8	The azimuthal component of the Malkus state magnetic field within the stratified layer at a radius of $r = 0.97R$ , approximately the radius of maximum rms azimuthal toroidal field. . . . .	129
7.1	$u_\phi$ , $E = 10^{-6}$ , $R_a = 10^8$ , $N_0 = 0.0707$ . . . . .	139
7.2	Radial flow contours of the steady state, with a thermally stratified layer in the region ( $r = 0.9 - 1$ ) . . . . .	140
B.1	Fully nonlinear Malkus state with $L_{max} = 3$ , $N_{max} = 3$ with minimal toroidal field. . . . .	148
B.2	Linear Malkus state with minimal toroidal field, showing $B_\phi$ at $r = 0.9R$ , using the method outlined in §6.5 and used for the Earth-like solutions. . . . .	148

# Chapter 1

## Introduction

### 1.1 Earth's interior

The interior of Earth is a complex, non-uniform environment, comprising four clearly distinct layers: a solid inner core, a liquid outer core, a rocky mantle and a thin crust at the surface. This is illustrated in figure 1.1. Each of these regions are distinguishable due to the very different properties and dynamics present within them. The inner core is predominately iron, which is in a solid state as a result of the extremely high pressures near the centre of Earth that lead to freezing of iron despite the high temperature environment. In contrast, within the outer core conditions are such that the iron is in a molten state, where it is able to flow freely. This is a vitally important region, and is the one we are most concerned with in this thesis, as it is this fluid motion of an electrical conductor that is responsible for generating and sustaining Earth's magnetic field. Hence the features of the magnetic field are highly dependent on the currently relatively poorly understood motion in the outer core. Atop the core is the mantle, which is primarily silicate and as such has a very small conductivity and to a reasonable approximation can be considered an electrical insulator that contains no magnetic sources. Finally, there exists a thin crust layer near the surface, which contains the tectonic plates and is made up of rocks that are less dense than the mantle, notably some of which are weakly magnetised, encapsulating the field present during their formation.

The formation of this well established basic picture of Earth's interior shown in figure 1.1 has relied heavily on seismology. The interior structure of Earth can be sensed remotely through the use of teleseismic data, and since the first measurement of an earthquake occurring, performed by Von Reuber Pachwitz in 1889,

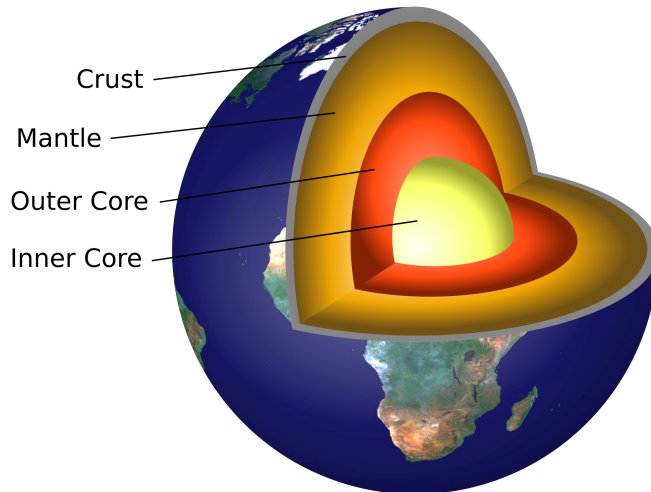


Figure 1.1: The interior structure of Earth.

seismological studies have revealed the structure of the Earth. Two types of particle motion result in two types of body waves in the Earth's interior: Pressure (P) and Shear (S) waves. When an earthquake occurs, teleseismic records show two clear arrivals: a P wave and an S wave. These seismic waves are waves of energy that travel through the Earth. P waves are compressional waves that are longitudinal in nature. These waves can travel through any type of material, including fluids, and can travel at nearly twice the speed of S waves. S waves are shear waves that are transverse in nature, they can travel only through solids, as fluids do not support shear stresses. The propagation velocity of these body waves through the Earth are controlled by the material properties of the medium they are travelling through, specifically the density and elasticity. The density and elasticity, in turn, vary according to temperature, composition, and material phase. Hence the different paths taken by waves detected can reveal information about the structure of the Earth's interior. During the 20th century, seismic observations have led to many notable discoveries that have increased our knowledge of the complex, non-uniform nature of Earth's structure. [Oldham \(1906\)](#) identified the existence of a distinct core through measurements of the delayed arrival times of S waves, and within a few years, [Gutenberg \(1912\)](#) had built on this work to determine the depth of the core-mantle boundary (CMB) to an extraordinarily accurate estimate of 2,900 km, a value extremely close the current best estimate of 2,891km ([Dziewonski and Anderson, 1981](#)). [Lehmann \(1936\)](#) then showed that the core itself is not continuous through the detection of P waves in a region called the 'shadow zone' where no P waves would arrive without reflection at a discontinuity within the core. This was evidence that there must exist an inner core, with different properties compared to the rest of the core and these waves, known as PKiKP waves, must be reflected at the Inner Core boundary (ICB), see [figure 1.2](#).

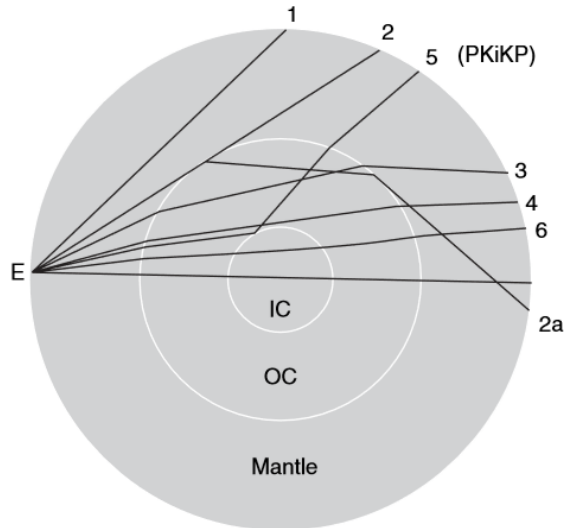


Figure 1.2: The phase PKiKP reflected at the inner core boundary (ray 5) is observed in the shadow zone of the core (between rays 2 and 3), a zone where no P-wave is supposed to arrive [Souriau \(2007\)](#).

This results in the simple ‘low resolution’ picture of Earth’s interior shown in figure 1.1 of inner core, outer core, mantle and crust. However, in more recent years, accuracy and resolution of seismic data has increased, and the layered core-mantle system is seen to exhibit non-uniform structure within each region ([Souriau, 2007](#); [Kind and Li, 2015](#)). Seismic body wave measurements of smaller wave velocities are found in this region immediately beneath the CMB, compared to the bulk of the core. This has helped reignite a long standing debate over the presence of a stratified layer at the outermost part of core ([Bergman, 1993](#); [Braginsky, 1984, 1987](#)). This idea that the outermost part of the core may have a different density and/or elasticity than the rest of the core, and therefore forms a stably stratified layer, can have profound consequences for our understanding of the Earth’s internal structure and dynamics. This will be explored in this thesis, specifically with reference to another key feature of the Earth, its magnetic field.

## 1.2 Earth’s magnetic field

### 1.2.1 Origin of Earth’s magnetic field

William Gilbert first identified that the origin of the Earth’s magnetic field was inside the Earth after conducting a series of experiments and published his results in the classic work *De Magnete* (1600). While this correctly located the origin,

---

Gilbert incorrectly conjectured that the source was a permanent magnet at the centre of the Earth. It was three centuries later that [Larmor \(1919\)](#) suggested that large astronomical bodies might have magnetic fields maintained by a self-sustaining dynamo process. He argued that the circulation of conducting fluid in the presence of a magnetic field would induce an electric field and if a suitable path for electric currents was created in the fluid then a stronger magnetic field could be sustained indefinitely. While he was principally concerned with the sun, it was clear that the same mechanism could be applicable to the Earth.

There are two key strands of evidence that support dynamo theory as the regeneration mechanism responsible for producing the main geomagnetic field. Firstly, paleomagnetic data shows that the field was present as early as 3.4 - 4.2 billion years ago ([Tarduno et al., 2015](#)) and has persisted since this epoch, hence this necessitates the long term sustenance of the field. It would not be possible for permanent magnetism to persist in the conditions of Earth's interior as the ferromagnetic properties of Earth materials means they would lose their permanent magnetisation at the Curie temperature, which occurs at a few tens of kilometres below the Earth's surface ([Maus et al., 1997](#)). Secondly, the dynamic nature of Earth's magnetic field is not compatible with permanent magnetism, but is consistent with dynamo action as its continued source, both in terms of short time scale secular variation, as well as full magnetic polarity reversals, with the latter notably satisfying the feature of the governing equations of dynamo theory, that if a magnetic field  $\mathbf{B}$  is a solution then so must  $-\mathbf{B}$ .

There was a major setback for dynamo theory when the anti-dynamo theorem derived by [Cowling \(1933\)](#), which proves explicitly that no axisymmetric magnetic field can be maintained through a self-sustaining dynamo action by an axially symmetric current, was over-interpreted. He claimed that "Since, then, fields possessing a general similarity to an axially symmetric field cannot be self-maintained, we are led to conclude that the magnetic field of a sunspot is not self-maintained. For the same reason the general magnetic fields of the Sun and the Earth cannot be self-maintained, as was suggested by Larmor". It has since been shown through many example simulations ([Glatzmaier and Roberts, 1995](#)), that while this result prohibits exactly axisymmetric dynamo action, it does not prevent the more general asymmetric magnetic fields thought to be present within the Sun and the Earth. Hence is now widely accepted today that the main geomagnetic field is produced by a dynamo operating in the Earth's fluid outer core.

## 1.2.2 Core convection

Within Earth's outer core, convection is responsible for driving the motion of electrically conducting molten iron, which in the presence of a magnetic field then generates electric currents. The Earth's rotation breaks spherical symmetry, so that the dynamics of convection favours motions in columns parallel to the rotation axis. Hence, the existing magnetic field generates currents that have a favoured orientation, which results in a positive feedback mechanism as they act to enhance the magnetic field. This produces the large magnetic field we observe to be engulfing our planet. One of the main sources of power driving the geodynamo is from the Earth slowly cooling, as primordial heat left over from its formation is lost at the surface. This flow of internal heat drives vigorous convection in the metallic liquid outer core, thus powering the dynamo that sustains the magnetic field. Thermal and compositional convection are normally thought to occur over the entirety of the liquid outer core, except in thin boundary layers at the top and bottom (Jones, 2007). The Earth's core is mainly composed of iron (around 85 wt.%), and a significant fraction of its mass consists of a poorly constrained combination of lighter elements including: silicon, nickel, sulfur, oxygen, carbon and hydrogen (Nimmo, 2007). It is conventionally assumed that vigorous convection leaves the outer core in a well-mixed, adiabatic state on the timescales of interest, that are long compared to convective motions and short compared to Earth's slow evolution (Gubbins et al., 2003). However, the presence of stably-stratified layers at the top and bottom of the core significantly alters this traditional view of a completely mixed and homogenous liquid core.

A stably stratified fluid is arranged in a stable configuration that is denser at the bottom and lighter at the top. Stably stratified fluids are ubiquitous in nature, and within geophysics the most comprehensively studied applications are within atmospheric and oceanic fluid dynamics (Vallis, 2017). While it is relatively simple to observe Earth's stratified atmosphere, which divides naturally into layers based on characteristics such as temperature and composition, it is more challenging to identify such layers within Earth's core. This is largely due to the remote nature of Earth's core, since thousands of kilometres of rock lie between us and the core that evidently inhibits our ability to make direct measurements of the temperature, pressure and composition. If stratified layers do exist within Earth's core, then they could have profound effects on core dynamics and our current understanding of many geophysical phenomena. Stably stratified fluids are dynamically very different from convecting regions. A key distinctive feature inherent to stratified layers is the suppression of radial motion of the fluid, as illustrated in figure 1.3.

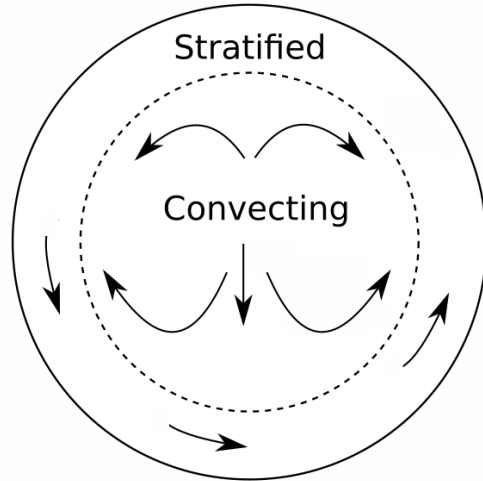


Figure 1.3: Schematic of the fluid motions within convecting and stratified regions.

Radial motion is crucial for radial heat transport within the core to power the geodynamo. This motion is important in the bulk of the liquid core, therefore the existence of any layers in which no radial fluid motion exists would have profound consequences on the nature of Earth’s dynamo. We know from the ‘toroidal theorem’ of [Bullard and Gellman \(1954\)](#) that a purely toroidal flow cannot drive a successful dynamo. In fact this has been generalised by [Proctor \(2004\)](#) to show that a lower bound on the ratio of the poloidal to toroidal velocity exists in order for dynamo action to be possible. Also [Busse \(1975\)](#) independently derives a necessary dynamo condition for the radial velocity in relation to the radial magnetic field. Hence no magnetic field generation can be expected within such stratified layers where radial flow is absent. It is important to note through, that this does not of course preclude the geodynamo within the bulk of the core, but simply provide a physical separation between the extent of the dynamo region and the CMB.

### 1.2.3 Paleomagnetism

Observations of Earth are able to show that not only does it have a magnetic field in the present day, but has done so throughout much of its history. The evidence for this comes from paleomagnetic data and dates back to the first observations that some rocks were magnetised parallel to the Earth’s magnetic field, made by Delesse in 1849 and Melloni in 1853. [Folgerhaiter \(1899\)](#) studied the magnetisation of bricks and pottery and noted that upon firing in the kiln these objects acquired a magnetisation and hence encoded a record of the Earth’s magnetic field at the time and place of firing. It is this same idea which means that ancient rocks provide

snapshots of the Earth's magnetic field throughout history.

The study of rocks formed by lava flows led to a surprising result, as material with natural remanent magnetisation approximately opposite to the present field was discovered. This triggered the first speculation that the Earth's magnetic field had reversed during its past; [Mercanton \(1926\)](#) correctly identified that if a reversal of the Earth's magnetic field had taken place then examples of reversely magnetised rocks should exist in all parts of the world and so spent much of his life obtaining such samples from around the globe.

Paleomagnetism can not only identify polarity reversals but it can also measure smaller variations in the intensity, inclination (the angle made with the horizontal by the Earth's magnetic field lines) and declination (the angle on the horizontal plane between magnetic North and true North) of the Earth's magnetic field. Paleomagnetism is therefore an effective tool for measuring the geomagnetic field over its long time scale evolution. However, due to the limited number of rock samples available and the uncertainties in the estimates, this forms a relatively low resolution picture, that it is not capable of capturing the smaller lengthscale and shorter timescale features of Earth's magnetic field.

#### 1.2.4 Magnetic field observations

The procedure of taking direct magnetic field measurements at different locations on Earth's surface and at different times can reveal many of its spatial and temporal features. These observations of the magnetic field's properties at specific locations in space and time provided the cornerstone for determining the Earth's magnetic field in the pre-satellite era. Ground station observatories and measurements taken on ships, were used to build up a global picture of the geomagnetic field. In 1835 Gauss collated this information and constructed a model of the magnetic field at the Earth's surface; a visualisation of this from [Kono \(2015\)](#) is shown in figure 1.4. Even these relatively sparse data give a sense that the Earth's magnetic field is not uniform but has some distinctive features.

The full dataset of surface observations of the geomagnetic field over the four centuries up to the year 1990 was compiled by [Jackson et al. \(2000\)](#) to construct the `gufm1` model, which provided the most complete update to Gauss' original work. In recent decades satellite measurements have vastly improved global data coverage and resolution and have allowed even more accurate models to be created, for example the `CHAOS-6` model by [Finlay et al. \(2016\)](#) shown in figure 1.5. This

is based on the data from the Swarm satellite launched by the European Space Agency in 2013, which continually measures all magnetic field components to a high accuracy and spatial and temporal resolution.

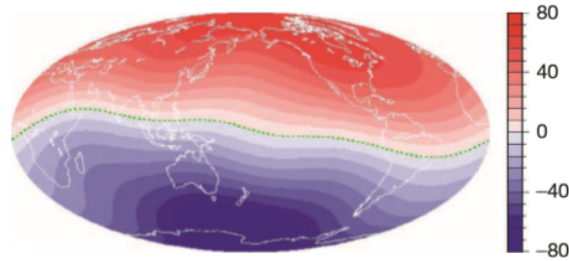


Figure 1.4: Vertical (downward) component of the magnetic field (in microtesla) at the surface of the Earth in 1835 according to the Gauss model. Figure from [Kono \(2015\)](#).

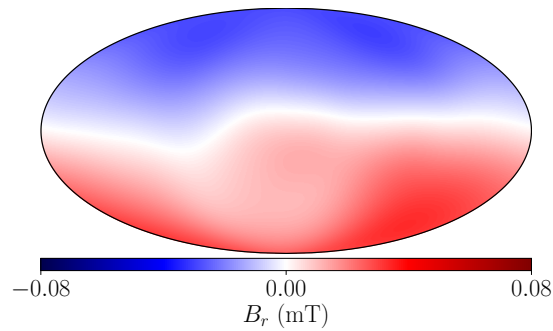


Figure 1.5: Radial (outward) component of the magnetic field at the surface of the Earth in 2015 according to the CHAOS-6 model ([Finlay et al., 2016](#)). Visualised using the Mollweide projection and centred on the Greenwich meridian

The results of these two models visualised in figures 1.4 and 1.5 appear very similar at the Earth's surface with the primary large scale features agreeing, such as the dominantly dipole nature. However, there is increased resolution in the CHAOS-6 model of around 3000km or degree  $l \approx 13$  compared to the Gauss model resolution of around 10000km or degree  $l \approx 4$ . The small wavelength features, by which these models differ, although not important at the Earth's surface, are very significant if the field is downward continued to the CMB, see figures 1.6 and 1.7.

In order to implement the downward continuation of the magnetic field, we introduce the assumption that all material between the observations and the CMB is electrically insulating, and then since conductivity is zero, by Ampère's law  $\nabla \times \mathbf{B} = 0$ , and the magnetic field in the electrical insulator can be written as a potential  $\mathbf{B} = -\nabla V$ , where  $V$  is a scalar function.

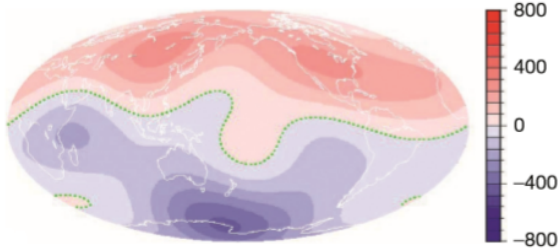


Figure 1.6: Vertical (downward) component of the magnetic field (in microtesla) at the core mantle boundary of the Earth based on Gauss model (1835). Figure from [Kono \(2015\)](#).

Since  $\nabla \cdot \mathbf{B} = 0$ , then  $\nabla^2 V = 0$  and the general solution of Laplace's equation in spherical coordinates gives

$$V = a \sum_{l=1}^{L_{max}} \sum_{m=0}^l \left(\frac{a}{r}\right)^{l+1} (g_l^m \cos(m\phi) + h_l^m \sin(m\phi)) P_l^m(\cos \theta),$$

where  $P_l^m$  is an associated Legendre function,  $a = 6371\text{km}$  is the Earth's mean radius, and  $g_l^m$  and  $h_l^m$  are the Gauss coefficients, which are determined by observations, allowing the magnetic field to be calculated from  $\mathbf{B} = -\nabla V$ . Hence

$$\mathbf{B}_r = \sum_{l=1}^{L_{max}} \sum_{m=0}^l (l+1) \left(\frac{a}{r}\right)^{l+2} (g_l^m \cos(m\phi) + h_l^m \sin(m\phi)) P_l^m(\cos \theta), \quad (1.1)$$

$$\mathbf{B}_\theta = - \sum_{l=1}^{L_{max}} \sum_{m=0}^l \left(\frac{a}{r}\right)^{l+2} (g_l^m \cos(m\phi) + h_l^m \sin(m\phi)) \frac{dP_l^m(\cos \theta)}{d\theta}, \quad (1.2)$$

$$\mathbf{B}_\phi = \frac{1}{\sin \theta} \sum_{l=1}^{L_{max}} \sum_{m=0}^l m \left(\frac{a}{r}\right)^{l+2} (g_l^m \sin(m\phi) - h_l^m \cos(m\phi)) P_l^m(\cos \theta). \quad (1.3)$$

It is the factor of  $\left(\frac{a}{r}\right)^{l+2}$  in this expression for the radial magnetic field (1.1) that is responsible for the effect mentioned above, where the higher degree terms are of enhanced importance at smaller radii.

Downward continuation is an inverse problem, we have surficial observations of the field and we aim to determine the source at the CMB that results in the observed surface field. Inversions can be complex due their ill-posed nature: there are many sets of time-dependent Gauss coefficients that match the observations within a small error. As such the methods used seek a unique solution through calculating a CMB field that minimises both the error to observations and model complexity, resulting in the simplest model that can accurately describe the data. As mentioned earlier the accuracy of the solution is heavily dependent on the accuracy and resolution of observational data. However, despite substantial progress

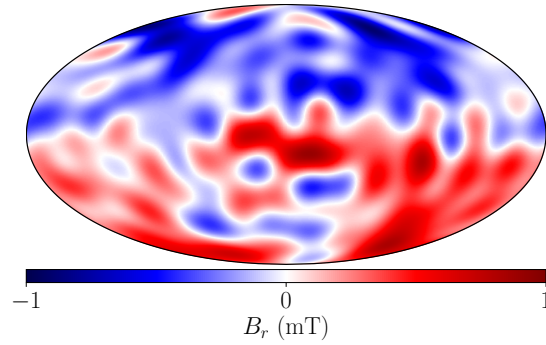


Figure 1.7: Radial (outward) component of the magnetic field at the CMB in 2015 according to the CHAOS-6 model (Finlay et al., 2016).

in satellite measurement technology, there is an additional inherent limitation on the accuracy to which we can estimate the CMB field. This limit to the precision achievable when using observations continued down to the CMB to determine the magnetic field arises due to the Earth's crust. Although very thin, the crust is a source of magnetic field through the permanent magnetism present. It may have only a small intensity in comparison to that from the core, but nevertheless due to its proximity to the surface and hence the observation location, its intensity of  $\mathbf{B} \approx 10\text{nT}$  is similar to the degree 13 terms from the core field. This means that for degrees  $l > 13$  there are two sources of comparable magnitude and hence it is not possible to perfectly isolate and measure the contribution from the core.

### 1.2.5 Archeomagnetic models

Continuous magnetic field models over the long timescales of the human civilisation can be devised through combining the direct observational data available since the sixteenth century, with earlier paleomagnetic records from both geological materials and archaeological artifacts. This allows the construction of models for the last 10-100 ka.

However, archeomagnetic and paleomagnetic observations are difficult. The samples are relatively sparse and even identifying the time and location of these samples requires estimation that can have significant uncertainty. The magnetic field readings provided are then only of one or more components of the field at a specific time and location. This discrete data series therefore needs to be interpolated to create a field model, which normally involves a regularisation process in order to prevent over-fitting, assuming simple consistent behaviour between the data points.

An appropriate weighting is also attached to each data point based on its uncertainty, in order to best achieve robustly accurate models. Uncertainties in the field produced by these models can still be large though, particularly in comparison to direct magnetic field observations (Panovska et al., 2012).

These models include the CALS10k.2 model from Constable et al. (2016) and GGF100k model from Panovska et al. (2019), which provide global magnetic field estimations, continuous in space and time over the last 10 ka and 100 ka respectively. However, the temporal and spatial averaging required in order to achieve such a complete model does have significant effects, most notably in spatial complexity of the resultant field. Although the model is defined up to degree 10 it has power concentrated mostly at degrees 1–4 because of strong regularisation of the sparsely-observed ancient magnetic field structures. Rapid secular variation cannot be deduced from these models either, as the data used have a relatively sparse temporal resolution. These models are valuable when seeking comparisons for many of the theoretically derived models we focus on in this thesis, as it is this slowly evolving large scale field we are concerned with. Rapid and small scale dynamics are directly omitted within many of the approximations made within the dynamo models used.

## 1.3 Dynamo theory

### 1.3.1 Electromagnetism

The term “dynamo” coined by Michael Faraday in 1831 refers to the mechanism by which kinetic energy is converted to magnetic energy. The underlying principles facilitating this phenomenon are that motion of an electrical conductor in the presence of an existing magnetic field will induce electric currents within the conductor and that all electric currents will produce their own magnetic fields.

This means that it is possible for such a process to result in growth of an initial magnetic field and hence successful dynamo action. However, this is not universally the case and is known to be geometry dependent. While successful in some tightly constrained experiments, for example the homopolar disc dynamo (Bullard, 1955), there is no guarantee that the fields will not merely decay for the more complex situations of geophysical and astrophysical interest, which contain a greater number of degrees of freedom for the electric current.

The laws of electromagnetism govern the behaviour of these electric and magnetic fields, which can be written concisely in the form of Maxwell's equations

$$\nabla \cdot \mathbf{E} = \frac{\rho_c}{\epsilon_0}, \quad (1.4)$$

$$\nabla \cdot \mathbf{B} = 0, \quad (1.5)$$

$$\nabla \times \mathbf{E} = -\frac{\partial \mathbf{B}}{\partial t}, \quad (1.6)$$

$$\nabla \times \mathbf{B} = \mu_0 \mathbf{J} + \epsilon_0 \mu_0 \frac{\partial \mathbf{E}}{\partial t}, \quad (1.7)$$

where  $\mathbf{E}$  is the electric field,  $\mathbf{B}$  is the magnetic field,  $\mathbf{J}$  is the electric current and  $\rho_c$  is the charge density. The permittivity of free space  $\epsilon_0$  and magnetic permeability  $\mu_0$  are constants, which are related to the speed of light  $c$  through the following expression

$$c = (\epsilon_0 \mu_0)^{-\frac{1}{2}}. \quad (1.8)$$

It is Faraday's law (1.6) and Ampère's law (1.7), which demonstrate the dynamo mechanism described above, formalising the generation of magnetic field from electric field and vice versa, respectively. Hence the self-sustaining nature of the geomagnetic field is reliant upon the motion of the electrically conductive molten iron within Earth's core being sufficient such that it induces the magnetic field required to produce the necessary current to maintain the same magnetic field.

In order to close the system of electromagnetic equations the empirically derived closure relation, Ohm's law, is introduced

$$\mathbf{J} = \sigma(\mathbf{E} + \mathbf{u} \times \mathbf{B}), \quad (1.9)$$

where  $\mathbf{u}$  is the conductor velocity and  $\sigma$  is the electrical conductivity.

We are able to combine equations (1.4) to (1.7) and (1.9) in order to eliminate  $\mathbf{E}$  and  $\mathbf{J}$  and arrive at an equation solely for the evolution of the magnetic field, known as the induction equation

$$\frac{\partial \mathbf{B}}{\partial t} = \nabla \times (\mathbf{u} \times \mathbf{B}) + \eta \nabla^2 \mathbf{B}, \quad (1.10)$$

where  $\eta = (\mu_0 \sigma)^{-1}$  is the magnetic diffusivity. In order to do so we have made what is known as the "MHD approximation", which is valid provided all velocity magnitudes are small in comparison to the speed of light and hence relativistic effects can be neglected. We will use this approximation throughout, as it is generally valid for planetary core dynamics; it is this which facilitates the neglect of the final term in equation (1.7), as can be shown by a trivial scaling analysis (Desjardins and

Dormy, 2007).

Equation (1.10) describes the conversion between kinetic and magnetic energy, however in order to sustain both fields against dissipation, an external source of energy is required. Within the Earth's core this is the cooling and growth of the inner core, driving thermochemical convection throughout the outer core, with the continual source of energy responsible for the persistent powering of the dynamo that sustains the geomagnetic field. This is represented by the following equation, which arises from the requirement of conservation of energy

$$\frac{\partial T}{\partial t} = -(\mathbf{u} \cdot \nabla)T + S + \kappa \nabla^2 T, \quad (1.11)$$

where  $T$  is Temperature,  $S$  is a heat source and  $\kappa$  is thermal diffusivity.

### 1.3.2 Fluid dynamical equations

In order to understand the Earth's dynamo problem and accurately predict the resulting magnetic field, we need a more general study of the motion of rotating fluids under electromagnetic and buoyancy forces. Throughout this work we will use the Boussinesq approximation, which assumes that changes in fluid density are accounted for only in the buoyancy force. This approximation is reasonable in Earth's core (Gubbins and Roberts, 1987) and hence is widely used as it considerably simplifies the governing equations and required numerical methods.

In a cylindrical coordinate system  $(s, \phi, z)$  rotating with the Earth at angular speed  $\Omega$  where the  $z$ -axis is the axis of rotation, the governing fluid equations arising from conservation of mass and momentum, when coupled with equations (1.10) and (1.11), govern the evolution of fluid velocity  $\mathbf{u}$  and magnetic field  $\mathbf{B}$ .

From the requirement of conservation of mass, we have the Continuity equation:

$$\nabla \cdot \mathbf{u} = 0. \quad (1.12)$$

Due to conservation of momentum, we have the Navier-Stokes equation:

$$\rho_0 \frac{D\mathbf{u}}{Dt} = -\nabla p' + \mu \nabla^2 \mathbf{u} - 2\rho_0(\boldsymbol{\Omega} \times \mathbf{u}) + (\mathbf{J} \times \mathbf{B}) + \rho' \mathbf{g} + \rho' \boldsymbol{\Omega} \times (\boldsymbol{\Omega} \times \mathbf{s}), \quad (1.13)$$

where  $\mathbf{g}$  is gravitational acceleration,  $\mu$  is dynamic viscosity, related to the later used kinematic viscosity  $\nu = \mu/\rho_0$ ,  $\frac{D\mathbf{u}}{Dt} = \frac{\partial \mathbf{u}}{\partial t} + \mathbf{u} \cdot \nabla \mathbf{u}$  is the material velocity derivative,  $\rho_0$  is the background density and  $\rho'$  is the density perturbation from  $\rho_0$ .

We can simplify this by defining the buoyancy force  $F_B$ , which includes both gravitational and centrifugal forces, is purely spherically radial and given by

$$F_B \hat{\mathbf{r}} = \rho' \mathbf{g} + \rho' \boldsymbol{\Omega} \times (\boldsymbol{\Omega} \times \mathbf{s}) = \rho' \mathbf{g} + \rho' \nabla \left( \frac{1}{2} (\mathbf{s} \times \boldsymbol{\Omega})^2 \right).$$

This reduces the Navier-Stokes equation to

$$\rho_0 \frac{D\mathbf{u}}{Dt} = -\nabla p' + \mu \nabla^2 \mathbf{u} - 2\rho_0 (\boldsymbol{\Omega} \times \mathbf{u}) + (\mathbf{J} \times \mathbf{B}) + F_B \hat{\mathbf{r}}. \quad (1.14)$$

Dimensionless variables indicated by bars can be introduced through factoring out the characteristic global scales of each quantity, in order to non-dimensionalise equation (1.14).

$$\mathbf{u} = U \bar{\mathbf{u}}, \quad \mathbf{s} = L \bar{\mathbf{s}}, \quad \boldsymbol{\Omega} = \Omega \bar{\boldsymbol{\Omega}}, \quad p' = \rho_0 \Omega U L \bar{p}', \quad \mathbf{B} = B \bar{\mathbf{B}}, \quad \mathbf{J} = \sigma U B \bar{\mathbf{J}}, \quad F_B = b \bar{F}_B.$$

The specific set of quantities for which characteristic scales of all quantities are expressed in terms of, is not a unique choice, many such spanning sets exist. All choices are physically equivalent, but can in turn lead to a different set dimensionless control parameters. In this choice velocity is explicitly scaled, as opposed to time,  $\mathbf{J}$  is scaled according to Ohm's law (1.9) and the buoyancy force is simply scaled by  $b$ , a parameter introduced to explicitly represent this.

The non-dimensionalisation process is useful as it leads to a system influenced solely by dimensionless parameters, which represent the relative importance of different terms in the equations. It is then the magnitudes of these parameters, which can be compared between a simulated problem and the physical problem of interest, that can be used to deduce applicability. It also facilitates the construction of reduced models, which utilise approximations devised to capture the essence of the problem through the dominant force balance. Through this we arrive at the dimensionless equation

$$R_o \frac{D\bar{\mathbf{u}}}{D\bar{t}} = -\nabla \bar{p}' + E \nabla^2 \bar{\mathbf{u}} - 2(\bar{\boldsymbol{\zeta}} \times \bar{\mathbf{u}}) + El (\bar{\mathbf{J}} \times \bar{\mathbf{B}}) + R_a \bar{F}_B \hat{\mathbf{r}}, \quad (1.15)$$

where we have introduced four important dimensionless numbers: The Ekman number, Rossby number, Elsasser number and modified Rayleigh number. The Ekman number  $E = \frac{\nu}{L^2 \Omega}$  describes the ratio of viscous forces to rotational forces. Within the setting of the Earth's outer core this characterises the relative significance of viscous forces within the molten iron and nickel fluid, and the Coriolis forces arising from the planetary rotation and is notably small, at approximately  $10^{-15}$ . The

Rossby number  $R_o = \frac{U}{L\Omega}$  defines the ratio of inertial forces to rotational forces and thus represents the importance of Coriolis accelerations due to the Earth's rotation and also has a small value of approximately  $10^{-9}$ . The Elsasser number  $El = \frac{\sigma B^2}{\rho_0 \Omega}$  defines the ratio of the Lorentz force to the Coriolis force and expresses the magnitude of the Earth's magnetic field in relation to its rotational forces, believed to be around unity. The modified Rayleigh number  $R_a = \frac{b}{U\Omega\rho_0}$  specifies the ratio of buoyancy forces to rotational forces, it indicates the strength of convection body in comparison to the Coriolis forces. In the vigorously convecting outer core fluid this is estimated to be in the range of  $10^{20} - 10^{30}$ .

We note that it is also possible to express this system in an equivalent manner using a combination of different dimensionless numbers to define parameter space. The Reynolds number  $R_e = \frac{UL}{\nu}$ , Magnetic-Prandtl number  $P_m = \frac{\nu}{\eta}$  and Alfvén number  $A = \frac{U(\mu_0\rho_0)^{1/2}}{B}$  are all widely used, with estimated values for the Earth of  $10^{15}$ ,  $10^{-6}$  and  $10^{-2}$  respectively.

### 1.3.3 Numerical Dynamo models

Numerical simulations of rotating magnetoconvection within a spherical shell domain, as governed by equations (1.10) to (1.12) and (1.14), are a very useful tool for understanding the motion within Earth's outer core. This has been a very active field of research in the last 25 years, since the first self-consistent three-dimensional geodynamo simulations were carried out by [Glatzmaier and Roberts \(1995\)](#) and [Kageyama and Sato \(1995\)](#). Analysing these computational simulations has been insightful in furthering knowledge of many properties of the geomagnetic field, from rapid field fluctuations to full polarity reversals

Many spectral method codes have since been developed for the task of simulating the coupled non-linear system of the Navier-Stokes, induction and temperature equations (1.10), (1.11) and (1.14) for an incompressible fluid in a spherical cavity. Some of the best examples include those by [Schaeffer \(2013\)](#); [Aubert et al. \(2008\)](#); [Hollerbach \(2000\)](#); [Tilgner and Busse \(1997\)](#), which have been used for a large range of numerical studies into the nature of dynamo action.

Great efforts have been made to best optimise these codes to achieve fast convergence and run efficiently in parallel. However, despite this, even using modern supercomputers does not allow one to run simulations with Earth-like parameters ([Roberts and Aurnou, 2011](#)). This is because the motion in Earth's outer core is in the very extreme parameter range mentioned previously. Some forces are very small

in comparison to others, specifically rotational forces are dominant over inertial and viscous forces, which means the Ekman and Rossby numbers are inaccessibly small.

Recent simulations have been able to probe more Earth-like parameter regimes than previously possible, however Ekman numbers of  $E = 10^{-7} - 10^{-8}$  (Schaeffer et al., 2017; Aubert, 2019) remain at the limit of computing power. Despite the progress, these simulations remain in parameter regimes vastly different to that of the Earth (Christensen and Wicht, 2015), (also see figure 1.8). The problem of increased computational expense when attempting to move toward Earth parameters arises because smaller  $E$  values require both fine spatial and temporal resolution in order to fully resolve a direct numerical simulation. In spite of this significant challenge, numerical models have been used with great success to simulate aspects of the geodynamo, reproducing features such as torsional oscillations (Wicht and Christensen, 2010) that are consistent with observational models (Gillet et al., 2010), geomagnetic jerks (Aubert and Finlay, 2019) and allowing predictions of the Earth’s magnetic field strength (Christensen et al., 2009). The inescapable question of how representative of the Earth they really are is ever-present though, as force balances can still vary significantly between the simulation regime and the correct regime of the Earth (Wicht and Sanchez, 2019), with the ability to simultaneously reproduce Earth-like field morphology and reversal frequency still beyond current capabilities (Christensen et al., 2010). The assessments conducted by Sprain et al. (2019) show that present geodynamo models are unable to satisfactorily reproduce all aspects of Earth’s long term field behaviour. This highlights the potential value in the alternative idealised models that we focus on in this thesis.

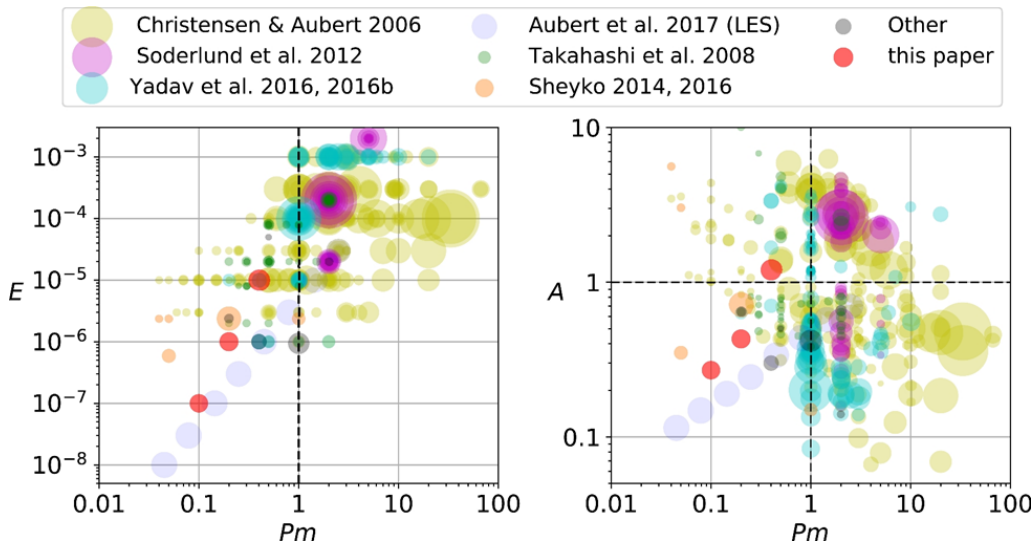


Figure 1.8: Ekman - Magnetic Prandtl and Alfvén - Magnetic Prandtl regime diagrams showing the currently possible range of simulation parameters. The Earth’s core lies far away beyond the bottom left corner at  $E = 10^{-15}$ ,  $P_m = 10^{-6}$ ,  $A = 10^{-2}$ . Figure from Schaeffer et al. (2017) (to which the ‘this paper’ points refer.)

## 1.4 Data assimilation models

Establishing an understanding of the flow and magnetic field inside the core has proved a very challenging task as observations can only reveal information of the exterior surface of the core. A method that has recently been developed to image inside the core is using data assimilation to construct an inverse model. The principle is to combine the knowledge from observational data and numerical simulations, in order to seek the most likely core state accounting for the CMB field and secular variation data, while being statistically compliant with the output of a numerical model of the geodynamo. Using first principle dynamical equations, describing the convective dynamo allows a construction of physical laws linearly connecting some quantities of the system as well as the long-range statistical correlations that exist between these quantities. This allows underlying properties of the internal core to be inferred through knowledge of only surface observations.

[Fournier et al. \(2007\)](#) outlines how to implement this method and explains why it may be a promising path to pursue as a way of translating knowledge of the CMB magnetic field into information on the field dynamics interior to the core. Subsequent studies have built upon this through the use of three-dimensional numerical simulations of the geodynamo along with observational data of the geomagnetic field and its secular variation at the CMB. For a fully convective core recent work by [Aubert and Fournier \(2011\)](#); [Aubert \(2012, 2014\)](#) has implemented the inverse geodynamo model and iteratively improved it to provide whole core inversions for the three unknown physical fields characterising Earth's core dynamics: the velocity, density anomaly and magnetic fields, at snapshots where the main magnetic field, its secular variation and their error statistics are supplied by observational geomagnetic field data.

However, we note that the existence of a stratified layer has obvious implications for the applicability of this approach, which is founded on observations at the CMB revealing the correct free stream magnetic field, whereas a stratified layer would provide a disconnect between them. The force balance may differ considerably within a stratified layer. The compatibility of classes of externally observable magnetic fields with a stratified layer is something we consider in Chapter 6, as we investigate whether all structures of exterior potential fields are consistent with an assumed magnetostrophic balance and the presence of a strongly stratified layer.

## 1.5 Thesis outline

How the geomagnetic field is generated in Earth’s liquid outer core by the geodynamo remains one of the greatest outstanding problems in Earth science. This magnetic field is important because it protects us from harmful radiation from solar and cosmic rays. As we have discussed, observations from Earth’s surface can only constrain the structure of the magnetic field at the edge of the core and the correct parameter regime of the Earth is unachievable by numerical simulations and as a result many unanswered questions remain.

The objective of this thesis is to advance our understanding of how the geomagnetic field is generated in Earth’s liquid outer core by the geodynamo and to constrain the possible structure of the field within the core. We approach this through considering the limit of negligibly small inertia and viscosity, characterised by  $E = R_o = 0$ , resulting in what is termed the magnetostrophic force balance. In his seminal work, [Taylor \(1963\)](#) argued that this is the geophysically relevant limit for dynamo action within the outer core. Within this limit, he showed the existence of a necessary condition, now well known as Taylor’s constraint, which requires that the cylindrically-averaged Lorentz torque must everywhere vanish; magnetic fields that satisfy this condition are termed Taylor states. This provides the foundation for much of our work, as we utilise the mathematical framework to develop a realistic model of the large-scale background structure of the internal magnetic field operating within this constrained dynamical system. We specifically extend current understanding through considering temporal field evolution and investigating the impact of a stratified layer, all while remaining consistent with geomagnetic observations.

In chapter 2 we introduce in detail the necessary theory behind the magnetostrophic dynamo system, discussing the assumptions and features within the model and the approaches that one can take to best apply this to the geodynamo. In chapter 3 we consider the evolution of Taylor states, and develop the first complete description of the fluid flows generated by a Taylor state magnetic field in three-dimensions. As we show, it becomes necessary to separate the flow into an ageostrophic flow, which has zero cylindrical average, and a geostrophic component acting solely in the azimuthal direction  $\mathbf{u} = \mathbf{u}_a + u_g \hat{\phi}$ . It is the geostrophic flow  $u_g$ , which is challenging to solve for. We prove that the ordinary differential equation (ODE) derived by [Taylor \(1963\)](#) is generally in error due to an incomplete treatment of the boundary conditions. We provide a correction to this through the means of an alternate solution method. In chapter 4 we consider the evolution of Taylor

states. Through computing the magnetic fields induced by these correct instantaneous flows, as well as running dynamical magnetostrophic simulations with a range of Taylor state initial conditions, we examine how rapidly these fields change. We find that many Taylor states exist that have a comparable rate of change to that of the geomagnetic field. However, very few steady stable Taylor states are found to exist, that is Taylor states which are capable of remaining constant through self-sustenance over prolonged periods of time.

In chapter 5 we summarise the evidence for and against the existence of a stratified layer at the top of Earth's core. We discuss how such a layer may have formed and the possible implications of its presence for observations of the geomagnetic field. The work presented in chapter 6 extends the concept of a Taylor state to stratified fluids in order to account for any stratified layer in Earth's core. This leads to introducing the idea of "Malkus states", building on the work by [Malkus \(1979\)](#). We provide the first example of such fields and find solutions consistent with geomagnetic observations, which reveals notable features of the required magnetic field at the top of the Earth's core, within such a stratified layer. Finally, in chapter 7 we conclude with a summary of our results and a discussion of possible future work.



## Chapter 2

# Magnetostrophy

### 2.1 The Magnetostrophic approximation

As we showed in §1.3.2, the full momentum equation which describes the motion of a convectively driven, rotating, electrically conductive fluid, within the presence of a magnetic field is:

$$R_o \frac{D\mathbf{u}}{Dt} = -\nabla p' + E\nabla^2 \mathbf{u} - 2(\hat{\mathbf{z}} \times \mathbf{u}) + El(\mathbf{J} \times \mathbf{B}) + R_a F_B \hat{\mathbf{r}}. \quad (2.1)$$

This equation represents a balance of the forces acting on the fluid: inertia, pressure, viscosity, Coriolis, Lorentz, and buoyancy. However, these forces are not always of equal importance for impacting the fluid behaviour. In many systems there is a hierarchy of force balances. The leading order balance is dominantly responsible for governing the dynamics, while there also exists a series of subdominant balances, which include different forces and modify the overall dynamics by a lesser degree. This motivates the idea of obtaining a simpler system to analyse, which remains accurate to a first order approximation, through neglecting those forces absent from the dominant force balance.

The relative magnitude of these forces are encapsulated in the dimensionless numbers. Within the Earth's outer core the fluid is subject to rapid rotation, while the inertia and viscosity of the fluid are comparatively small; this results in  $E, R_o \ll 1$  (estimates suggest  $E \approx 10^{-15}$  and  $R_o \approx 10^{-9}$  (Gubbins and Roberts, 1987)). The magnitude of the Elsasser number is not so obvious as both rotational and magnetic forces can be large. However, it is argued that Lorentz forces in the

core approximately balance with Coriolis forces, and although this is somewhat uncertain, (not least due to incomplete knowledge of the toroidal field strength) best estimates put  $El \approx 1$  (Fearn and Roberts, 2007), at least at the large scale of a global force balance (Aurnou and King, 2017). Therefore it has been proposed that the flow within Earth’s outer core falls within the dynamical regime characterised by the so-called ‘magnetostrophic balance’, between the Coriolis, pressure, buoyancy and Lorentz forces.

It is important to note that which forces are pre-eminent is often dependent on the length and times scales of interest. Here we have nondimensionalised based on the global length-scale of the core radius, so are focusing on the global force balance. At smaller scales the scenario can differ considerably, for example viscous effects are inversely correlated with length-scale so are key in very small scale fluid behaviour.

The resulting dimensionless magnetostrophic regime then involves the following exact balance between the four remaining forces

$$2(\hat{\mathbf{z}} \times \mathbf{u}) = -\nabla p' + F_B \hat{\mathbf{r}} + (\nabla \times \mathbf{B}) \times \mathbf{B}, \quad (2.2)$$

or

$$2(\hat{\mathbf{z}} \times \mathbf{u}) = \mathbf{A} + F_B \hat{\mathbf{r}}, \quad \text{where } \mathbf{A} \equiv -\nabla p' + (\mathbf{J} \times \mathbf{B}). \quad (2.3)$$

## 2.2 Derivation of Taylor’s constraint

From equation (2.2) an important constraint can be derived, which is a necessary condition for the existence of a solution to the magnetostrophic system (Taylor, 1963) and a fundamental building block for the research area our work lies within. Hence we outline here the derivation of the ‘Taylor constraint’ (Taylor, 1963) within the simple geometry of a full sphere domain.

Consider a cylinder with radius  $s_0$ , co-axial with the axis of rotation of a full sphere domain. Integrate the azimuthal component of equation (2.2) (noting that the buoyancy force has no  $\phi$  component) over the part of the cylinder which lies within the fluid sphere (as shown in figure 2.1)

$$2 \int_{s=s_0} (\hat{\mathbf{z}} \times \mathbf{u})_\phi s \, d\phi dz = \int_{s=s_0} s A_\phi \, d\phi dz,$$

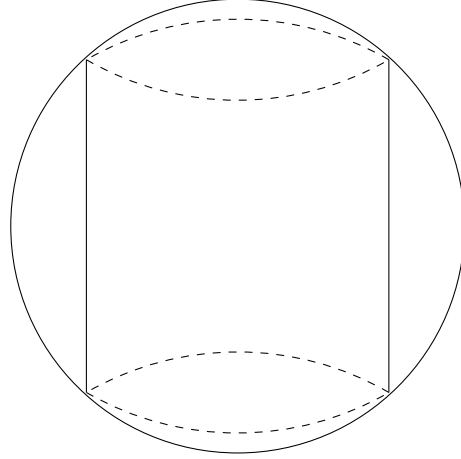


Figure 2.1: A schematic diagram illustrating the cylindrical surface within a spherical domain and the closure this surface using the spherical caps (dashed lines).

since  $(\hat{\mathbf{z}} \times \mathbf{u})_\phi = u_s$ , we have

$$2 \int_{s=s_0} u_s s \, d\phi dz = \int_{s=s_0} s A_\phi \, d\phi dz,$$

or

$$2 \int_{s=s_0} \mathbf{u} \cdot \hat{\mathbf{n}} \, d\Sigma = \int_{s=s_0} s A_\phi \, d\phi dz, \quad (2.4)$$

where  $\Sigma$  is the surface of revolution of the cylinder and  $\hat{\mathbf{n}}$  is the unit normal vector to the surface.

Since  $\mathbf{u} \cdot \hat{\mathbf{n}} = 0$  over the spherical caps we can extend the integral from being over the surface of revolution to being over the closed surface of the cylinder plus the spherical caps. This means including the surfaces outlined with dashed lines in figure 2.1. Now the surface is closed we can apply Gauss' divergence theorem

$$\int \mathbf{u} \cdot \hat{\mathbf{n}} \, d\Sigma_T = \int \nabla \cdot \mathbf{u} \, dV,$$

where  $\Sigma_T$  is the closed surface of the surface of revolution of the cylinder plus the spherical caps. Then equation (2.4) becomes

$$2 \int \nabla \cdot \mathbf{u} \, dV = \int_{s=s_0} s A_\phi \, d\phi dz,$$

and since for an incompressible Boussinesq fluid  $\nabla \cdot \mathbf{u} = 0$ , we obtain the result

$$\int_{s=s_0} s A_\phi \, d\phi dz = 0 \quad \Rightarrow \quad \int_{s=s_0} A_\phi \, d\phi dz = 0, \quad (2.5)$$

or explicitly in terms of the magnetic field  $\mathbf{B}$ , since pressure is single-valued its

contribution is zero and we have that as a direct consequence of the magnetostrophic balance, the magnetic field must obey at all times the condition

$$\int_{C(s)} ((\nabla \times \mathbf{B}) \times \mathbf{B})_{\phi} d\phi dz = 0, \quad (2.6)$$

for any right cylinder  $C(s)$  of radius  $s$ , coaxial with the rotation axis. [Taylor \(1963\)](#) proved this result and hence that the couple on any annular cylinder co-axial with the axis of rotation must be zero. The following theorem is what is known as, and will be referred to throughout this thesis, as Taylor's constraint, and any magnetic field which exactly satisfies this is known as a Taylor state.

**Theorem 2.2.1.** *If a rotating fluid is contained in a rigid envelope in the form of a surface of revolution then for there to exist a velocity  $\mathbf{u}$  compatible with the magnetostrophic system (2.2) it is necessary for the magnetic field to satisfy a constraint which can be written as*

$$T(s, t) \equiv \int_{C(s)} ((\nabla \times \mathbf{B}) \times \mathbf{B})_{\phi} d\phi dz = 0. \quad (2.7)$$

[Taylor \(1963\)](#) also proved that not only is this a necessary condition for the existence of a solution for  $\mathbf{u}$ , but it is also a sufficient condition, meaning that if it is satisfied then a solution for  $\mathbf{u}$  must exist. The search for such solutions however, is a non-trivial task and is the focus of Chapter 3 of this thesis.

The geometry of Earth's outer core is of course a spherical shell rather than a full sphere. This leads to additional complications for Taylor's constraint as shown by [Livermore et al. \(2008\)](#). The presence of an inner core splits up the geostrophic cylinders over which Taylor's constraint applies into three distinct regions. Cylinders of radii greater than the inner core (outside of what is known as the tangent cylinder) remain unchanged, but within the tangent cylinder the north and south polar regions are disconnected, and the geostrophic contours are partitioned into two distinct sets. This results in a total of three separate sets of Taylor constraints, which makes enforcing the condition more challenging. In the majority of work reported in this thesis we restrict ourselves to a full sphere domain to avoid such difficulties.

## 2.3 Magnetostrophic Dynamo simulations

This approach of utilising an explicit assumption of an exact magnetostrophic balance (2.2) is not only useful for theoretical analysis but can also be used as the

basis to formulate numerical models. These are an alternative to the full numerical dynamo models discussed in §1.3.3, overcoming the difficulties caused by the extreme parameter regime through using them in our favour to apply an *a priori* magnetostrophic approximation. The advantage of this is that the challenging aspects of rapid timescales and very short viscous lengthscales are removed and this approximation will likely lead to a computationally less demanding set of equations to solve. The idea that this allows a different and geophysically relevant parameter space to be explored is visualised in figure 2.2.

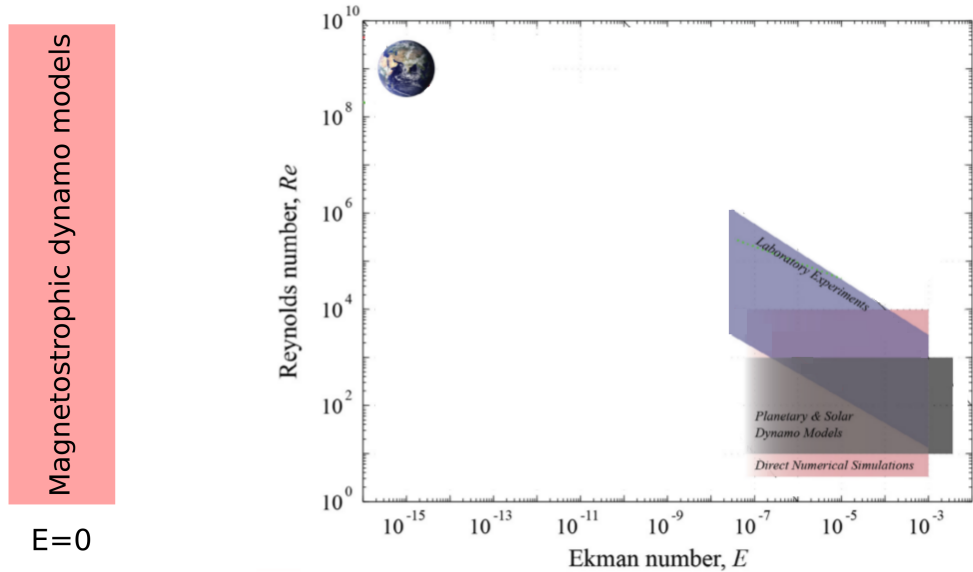


Figure 2.2: Reynolds–Ekman regime diagram showing the different capabilities of various methods of studying rotating convection and dynamo physics. The regions of parameter space occupied by Earth and magnetostrophic models are also indicated. Figure modified from [Aurnou et al. \(2015\)](#).

This is a very new and actively developing field; dynamical models produced by evolving the magnetic field subject to Taylor’s constraint have appeared very recently ([Wu and Roberts, 2015](#); [Roberts and Wu, 2018](#); [Li et al., 2018](#)). These are currently restricted to axisymmetry, although the model of [Li et al. \(2018\)](#) is general enough that it can be simply extended to a three-dimensional system. In this framework, the full sphere model (neglecting the solid inner core), of the geodynamo requires a solution of (2.2) alongside equations describing the evolution of  $\mathbf{B}$  and  $F_B$  within the core, whose boundary conditions derive from the surrounding electrically-insulating impenetrable overlying mantle.

However, as we cover in detail in Chapter 3, calculating the flow required to maintain a magnetostrophic balance, specifically the geostrophic component of the flow, is far from straightforward. Despite this, some methods to evolve the

magnetostrophic equation have shown success. By treating a version of the Taylor integral (2.7) that is specific to axisymmetry (Braginsky, 1970; Jault, 1995), Wu and Roberts (2015) demonstrated that they could evolve the magnetostrophic system by solving a first-order differential equation for the geostrophic flow, rendering the Taylor integral zero to first order, and went on to apply it to a variety of examples. In an independent line of investigation Li et al. (2018) showed that, by using control theory, it is possible to find  $u_g$  implicitly such that the Taylor integral is zero at the end of any finite timestep.

The advancement of these models, which are currently in their relative infancy, is a promising area of research within the community. A breakthrough here would provide a valuable resource as a route to create a fully 3D model for simulating dynamo action within a full three-dimensional sphere, which is capable of representing the Earth-like magnetostrophic force balance. This would act as an alternative to the mainstream numerical models with weak viscosity and inertia. Additionally, these models can be modified in order to probe the effect of re-introducing a linear inertial force, permitting short timescale deviations from an exact magnetostrophic balance and incorporating the behaviour driven by torsional waves (Roberts and Wu, 2014; Li et al., 2018).

## 2.4 The magnetostrophic limit

There is a further, intermediate approach to investigating the approximately magnetostrophic geodynamo, through formally including viscosity and inertia and then investigating the limit as both  $E$  and  $R_o$  become small (Jault, 1995). In such models, it is important that the Lehnert number,  $\lambda = \frac{B}{\Omega L(\mu_0 \rho_0)^{1/2}}$  (estimated to be  $10^{-4}$  in Earth's core) is small in order that inertial modes separate from magneto-Coriolis waves and can be filtered out (Jault, 2008). It is also worth noting that since a significant part of the Coriolis term may be balanced by the pressure gradient (e.g. Aubert et al., 2017), the simple estimates of the Rossby number reported earlier may be too small. A different estimate of importance of inertia is the Alfvén number (measuring the square root of the ratio of kinetic to magnetic energies), whose small value of  $A \sim 10^{-2}$  still supports neglecting the inertial term although with weaker justification (Schaeffer et al., 2017). Arguably retaining inertia and viscosity would result in models closer to geophysical reality than those that are purely magnetostrophic as this is precisely the regime of the Earth's core. A variety of studies reported evidence of behaviour independent of  $E$  in the inviscid

Taylor-state limit, either from a direct solution (Fearn and Rahman, 2004), or from solving the equations assuming asymptotically small  $E$  (Hollerbach and Ierley, 1991; Soward and Jones, 1983). To date, all models of this type have been axisymmetric and there have been no attempts at a general 3D implementation of these ideas. One difficulty with treating asymptotically-small  $E$  is that the resulting equation for  $u_g$  is an extremely delicate ratio of two small terms, whose form is dependent on the specific choice of mechanical boundary conditions (Livermore et al., 2016). The convergence of magnetostrophic and asymptotically low- $E$  models remains an outstanding question, as it is unclear whether the limit is regular or singular.

## 2.5 Mean field theory

The geomagnetic field is observed to be approximately axisymmetric (figure 1.7), with a dominant and stable axial dipole component. Therefore an obvious reduced model to simply represent the geodynamo is one that is restricted to this symmetry. The two-dimensional system, allows faster numerical computation and additional theoretical analysis to be carried out. Unfortunately, the anti-dynamo theorem of Cowling (1933) proved that it is not possible for an axisymmetric magnetic field to be maintained through a self-sustaining dynamo action by an axially symmetric current.

While problematic, this does not entirely preclude the use of axisymmetric models. The theory of mean field electrodynamics first proposed by Parker (1955), provides a mechanism to circumvent Cowling’s theorem. He provided the first simple conceptual picture of how a two scale process might operate a dynamo. The concept is that the velocity of small scale ‘cyclonic’ fluid motions are crucial for twisting magnetic field lines, and therefore via Ampère’s law (1.6), inducing a component of electromotive force (EMF) parallel to the original large scale magnetic field. This simple but powerful model of Parker (1955) relies on the basic assumption, that it is possible to decompose the flow and magnetic field into distinct large and small scale components, and the generation of the small scale fluctuating parts of the magnetic field, is proportional to the large scale averaged magnetic field.

Using this two-scale approach we split the full velocity  $\mathbf{u}$  and magnetic field  $\mathbf{B}$  into mean and fluctuating components, denoted by overbars and primes respectively,

$$\mathbf{u} = \bar{\mathbf{u}} + \mathbf{u}', \quad \mathbf{B} = \bar{\mathbf{B}} + \mathbf{B}'.$$

The choice of averaging here can take many forms, but importantly it must obey the Reynolds averaging rules: it must be a linear operation, commute with differentiation, and once averaged, further averaging of that quantity must have no effect.

Given a small scale turbulent flow and a large scale mean field, we can average over an intermediate length scale. Similarly a temporal average can instead be applied over an intermediate timescale, so long as the turbulence has a short correlation time. Alternatively, for axisymmetric dynamo models we can average over a particular coordinate, namely  $\phi$ , such that the large scale field is entirely axisymmetric, while non-axisymmetric fluctuations are present.

After applying the decomposition and a suitable average the induction equation becomes

$$\frac{\partial \bar{\mathbf{B}}}{\partial t} = \nabla \times (\bar{\mathbf{u}} \times \bar{\mathbf{B}}) + \nabla \times \overline{(\mathbf{u}' \times \mathbf{B}')} + \eta \nabla^2 \bar{\mathbf{B}} = \nabla \times (\bar{\mathbf{u}} \times \bar{\mathbf{B}}) + \nabla \times \boldsymbol{\varepsilon} + \eta \nabla^2 \bar{\mathbf{B}},$$

and

$$\frac{\partial \mathbf{B}'}{\partial t} = \nabla \times (\mathbf{u}' \times \bar{\mathbf{B}}) + \nabla \times (\bar{\mathbf{u}} \times \mathbf{B}') + \nabla \times (\mathbf{u}' \times \mathbf{B}') - \nabla \times \overline{(\mathbf{u}' \times \mathbf{B}')} + \eta \nabla^2 \mathbf{B}',$$

where  $\boldsymbol{\varepsilon} = \overline{(\mathbf{u}' \times \mathbf{B}')}$  is the mean EMF.

This is now a complicated equation that in general can not be solved analytically, so this is where it was proposed by [Steenbeck et al. \(1966\)](#) that we assume  $\mathbf{B}'$  depends linearly on  $\bar{\mathbf{B}}$  and hence  $\boldsymbol{\varepsilon}$  is a linear functional of  $\bar{\mathbf{B}}$ . Assuming the simplest possible such relation allows us to write

$$\varepsilon_i = \alpha_{ij} \bar{B}_j + \beta_{ijk} \frac{\partial \bar{B}_j}{\partial x_k},$$

where the tensors  $\alpha_{ij}$  and  $\beta_{ijk}$  depend only on the flow and are assumed to be isotropic, and hence  $\alpha_{ij} = \alpha \delta_{ij}$  and  $\beta_{ijk} = \beta \epsilon_{ijk}$ .

This results in the mean field dynamo equations

$$\frac{\partial \bar{\mathbf{B}}}{\partial t} = \nabla \times (\bar{\mathbf{u}} \times \bar{\mathbf{B}}) + \nabla \times \alpha \bar{\mathbf{B}} + (\eta + \beta) \nabla^2 \bar{\mathbf{B}}.$$

The first term on the right hand side here represents the inductive effect of large scale shear flow and is known as the  $\omega$ -effect. The new second term represents the crucial difference in this averaged version of the induction equation, it acts as a source term for the mean field through the process of small scale turbulent motions acting on a toroidal field to produce a source term for the averaged poloidal field and vice versa, and is known as the  $\alpha$ -effect. The  $\beta$  contribution can just be regarded as an additional turbulent contribution to the diffusivity as shown in the third term.

It must be noted that this argument is very heuristic and difficult to rigorously justify within the geophysical setting, and even if accepted, the way in which to choose both the spatial form and magnitude of  $\alpha$  for a given problem is fairly arbitrary. One of the most commonly chosen forms for the spatially-dependent prescribed scalar  $\alpha$  is

$$\alpha = \alpha_0 \frac{729}{16} r^8 (1 - r^2) \cos \theta,$$

for some constant  $\alpha_0$ , which specifies the magnitude of the  $\alpha$ -effect (Roberts, 1972; Hollerbach and Ierley, 1991; Wu and Roberts, 2015; Li et al., 2018).

Despite its flaws, in the 1980's in particular, the mean-field approach was widely used with some success as a method with which to attack the dynamo problem through focusing solely on the large scale hydromagnetic processes, with this  $\alpha$ -effect parameterizing the small scales (Krause and Rädler, 1980). The  $\alpha$ -effect provides the additional source required to circumvent the anti-dynamo theorem of Cowling (1933) and therefore has proved particularly useful for studying simple dynamos. Within the setting of a magnetostrophic balance this has been explored extensively. With the  $\alpha$ -effect term being the source of energy input to the system necessary to balance diffusion and achieve successful dynamo action, removing the need to incorporate a buoyancy force explicitly and solve the temperature equation (1.11). The  $\alpha$ -effect drives an inverse cascade of energy, where the small scales now fuel the large scales rather than acting as an energy sink. This allows dynamic magnetostrophic model simulations in the form of either  $\alpha^2$  or  $\alpha\omega$  dynamos (Soward and Jones, 1983; Abdel-Aziz and Jones, 1988).

## 2.6 The segregation of time scales

We know that the internal geomagnetic field, which is produced by dynamo action, is not constant in time. The evidence from geomagnetic observations unequivocally shows that the field is constantly fluctuating. Not only this, but there are in fact multiple different timescales associated with the variation of Earth's magnetic field

(Jackson and Finlay, 2007; Hollerbach, 2003).

For example, paleomagnetic data shows that on the long timescale of 100-1000 ka the geomagnetic field undergoes polarity reversals, where the dominantly dipole field that is aligned with the rotation axis, switches orientation (Constable, 2000). The large scale field is also evolving on somewhat shorter timescales, as it is observed that it appears to be migrating westward. This is referred to as ‘westward drift’ and operates at a speed of around one degree in longitude per year (Jault et al., 1988). Earth’s magnetic field is observed to vary considerably on a yearly timescale too: these can take the form of periodic oscillations thought to be due to magnetic waves, the movement of the geomagnetic pole (Livermore et al., 2020), and toward the shortest end of the spectrum, so-called geomagnetic jerks, in which the second time-derivative of the field changes abruptly within a single year (Bloxham et al., 2002).

This makes it challenging to model the dynamo by resolving features across this broad range of timescales. Ideally we would seek to model the geodynamo as a fully continuous system capable of cross-interaction between processes on all scales. However, given the difficulty in being able to do this, it is fruitful to adopt a practical, discretized approach, similar to the separation of dynamics based on lengthscale employed in mean field theory (§2.5) and seek to understand these features initially under the assumption that they are fundamentally distinct.

The dominant force balance of the magnetostrophic equations, which neglect inertial and viscous effects as discussed in §2.1, operates on a timescale governed by the induction equation (1.10) and determined by Ohmic diffusion, of  $\frac{L^2}{\pi^2\eta} \approx 10^4$  years. Therefore one could argue that this is the theoretically predicted timescale of a slowly evolving background state of Earth’s magnetic field. This is of course the timescale on which the Taylor constraint acts, due to the derivation arising directly from the magnetostrophic equations, so a Taylor state describes the background geomagnetic field but does not incorporate fast perturbations in the field. This is the reason that a magnetostrophic dynamo requires coarser temporal resolution to simulate, as discussed in §2.3. Such a model relies on the key assumption that the variability in any rapid dynamics do not interfere with the slowly evolving background they may perturb.

The theoretical basis for these rapid dynamics is in the form of magnetic waves. These are small oscillations within an electrically conducting fluid under the influence of inertial, Lorentz, Archimedean, and Coriolis forces. These waves are predicted to have periods in variations in the geomagnetic field on the much

shorter timescale of years to decades (Braginsky, 1979). It is this vast discrepancy in timescales that stimulates the concept of distinguishing between a background state and perturbations from it and considering these two features separately. However, it remains difficult to accurately study the faster mechanisms, because while the shorter timescale dynamics aren't thought to significantly affect the background state, the converse is not believed to necessarily be true. Understanding the underlying background state is the focus of the work in this thesis and is vitally important in describing the full time evolving field, including as the correct foundation for studying the rapid dynamics, which can be highly dependent on the choice of background state that they perturb. Therefore to accurately model features of Earth's secular variation, a time evolving background state, derived from the magnetostrophic model we consider provides the appropriate foundation in order to then explore rapid instabilities that are superimposed on such a state.

## 2.7 Torsional oscillations

Departures from a Taylor state result in Taylor's constraint not being satisfied and Taylor (1963) comments that "this would result in rapid torsional motion being set up in which each concentric cylindrical annulus rotates as a rigid body, the adjacent annuli are coupled together, as if by elastic strings, through the cylindrically radial component of the magnetic field  $B_s$ . Because of this linkage the torsional motion would modify the fields until a state is reached in which Taylor's constraint is satisfied". This is the excitation of so called torsional waves, which are essentially rigid accelerations of cylindrical surfaces that seek to re-establish the state by stretching radial magnetic field into azimuthal field.

Torsional waves consist of geostrophic motions and arise because the geostrophic cylinders, as depicted in figure 2.3, are not free to rotate; each one is connected to its neighbours by  $B_s$  so torsional waves form a pattern of nested cylinders of fluid that rotate in different directions. Geostrophic flows depend only on the distance to the rotation axis and any differential rotation between rigid geostrophic cylinders shears the magnetic field causing the Lorentz force to result in a restoring magnetic tension. This leads to the torsional waves propagating cylindrically radially similarly to Alfvén waves and with the same timescale, which is both short (6-8 years for the Earth's core) and highly dependent on the background field.

Studies of such waves in the Earth's interior have proved useful because applying inverse methods to geophysical data allows us to infer aspects of the structure

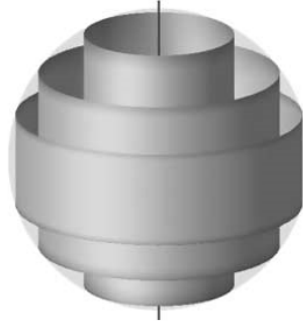


Figure 2.3: An illustration of some of the geostrophic cylinders over which Taylor’s constraint is defined [Livermore et al. \(2008\)](#).

and physical properties of the interior of the core that are otherwise inaccessible. The use of numerical geodynamo simulations and geomagnetic data through the data assimilation described in §1.4 can be further supplemented by our theoretical understanding of the behaviour of specific features within the geodynamo, in particular the way these torsional waves propagate. An ensemble inversion of core flow models can be applied, and since  $B_s$  threads the adjacent cylindrical fluid annuli whose rotation represents torsional oscillations, then knowledge of the torsional wave equation has been used by [Gillet et al. \(2010\)](#) to constrain  $B_s$  throughout the core and obtain both strength and profile estimates. [Buffett et al. \(2009\)](#) use the same principle by combining a time-dependent model of flow at the top of the core ([Jackson, 1997](#)) and a simple theory for torsional oscillations ([Buffett and Mound, 2005](#)) to estimate the internal structure of the magnetic field. This method has proven extremely useful as it allows us to “peer inside the core” and it has led to results for the internal field, such as suggesting that somewhat surprisingly the magnetic field induced by columnar convection is of similar strength in the interior of the core as it is at the CMB, with a value of approximately 0.3 m T.

## Chapter 3

# Determination of the instantaneous geostrophic flow within the three-dimensional magnetostrophic regime

### 3.1 Introduction

Throughout this thesis we focus on utilising the ideas of [Taylor \(1963\)](#), who argued in this seminal work that the geophysically relevant limit for dynamo action within the outer core is one of negligibly small inertia and viscosity. In this approach, we are in the magnetostrophic regime governed by equation (2.2), from which [Taylor \(1963\)](#) showed the existence of a necessary condition, now well known as Taylor's constraint, which requires that the cylindrically-averaged Lorentz torque must everywhere vanish; that is, the magnetic field must obey at all times  $t$  the condition

$$T(s, t) \equiv \int_{C(s)} ([\nabla \times \mathbf{B}] \times \mathbf{B})_\phi s d\phi dz = 0, \quad (3.1)$$

for any right cylinder  $C(s)$  of radius  $s$ , coaxial with the rotation axis. Magnetic fields that satisfy this condition are termed Taylor states.

While on the face of it, this is only a constraint on the magnetic field structure, in fact it also has important consequences for which fluid flows are compatible with maintaining a magnetostrophic balance. Within this chapter we detail the calculation of fluid flows necessary to maintain a Taylor state magnetic field, evaluate

the validity of the method proposed by [Taylor \(1963\)](#) himself, and derive a more general approach. In order to proceed it is expedient to partition the magnetostrophic flow of (2.2), using a cylindrical average, into geostrophic and ageostrophic parts:

$$\mathbf{u} = u_g(s)\hat{\phi} + \mathbf{u}_a(s, \phi, z),$$

where  $\mathbf{u}_a$  is such that  $\int_{C(s)} \mathbf{u}_a \cdot \hat{\phi} \, d\phi dz = 0$ . For a magnetic field  $\mathbf{B}$ , which is an exact Taylor state it is possible to solve the magnetostrophic equation

$$2\hat{z} \times \mathbf{u} = -\nabla p' + (\nabla \times \mathbf{B}) \times \mathbf{B} + F_B \hat{r}, \quad (3.2)$$

to determine the ageostrophic part of the fluid velocity  $\mathbf{u}_a$ . This can be done either through the integral method of [Roberts and King \(2013\)](#), the constructive method of [Taylor \(1963\)](#) or the following spectral method outlined in §3.3. However we note that the geostrophic flow is unconstrained by this equation as

$$\hat{z} \times u_g(s)\hat{\phi} = -u_g(s)\hat{s} = -\nabla \int u_g(s) \, ds, \quad (3.3)$$

and so, as it can be written as a gradient, it can be absorbed into the pressure term.

## 3.2 Magnetic field and fluid velocity representations

In our full sphere of unit radius, the position  $\mathbf{r}$  is naturally described in spherical coordinates  $(r, \theta, \phi)$ , although the importance of the rotation axis also leads us to use cylindrical coordinates  $(s, \phi, z)$ . The divergence free magnetic field  $\mathbf{B}$  can be written using a toroidal (T)-poloidal (S) framework

$$\mathbf{B} = \nabla \times \nabla \times \mathcal{S} \hat{r} + \nabla \times \mathcal{T} \hat{r}, \quad (3.4)$$

with  $\mathcal{S}$  and  $\mathcal{T}$  expanded as

$$\mathcal{S} = \sum_{l,m} \mathcal{S}_l^m(r) Y_l^m(\theta, \phi), \quad \mathcal{T} = \sum_{l,m} \mathcal{T}_l^m(r) Y_l^m(\theta, \phi),$$

where  $Y_l^m$  is a spherical harmonic of degree  $l$  and order  $m$ . The functions  $\mathcal{S}$  and  $\mathcal{T}$  must be chosen to satisfy both Taylor's condition (3.1), along with the electrically insulating boundary conditions at  $r = 1$ , which are shown in appendix C.4 to take

the form

$$\frac{d\mathcal{S}_l^m}{dr} + l\mathcal{S}_l^m = \mathcal{T}_l^m = 0. \quad (3.5)$$

The fluid is assumed to be incompressible and hence the flow  $\mathbf{u}$  can also be written in a comparable form, and due to the absence of viscosity only satisfies an impenetrability condition:  $u_r = 0$  on  $r = 1$ . We cannot impose no-slip or stress-free conditions, there being no boundary layer to accommodate any adjustment from the free-stream inviscid structure.

### 3.2.1 A Galerkin representation

A simple way of constructing magnetic states is to take combinations of single-mode toroidal or poloidal vectors, whose scalars are each defined in terms of a single spherical harmonic:

$$\mathbf{B} = \sum_{l,m,n} a_{l,n}^m \mathcal{T}_{l,n}^m + b_{l,n}^m \mathcal{S}_{l,n}^m$$

where  $\mathcal{T}_{l,n}^m = \nabla \times (\chi_{l,n}(r) Y_l^m \hat{\mathbf{r}})$  and  $\mathcal{S}_{l,n}^m = \nabla \times \nabla \times (\psi_{l,n}(r) Y_l^m \hat{\mathbf{r}})$  and the harmonics are fully normalised over solid angle:

$$\oint [Y_l^m]^2 d\Omega = 1.$$

We choose the scalar functions  $\chi_{l,n}$  and  $\psi_{l,n}$ ,  $n \geq 1$ , to be of polynomial form and match an electrical insulator at  $r = 1$  (Li et al., 2010, 2011), defined in terms of Jacobi polynomials  $P_n^{(\alpha,\beta)}(x)$  (Szegő, 1939), by

$$\begin{aligned} \chi_{l,n} &= r^{l+1} (1 - r^2) P_{n-1}^{(2,l+1/2)}(2r^2 - 1), \\ \psi_{l,n} &= r^{l+1} \left( c_0 P_n^{(0,l+1/2)}(2r^2 - 1) + c_1 P_{n-1}^{(0,l+1/2)}(2r^2 - 1) + c_2 \right), \end{aligned} \quad (3.6)$$

where

$$\begin{aligned} c_0 &= -2n^2(l+1) - n(l+1)(2l-1) - l(2l-1), \\ c_1 &= 2(l+1)n^2 + (2l+3)(l+1)n + (2l+1)^2, \\ c_2 &= 4nl + l(2l+1). \end{aligned} \quad (3.7)$$

These normalised vector modes then satisfy (A) the boundary conditions of equation (3.5); (B) regularity at the origin and (C)  $L_2$  orthonormality of the form

$$\begin{aligned} \int_V \mathbf{s}_{l,n}^m \cdot \mathbf{s}_{l',n'}^{m'} dV &= \int_V \mathcal{T}_{l,n}^m \cdot \mathcal{T}_{l',n'}^{m'} dV = \delta_{l,l'} \delta_{m,m'} \delta_{n,n'}, \\ \int_V \mathbf{s}_{l,n}^m \cdot \mathcal{T}_{l',n'}^{m'} dV &= 0, \end{aligned} \quad (3.8)$$

where all integrals are over the spherical volume  $V$ . These conditions reduce to the equations (when  $l = l'$ ,  $m = m'$ )

$$l(l+1) \int_0^1 \frac{l(l+1)}{r^2} \psi_n \psi_{n'} + \frac{\partial \psi_n}{\partial r} \frac{\partial \psi_{n'}}{\partial r} dr = \delta_{n,n'}, \quad \text{and} \quad l(l+1) \int_0^1 \chi_n \chi_{n'} dr = \delta_{n,n'}.$$

For the velocity field, the ageostrophic flow satisfies only the impenetrable condition  $u_r = 0$  on  $r = 1$ , which constrains only the poloidal representation. A modal set that satisfies this boundary condition, regularity at the origin and  $L_2$  orthonormality is given by Li et al. (2018)

$$\mathbf{u} = \sum_{l,m,n} c_{l,n}^m \mathbf{t}_{l,n}^m + d_{l,n}^m \mathbf{s}_{l,n}^m$$

where  $\mathbf{t}_{l,n}^m = \nabla \times (\omega_{l,n}(r) Y_l^m \hat{\mathbf{r}})$  and  $\mathbf{s}_{l,n}^m = \nabla \times \nabla \times (\xi_{l,n}(r) Y_l^m \hat{\mathbf{r}})$ . The radial functions are given by

$$\begin{aligned} \xi_{l,n} &= r^{l+1} (1-r^2) P_{n-1}^{(1,l+1/2)}(2r^2-1) \\ \omega_{l,n} &= r^{l+1} P_{n-1}^{(0,l+1/2)}(2r^2-1) \end{aligned} \quad (3.9)$$

for  $n \geq 1$ .

### 3.3 Solving for the ageostrophic flow

The procedure to determine  $\mathbf{u}_a$ , given  $\mathbf{B}$  and  $F_B$ , firstly consists of taking the curl of the magnetostrophic equation (3.2), which removes the pressure. Then due to the condition that  $\mathbf{B}$  is solenoidal, the poloidal-toroidal decomposition results in just 2 remaining scalar equations, from which the scalar modal coefficients can be solved for.

$$\begin{aligned} \hat{\mathbf{r}} \cdot \nabla \times (2\hat{\mathbf{z}} \times \mathbf{u} - (\nabla \times \mathbf{B}) \times \mathbf{B} + F_B \hat{\mathbf{r}}) &= 0, \\ \hat{\mathbf{r}} \cdot \nabla \times \nabla \times (2\hat{\mathbf{z}} \times \mathbf{u} - (\nabla \times \mathbf{B}) \times \mathbf{B} + F_B \hat{\mathbf{r}}) &= 0. \end{aligned}$$

The trial form from §3.2.1 is then proposed for the fluid velocity  $\mathbf{u}$ , in terms

of modes with unknown coefficients. The choice of bases has ensured that each basis function individually satisfies all the relevant boundary conditions and so we do not need to explicitly include them when we solve the system. The flow and magnetic field are then expanded in the appropriate spectral bases, as a linear sum of known basis functions, which are orthonormal by the definition of equation (3.8). They are substituted into the differential equations above and orthogonality of the equation with respect to each basis function is imposed. Because  $\hat{\mathbf{z}}$  is a constant vector and  $\mathbf{B}$  is based on Galerkin modes of polynomial form of known maximum degree, the modal representation for the flow then also has a known maximum degree. The unknown coefficients can then be found by either simply equating powers of  $r$  and solving the resulting system analytically, as we shall do for the instantaneous flow calculations in this chapter (with the assistance of computer algebra (Maple)), or through back-projecting onto the set of velocity modes by integrating against the basis functions defined above §3.2.1, as is done by Li et al. (2018).

This method provides a solution for  $\mathbf{u}$  that is consistent with the magnetostrophic equation (2.2). However, it is important to note that such a solution (obtained through any method solving (2.2)) is not unique. The geostrophic component of  $\mathbf{u}$ , that is, the component in the azimuthal direction that is solely a function of the cylindrically radial coordinate, remains arbitrary, as we showed earlier (equation (3.3)). Hence, in order to ensure uniqueness for the geostrophic flow, any solution for the flow from the magnetostrophic equation (2.2) must first be made consistent. We achieve this through removing the cylindrically-averaged azimuthal component of  $\mathbf{u}$  to obtain the ageostrophic flow  $\mathbf{u}_a$  which contains zero geostrophic component.

### 3.4 The initial state

All time-dependent magnetostrophic models, axisymmetric or 3D, require an initial state from which the system evolves. Because the flow is defined completely by the magnetic field and  $F_B$ , only the initial structure of the magnetic field  $\mathbf{B}(0)$  and  $F_B(0)$  are needed: there is no need to specify the initial flow. A general scheme for finding an exact initial Taylor state using a poloidal-toroidal representation was described in Livermore et al. (2008); in general it requires a highly specialised magnetic field to render its integrated azimuthal Lorentz force zero over all geostrophic cylinders. However, in a full sphere such cancellation can be achieved in a simple way by exploiting reflectional symmetry in the equator (Livermore et al., 2009). Using the Galerkin basis of single-spherical-harmonic modes that satisfy the boundary

conditions (see §3.2.1), suitable simple modal expansions are automatically Taylor states. The examples we consider in this chapter all fall into the following classes of magnetic fields, which are guaranteed to be Taylor states

- (A) any magnetic field based on a single spherical harmonic
- (B) any axisymmetric purely toroidal or poloidal field
- (C) any field that has a single harmonic of each wavenumber  $m$
- (D) any field that is either symmetric or anti-symmetric with respect to a rotation of  $\pi$  radians about the  $x$ -axis (as defined in appendix C.3.2).

### 3.5 Overview of time evolution and the geostrophic flow

Because of the absence of inertia, at each instant the magnetostrophic flow is entirely determined by  $\mathbf{B}$  and  $F_B$  from equation (2.2): therefore the system, as a whole, only evolves through time-evolution of the quantities  $F_B$  and  $\mathbf{B}$ . The evolution of  $F_B$  is assumed to be tractable and lies outside the scope of this study: for simplicity we shall henceforth assume that  $F_B = 0$ , although we note that all the methods nevertheless apply in the case of non-zero  $F_B$ . The evolution of the magnetic field is described by the induction equation:

$$\partial_t \mathbf{B}(\mathbf{r}, t) = \mathcal{I}(\mathbf{B}, \mathbf{u}) \equiv \nabla \times [\mathbf{u} \times \mathbf{B}(\mathbf{r}, t)] + \eta \nabla^2 \mathbf{B}(\mathbf{r}, t) \quad (3.10)$$

where  $\eta \neq 0$  is the magnetic diffusivity (assumed constant) and  $\partial_t = \partial/\partial t$ . Assuming that we can evolve  $\mathbf{B}$  and  $F_B$  (using standard methods), the major outstanding task is then to determine the flow at any instant given  $\mathbf{B}$  and  $F_B$ .

In contrast to the relatively simple procedure for computing the three-dimensional ageostrophic flow described above (§3.3), the structurally more elementary, geostrophic flow, depending only on  $s$ , is surprisingly difficult to compute, owing to its key role of maintaining Taylor's constraint. It is the requirement of this constraint being continuously satisfied through time which prescribes the evolution of the geostrophic flow. That is, it is the task of  $u_g$  to keep the magnetic field on the manifold of Taylor states (Livermore et al., 2011), where, in such a model, at all times the flow is enslaved to  $\mathbf{B}$  and  $F_B$ .

There are two ways in which the geostrophic flow may be found, which differ in philosophy. In the first, we may undertake an instantaneous analysis to find the geostrophic flow that gives zero rate of change of Taylor's constraint:  $\partial_t T(s, t) = 0$  (Taylor, 1963). Because of the resulting closed-form analytic description, such methods can be useful in computing snapshot solutions that elucidate the mathematical structure of the geostrophic flow, for example, the presence of any singularities. However, as a practical time-evolution tool, their utility is not so obvious. For example, the simple explicit time-evolution scheme, defined by assuming an instantaneous solution is constant over a finite time interval, would lead to a rapid divergence from the Taylor manifold (see Livermore et al., 2011, for an example).

In his 1963 paper, Taylor used the idea of this approach and a simple methodology to show that (for a fully 3D system) the geostrophic flow was at every instant the solution of a certain second order differential equation (ODE) (that given in equation (3.24)) whose coefficients depend on  $\mathbf{B}$  and  $F_B$ . His elegant and succinct analysis has been reproduced many times in the literature. It may then come as some surprise that in the intervening five decades there have been no published implementations of his method (that we are aware of). Very likely, this is due to a subtle issue concerning the treatment of the magnetic boundary conditions. As we shall show, rather than being applicable to a general (Taylor state)  $\mathbf{B}$ , Taylor's method is only valid for a small subset of Taylor states. Of crucial importance is that this subset does not include those states likely to be realised in any analytical example or in any practical numerical scheme to solve the magnetostrophic equations. The main goal of this chapter is to describe why this happens, and to modify Taylor's method in order to obtain a general method for calculating the instantaneous geostrophic flow.

In the second, alternative type of method, we may consider taking a time step (of size  $h$ ), determining the geostrophic flow implicitly by the condition that the magnetic field  $\mathbf{B}(t+h)$  satisfies Taylor's constraint (Li et al., 2018; Wu and Roberts, 2015). In general, implicit and instantaneous methods will only produce the same geostrophic flow in a steady state, or for a time-dependent state for infinitesimally small  $h$ .

All methods to determine the geostrophic flow require solving an ordinary differential equation for the quantity  $u_g/s$  and hence introduce a constant of integration and the solution contains an arbitrary solid body rotation:  $u_g = as$ . The constant  $a$  can be found through requiring zero global angular momentum

$$\int_0^1 \int_{-Z_T}^{Z_T} \int_0^{2\pi} s(\mathbf{u}_a \cdot \hat{\boldsymbol{\phi}} + u_g) d\phi dz ds = 0, \quad (3.11)$$

where  $Z_T = \sqrt{1 - s^2}$  is the half-height of  $C(s)$ . We also assume the geostrophic flow is everywhere finite (although we permit singularities in the higher order derivatives), which is implemented by additional conditions where necessary.

### 3.6 Braginsky's formulation

Before discussing the determination of the geostrophic flow in more detail, we briefly review a crucial alternative formulation of Taylor's constraint due to [Braginsky \(1970\)](#), which laid the foundations of many subsequent works on the subject (e.g. [Roberts and Aurnou, 2011](#); [Wu and Roberts, 2015](#); [Braginsky, 1975](#); [Fearn and Proctor, 1992](#); [Jault, 2003](#)). The Taylor integral (3.1) can be equivalently written

$$T(s, t) = \frac{1}{s} \frac{\partial}{\partial s} \left[ s^2 \int_{C(s)} B_\phi B_s d\phi dz \right] + \frac{s}{\sqrt{1 - s^2}} \oint_{N+S} (B_\phi B_r) d\phi, \quad (3.12)$$

where  $N$  and  $S$  are the northern and southern, horizontal circular end caps of the cylinder  $C(s)$  at the intersection with the spherical boundary at  $r = 1$  ([Braginsky, 1970](#)). The full derivation of this form of Taylor's constraint is carried out in appendix [A](#).

It is also useful to consider the net magnetic torque on all fluid enclosed within  $C(s)$ ,  $\Gamma_z$ , defined by

$$T(s, t) = \frac{1}{s} \frac{\partial \Gamma_z}{\partial s} \quad \text{or} \quad \Gamma_z(s, t) = \int_0^s s' T(s', t) ds'.$$

In our full-sphere geometry, it is clear that  $\Gamma_z(s, t)$  is zero if and only if  $T(s, t)$  is identically zero, although in a spherical shell it is possible that a piecewise (non-zero) solution exists for  $\Gamma_z$ . The condition  $\Gamma_z = 0$  defines what we refer to as the Braginsky constraint ([Braginsky, 1970](#)):

$$0 = \Gamma_z \equiv s^2 \int_{C(s)} B_\phi B_s d\phi dz + \int_0^s \oint_{N+S} \frac{s'^2 B_\phi B_r}{\sqrt{1 - s'^2}} d\phi ds', \quad (3.13)$$

which is equivalent to Taylor's constraint, and simplifies for specific classes of magnetic fields that cause the boundary term to vanish. There are two such classes of magnetic fields which have no sources in the exterior of  $r = 1$ : fields with no radial component on  $r = 1$  (e.g. toroidal fields) and fields that have a vanishing azimuthal component on  $r = 1$  (e.g. axisymmetric fields).

It is important to note the significant difference in the mathematical struc-

ture between the constraints of Braginsky (3.13) and Taylor (3.1). In (3.13) there is a clear partition between the two surface integral terms on the right hand side: the first term is an integral defined over  $C(s)$  that is independent of the magnetic field values on the end caps (these being a set of measure zero); the second end-cap term depends only on the boundary values of the magnetic field. By contrast, although ostensibly Taylor's integral (3.1) is an integral over the surface  $C(s)$ , the integrand involves a spatial derivative (the curl of  $\mathbf{B}$ ) leading to a dependence on the boundary values of the magnetic field. As we will see later, this hidden dependence on the boundary conditions has a deep consequence on Taylor's method for determining the geostrophic flow.

## 3.7 Existing methods to determine the geostrophic flow

Our modification of Taylor's method described in §3.10 determines the instantaneous geostrophic flow in a fully 3D geometry. In this section, we briefly review the existing methods available to calculate the geostrophic flow. All these methods have different working assumptions: either the field is assumed to be axisymmetric, or the methods are designed to take a finite time step and are not instantaneous. Where there is overlap in applicability, we will use these methods to numerically confirm our solutions.

### 3.7.1 An axisymmetric first-order implicit method

As noted above, under axisymmetry Braginsky's condition collapses to

$$\Gamma_z = 2\pi s^2 \int_{-Z_T}^{Z_T} B_\phi B_s dz = 0. \quad (3.14)$$

This simple form was exploited by [Wu and Roberts \(2015\)](#) who considered taking a single timestep of duration  $h$ , after which they required

$$\Gamma_z(s, t) + h \frac{\partial \Gamma_z(s, t)}{\partial t} = 0. \quad (3.15)$$

The left hand side here approximates  $\Gamma_z(s, t + h)$ , so this ensures that (3.14) is satisfied to first order. To find an equation for the geostrophic flow they differentiated equation (3.14) with respect to time and used the fact that the geostrophic term in

the induction equation reduces to

$$\nabla \times (u_g(s)\hat{\phi} \times \mathbf{B}) = sB_s \frac{d(u_g/s)}{ds} \hat{\phi}. \quad (3.16)$$

They obtained the following first order ordinary differential equation describing the geostrophic flow

$$s\alpha_0(s) \frac{d}{ds} \left( \frac{u_g(s)}{s} \right) = -S_0(s) - \frac{\Gamma_z(s, t)}{h}, \quad (3.17)$$

where

$$S_0(s) = 2\pi s^2 \int_{-Z_T}^{Z_T} (B_s C_\phi^a + B_\phi C_s^a) dz, \quad \alpha_0(s) = 2\pi s^2 \int_{-Z_T}^{Z_T} B_s^2 dz,$$

and

$$\mathbf{C}^a = \nabla \times (\mathbf{u}_a \times \mathbf{B}) + \eta \nabla^2 \mathbf{B}. \quad (3.18)$$

The subscripts of zero denote a restriction to axisymmetry of (more general) 3D quantities that are defined subsequently (§3.7.4). [Wu and Roberts \(2015\)](#) implemented this method by solving equation (3.17) using a finite difference scheme and a Taylor state initial condition. It is worth remarking that this scheme allows small numerical deviations from a Taylor state (since (3.15) is only approximate). Because the method depends upon (3.14) which is tied to axisymmetry, their method is not extendable to 3D.

### 3.7.2 A 3D fully implicit scheme

An alternative implicit scheme proposed by [Li et al. \(2018\)](#), was to seek a geostrophic flow that ensured Taylor's constraint is satisfied (without error) in a numerical scheme after taking a single timestep  $h$ . By extending to multiple timesteps, this method is suitable to describe fully 3D time-dependent dynamics. Although the authors only demonstrated its utility on axisymmetric examples, in this thesis we will show how the method applies to 3D with a single short time-step.

The key idea is to minimise (hopefully to zero) the target function

$$\Phi = \int_0^1 T^2(s, t + h) ds \quad (3.19)$$

by optimising over all possible choices of  $u_g$ , assumed constant throughout the interval  $0 \leq t \leq h$ . Although [Li et al. \(2018\)](#) set out a sophisticated algorithm to do this in general based on control theory, here we describe a simplification of the method

which is suitable for  $h \ll 1$ , which we can use to benchmark our instantaneous solutions of the generalised 3D Taylor methodology.

We adopt a modal expansion of  $u_g$ , of which a general form is

$$u_g = s \sum_{i=0}^I A_i T_i(2s^2 - 1) + Bs \ln(s), \quad (3.20)$$

where  $T_i(2s^2 - 1)$  are even Chebyshev polynomials of the first kind, which are chosen as they form a complete orthogonal system and because Chebyshev series converge exponentially fast (Boyd, 2001). The additional logarithmic term has been specifically added in order to directly exploit the form observed in our analytic results in §3.9.1 (see also §3.13). The presence of weak logarithmic singularity at the origin, has been detected within axisymmetry (Jault, 1995; Wu and Roberts, 2015; Fearn and Proctor, 1987). It is unclear from previous studies whether the singularity is also a feature present within the fully three-dimensional system. We shall examine this thoroughly in §3.13. In order to keep our representation as general as possible, we use the same expansion in 3D as in axisymmetry. This includes the ability to capture any singular features that may (or may not) be present and would otherwise not be well represented by a purely polynomial series.

Because we plan to take only a single time step of size  $h \ll 1$ , we adopt a very simple first order explicit Euler time evolution scheme

$$\mathbf{B}(t+h) = \mathbf{B}(t) + h \partial_t \mathbf{B}(t)$$

which is then substituted into (3.19). For simplicity we assume that the ageostrophic flow, calculated at  $t = 0$ , is also constant over the time-step. As a representation of the magnetic field (and its rate of change), we use a Galerkin scheme (see §3.2.1), which satisfies the boundary conditions (3.5) automatically. Practically, this means that we use  $\bar{\mathcal{I}}$  (see equation (3.10)) in place of  $\partial_t \mathbf{B}$ , where the overbar denotes the projection onto the Galerkin basis. The coefficients  $A_i$  and  $B$  are then found through minimising  $\Phi$ . We note that since  $\mathbf{B}(t+h)$  is formally linear in  $u_g(s)$ ,  $T(s, t+h)$  is then quadratic and hence  $\Phi$  quartic in the coefficients  $A_i$  and  $B$ . Li et al. (2018) found the minimum using an iterative scheme, although we note that, in general (and without a good starting approximation), finding such a minimum may be problematic.

It is noteworthy, however, that in the axisymmetric case this analysis is greatly simplified. Through equation (3.16) only the azimuthal component of  $\mathbf{B}(t+h)$  depends on  $u_g$ , and equation (3.12) shows that  $T(s)$  is now linear and  $\Phi$

quadratic in  $u_g$ , hence finding the minimum of  $\Phi$  is more straightforward.

### 3.7.3 An instantaneous axisymmetric method

Wu and Roberts (2015) also presented a method for finding an instantaneous solution for the geostrophic flow in axisymmetry. Through differentiating with respect to time equation (3.14) they arrive at the following first order ODE, here referred to as the BWR<sup>1</sup> (Braginsky-Wu-Roberts) equation:

$$\mathcal{L}_{BWR} \equiv s\alpha_0(s) \frac{d}{ds} \left( \frac{u_g(s)}{s} \right) = -S_0(s), \quad (3.21)$$

which is the same as (3.17) without the final term. This gives  $u_g(s)$  explicitly as

$$u_g(s) = -s \int_0^s \frac{S_0(s')}{s' \alpha_0(s')} ds'. \quad (3.22)$$

If  $\alpha_0(s) > 0$  then this equation is integrable. A continuous solution for  $u_g$  does not exist, however, if  $B_s^2$  is everywhere zero on a geostrophic cylinder  $C(s^*)$  (rendering  $\alpha_0(s^*) = 0$ ). Physically, this would mean that the magnetic field fails to couple cylinders on either side of  $s = s^*$ , leading to a discontinuity in the geostrophic flow. In all the cases we consider, (3.22) can be solved analytically (with the assistance of computer algebra). The Taylor states  $\mathbf{B}$  that we use are of polynomial form and it then follows that  $S_0$  and  $\alpha_0$  are also polynomial (up to a square root factor arising from the geometry) and therefore  $u_g$  can (in general) be found in closed form. We note that, in general,  $S_0/\alpha_0$  is  $O(1)$  and so  $u_g$  behaves as  $s \ln(s)$  as  $s \rightarrow 0$ . A further property of this equation is that, for a purely-poloidal axisymmetric magnetic field, the solution  $u_g$  is independent of the magnetic diffusivity  $\eta$ . This is because  $\nabla^2 \mathbf{B}$  is also purely-poloidal and a purely-poloidal field has no azimuthal component. Thus

$$B_s(\nabla^2 \mathbf{B})_\phi = B_\phi(\nabla^2 \mathbf{B})_s = 0$$

and the diffusion term (within  $S_0$ ) then never appears in (3.21). This differs from the case of a more general magnetic field with both toroidal and poloidal components, where  $u_g$  depends upon  $\eta$ .

We also observe that for an axisymmetric purely-toroidal field, since  $B_s = 0$

---

<sup>1</sup>The name here is in recognition of two important contributions: that of the functional form of the Taylor integral due to Braginsky (1970), and the subsequent application to the discovery of the geostrophic flow due to Wu and Roberts (2015). We note that magnetic diffusion (included in equation (4.8)) was neglected in Braginsky's 1970 study on torsional waves, but was reinstated by Wu and Roberts (2015).

everywhere equation (3.21) is null because  $\alpha_0 = S_0 = 0$  reducing it to the tautology  $0 = 0$  and hence placing no constraint on the geostrophic flow.

### 3.7.4 Taylor's 3D instantaneous method

We end this section by discussing the well known (instantaneous) method of Taylor, who determined the unknown geostrophic flow by differentiating with respect to time (denoted by the over-dot shorthand) the Taylor integral in equation (3.1) to produce:

$$0 = \int_{C(s)} \{[\nabla \times \dot{\mathbf{B}}] \times \mathbf{B} + [\nabla \times \mathbf{B}] \times \dot{\mathbf{B}}\}_\phi s d\phi dz. \quad (3.23)$$

On substituting directly for  $\dot{\mathbf{B}}$  from equation (3.10) in addition to its curl (describing  $\nabla \times \dot{\mathbf{B}}$ ), Taylor showed that for fully 3D Taylor states  $\mathbf{B}$  the resulting equation for the geostrophic flow can be written in a remarkably succinct form as the second order ordinary differential equation

$$\mathcal{L}_T(u_g) \equiv \alpha(s) \frac{d^2}{ds^2} \left( \frac{u_g(s)}{s} \right) + \beta(s) \frac{d}{ds} \left( \frac{u_g(s)}{s} \right) = G(s). \quad (3.24)$$

In the above, the coefficients are

$$\alpha(s) = \int_{C(s)} s^2 B_s^2 d\phi dz, \quad \beta(s) = \int_{C(s)} [2B_s^2 + s \mathbf{B} \cdot \nabla B_s] s d\phi dz, \quad (3.25)$$

and  $G(s)$  is a function describing the interaction of  $\mathbf{u}_a$  and the magnetic field defined as

$$G(s) = -\frac{1}{s} \frac{\partial}{\partial s} \left[ s^2 \int_{C(s)} \mathbf{C}_\phi^a B_s + \mathbf{C}_s^a B_\phi d\phi dz \right].$$

Note the mistake in [Taylor \(1963\)](#) where a factor of  $s$  is omitted within the coefficient  $\beta$ . The functions  $\alpha_0$  and  $S_0$ , previously defined, are simply axisymmetric variants of  $\alpha$  given above and  $S(s)$  defined as

$$S(s) = s^2 \int_{C(s)} (C_\phi^a B_s + C_s^a B_\phi) d\phi dz + \int_0^s s' \left[ \frac{s'}{\sqrt{1-s'^2}} \oint_{N+S} (B_\phi C_r^a + B_r C_\phi^a) d\phi \right] ds',$$

where  $\mathbf{C}^a$  is as defined in equation (4.6). The fact that the coefficients  $\alpha(s)$  and  $\beta(s)$  are spatially dependent means that analytic solutions to (3.24) are very rare and in general only numerical solutions are possible. Of crucial note is that the boundary conditions played no part in the derivation above.

## 3.8 Technical aside: higher order boundary conditions

### 3.8.1 Higher order boundary conditions in the heat equation

Taylor's method is based on the instantaneous evolution (which we can take to be at time  $t = 0$ ) of the magnetostrophic system whose magnetic field is prescribed and must satisfy Taylor's constraint. Here we discuss higher order boundary conditions, the importance of which has so far been overlooked. We start by introducing this concept in a simple PDE, then we discuss the relevance for Taylor's equation.

Suppose we are interested in finding  $f(x, t)$  on  $x \in [0, 1]$ , whose evolution is described by the heat equation in the interior of the domain

$$\frac{\partial f}{\partial t} = \frac{\partial^2 f}{\partial x^2},$$

to be solved with the boundary conditions  $f(0, t) = f(1, t) = 0$ . For this simple equation, the general solution can be written in the form

$$f(x, t) = \sum_{n=1}^{\infty} A_n e^{-n^2 \pi^2 t} \sin(n \pi x).$$

Let us now suppose we have an initial state:

$$f(x, 0) = x^2(1 - x)$$

which satisfies the boundary conditions. Its future evolution would be given by the projection onto the normal modes as above.

In Taylor's analysis, part of the integral in (3.1) could be converted to a boundary term. Here we consider an analogy which is exactly integrable:

$$\frac{d}{dt} \int_0^1 \frac{\partial f}{\partial x} dx = \frac{d}{dt} [f(1) - f(0)] = 0 \quad (3.26)$$

using the boundary conditions. In Taylor's derivation, he differentiated under the integral sign and substituted directly for  $\partial f / \partial t$ , in order to find the equation that  $u_g$  must satisfy using an instantaneous initial magnetic field. In our example, this

produces

$$\frac{d}{dt} \int_0^1 \frac{\partial f}{\partial x} dx = \int_0^1 \frac{\partial^2 f}{\partial x \partial t} dx = \int_0^1 \frac{\partial^3 f}{\partial x^3} dx = [f_{xx}(1, t) - f_{xx}(0, t)]. \quad (3.27)$$

At  $t = 0$ , we evaluate the above expression as  $-6$  (note that  $f_{xxx}(x, 0) = -6$ ) resulting in an apparent contradiction with (3.26) and illustrating that this approach is not generally valid.

The problem arises because the initial state does not satisfy the condition  $f_{xx}(0, t) = f_{xx}(1, t) = 0$ , which arises from differentiating  $f(0, t) = f(1, t) = 0$  with respect to time and substituting the PDE. The condition  $f_{xx}(0, t) = f_{xx}(1, t) = 0$  is called the first-order boundary condition (Evans, 2010). The consequence of the initial state not satisfying the first-order boundary condition is that the solution is not smooth at the boundary at  $t = 0$ . Specifically, the derivatives in (3.27) do not exist and thus the above derivation is not valid. As a simple illustration of the issue, note that the general solution implies that  $f_{xxx}(x, 0) = -\sum_n n^3 \pi^3 A_n \cos(n\pi x)$ , which cannot represent the constant function  $f_{xxx}(x, 0) = -6$  associated with the initial state. This lack of smoothness only occurs at the initial time  $t = 0$ . At any later time ( $t > 0$ ), the solution is infinitely smooth; this is the smoothing property of the heat equation.

In the very special case that the initial state satisfies the first order boundary conditions (e.g.  $f(x, 0) = x^3(1-x)^3$ ) then there is no contradiction and (3.26) and (3.27) are consistent. However, for a general initial condition, the procedure adopted is not valid.

### 3.8.2 The relevance for Taylor's equation

We now discuss the relevance of the above discussion of higher-order boundary conditions in the context of the Earth's magnetic field. In the derivation of Taylor's second-order ODE (3.24), it is implicitly assumed that  $\mathbf{B}$  and all its time derivatives are (initially) smooth everywhere. Although it is somewhat hidden in Taylor's original derivation, taking the time-derivative of the equivalent form of (3.12) makes this explicit:

$$\frac{1}{s} \frac{\partial}{\partial s} \left[ s^2 \int_{C(s)} (\dot{B}_\phi B_s + B_\phi \dot{B}_s) d\phi dz \right] + \frac{s}{\sqrt{1-s^2}} \oint_{N+S} (\dot{B}_\phi B_r + B_\phi \dot{B}_r) d\phi = 0. \quad (3.28)$$

Taylor substituted everywhere the induction equation (3.10),  $\partial_t \mathbf{B} = \mathcal{I}(\mathbf{u}, \mathbf{B})$ , but in view of the above discussion, we need to take care, particularly for the boundary

terms.

We appeal to a reduced version of the magnetostrophic equations in order to probe what can be said about the behaviour of  $\mathbf{B}(t)$  on the boundary at  $t = 0$ . Assuming that  $\mathbf{u}(t)$  is given and is independent of  $\mathbf{B}$ , the induction equation (3.10) is of standard parabolic form (like the heat equation), so its solution is smooth for all  $t > 0$ . If the initial condition  $\mathbf{B}(0)$  is also smooth and satisfies the boundary condition (3.5), then the solution is smooth also at  $t = 0$ , except possibly at  $r = 1$ . For the solution to be smooth everywhere, including at  $r = 1$ , and for Taylor's substitution to be valid, we need the initial condition to satisfy not only the usual boundary condition (also termed the zero order boundary conditions) but also the first order boundary conditions: that  $\partial_t \mathbf{B}$ , given by  $\mathcal{I}(\mathbf{B}, \mathbf{u})$  of (3.10) satisfies the boundary condition (3.5). Higher-order variants of the boundary conditions pertain to higher-order time derivatives. Assuming that this analysis extends to the full magnetostrophic equations, it provides strong constraints on the form of the initial condition that produces a solution that is smooth for  $t \geq 0$  and all  $r \geq 0$ .

This issue of lack of smoothness of  $\mathbf{B}$  occurs only instantaneously at  $t = 0$ . One may ask if it is possible to specify an initial field that satisfies Taylor's constraint and higher order boundary conditions, making it possible to use equation (3.24) directly. Although in principle the answer is yes, it would be practically impossible because an evaluation of the first order boundary condition requires knowledge of  $\partial_t \mathbf{B}$  and therefore  $u_g$ . The logic is therefore circular: we need to know  $u_g$  in order to check the method that enables us to find  $u_g$  in the first place. It would seem that some additional insight or good fortune would be required to find a geostrophic flow that self-consistently satisfies the boundary conditions. The complication compounds the already difficult task of finding an initial condition that satisfies the necessary condition of being a Taylor state.

It is worth noting, however, that once the system has evolved past the initial condition many of these problems vanish. For  $t > 0$ , solutions to parabolic systems are smooth and so automatically satisfy all higher order boundary conditions. It follows that equation (3.24) is valid for  $t > 0$ , although this does not help find the geostrophic flow at  $t = 0$ .

### 3.8.3 Schemes in which the boundary information is included

These concerns described above regarding boundary conditions do not carry over to the axisymmetric case, the plane layer situation nor the 3D implicit schemes described. In the axisymmetric and Cartesian cases (e.g. [Abdel-Aziz and Jones, 1988](#)), the boundary conditions evaluate to zero and the boundary value of the magnetic field or any of its time derivatives never enter any subsequent calculations. In the 3D implicit scheme, because of the representation of all quantities (including  $\mathbf{B}$  and any of its time derivatives) in terms of a Galerkin basis, boundary conditions to all orders are satisfied.

Thus in the axisymmetric and Cartesian cases, equation (3.21) and equation (3.17) are correct irrespective of the initial choice of Taylor state, as is the fully implicit method of §3.7.2 for the 3D case. This is to be contrasted with (3.24) that is valid only for the subset of Taylor states satisfying zero and first order boundary conditions.

## 3.9 An appraisal of Taylor’s method

### 3.9.1 An illustration of when Taylor’s method fails

We are now in a position to provide a first explicit demonstration that Taylor’s ODE equation (3.24) fails when using an initial Taylor state that does not satisfy first order boundary conditions. We show this in two parts. Firstly, within axisymmetry, we demonstrate that Taylor’s equation (3.24) is formally inconsistent with the BWR equation (3.21); secondly, we plot an explicit solution of Taylor’s equation and show that it does not agree with those derived from other methods known to be correct. In sections 3.10 to 3.12 we will provide a generalised version of Taylor’s method, which shows agreement among all methods.

In all of the examples considered here, we have non-dimensionalised and scaled to ensure a magnetic field strength of  $\mathcal{B} \approx 1.7 - 2.4$  mT, consistent with the estimate of the geomagnetic field strength of [Gillet et al. \(2010\)](#). Length is scaled by  $L$ , the outer core radius  $3.5 \times 10^6$  m, time by the Ohmic diffusion time  $\tau$ , (50 kyr) ([Davies et al., 2015](#)), and speed by  $\mathcal{U} = L\tau^{-1} \approx 2 \times 10^{-6}$  m s<sup>-1</sup>. The scale used for the magnetic field is  $\mathcal{B} = (2\Omega_0\mu_0\rho_0\eta)^{\frac{1}{2}}$  ([Fearn, 1998](#)), where for Earth the physical parameters take the following values: angular velocity  $\Omega_0 = 7.272 \times$

$10^{-5} \text{ s}^{-1}$ , permeability  $\mu_0 = 4\pi \times 10^{-7} \text{ N A}^{-2}$ , density  $\rho_0 = 10^4 \text{ kg m}^{-3}$  and magnetic diffusivity  $\eta = 0.6\text{--}1.6 \text{ m}^2 \text{ s}^{-1}$ . (These parameters lead to the non-dimensional parameters  $R_o = \eta/(2\Omega L^2) \approx 10^{-9}$  and  $E = \nu/(2\Omega L^2) \approx 10^{-15}$ , whose small values motivate neglecting the terms they multiply.) We then use dimensionless magnetic fields with toroidal or poloidal components of rms (root mean squared) strength of unity. This corresponds to a dimensional rms magnitude of 1.7 mT for purely toroidal or purely poloidal fields and  $1.7\sqrt{2} \approx 2.4 \text{ mT}$  for mixed states. Using  $\mathcal{U}$ , this choice enables the immediate interpretation of the dimensional scale of any flow that we show.

First, we consider the simple case of the dipolar, single spherical harmonic  $l = 1$  axisymmetric poloidal magnetic field

$$\mathbf{B} = \nabla \times \nabla \times Ar^2(30r^4 - 57r^2 + 25) \cos(\theta) \hat{\mathbf{r}},$$

where  $A = \sqrt{231/20584}$  is a scaling constant (see non-dimensionalisation above). We note that  $\mathbf{B}$  satisfies the electrically insulating boundary conditions (3.5), and is an exact Taylor state owing to its simple symmetry.

The ageostrophic flow (determined for example by the method described in §3.3) has only an azimuthal component given by

$$u_\phi = A^2 [9120s^7 + (50400z^2 - 26184)s^5 + (50400z^4 - 95760z^2 + 23888)s^3 + (16800z^6 - 47880z^4 + 42000z^2 - 6824)s]. \quad (3.29)$$

For this choice of  $\mathbf{B}$ , equation (3.21) then provides an exact expression for the first derivative of  $u_g$ . Substituting this into Taylor's second order equation (3.24) renders it unbalanced, demonstrating its invalidity. From equation (3.21), the geostrophic flow satisfies

$$\frac{d}{ds} \left( \frac{u_g(s)}{s} \right) = -\frac{S_0(s)}{s\alpha_0(s)} = -\frac{Q_5(s^2)}{sQ_2(s^2)} \quad (3.30)$$

where we have used

$$\begin{aligned} \alpha_0(s) &= \alpha(s) = \frac{198}{2573} s^4 \pi (1-s^2)^{3/2} (640s^4 - 1168s^2 + 535), \\ S_0(s) &= S(s) = -\frac{66528}{86064277} s^4 \pi (1-s^2)^{5/2} (46387200s^8 - 138624000s^6 + \\ &\quad 142265512s^4 - 57599212s^2 + 7255185), \end{aligned}$$

and where, for typographic purposes,  $Q_N(s^2)$  is used for brevity to represent a polynomial of order  $N$  in  $s^2$ . Substituting these into Taylor's equation (3.24), along with

$$\beta(s) = -\frac{198}{2573}s^3\pi(1-s^2)^{1/2}(7680s^6 - 17440s^4 + 12456s^2 - 2689),$$

leaves an unbalanced equation: the left and right hand sides of (3.24) are the distinct quantities

$$\frac{\sqrt{1-s^2}Q_9(s^2)}{Q_2(s^2)}, \quad \text{and} \quad \sqrt{1-s^2}Q_7(s^2),$$

where

$$\begin{aligned} Q_9(s^2) &= -\frac{66528\pi s^2}{86064277}(504692736000s^{16} - 3112801075200s^{14} + 8179698058240s^{12} \\ &\quad - 11895688291968s^{10} + 10389468804472s^8 - 5513724758708s^6 \\ &\quad + 1702884326747s^4 - 270157468073s^2 + 15627668490), \\ Q_2(s^2) &= 640s^4 - 1168s^2 + 535, \\ Q_7(s^2) &= -\frac{66528\pi s^2}{86064277}(788582400s^{12} - 3424588800s^{10} + 5871698056s^8 \\ &\quad - 5008127804s^6 + 2183964721s^4 - 440479243s^2 + 28950670). \end{aligned}$$

Therefore none of the solutions of the first order ODE (3.21), satisfy the second order ODE (3.24).

This specific case (which is illustrative of the general case) shows that equation (3.24) and equation (3.21) are inconsistent: in particular the first order equation (3.21) is not simply the first integral of the second order equation (3.24). The reason why they are not consistent is that although the ODEs are derived from the equivalent forms (3.13) and (3.1), the boundary terms are used to derive (3.21) but not (3.24). Thus the two equations embody different information. In this example, Taylor's method is equivalent to the erroneous replacement of  $\partial_t B_\phi$  (which is zero) in the boundary term of (3.28), by  $\mathcal{I}_\phi \neq 0$ . This can be seen in the expression for the coefficient  $\beta$  given in equation (3.39), where the boundary term is such that it does not vanish in the axisymmetric case. While the initial magnetic field has been chosen such that it satisfies the boundary condition (3.5), through computing  $\partial_t \mathbf{B}$  we can show that, based on Taylor's solution, the initial rate of change of the magnetic field violates this boundary condition.

To confirm that Taylor's method is not generally valid, we now directly compare solutions from various methods. Integrating equation (3.21) analytically

gives the solution

$$u_g = \frac{A^2 s}{918060} \left[ 9926860800 s^6 - 32213813760 s^4 + 37855940880 s^2 + C - 11143964160 \ln s + 30664844 \sqrt{21} \arctan \left( (80 s^2 - 73) / \sqrt{21} \right) + 101695629 \ln (640 s^4 - 1168 s^2 + 535) \right]. \quad (3.31)$$

We note that the solution is a sum of odd polynomials, an  $s \ln(s)$  term and additional (and non-singular)  $\ln$  and  $\arctan$  terms. The constant  $C$  is determined through enforcing zero solid body rotation (equation (3.11)). The solution for  $u_g$  is everywhere continuous and finite, only at  $s = 0$  is there a weak singularity:  $\partial_s(u_g/s) \sim 1/s$ . We also observe that there is no singularity at  $s = 1$ . A comparable analytic solution but for a quadrupolar axisymmetric magnetic field was given in [Li et al. \(2018\)](#), which is also regular everywhere except for a weak  $s \ln(s)$  singularity at  $s = 0$ .

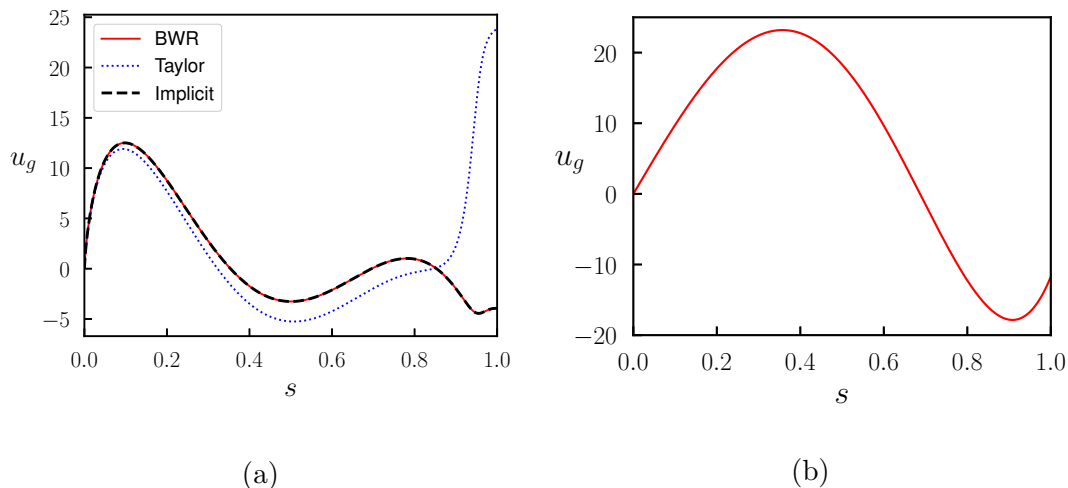


Figure 3.1: A comparison of the cases where Taylor’s method fails and where it succeeds. (a) Compares the solutions for the geostrophic flow for an axisymmetric dipolar poloidal initial field. Red is the analytic solution of the first order BWR equation (3.21), dotted blue is a numerical solution of Taylor’s second order ODE (see text) and dashed black is the solution using the implicit time step method with  $h = 10^{-9}$ . (b) Shows the geostrophic flow corresponding to a non-axisymmetric  $l = 1$ ,  $m = 1$  purely-toroidal Taylor state, on which all methods agree.

That the analytic expression (3.31) is indeed the true solution is confirmed by figure 3.1a which compares it to the geostrophic flow given by the independent 3D implicit scheme of section 3.7.2; the two solutions over-plot. A contour plot of the total azimuthal flow is shown in §3.12 (figure 3.6a).

We now directly compare this solution with that obtained by solving Taylor’s equation (3.24), shown as the blue line of figure 3.1a. This solution is found by

adopting the expansion (3.20) and minimising the integrated squared residual

$$\int_0^1 [\mathcal{L}_T(u_g) - G(s)]^2 ds. \quad (3.32)$$

with respect to the spectral coefficients, whose truncation is increased until the solution converges. Although all solutions agree at small  $s$ , Taylor's solution shows significant differences from the others for  $s > 0.8$ .

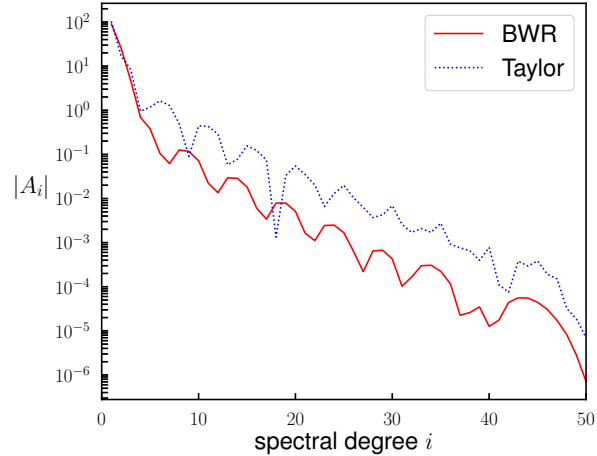


Figure 3.2: A comparison of the absolute value of the polynomial spectral coefficients  $A_i$ , defined in equation (3.20), against degree for numerical solutions using the Braginsky-Wu-Roberts and Taylor formulations.

It is also of interest to assess numerical convergence to solutions of equations (3.21) and (3.24). Although we have an analytic solution to (3.21), we use the same numerical method as given above but now applied to (3.21) by minimising

$$\int_0^1 [\mathcal{L}_{BWR}(u_g) + S_0(s)]^2 ds. \quad (3.33)$$

Figure 3.2 demonstrates that convergence of the solution is faster for the correct, first order equation (3.21) than for Taylor's equation (3.24). Therefore, aside from Taylor's equation being generally inapplicable, it seems that converged solutions are also relatively more difficult to find.

### 3.9.2 Specific cases when Taylor's method succeeds

For arbitrary purely-toroidal Taylor states bounded by an electrical insulator,  $\mathbf{B}$  vanishes on  $r = 1$  and in this special case Taylor's methodology is correct. This

is because the boundary term involving  $B_\phi B_r$  (see equation (3.13)) has a “double zero” and so, when considering its time derivative, erroneous substitution for  $\partial_t \mathbf{B}$  leaves it invariant as zero.

Taking the time derivative of (3.13), noting that the boundary term is zero, we obtain

$$s^2 \int_{C(s)} \left( \frac{\partial B_\phi}{\partial t} B_s + B_\phi \frac{\partial B_s}{\partial t} \right) d\phi dz = 0. \quad (3.34)$$

From the 3D extension of (3.16), the geostrophic induction is

$$\nabla \times (u_g(s) \hat{\phi} \times \mathbf{B}) = s B_s \frac{d(u_g/s)}{ds} \hat{\phi} - \frac{u_g}{s} \frac{\partial_1 \mathbf{B}}{\partial \phi}, \quad (3.35)$$

where  $\partial_1/\partial\phi$  is a derivative with respect to  $\phi$  that leaves invariant the unit vectors (see e.g. Jault, 2003). Substituting this into (3.34), the terms involving  $u_g$  become

$$s^2 \int_{C(s)} \left( \left( s B_s \frac{d(u_g/s)}{ds} - \frac{u_g}{s} \frac{\partial B_\phi}{\partial \phi} \right) B_s + B_\phi \left( -\frac{u_g}{s} \frac{\partial B_s}{\partial \phi} \right) \right) d\phi dz = 0$$

Therefore

$$s \frac{d}{ds} \left( \frac{u_g(s)}{s} \right) \int_{C(s)} B_s^2 d\phi dz - \frac{u_g}{s} \int_{C(s)} \frac{\partial}{\partial \phi} (B_\phi B_s) d\phi dz = 0.$$

Noting that the last integral is zero, we obtain an equation (that holds in 3D) that can be written in terms of  $\alpha(s)$  and  $S(s)$  (defined in §3.7.4), and is of the same form as the axisymmetric BWR equation (3.21)

$$s\alpha(s) \frac{d}{ds} \left( \frac{u_g(s)}{s} \right) = -S(s). \quad (3.36)$$

As an illustration we consider the non-axisymmetric  $l = 1, m = 1$  toroidal magnetic field

$$\mathbf{B} = \nabla \times A r^2 (1 - r^2) \cos(\phi) \sin(\theta) \hat{\mathbf{r}},$$

where  $A$  is a scaling constant which takes the value  $\frac{3}{4}\sqrt{105}$ . The ageostrophic flow is

$$\begin{aligned} \mathbf{u}_a &= \frac{A^2}{3} s \sin \phi \cos \phi (5s^4 - 6s^2 z^2 - 3z^2 - 3z^4 - 10s^2 + 6z^2 + 5) \hat{\mathbf{s}} \\ &+ \frac{A^2}{15} (\cos^2 \phi (105s^5 - 30z^2 s^3 - 130s^3 - 15z^4 s + 30z^2 s + 25s) - 56s^5 + 72s^3 - 16s) \hat{\phi} \\ &+ \frac{4A^2}{3} s^2 z (3s^2 + z^2 - 3) \cos \phi \sin \phi \hat{\mathbf{z}}, \end{aligned} \quad (3.37)$$

and, solving (3.36), the geostrophic flow is

$$u_g(s) = A^2 \left( \frac{97}{30}s^5 - \frac{77}{15}s^3 + sC_1 \right), \quad (3.38)$$

where  $C_1$  is determined through considerations of angular momentum. Note the absence of singularities in this solution.

This geostrophic flow is shown in figure 3.1b, and we note that the 3D implicit method and Taylor's method give the same solution (not shown).

It is in fact simple for us to show analytically that for any purely toroidal field, Taylor's equation (3.24) and equation (3.36) are equivalent, up to the requirement of a further boundary condition for the second order differential equation (3.24).

We note that via integration by parts, (3.25) can be written in the following way, which allows identification of the boundary term present within Taylor's method, as the second term in the following expression for the coefficient  $\beta$

$$\beta(s) = \frac{1}{s} \frac{d}{ds}(s\alpha(s)) + \frac{s^2}{Z_T} \left[ \oint B_s B_r d\phi \right]_{-Z_T}^{Z_T}. \quad (3.39)$$

We observe that since  $B_r = 0$  for a purely toroidal field, then the boundary term within equation (3.39) will always vanish in this case, reducing Taylor's equation (3.24) to the BWR equation (3.36).

## 3.10 A generalisation of Taylor's analysis

To modify the method of Taylor so that it applies to a magnetic field that does not satisfy the first order boundary conditions, we use (3.28) to impose stationarity of the Taylor constraint. Equally, we could impose stationarity of the equivalent equation (3.13) but it is simpler to avoid the additional integral in  $s$ . Bearing in mind our discussion in §3.8, we take particular care to ensure correct handling of the boundary term.

The magnetic field matches continuously (since  $\eta \neq 0$ ) with an external potential field within the mantle  $r \geq 1$ . Note that our assumption of a globally continuous solution differs from the case when  $\eta = 0$ , for which horizontal components of  $\mathbf{B}$  may be discontinuous on  $r = 1$  (Backus et al., 1996). In our setting where

$\eta \neq 0$ , the field matches continuously but not necessarily smoothly across  $r = 1$ . We note however that owing to  $\nabla \cdot \mathbf{B} = 0$ , the radial component of  $\mathbf{B}$  (and all its time derivatives) are always smooth at  $r = 1$  (see e.g. [Gubbins and Roberts, 1987](#)): thus only the horizontal components  $B_\theta$  and  $B_\phi$  are not in general smooth.

Thus, in the first term of equation (3.28) we may substitute at  $t = 0$

$$\begin{aligned}\partial_t B_s &= \mathcal{I}_s(\mathbf{u}, \mathbf{B}), & 0 \leq r < 1, \\ \partial_t B_\phi &= \mathcal{I}_\phi(\mathbf{u}, \mathbf{B}), & 0 \leq r < 1.\end{aligned}\tag{3.40}$$

For the second (boundary) term, we may substitute  $\partial_t B_r = \mathcal{I}_r(\mathbf{u}, \mathbf{B})$  but the initial value of  $\partial_t B_\phi$  at  $r = 1$  is not specified by  $\mathcal{I}_\phi$  alone, as assumed in Taylor's derivation.

The key remaining issue is then to find the initial boundary value of  $\dot{B}_\phi$ , for which we present three methods below. Having done this, all terms are defined and (3.28) provides an implicit determination of  $u_g$  up to the usual considerations of solid body rotation and regularity.

We observe that the form of equation (3.28) differs markedly from equations (3.21) and (3.24): in addition to the spatial derivatives of  $u_g$  (in the leftmost term), there is an explicit boundary term. For the general case, this boundary term must be retained, although it may be neglected under certain circumstances: e.g. those of sections 3.9.2 and 3.12.

We remark that the above instantaneous method can be amended to a first order implicit scheme (akin to equation (3.17)) by considering

$$\frac{1}{s} \frac{\partial}{\partial s} \left[ s^2 \int_{C(s)} (\dot{B}_\phi B_s + B_\phi \dot{B}_s) d\phi dz \right] + \frac{s}{\sqrt{1-s^2}} \oint_{N+S} (\dot{B}_\phi B_r + B_\phi \dot{B}_r) d\phi = -\frac{1}{hs} \frac{\partial \Gamma_z(s, t)}{\partial s},\tag{3.41}$$

As before, this equation is applicable even when  $\Gamma_z \neq 0$ , that is, if the solution is close but not exactly on the Taylor manifold.

### 3.10.1 A potential-based spherical transform method

One way to find  $\dot{B}_\phi$  on  $r = 1$  is to note that it is the azimuthal component of the potential field in  $r \geq 1$

$$\dot{\mathbf{B}} = -\nabla \dot{V}, \quad \nabla^2 \dot{V} = 0.$$

The potential  $\dot{V}$  is itself determined through continuity of the radial component  $\dot{B}_r$  at  $r = 1$  and thus depends upon  $u_g$ . This method of determining  $\dot{B}_\phi$  has been

introduced in the study of torsional waves by [Jault \(2003\)](#), but is implemented here for the evaluation of the geostrophic flow.

The time derivative of the potential  $\dot{V}$  can be written in terms of orthonormal spherical harmonics  $Y_{lm}$  with unknown coefficients  $a_{lm}$  as

$$\dot{V} = \sum_{l,m} \dot{a}_{lm} r^{-(l+1)} Y_{lm},$$

where  $0 \leq l \leq L_{max}$  and  $-l \leq m \leq l$  and

$$\dot{a}_{lm} = \frac{1}{l+1} \oint_{r=1} \dot{B}_r Y_{lm} d\Omega,$$

where  $\Omega$  is an element of solid angle. It follows then that on  $r = 1$

$$\dot{B}_\phi = -\frac{1}{\sin \theta} \sum_{l,m} \dot{a}_{lm} \frac{\partial Y_{lm}}{\partial \phi}.$$

Key to the implementation of this method here is a spectral expansion of  $u_g$ , for example (3.20), because it allows  $\dot{B}_r$  (which depends on the  $I + 2$  spectral coefficients of  $u_g$ ) to be evaluated everywhere on the boundary, as required in the above spherical transform. This is to be contrasted for example with a finite difference representation of  $u_g$  where no such evaluation is possible.

To find  $u_g$ , we note that all time-derivative terms in the left hand side of (3.28), including those evaluated on the boundary, are linear in the unknown coefficients  $(A_0, A_1, \dots, A_I, B)$ , and hence the residual is of the form

$$R(s) = \sum_{i=0}^I A_i a_i(s) + B b(s) + c(s)$$

for some functions  $a_i$ ,  $b$  and  $c$  that depend on  $\mathbf{B}$  and  $\mathbf{u}_a$ . We formulate a single equation for the coefficients defining  $u_g$  by minimising the quantity  $\int_0^1 R^2 ds$  (which is quadratic in the coefficients that we seek). Note that the solution is approximate and depends on two parameters  $I$  and  $L_{max}$ , which represent the truncation of the expansion used and care must be taken to ensure we achieve convergence in each.

### 3.10.2 A potential-based Green's function method

An alternative method for determining the potential  $\dot{V}$  at the core mantle boundary is through the use of a Green's function convolved with  $\dot{B}_r$  on  $r = 1$ . Following [Gubbins and Roberts \(1983\)](#); [Johnson and Constable \(1997\)](#), the relevant Green's function associated with the Laplace equation in the exterior of a sphere with Neumann boundary conditions is

$$N(x, \mu) = \frac{1}{4\pi} \left( \ln \left( \frac{f + x - \mu}{1 - \mu} \right) - \frac{2x}{f} \right),$$

where  $x = \frac{1}{r}$ ,  $f = (1 - 2x\mu + x^2)^{\frac{1}{2}}$ ,  $\mu = \cos \theta \cos \theta' + \sin \theta \sin \theta' \cos(\phi - \phi')$ . This can be expressed as  $N(x, \mu) = N\left(\frac{1}{r}, \theta, \theta', \phi - \phi'\right)$ , which is the potential at location  $(r, \theta, \phi)$  in  $r \geq 1$  due to a singularity of unit strength in the radial field at  $(\theta', \phi')$  on the core-mantle boundary. Making use of the periodicity of  $\phi$ , the magnetic potential in the region  $r \geq 1$  can then be written as

$$\dot{V} = \int_0^{2\pi} \int_0^\pi \dot{B}_r(1, \theta', \phi - \phi') N\left(\frac{1}{r}, \theta, \theta', \phi\right) \sin \theta' d\theta' d\phi',$$

and so

$$\dot{B}_\phi(1, \theta, \phi) = -\frac{1}{r \sin \theta} \int_0^{2\pi} \int_0^\pi \frac{\partial \dot{B}_r(1, \theta', \phi - \phi')}{\partial \phi} N\left(\frac{1}{r}, \theta, \theta', \phi'\right) \sin \theta' d\theta' d\phi'.$$

Like the previous method, this procedure of evaluating  $\dot{B}_\phi$  on  $r = 1$  requires an integral over all solid angle. Using again our spectral expansion [\(3.20\)](#) this results in  $\dot{B}_\phi$  being a linear function of the unknown spectral coefficients; thus using equation [\(3.28\)](#) the geostrophic flow can then be determined as in section [3.10.1](#).

### 3.10.3 A modal projection

A further alternative method to find  $\dot{B}_\phi$  on  $r = 1$ , which does not rely on a magnetic potential, is to employ a modal basis set for the magnetic field that is complete and satisfies the required boundary conditions. Here we adopt a numerically expedient Galerkin basis set (see [§3.2.1](#) for details), whose orthonormal poloidal and toroidal modes are written respectively as  $\mathcal{S}_{l,n}^m$  and  $\mathcal{T}_{l,n}^m$ .

By using such a representation, boundary conditions to all orders are automatically satisfied and therefore a direct substitution of the projected representation

of  $\mathcal{I}$ ,

$$\bar{\mathcal{I}} = \sum_{l,m,n} c_{l,n}^m \mathbf{S}_{l,n}^m + d_{l,n}^m \mathcal{T}_{l,n}^m, \quad (3.42)$$

for  $\partial_t \mathbf{B}$  in all three components for the whole sphere  $r \leq 1$  is justified. In the above,  $l$  is bounded by  $L_{max}$ ,  $0 \leq n \leq N_{max}$  and  $\bar{\mathbf{x}}$  indicates the modal projection of  $\mathbf{x}$ .

This projection we require here is that of a divergence-free magnetic field  $\mathbf{B}$  onto the magnetic Galerkin basis up to a truncation  $L_{max}$  in spherical harmonic degree and  $N_{max}$  in radial index:

$$\bar{\mathbf{B}} = \sum_{l=1}^{L_{max}} \sum_{m=-l}^l \sum_{n=1}^{N_{max}} a_{l,n}^m \mathcal{T}_{l,n}^m + b_{l,n}^m \mathbf{S}_{l,n}^m$$

Determination of the coefficients  $a_{l,n}^m$  and  $b_{l,n}^m$  can either be accomplished through use of the 3D integral (3.8) directly, or equivalently by first taking the transform in solid angle to find the toroidal and poloidal parts of  $\mathbf{B}$

$$\mathcal{T}_l^m(r) = \frac{r^2}{l(l+1)} \oint (\nabla \times \mathbf{B}_l^m)_r Y_l^m(\theta, \phi) d\Omega, \quad \mathcal{S}_l^m(r) = \frac{r^2}{l(l+1)} \oint (B_l^m)_r Y_l^m(\theta, \phi) d\Omega, \quad (3.43)$$

where  $d\Omega = \sin \theta d\theta d\phi$ , and secondly integrating in radius to give

$$a_{l,n}^m = \int_0^1 \mathcal{T}_l^m \chi_{l,n} dr, \quad b_{l,n}^m = \int_0^1 \frac{l(l+1)}{r^2} \mathcal{S}_{l,n}^m \psi_{l,n} + \frac{\partial \mathcal{S}_l^m}{\partial r} \frac{\partial \psi_{l,n}}{\partial r} dr.$$

As before, key to the method here is the spectral representation (3.20) for  $u_g$ ; the coefficients  $c_{l,n}^m$  and  $d_{l,n}^m$ , found by integration, then depend linearly on the unknown coefficients  $A_i$  and  $B$ .

Equation (3.28) can be then written as the following, in which  $u_g$  appears explicitly

$$\begin{aligned} & \frac{1}{s} \frac{d}{ds} \left[ s \alpha(s) \frac{d}{ds} \left( \frac{u_g(s)}{s} \right) \right] \\ & + \frac{s}{\sqrt{1-s^2}} \oint_{N+S} \left[ B_\phi \{ \nabla \times (u_g \hat{\phi} \times \mathbf{B}) \}_r + B_r \{ \overline{\nabla \times (u_g \hat{\phi} \times \mathbf{B})} \}_\phi \right] d\phi = \tilde{G}(s) \end{aligned} \quad (3.44)$$

and

$$-\tilde{G}(s) = \frac{1}{s} \frac{\partial}{\partial s} \left[ s^2 \int_{C(s)} (C_\phi^a B_s + C_s^a B_\phi) d\phi dz \right] + \frac{s}{\sqrt{1-s^2}} \oint_{N+S} B_\phi (C_r^a + B_r [\overline{C^a}]_\phi) d\phi, \quad (3.45)$$

where the modal projection onto the Galerkin basis is required for an accurate representation of  $\dot{B}_\phi$  within the boundary term. Note that it is not necessary to project the term representing  $\dot{B}_r$ , due to the fact that the radial component of a divergence-free field must be smooth at the boundary.

This approach may be considered as the most direct generalisation of the BWR equation (3.21) to three-dimensions. We note that under the assumption of axisymmetry, equation (3.44) can be directly integrated to obtain the BWR equation (3.21).

Although on one level a simpler method than those previously presented because we do not need to calculate  $\dot{V}$ , in fact the method is more computationally expensive for two reasons. First, we need to check convergence in three parameters:  $I, L_{max}, N_{max}$ , rather than just the first two; second, because the orthonormality requires an integration over radius, in addition to the integration over solid angle required by both methods.

### 3.11 Examples of the geostrophic flow in 3D

We now give some examples to illustrate our generalised methodology for computing the instantaneous geostrophic flow associated with 3D Taylor states, using our spherical-transform method, as explained in §3.10.1. These will be compared with the solution obtained using the fully implicit 3D method with a very small timestep of  $h = 10^{-9}$ ; in all cases the solutions overplot. In none of the cases is an analytic solution available for comparison. For further comparison we plot also the solution of Taylor's ODE (see equation (3.32)).

We consider firstly an example of a non-axisymmetric  $l = 2, m = 2$  poloidal magnetic field

$$\mathbf{B} = \nabla \times \nabla \times A \frac{45\sqrt{3}}{4} r^3 (7 - 5r^2) \sin^2 \theta \cos 2\phi \hat{\mathbf{r}} \quad (3.46)$$

where  $A = 1/(6\sqrt{390})$ . Figure 3.3 shows that the implicit and instantaneous solutions agree, whereas similarly to the axisymmetric case of figure 3.1a we can see that Taylor's solution differs significantly particularly near  $s = 1$ .

For all our three-dimensional solutions the expansion for  $u_g$  differs from that in axisymmetry given in equation (3.20). We now don't include a logarithmic term. As discussed in §3.13.1, the logarithmic behaviour is not expected outside of

axisymmetry and would violate the assumed regularity of the magnetic field.

The approximate polynomial solution, with coefficients rounded to 5 significant figures, is

$$u_g = -94.079s + 550.14s^3 - 2196.4s^5 + 3292.7s^7 - 2178.4s^9 + 11996s^{11} - 35435s^{13} + 42961s^{15} - 24113s^{17} + 5248.3s^{19},$$

where the expansion has been truncated at  $s^{19}$  and convergence achieved with parameters  $I = L_{max} = 20$ .

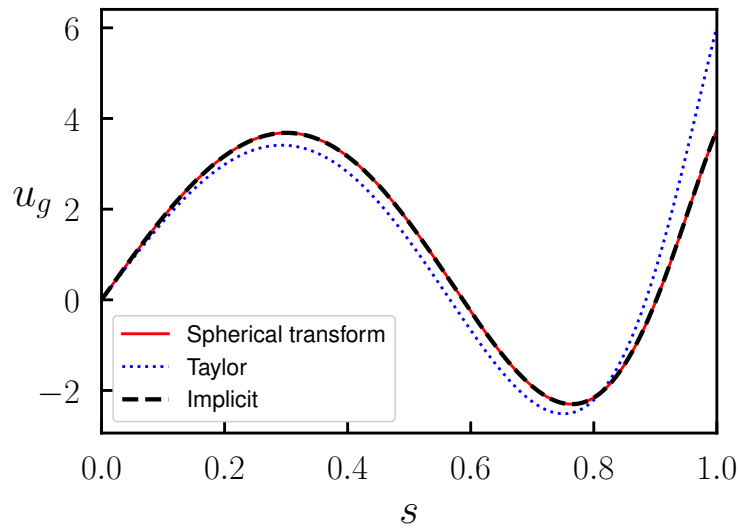


Figure 3.3: The geostrophic flow for the non-axisymmetric  $l = 2$ ,  $m = 2$  poloidal Taylor state of equation (3.46). Solutions using the spherical transform method, the implicit timestep method with  $h = 10^{-9}$  and Taylor's ODE are compared.

We secondly consider a more complex example of a non-axisymmetric magnetic field, which contains both  $l = 2$ ,  $m = 1$  toroidal and poloidal components

$$\begin{aligned} \mathbf{B} = & \nabla \times A_t \sqrt{3} r^3 (1 - r^2) \sin \theta \cos \theta \cos \phi \hat{\mathbf{r}} \\ & + \nabla \times \nabla \times A_p \frac{45\sqrt{3}}{2} r^3 (7 - 5r^2) \sin \theta \cos \theta \cos \phi \hat{\mathbf{r}} \end{aligned} \quad (3.47)$$

where  $A_t = \frac{5}{4}\sqrt{21}$  and  $A_p = \sqrt{7/262440}$ . Figure 3.4 shows that again the solution using the instantaneous method is validated by the implicit method, whereas Taylor's solution deviates as  $s \rightarrow 1$ . The figure also shows the geostrophic flow generated separately by either the purely-toroidal, or purely-poloidal magnetic field component, each individually a Taylor state. As anticipated by the structure of the equation for  $u_g$  (nonlinear in  $\mathbf{B}$ ), the geostrophic flow driven by the total field does not equal the sum of the individually driven geostrophic flows.

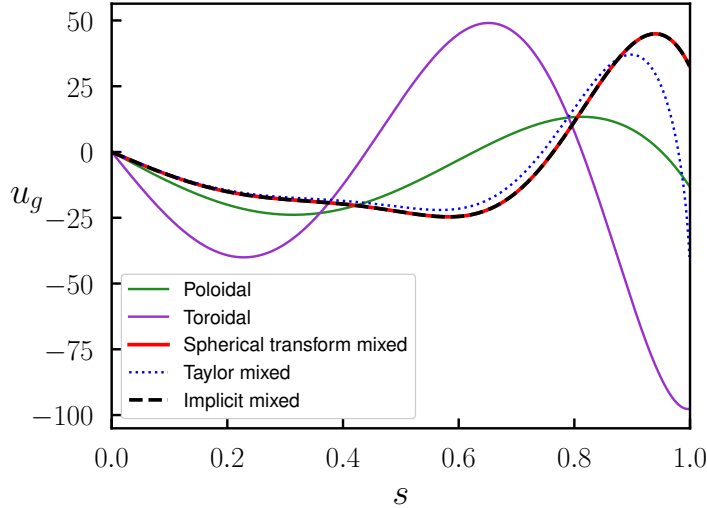


Figure 3.4: The geostrophic flow for the  $l = 2$ ,  $m = 1$  non-axisymmetric mixed Taylor state of equation (3.47). Solutions using the spherical transform method, the implicit timestep method with  $h = 10^{-9}$  and Taylor’s ODE are compared. Solutions for solely either the poloidal and toroidal components of the Taylor state using the spherical transform method are also shown.

### 3.12 Analytic approximation for an Earth-like field

Based on the present structure of the geomagnetic field, various studies show that it is reasonable to neglect the boundary term in equation (3.13) in an Earth-like context (Roberts and Wu, 2014; Roberts and King, 2013). This is because not only is the magnetic field likely much stronger inside the core than on  $r = 1$ , but also because only the non-axisymmetric field contributes to the boundary term and it is relatively weak. The estimated strength of the magnetic field inside the core is 5 mT, and that of the non-axisymmetric field on  $r = 1$  is 0.5 mT; therefore the relative magnitude of the boundary to the interior terms is about  $1/10^2$  or 1%. The negligible effect of the boundary term has been verified in the case of related studies of torsional waves (Jault and L egaut, 2005; Roberts and Aurnou, 2011).

Should we neglect the boundary term entirely, then the geostrophic flow is described by the same equation (3.36) that pertains to a purely-toroidal field, whose solution is

$$u_g(s) = -s \int_0^s \frac{S(s')}{s' \alpha(s')} ds'. \quad (3.48)$$

We note that, in general,  $S/\alpha$  is  $O(1)$ , therefore similar to the axisymmetric case described in §3.7.3, this approximate solution for  $u_g$  behaves as  $s \ln(s)$  as  $s \rightarrow 0$ .

This is despite an exact non-axisymmetric solution being regular at the origin, as explained in §3.13.1.

As an example of this approach, here we construct an Earth-like Taylor state comprising an axisymmetric poloidal mode and a non-axisymmetric toroidal mode, scaled such that the magnitude of the asymmetric part is 20% of the magnitude of the axisymmetric part, but that the total rms field strength is unity:

$$\mathbf{B} = \nabla \times \left[ A_t \frac{\sqrt{3}}{2} r^3 (1-r^2) \sin^2 \theta \cos 2\phi \right] \hat{\mathbf{r}} + \nabla \times \nabla \times \left[ A_p \frac{21}{2} r^2 (5-3r^2) \cos \theta \right] \hat{\mathbf{r}} \quad (3.49)$$

where  $A_t = \sqrt{28875}/4$  and  $A_p = 1/\sqrt{966}$ . The analytic solution of (4.7) is

$$\begin{aligned} u_g(s) = & \frac{s}{1185586336} \left[ -3645348420 \sqrt{10626} \arctan \left( \frac{(5s^2 - 5) \sqrt{10626}}{42} \right) \right. \\ & + 9801464537150 s^6 - 12073529601375 s^4 \\ & - 633064443000 s^2 - 25808428800 \ln(s) \\ & \left. + 25531026444 \ln(6325 s^4 - 12650 s^2 + 6367) + 1185586336 C_1 \right], \end{aligned}$$

which is shown in figure 3.5 and compared to our solution by the method in §3.10.1 in which full account is taken of the boundary terms. As anticipated, the two solutions are very similar and diverge only close to  $s = 1$  (where the boundary term has most effect), with an rms difference of about 1%, all of which occurs very close to the outer boundary. This validates the neglect of the boundary term for this example, and indicates the significance of equation (4.7) which can be used with confidence to analytically approximate the geostrophic flow generated by an Earth-like field. However, we note the presence of a logarithmic singularity that (in view of an earlier comment) we do not expect in a non-axisymmetric case; this is discussed in the following section.

Finally figure 3.6(b) shows contours of the total azimuthal component of the flow. Of note is the much higher amplitude of flow associated with the increased complexity of the magnetic field compared to the single-mode magnetic field example of figure 3.6(a). The scale of this flow is as would be expected geophysically: maximum dimensionless velocities are of order 100, corresponding to dimensional velocities of order  $10^{-4} \text{ m s}^{-1}$  consistent with large-scale core flows inferred by secular variation (Holme, 2015).

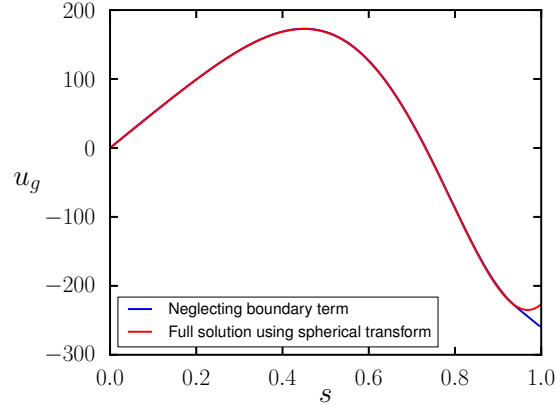


Figure 3.5: The geostrophic flow for a non-axisymmetric Earth-like Taylor state. Numerical solution using the spherical transform method (red) is compared to the analytic solution neglecting the boundary term (blue).

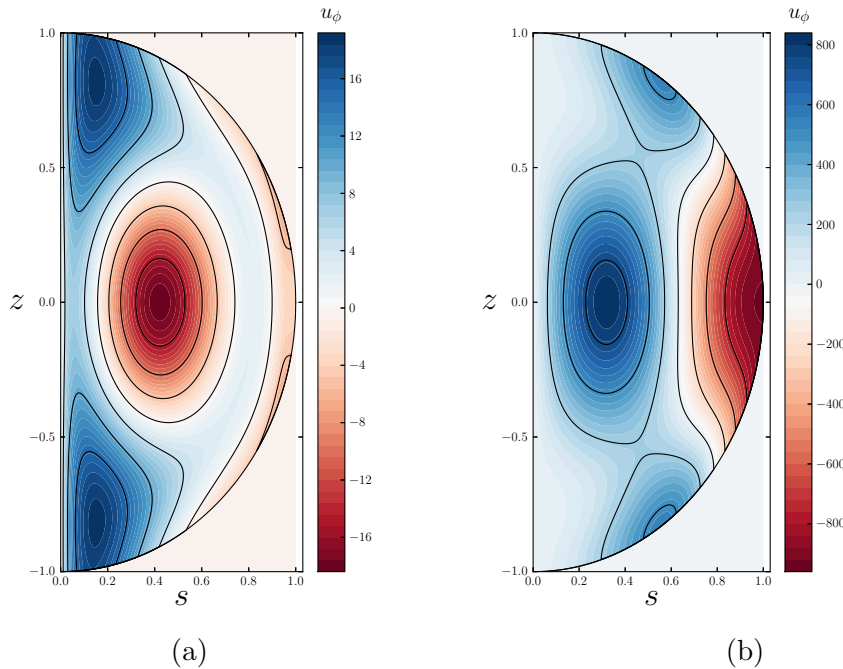


Figure 3.6: Contour plots of (a) the total azimuthal flow  $u_\phi$  driven by the axisymmetric poloidal field in §3.9.1, (b) the axisymmetric part of the total azimuthal flow driven by the Earth-like field of (3.49). The azimuthal flow is shown to be approximately 50 times stronger in (b) and similar to values expected in Earth’s core (Holme, 2015).

### 3.13 Singularities of $u_g$

A key benefit of having an instantaneous description of the geostrophic flow is to make explicit its analytic structure, which then motivates spectral expansions such as (3.20) for use with other methods. Assuming  $\alpha(s) > 0$ , because the equation describing  $u_g$  is smooth and regular,  $u_g$  is expected to be an odd (Lewis and Bellan,

1990) finite function on  $0 < s < 1$ . There are three places however where the solution may be singular: (i)  $s = 0$ ; (ii)  $s = 1$  and (iii) in the complex plane  $s = x + iy$ , away from the real axis ( $y \neq 0$ ). We discuss each in turn.

### 3.13.1 Singularities at $s = 0$

Firstly we consider the presence of a singularity at  $s = 0$ . In axisymmetry, it is well established that  $u_g \sim s \ln(s)$  as  $s \rightarrow 0$ , resulting in a  $s^{-1}$  singularity in  $\partial_s(u_g/s)$  (Jault, 1995; Wu and Roberts, 2015; Fearn and Proctor, 1987), reproduced in our example (3.31). However it has not been quite clear whether the logarithmic singularity pertains to a general asymmetric Taylor state: in particular, in axisymmetry  $s = 0$  is a singular line of the coordinate system, whereas in 3D spherical coordinates the only singular point is the origin  $r = 0$ . Roberts and Wu (2014) showed that either by neglecting the boundary term (their (25a)) or considering Taylor's ODE directly, which we have shown to be of limited validity, (see their Appendix B) leads to a general logarithmic behaviour.

At first inspection it appears that the boundary term is negligible as  $s \rightarrow 0$ . For a general 3D field, both  $\mathbf{B}$  and  $\dot{\mathbf{B}}$  are  $\mathcal{O}(1)$  on  $s = 0$ , suggesting that the interior term in equation (3.28) is  $\mathcal{O}(1)$ , whereas the boundary term is  $\mathcal{O}(s)$  as  $s \rightarrow 0$ . Motivated by the example in §3.12, this suggests that a full treatment (including the boundary term) retains the singularity in 3D — however, we do not find this to be the case. Significant cancellation in the interior term occurs and while the integrand is  $\mathcal{O}(1)$ , the integral itself is  $\mathcal{O}(s)$ , as expected since we know that the interior term and boundary term must sum to zero for all  $s$ . Therefore, there is no evidence that the 3D case has a logarithmic singularity at  $s = 0$ , and indeed all our numerical solutions and analytic solutions are regular there. In the purely toroidal field explored in §3.9.2, the analytic solution given in equation (3.38) is purely polynomial, with no singular behaviour at the origin. This assertion can be strengthened into a theorem.

**Theorem 3.13.1.** *The assumption of a magnetic field that is regular initially and remains so for all time places a restriction on the permitted behaviour of the geostrophic flow. In axisymmetry, the space of solutions allows a weak singularity in the geostrophic flow at  $s = 0$ . However, in three dimensions it is required that the geostrophic flow is regular at the origin in order to maintain regularity of the magnetic field.*

*Proof.* This result directly follows from the form of the geostrophic term in the induction equation. In axisymmetry this is given by equation (3.16), from which it

is clear that it is permissible for  $u_g$  to contain a weak logarithmic singularity while maintaining a regular  $\mathbf{B}$ . In 3D the geostrophic term in the induction equation is given by equation (3.35). In the presence of a non-axisymmetric magnetic field, any logarithmic singularity in  $u_g$  would render  $\partial_t \mathbf{B}$  non-regular. Hence the assumption of regular  $\mathbf{B}(t)$  is incompatible with such a singular solution.

□

While the analytic approximation in §3.12 is shown to produce accurate geostrophic flows for Earth-like magnetic fields, it should be used with caution, since the analytic structure of the solution will contain an  $s \ln s$  dependence, that does not persist when the full balance including the boundary term is considered. For axisymmetric magnetic fields this weak logarithmic singularity is not a significant concern since the geostrophic flow only enters the induction equation through  $\partial_s(u_g/s)$  and so the magnetic field remains regular everywhere. By contrast, in 3D the structure of the geostrophic term in the induction equation (given in equation (3.35)) means that the logarithmic singularity is imparted to the magnetic field itself, causing the magnetic field to diverge at the rotation axis and violating the standard assumption of a regular field. Thus, in a practical implementation, such singular behaviour must be filtered out of  $u_g$ .

### 3.13.2 Singularities at $s = 1$

We also address the possible existence of a singularity at  $s = 1$ . For the specific case of an axisymmetric dipolar magnetic field, Roberts and Wu (2014) presented an argument that  $\partial_s u_g \sim (1 - s^2)^{-1/2}$ , although they conceded that this was not supported by their numerical examples. The same form of singular behaviour for  $u_g$  has been predicted for torsional waves (Schaeffer et al., 2012; Maffei and Jackson, 2016), perturbations to Taylor states, whose eventual steady state at  $t = \infty$  would be exactly magnetostrophic (if indeed steady Taylor states exist, a topic considered in the research presented in Chapter 4 of this Thesis). However, there is no reason why the analytic structure of the oscillations should mirror that of the underlying background state, particularly as the manner of how the limit  $t \rightarrow \infty$  is reached at the end points where the wave speed may vanish is unclear (Li et al., 2018; Roberts and Wu, 2018).

Although we are not in a position to prove one way or the other the existence of singular behaviour at  $s = 1$ , we demonstrate by example that it is not generally present.

We find no singularity at  $s = 1$  in the non-axisymmetric example of §3.11. A similar regular behaviour is shown in figure 3.7 (red curve) for an axisymmetric example. Interestingly, for this latter case, the application of Taylor’s ODE (which is invalid for this example) gives a solution that does show a singularity at  $s = 1$  (blue curve). In this instance, singular behaviour is simply an artifact of applying Taylor’s ODE when it is not valid, and we have found no cases where a solution to our more general analysis behaves singularly at  $s = 1$ .

This observation may help explain why the prediction of a singularity at  $s = 1$  (Roberts and Wu, 2014) is not borne out in any numerical examples. They themselves discussed this discrepancy and hypothesized that a key issue is the lack of boundary information contained within Taylor’s equation. We speculate that should their magnetic field satisfy not only Taylor’s constraint and the boundary conditions but also crucially the first order boundary conditions, that this singular behaviour will vanish and the geostrophic flow will remain regular at  $s = 1$ . We note however that certain magnetic forcing terms can render the geostrophic flow singular at  $s = 1$ : for example, that of a non-polynomial mean-field  $\alpha$ -effect described in Appendix F of Li et al. (2018).

Finally, we remark that for a dipolar axisymmetric Taylor state, both Li et al. (2018) and Roberts and Wu (2018) showed evidence of non-singular but abrupt boundary-layer like behaviour close to  $s = 1$ , possibly because the equation describing the geostrophic flow is null at the equator (i.e.  $\alpha = S = 0$ ). A similar result was also found by Fearn and Proctor (1987) who abandoned constraining their geostrophic flows near  $s = 1$  due to anomalous behaviour. We note, however, in our analytical solutions, we find no evidence of such behaviour: for example figure 3.1a shows a smooth solution at  $s = 1$ .

### 3.13.3 Singularities off the $s$ -axis

Finally, inspecting an example solution (3.31) shows that there can be either branch cuts or logarithmic singularities away from the real line. These do not affect the solution itself (defined on the real interval  $0 \leq s \leq 1$ ) but can influence convergence of the numerical method used to find  $u_g$  (Boyd, 2001). The closer the singularities lie to the real interval  $[0, 1]$  the slower the convergence. In general, we speculate that such singularities can lie arbitrarily close to the real line, possibly being associated with the breakdown of the magnetostrophic balance, for example, torsional waves etc.

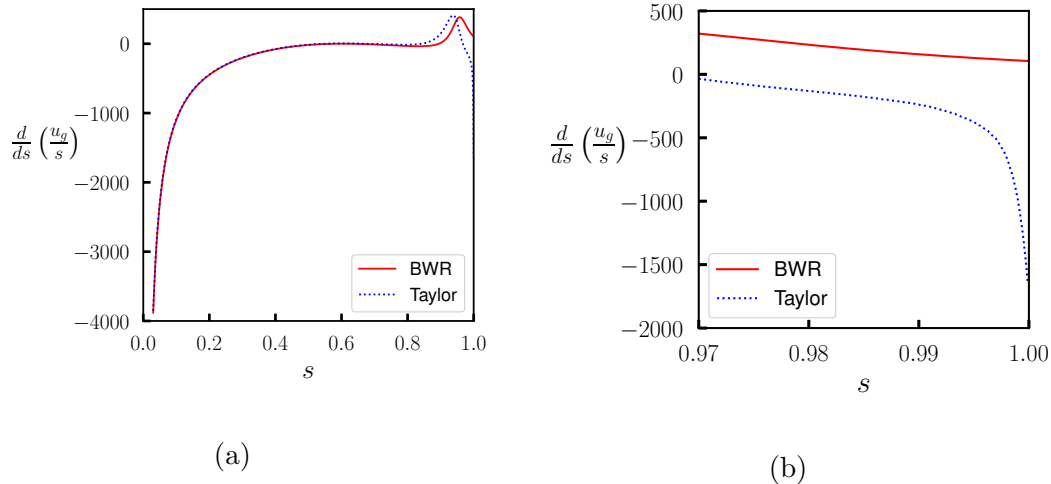


Figure 3.7: A plot of  $\partial_s(u_g/s)$  for solutions to a mixed axisymmetric Taylor state consisting of the poloidal field of the example of §3.9.1 with a  $l = 1$ ,  $m = 0$ ,  $n = 1$  toroidal Galerkin mode, using the BWR and Taylor equations. (a) Shows the whole domain, a singularity of the form  $s^{-1}$  is visible for both solutions at  $s = 0$  and for Taylor’s solution only, a weaker singularity also occurs at  $s = 1$ . (b) Zoomed-in plot of the  $s = 1$  singularity to show clearly that it only occurs when solving Taylor’s equation; it has the form  $(1 - s^2)^{-\frac{1}{2}}$ .

### 3.14 Discussion

In this chapter we have discussed in some detail how the geostrophic flow, a fundamental part of any magnetostrophic dynamo, might be determined. Of particular note is that we have shown why the method introduced by Taylor (1963) fails in most cases, because of its intrinsic (and, to date, unrecognised) assumption that the initial magnetic field structure must satisfy a higher-order boundary condition (that is, both the magnetic field and its time derivative must satisfy matching conditions pertaining to an exterior electrical insulator). We presented a generalised version of Taylor’s method valid for an arbitrary initial magnetic Taylor state that is not subject to higher order boundary conditions. In many of our examples, the magnetic fields of dimensional scale 1.7 mT drive flows of magnitude about  $10^{-4} \text{ m s}^{-1}$ , comparable to large-scale flows inferred for the core (Holme, 2015). Thus, in concert with weakly-viscous models, inviscid models also produce Earth-like solutions.

A broader point of note is the extent to which the restriction on the validity of Taylor’s approach impacts the related derivation of the equation describing torsional waves (Roberts and Aurnou, 2011). A general treatment of torsional waves includes boundary terms, whose proper evaluation would require a method such as described in Jault (2003). However, the troublesome boundary terms are usually neglected, either because of axisymmetry or because of arguments based on the rel-

ative size of the asymmetric magnetic field (Roberts and King, 2013). Either way, these approaches remain unconstrained by any consideration of higher order boundary conditions on the magnetic field and the theoretical description remains correct. However, in §3.13.1 we describe the danger of neglecting the boundary term, this leading to a logarithmic singularity not present in solutions of the full equation. This has potential implications for analysis of torsional waves, for which the avoidance of a logarithmic singularity may require the full boundary term.

It is worth noting that the weak logarithmic singularity  $u_g \sim s \ln(s)$  as  $s \rightarrow 0$  in axisymmetric magnetostrophic models stands in contrast with weakly viscous models which are anticipated to be regular everywhere. For example, in axisymmetry for both no-slip and stress-free boundary conditions, the formulae for  $u_g$  from Livermore et al. (2016) are

$$u_g(s) = -E^{1/2} \frac{(1-s^2)^{1/4}}{s^2} \frac{d}{ds} \left( s^2 \int_0^{Z_T} \mathcal{S} \frac{d\mathcal{T}}{dz} dz \right),$$

and

$$u_g(s) = E^{-1} \left( s \int_s^1 \left( \frac{1}{\rho \sqrt{1-\rho^2}} \int_0^{Z_T} \mathcal{S} \frac{d\mathcal{T}}{dz} dz \right) d\rho + sC_1 \right),$$

respectively, and since  $B_s, B_\phi \sim s$  as  $s \rightarrow 0$  this means that the asymptotic structure within axisymmetry for both boundary conditions is  $u_g = O(s)$ . While, in non-axisymmetry the asymptotic formulae from Hollerbach (1996) gives

$$u_g(s) = -E^{1/2} \frac{(1-s^2)^{1/4}}{4\pi s} \int_{C(s)} ([\nabla \times \mathbf{B}] \times \mathbf{B})_\phi d\phi dz,$$

and through the properties of general vectors described by Lewis and Bellan (1990), we have that  $([\nabla \times \mathbf{B}] \times \mathbf{B})_\phi \sim s$  and hence  $u_g = O(1)$ .

The presence of a weak logarithmic singularity is therefore a feature unique to the axisymmetric inviscid case, and serves to distinguish the exact magnetostrophic balance (with zero viscosity) from models with arbitrarily small but non-zero viscosity. However, in 3D there is no such distinction between the structure of  $u_g$  between  $E = 0$  and  $E \ll 1$ : in both cases  $u_g$  is regular.

We note that the instantaneous analysis of the induction equation considered here is akin to the kinematic dynamo framework of examining magnetic field evolution based solely on a pre-defined flow. This has important implications for the applicability of our theorem, which states that in three dimensions it is required that the geostrophic flow is regular at the origin in order to maintain regularity of

the magnetic field. If an  $s \ln s$  singularity were present in  $u_g$  then this would result in an  $s^{-1}$  singularity in the azimuthal component of equation (3.35) and therefore through the induction equation (3.10), a logarithmically singular induced magnetic field. However, as Roberts and Wu (2020) explain, within a fully dynamic MHD system, it is possible for a regular magnetic field to be maintained in spite of singular geostrophic flow. This is crucial in evading the disastrous consequences of violating regularity of the magnetic field at  $s = 0$ .

Given that the geometry of the outer core of the Earth is a spherical shell rather than a full sphere, a natural question to ask is how we would calculate the flow within this domain. The method for determining the ageostrophic flow would remain comparable although it could be discontinuous or singular across the tangent cylinder  $\mathcal{C}$ , the geostrophic cylinder tangent to the solid inner core (Livermore and Hollerbach, 2012). As for the geostrophic flow, in the absence of viscosity, there is no reason why it must be continuous across  $\mathcal{C}$ . Roberts and Wu (2020) have recently shown how singularities in both the zonal and other components of the fluid velocity, are related to the specified flow forcing function (the total force due to the Lorentz and buoyancy forces), and how flow discontinuities on the tangent cylinder can be determined by that function.

Although supplying an analytic structure of the evolving magnetostrophic flow, an instantaneous determination of the geostrophic component is not itself of practical use within a numerical method using finite timesteps of size  $h$ , as the solution will immediately diverge from the solution manifold (Livermore et al., 2011). However, as for the axisymmetric-specific method of Wu and Roberts (2015), our 3D instantaneous methods generalise simply to schemes that are accurate to first order in  $h$ , thus presenting a viable method for numerically evolving a 3D magnetostrophic dynamo. A direct comparison of this method with the fully implicit (3D) method of Li et al. (2018) would be an interesting study. Indeed, our 3D first-order-accurate solutions could be used as a starting guess for their nonlinear iterative scheme, enabling much larger timesteps to be taken for which the geostrophic flow does not need to be close to its structure at the previous step.

# Chapter 4

## Stable steady Taylor states

### 4.1 Introduction

Earth's magnetic field is observed to be a stable, consistent feature, existing continuously over the past 3.4 - 4.2 billion years (Tarduno et al., 2015). Over this time-span the geomagnetic field has undergone significant changes, including full geomagnetic reversals and the short time scale perturbations of secular variation. However, some field features, such as the longstanding dominance of the dipole moment, appear inherently maintained and consistent throughout time. Hence the question of whether the geodynamo process and resultant geomagnetic field is in a stable configuration, which is only slowly varying, is a non-trivial one to address.

Variations in the geomagnetic field have been observed on a range of timescales from archeomagnetic and paleomagnetic data (sections 1.2.3 and 1.2.5). Fast dynamics have also been reproduced in many state of the art dynamo simulations (Aubert, 2020; Schaeffer et al., 2017), however the computational expense of such simulation means they are restricted to short temporal ranges and hence the ability to investigate the evolution and stability of the background field is very limited. Simulations over longer timescales have been carried out in attempts to reproduce the longer term secular variation of the geomagnetic field (Davies and Constable, 2020). However, the price for this temporal range is in decreased resolution and hence a restriction to using parameter value further from those of the Earth ( $E > 10^{-5}$ ). The more fundamental question of whether the underlying physics of the dynamo process is intrinsically unstable has been explored by Zhang and Gubbins (2000), who suggest that the value of Ekman number is of crucial importance, with more unstable behaviour expected at lower Ekman numbers. In all these nu-

merical dynamo simulations where the Ekman number is of course finite and large in comparison to the Earth, this inflated significance of the role of viscosity is expected to be providing an artificially stabilizing effect, not present within Earth's core.

Here we will consider the magnetostrophic limit, deemed geophysically relevant as the asymptotic limit of Earth's dynamo, in which viscosity plays no role. The theoretically predicted timescale associated with this force balance describes the slow evolution of the magnetic field (as discussed in §2.6). This is of course the timescale on which the Taylor constraints act, due to their derivation arising from the magnetostrophic equations. A Taylor state (a field which satisfies Taylor's constraint) therefore describes the background geomagnetic field and does not incorporate fast perturbations in the field.

Recent studies by [Livermore et al. \(2008, 2009\)](#) have provided and implemented a complete algorithm for the non-trivial procedure of constructing a magnetic field such that it exactly satisfies Taylor's constraint (a Taylor state). This method is described in §6.4 and solved in a geophysical setting in figure 6.6. This work gives an insight into the potential structure of the magnetic field inside Earth's core. However, it only provides a methodology for creating instantaneous Taylor states, where due to the nature of the method, there is no consideration of the way in which the magnetic field will evolve. This time dependence is of course vitally important, because the Taylor state fields will drive flows within the fluid, which will induce magnetic field and perturb the Taylor state.

It is also noteworthy that the space of Taylor states is large. It is this lack of uniqueness, which makes it so challenging to know whether any one solution is representative of the Earth. Here we are in search of those Taylor states that are most realistic, which are self-sustaining and do not change more rapidly than the geomagnetic field. We seek Taylor states which are 'quasi-steady', that is, the instantaneous rate of change of magnetic field is close to zero.

This requires the computation of the flows generated by any given Taylor state field, which consists of both the ageostrophic flow, which is uniquely determined from the magnetostrophic equation and the more problematic geostrophic flow (see Chapter 3), which is only specified uniquely through the requirement that the Taylor constraint continues to be satisfied through time. In order to do this we compute the ageostrophic flow by using the procedure outlined in §3.3. We also calculate the geostrophic component of the flow exactly, through implementing the approach described in chapter 3. This method is valid within the fully three-dimensional system relevant for the convectively driven planetary dynamo problem. However,

in this work we focus on the axisymmetric problem, for which the geostrophic flow calculation is greatly simplified (Wu and Roberts (2015) and chapter 3). In axisymmetry the geostrophic flow can be calculated analytically without the need for the implementation of the more complex numerical methods of §3.10. Also the numerical magnetostrophic dynamo code of Li et al. (2018), which we will utilise, is, in its pre-existing state, restricted to axisymmetry (despite the fundamental method being extendable to 3D). This is of course not as general as the fully 3D system representative of Earth’s core, and it should be noted that some features may be different when restricted to axisymmetry (Fearn and Rahman, 2004). Nevertheless, this axisymmetric study will serve as a useful first foray into investigating Taylor state dynamics.

In this chapter we will seek to determine if any steady Taylor states exist and if so how abundant they are and what common properties they may have. Also, we will investigate the long time evolution and stability of Taylor states and compare their rate of change to geomagnetic observations.

## 4.2 Methodology

Our analysis consists of two approaches. Firstly, we focus on steady Taylor states, carrying out a systematic search over a chosen subset of the space of axisymmetric Taylor state magnetic fields. Computing the instantaneous rate of change, finding any steady Taylor states, and determining the sensitivity of this rate of change to small differences in some magnetic field coefficients.

Secondly, we analyse stability of Taylor states. We run a suite of dynamical simulations with different initial magnetic fields conditions. For each of these starting points, as the simulation evolves, satisfying Taylor’s constraint at every timestep, we analyse the path through the space of magnetic fields and ultimately to what solution, if any, the field converges. Thereby examining the stability of a given Taylor state initial condition and revealing any such stable states that may be converged to.

These approaches, although distinct, are complementary in our investigation of the evolution of Taylor states. The results from our calculations of magnetic fields whose instantaneous rate of change is small, termed ‘quasi-steady’ are not necessarily stable (unless the rate of change is precisely zero, which is impossible to numerically obtain), since any small initial change may lead to unstable growth.

However, they do provide prime candidates for stable steady Taylor states, since being ‘quasi-steady’ is a necessary condition for being a stable steady state. Therefore part of our study will involve these fields being directly used as initial conditions in dynamical simulations to test their stability.

For both of these methodologies the focus is to examine the rate of change of the magnetic fields. The equation that describes this is of course the induction equation

$$\partial_t \mathbf{B} = \nabla \times (\mathbf{u} \times \mathbf{B} - \mathbf{J}). \quad (4.1)$$

We restrict attention to the axisymmetric case, and therefore as explained in §2.5, an  $\alpha$ -effect is required in order to facilitate successful dynamo action.

The form of any  $\alpha$ -effect that is chosen is not unique, in fact the arbitrary nature of this is a notable model limitation (which we address in §4.4.5). The majority of results presented utilise the commonly used ‘Braginsky’ form (Roberts, 1972; Hollerbach and Ierley, 1991; Wu and Roberts, 2015; Li et al., 2018)

$$\alpha = \alpha_0 \frac{729}{16} r^8 (1 - r^2) \cos \theta, \quad (4.2)$$

where the constant  $\alpha_0$  specifies the magnitude of the  $\alpha$ -effect and a sufficiently high value is required to sustain a dynamo. This is a necessary condition for any energetically stable or growing magnetic fields to exist as it provides the means to balance Ohmic diffusion. The critical value above which dynamo action occurs for this structure of alpha within a magnetostrophic dynamo is  $\alpha_0 = 13.1$  (Li et al., 2018).

The induction equation in full, which represents the instantaneous rate of change in magnetic field, now becomes

$$\partial_t \mathbf{B}(r, \theta, \phi) = \nabla \times [(\mathbf{u}_a(r, \theta, \phi)) \times \mathbf{B}(r, \theta, \phi) - \mathbf{J} + \alpha(r, \theta) \mathbf{B}] + s B_s \frac{d(u_g/s)}{ds} \hat{\phi}, \quad (4.3)$$

where the contributions of the geostrophic and ageostrophic flow are explicitly distinguished.

The ageostrophic component of the flow is purely a function of the input magnetic field  $\mathbf{B}$  and can be solved for from the magnetostrophic equation (2.2), as described in §3.3. What remains is then the more complex task of explicitly solving for the geostrophic flow.

### 4.2.1 Method for calculating instantaneous $u_g$ and magnetic induction

In Chapter 3 various different methods for determining the geostrophic flow in differing circumstances are described. We utilise that work here; specifically it is the instantaneous geostrophic flow within axisymmetry that we seek here, which can be determined using the method outlined in §3.7.3.

In order to evaluate the induction equation we calculate the three components of  $\frac{\partial \mathbf{B}}{\partial t}$  separately. The terms  $\left(\frac{\partial \mathbf{B}}{\partial t}\right)_r$  and  $\left(\frac{\partial \mathbf{B}}{\partial t}\right)_\theta$  are independent of the geostrophic flow and hence are calculated from the magnetic field and ageostrophic flow, while the  $\alpha$ -effect also provides an additional energy source of energy. Hence

$$\left(\frac{\partial \mathbf{B}}{\partial t}\right)_r = (\nabla \times (\mathbf{u}_a \times \mathbf{B} - \mathbf{J} + \alpha(r, \theta)\mathbf{B}))_r,$$

and

$$\left(\frac{\partial \mathbf{B}}{\partial t}\right)_\theta = (\nabla \times (\mathbf{u}_a \times \mathbf{B} - \mathbf{J} + \alpha(r, \theta)\mathbf{B}))_\theta.$$

The induction in the azimuthal direction comprises two parts, the ageostrophic induction, which takes the same form as for the other components, but also, the geostrophic induction, which is shown in equation (3.16), in axisymmetry to be  $sB_s \frac{d(u_g/s)}{ds} \hat{\phi}$ . This results in

$$\left(\frac{\partial \mathbf{B}}{\partial t}\right)_\phi = (\nabla \times (\mathbf{u}_a \times \mathbf{B} - \mathbf{J} + \alpha(r, \theta)\mathbf{B}))_\phi + sB_s \frac{d(u_g/s)}{ds}. \quad (4.4)$$

Evaluating the geostrophic induction term first requires the computation of the intermediate quantities

$$S_0(s) = 2\pi s^2 \int_{-Z_T}^{Z_T} (B_s C_\phi^a + B_\phi C_s^a) dz, \quad \alpha_0(s) = 2\pi s^2 \int_{-Z_T}^{Z_T} B_s^2 dz, \quad (4.5)$$

where

$$\mathbf{C}^a = \nabla \times (\mathbf{u}_a \times \mathbf{B}) + \nabla^2 \mathbf{B}. \quad (4.6)$$

It is then possible to explicitly calculate the geostrophic flow

$$u_g(s) = -s \int_0^s \frac{S_0(s')}{s' \alpha_0(s')} ds'. \quad (4.7)$$

However, in practicality, within axisymmetry it is not required to carry out this integration in  $s$  and directly compute the geostrophic flow. If one merely seeks the

magnetic induction due to the geostrophic flow then it is only the following quantity that is of interest

$$\frac{\partial(u_g(s)/s)}{\partial s} = -\frac{S_0(s)}{s\alpha_0(s)}. \quad (4.8)$$

There is a complication here of using two different coordinate systems. The natural coordinates within a spherical domain, are generally spherical coordinates, therefore the magnetic field  $\mathbf{B}$  and ageostrophic flow  $\mathbf{u}_a$  are computed in this coordinate system. However, the geostrophic flow  $u_g(s)$ , purely a function of cylindrical radius, is best expressed in cylindrical coordinates. Care needs to be taken when transforming these quantities between coordinate systems. To calculate the geostrophic induction, cylindrical components of  $\mathbf{B}$  and  $\mathbf{C}^a$  need to be determined in order to find  $S_0(s)$  and  $\alpha_0(s)$ . The cylindrical components of vectors within spherical coordinates can easily be calculated from the spherical components:

$$\begin{aligned} B_s(r, \theta, \phi) &= B_r(r, \theta, \phi) \sin \theta + B_\theta(r, \theta, \phi) \cos \theta, \\ B_\phi(r, \theta, \phi) &= B_\phi(r, \theta, \phi), \\ B_z(r, \theta, \phi) &= B_r(r, \theta, \phi) \cos \theta + B_\theta(r, \theta, \phi) \sin \theta. \end{aligned}$$

The transformation between coordinate systems themselves is more complex; we carry this out via mapping to spectral space. All quantities for which this is necessary, can then be converted from physical space in spherical coordinates, to spectral space in terms of the Worland polynomials (Livermore et al., 2007) (which have no boundary condition embedded). This includes  $\mathbf{C}^a$ , for which the curl operation is conducted in spectral space (as described in section 2.4.2 of Li (2012)) and encompasses the diffusion term, since through using the solenoidal condition we can write  $\mathbf{C}^a = \nabla \times (\mathbf{u}_a \times \mathbf{B} - \mathbf{J})$ . The integrands in the expressions for  $S_0(s)$  and  $\alpha_0(s)$  (4.5) are also converted into spectral space, such that the integration in  $z$  can be carried out on each spectral mode function, using Gauss quadrature, e.g.

$$\int B_\phi dz = \sum_k w_k B_\phi(s_i, \phi_j, z_k),$$

where  $w_k$  is the Gauss-Legendre quadrature weight and  $z_k$  is the Gauss-Legendre location within  $[-Z_T, Z_T]$ . Each spectral mode here is integrated and then the products with the corresponding coefficients are summed. The resolution of the cylindrical grid used is determined through the requirement of Gauss quadrature being exact. When a polynomial is integrated between two limits, Gauss quadrature is exact for a polynomial of degree  $n$  if  $n/2 - 1$  points are used. Hence it is the maximum degree of any polynomial that will be integrated which provides the number of cylindrical grid points we need to use. Since all integrations that we

carry out are in the  $z$  direction, this does not provide a strict bound on the number of points in  $s$ , but we choose to use the same number of points, with the locations related by  $z = \sqrt{1 - s^2}$ .

Finally, for the induction equation (4.4), the geostrophic induction needs to be converted back to spherical coordinates (via spectral space) such that it can be added to the ageostrophic induction.

This allows us to now calculate the value of  $\frac{\partial \mathbf{B}}{\partial t}$ . However, in order to meaningfully compare the scale of the rate of change of different magnetic fields and ultimately carry out any parameter sweep or optimisation procedure in search of a steady Taylor states, we must represent this with a scalar quantity that takes a single value for a given field. This requires the spatial integration of the square of the previously calculated vector field.

The two quantities we consider to represent the rate of change in magnetic field are then the volumetric integral over the entire spherical domain  $\int \dot{\mathbf{B}}^2 dV$ , and the surface integral over the core surface  $\int \dot{\mathbf{B}}^2 dS$ , which allows a more direct comparison to the observational geomagnetic models that are limited to the CMB. These quantities also need to be normalised by the magnetic field strength in order to truly represent the rate of magnetic field variation without any effect due to the magnitude of the field itself. Therefore we arrive at the quantities

$$I_V = \frac{\int \dot{\mathbf{B}}^2 dV}{\int \mathbf{B}^2 dV},$$

and

$$I_S = \frac{\int \dot{\mathbf{B}}^2 dS}{\int \mathbf{B}^2 dS},$$

which we use throughout our analysis as measures of the normalised instantaneous rate of change of magnetic field.

This method acts as a useful tool to quickly and directly compute the instantaneous rate of change associated with any axisymmetric Taylor state magnetic field. However, it is a crucial point to note that in anything but a perfectly steady state then the solution for an instantaneous geostrophic flow, and associated rate of change of magnetic field, is not necessarily consistent with exactly maintaining a Taylor state over any finite timestep (Livermore et al., 2011), since the value of a constant  $u_g$  over the timestep that is required to remain on the manifold of Taylor states, can differ from the instantaneous solution. Therefore there is a subtle but vital distinction between ‘quasi-steady’ magnetic fields calculated from this method,

which have a small initial rate of change but given sufficient time may substantially change, and a magnetic field which we know will remain of the same form for a very long time, which we denote as a ‘stable steady state’. In order to investigate the stability of Taylor states we need to be able to evolve the fields with time and measure magnetic field change.

### 4.2.2 Time-dependent, implicit method for dynamically evolving B

It is possible for us to probe the time-dependence of any Taylor state and therefore test their stability, through a numerical, dynamical, magnetostrophic dynamo simulation. Within this approach, any stable steady Taylor states should become apparent, as we expect the magnetic field to converge towards them, and once there remain steady indefinitely. Such a dynamical code relies on an implicit method of determining the geostrophic flow, which guarantees that Taylor’s constraint is satisfied at the end of each timestep. One such method would be the axisymmetric first-order implicit method of [Wu and Roberts \(2015\)](#) described in §3.7.1. Another, is the one developed by [Li et al. \(2018\)](#); it is this one that is used here.

[Li et al. \(2018\)](#) introduced a new methodology that uses control theory to solve for the geostrophic flow, through setting up an optimisation problem at each timestep. In this method the value of  $u_g$  is determined implicitly such that the Taylor constraint is satisfied at end of each finite timestep. This is of course a numerical approach, which can give results that differ to the value of the exact instantaneous geostrophic flow determined by the method in the previous section. However, for sufficiently small timesteps then there will be convergence between these two solutions. (For further details of this code please see [Li et al. \(2018\)](#).)

### 4.2.3 Symmetry

Any magnetic field can be considered as the sum of symmetric and antisymmetric components, with respect to the equator. These are referred to as quadrupole and dipole symmetries respectively. Magnetic fields that fall entirely into one of these symmetry classes provide simple cases for us to consider. Importantly they have the feature that, provided  $\alpha$  is suitably chosen (e.g. (4.2)), the symmetry is preserved as time evolves. An initial field that is purely dipole/quadrupole symmetric will induce a purely dipole/quadrupole symmetric magnetic field, so the symmetry will

never change or become mixed, (as shown in Appendix A of [Li et al. \(2018\)](#)).

### 4.3 Searching for steady Taylor states

The total magnetic field is decomposed into the sum of two orthogonal components in the toroidal (T)-poloidal (S) framework (see §3.2)

$$\mathbf{B} = \nabla \times \nabla \times \mathcal{S}\hat{\mathbf{r}} + \nabla \times \mathcal{T}\hat{\mathbf{r}}.$$

In this section we consider the simple situation of imposing a fixed poloidal field, and varying only the toroidal field. This has the significant advantage that the Taylor constraints reduce to a linear system of equations for the toroidal coefficients.

The choice of poloidal field is a free one, as indeed we know that any arbitrary poloidal field can be modified into a Taylor state with the addition of a suitably chosen toroidal field (theorem 6.5.1). Our chosen poloidal field here is the one of the known stable steady Taylor state solutions from [Li et al. \(2018\)](#) within dipole symmetry. Therefore the space of Taylor states explored will include this stable steady solution and magnetic fields which are small to large perturbations from this. This choice is a useful one as it ensures that there will be at least this one steady Taylor state within the domain that we explore. This means crucially, that we have the opportunity to examine the behaviour immediately surrounding steady points, addressing the question of how isolated they may be, while also confirming that we are searching in a region in which it is at least possible for steady Taylor states to exist.

We are then able to sweep through many toroidal fields that are within the space of Taylor states compatible with the imposed poloidal field. As the toroidal field varies, then the associated induction, due to the total magnetic field will also change. Hence through modifying the toroidal field in a systematic way and calculating the instantaneous rate of change of magnetic field (as described in §4.2.1), we determine the nature of the surface of  $I_S$ . This allows us to find the locations within parameter space of magnetic fields for which the rate of change is small (quasi-steady Taylor states), while also examining the behaviour in close proximity to the known stable steady state.

In order to visualise this we carry out a complete search over two parameters, of the largest scale toroidal mode coefficients and visualise the surface of  $I_S$  within this space, with all other coefficients solved for through requiring a Taylor

state. This process is represented by the following expression for the magnetic field:

$$\mathbf{B} = \mathbf{S}_0 + \beta\mathcal{T}_1 + \gamma\mathcal{T}_2 + \mathcal{T}_3(\beta, \gamma, \mathbf{S}_0) + \mathcal{T}_0, \quad (4.9)$$

where  $\mathbf{S}_0$  is the imposed poloidal field,  $\beta$  and  $\gamma$  are free parameters that are systematically varied (the coefficients of the chosen independent toroidal modes) and  $\mathcal{T}_3$  is the remainder of the toroidal field, which is solved for by requiring that Taylor’s constraint is satisfied. However, as there are more degrees of freedom than constraints then this does not result in a unique solution for  $\mathcal{T}_3$ . To enable a unique solution, before solving for  $\mathcal{T}_3$  a number of the highest degree toroidal mode coefficients (equal to the number of excess degrees of freedom) are fixed to be those of the stable solution from which the poloidal field is used (Li et al., 2018), contributing the additional toroidal component  $\mathcal{T}_0$ . In the example presented here, the truncation of the magnetic field used is at degree  $L = 20$ ,  $N = 10$ . The means in the toroidal field there are 2 independently varied free parameters ( $\beta$  and  $\gamma$ ), 160 coefficients of the smallest scale modes fixed as  $\mathcal{T}_0$  and the remaining 38 toroidal mode coefficients solved for through Taylor’s constraints (to construct  $\mathcal{T}_3$ ). At this truncation the imposed field ( $\mathbf{S}_0 + \mathcal{T}_0$ ) is suitably resolved field, the energy spectrum has a drop of 9 orders of magnitude between degrees 1 and 20.

The results are illustrated in figure 4.1, where the axisymmetric version of the standard expansion §4.2.1 is used, and the coefficients of the  $L = 1$ ,  $N = 1$  and  $L = 1$ ,  $N = 2$  modes are varied and the magnitude of the normalised instantaneous rate of change of magnetic field on the core surface,  $I_S$  is plotted. This provides a visual representation of the shape of the surface of  $I_S$  as a function of these two parameters, in the proximity of a stable steady state demarcated by the vertical red line. We note how this point lies within an extended trough and hence that there are many Taylor states within this (restricted) parameter space for which  $I_S$  is small enough to represent a rate of magnetic field change no larger than that of the Earth ( $< 10^{-6} \text{ yrs}^{-2}$ , (see figure 4.8)). This is a key and not a priori obvious result, that demonstrates the abundance of ‘quasi-steady’ Taylor states.

The bottom of the valley seen in figure 4.1, appears to have a ‘spiked’ nature, with significant variation in some neighbouring evaluations, despite the smooth broader trends. This is likely not to be of geophysical interest but rather merely be an artefact of the uniform, finite resolution grid that has been used. Despite being high resolution ( $1000 \times 1000$ ), the steepness of the valley edge and the lack of alignment between the trough and the grid leads to a relatively large amount of fluctuations.

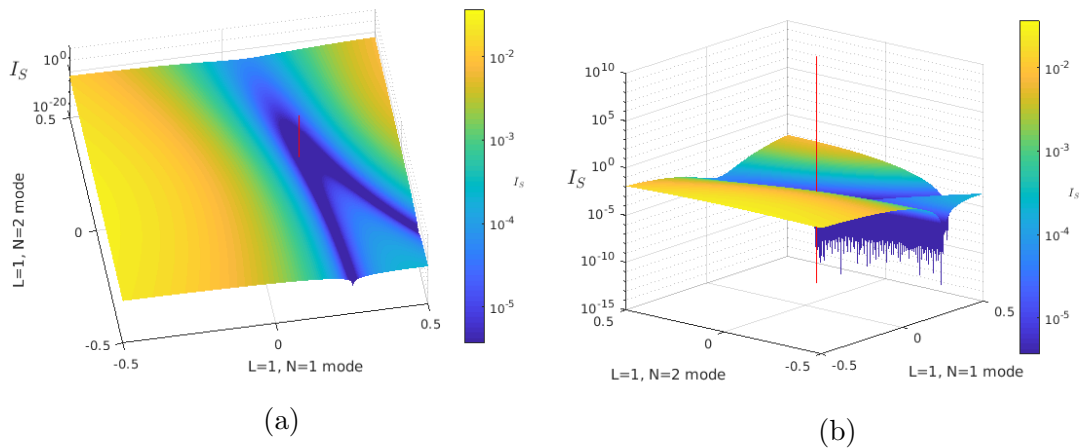


Figure 4.1: Surface plot of the normalised instantaneous rate of change of magnetic field on the core surface,  $I_S$ , as a function of the  $L = 1, N = 1$  and  $L = 1, N = 2$  coefficients values. The vertical red line corresponds to the coefficient values of the known stable steady solution of [Li et al. \(2018\)](#). The  $\alpha$ -effect form (4.2) is used, with an above critical magnitude of  $\alpha_0 = 18$ . (a) and (b) show the same 3D plot viewed from a different angle.

## 4.4 Dynamical magnetostrophic simulations in search of stable Taylor states

Here we run dynamical simulations of the magnetostrophic equations to evolve Taylor state magnetic field with time. All of these simulation use the code of [Li et al. \(2018\)](#) and are conducted at the sufficiently high resolution of maximum spherical harmonic degree  $L = 50$ . Throughout the majority of our simulations (all those reported in sections 4.4.1 to 4.4.4), the  $\alpha$ -effect form (4.2) is used, with an above critical magnitude of  $\alpha_0 = 18$ . The sensitivity of our results to this choice are then considered in §4.4.5.

There are several strands to our approach here. Firstly, we begin with simple initial conditions, purely within either the dipole or quadrupole symmetry. We analyse the progress of these Taylor states, tracking the magnitude of the rate of change of magnetic field throughout time and observing which end stable states are converged to. Secondly, we generalise this approach to a mixed symmetry situation for which no known stable Taylor states exist with energy in both symmetry classes, and search a large number of complex initial conditions in pursuit of a simulation that will converge to the first such example. Thirdly, we utilise our findings in §4.3 that we have found many ‘quasi-steady’ Taylor states that exist and seek to test the

stability of these fields, since we know that being ‘quasi-steady’ is a prerequisite of a stable steady Taylor state.

#### 4.4.1 Simulations with single mode initial conditions

The path taken from the initial condition toward an end steady state is mapped out for the dipole symmetric single mode poloidal  $L = N = 1$  initial condition in figure 4.2. The evolution through the space of Taylor states is represented by the toroidal and poloidal energy of the magnetic field. Initially the rate at which the field changes is fast, with large changes in the poloidal and toroidal energies between each one hundredth of a magnetic diffusion time, indicated by the red data points plotted. This is inextricably linked to relatively large values of normalised instantaneous rate of change of magnetic field throughout the domain  $I_V$ . The field progresses from this initial state towards a stable steady Taylor state with vanishingly small value of  $I_V$ . The initial evolution is not in a direction of purely monotonically decreasing  $I_V$ , but the system approaches the location of a stable point relatively rapidly, achieving a value of  $< 10^{-9} \text{ yrs}^{-2}$  within a magnetic diffusion time before progressing down further to approach  $< 10^{-15} \text{ yrs}^{-2}$ , where it is only limited by machine precision.

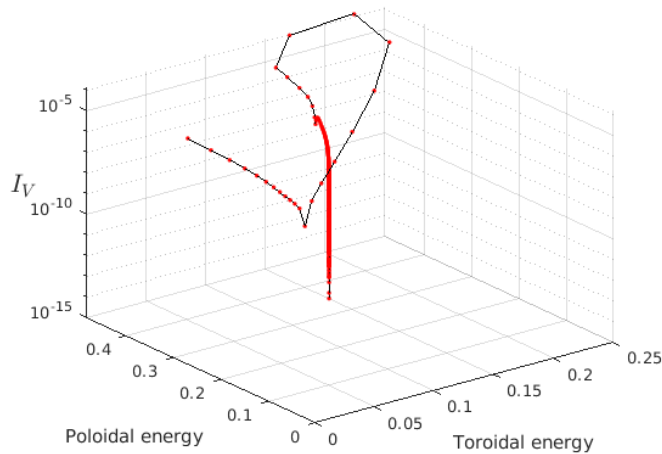


Figure 4.2: The path taken as this single poloidal  $L = N = 1$  mode Taylor state evolves toward a stable steady state with vanishingly small  $I_V$ , the red data points are plotted a frequency of every one hundredth of a magnetic diffusion time (500 yrs).

The reduction in  $I_V$  as the field evolves with time seen for the single initial condition shown in figure 4.2, is also observed in  $I_S$  and illustrated for a large suite of single poloidal mode initial conditions in figure 4.3. Single modes are used here as they allow us to explore a range of initial fields with different spatial scales that

are always strictly in either dipole or quadrupole symmetry, while being guaranteed to be an exact Taylor state (§6.5).

The field evolution along the manifold of Taylor states shows that within two magnetic diffusion times ( $10^5$  yrs), the initial fields have all converged to attracting steady states. The poloidal and toroidal energy of these final steady states for a range of initial conditions show that there are two clear stable states, in terms of energies, which correspond to the solutions within dipole symmetric and quadrupole symmetries, found by Li et al. (2018). We recall that the symmetry of the initial condition is preserved through time, so it is this that determines the end state, the convergence in these two cases occurs at slightly differing rates, as shown when they are distinguished by colour in figure 4.3. We do note that technically there are four distinct stable steady Taylor states, with each of the stable states found by Li et al. (2018) having anti-symmetric counterparts, representing the two possible configurations of  $\mathbf{B}$  and  $-\mathbf{B}$ .

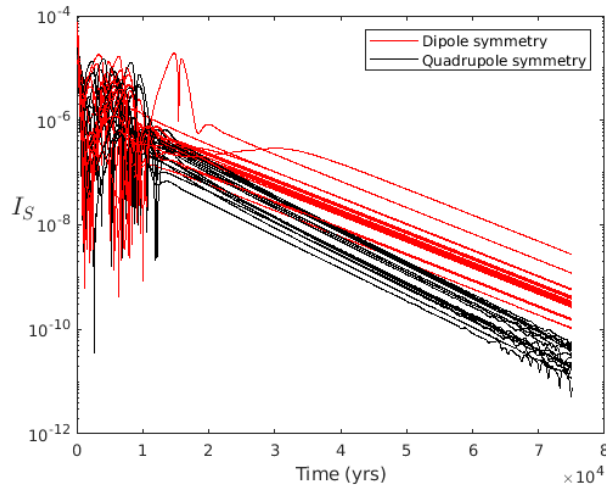


Figure 4.3: Graph showing the evolution of  $I_S$  with time for the suite of single poloidal mode initial conditions

It is significant though that we find that for all the single poloidal mode initial conditions we have used, the solution will always converge to one of these four states. This suggests that stable Taylor states are rare, and that few or no others exist within these symmetries (or these specific states are overwhelmingly attracting, a possibility that is explored in §4.4.4), in contrast to the large number of quasi-steady Taylor states found in §4.3.

## 4.4.2 Simulations with random mixed symmetry initial conditions

In order to broaden out our search for the existence of stable steady Taylor states, we now use the most general form of initial conditions and construct random Taylor states that have mixed symmetry and a combination of toroidal and poloidal modes, from which the magnetic field is free to evolve.

Here we have an initial condition of a large scale Taylor state magnetic field of maximum degree  $L = 4$ ,  $N = 2$ , this has 16 degrees of freedom and 6 Taylor constraints that need to be satisfied. Hence we assign the coefficients of the 10 largest scale modes to be randomly chosen from within the domain  $[-1, 1]$ . We then solve the linear system of constraints for the remaining 6 coefficients such that Taylor's constraints are satisfied. The magnetic field in this example has the following components:

$$\begin{aligned} \mathbf{B} = & a_{1,1}\mathcal{S}_{1,1} + a_{1,2}\mathcal{S}_{1,2} + a_{2,1}\mathcal{S}_{2,1} + a_{2,2}\mathcal{S}_{2,2} + a_{3,1}\mathcal{S}_{3,1} + a_{3,2}\mathcal{S}_{3,2} \\ & + a_{4,1}\mathcal{S}_{4,1} + a_{4,2}\mathcal{S}_{4,2} + b_{1,1}\mathcal{T}_{1,1} + b_{1,2}\mathcal{T}_{1,2} + b_{2,1}\mathcal{T}_{2,1} \\ & + b_{2,2}\mathcal{T}_{2,2} + b_{3,1}\mathcal{T}_{3,1} + b_{3,2}\mathcal{T}_{3,2} + b_{4,1}\mathcal{T}_{4,1} + b_{4,2}\mathcal{T}_{4,2}, \end{aligned} \quad (4.10)$$

where  $a_{1,1}$ ,  $a_{1,2}$ ,  $a_{2,1}$ ,  $a_{2,2}$ ,  $a_{3,1}$ ,  $b_{1,1}$ ,  $b_{1,2}$ ,  $b_{2,1}$ ,  $b_{2,2}$ ,  $b_{3,1}$  are the coefficients that are assigned randomly and the coefficients of the higher degree modes  $a_{3,2}$ ,  $a_{4,1}$ ,  $a_{4,2}$ ,  $b_{3,2}$ ,  $b_{4,1}$ ,  $b_{4,2}$  are calculated through solving Taylor's constraints.

These initial conditions then comprise a set of randomly structured large scale Taylor states, therefore each of them will evolve along a different path, and in doing so search through a large variety of possible field configurations, for a solution state that is stable.

The magnitude of  $I_S$  for each of these Taylor states as a function of time is plotted in figure 4.4. The fact that none of our large suite of models find a stable Taylor state reinforces the evidence that these states are very rare. In the general case considered in this section, when no restriction to a specific symmetry class is made, we fail to find any stable Taylor states. This is important as it is undoubtedly the situation of most geophysical interest, as the Earth's magnetic field is complex and of mixed symmetry, rather than confined to any one.

Another notable feature from these results is the plethora of troughs in the rate of change of magnetic field as the field evolves. The solution passes through fields which are 'quasi-steady' as  $I_S$  becomes smaller than  $10^{-9}$  yrs $^{-2}$ . This confirms

the results of the instantaneous rate of change of magnetic field results in the previous section, where we observed many different fields that were ‘quasi-steady’, but what we show here is that these fields are in general not stable and given time will diverge.

Figure 4.4 also appears to show a maximum value of  $I_S$  of approximately  $10^{-5} \text{ yrs}^{-2}$  for all simulations. A theoretical basis for this is unclear, although one might expect some limitation on the strength of field that can be induced from the flow driven by a field of a given magnitude. The nature of these dynamos, as driven by a mean field  $\alpha$ -effect of a fixed constant magnitude may also be responsible through providing a maximum bound on the driving force.

Focusing in more detail on the path taken in these simulations, it can be seen more clearly when the number plotted is reduced in figure 4.4b, that the variation in  $I_S$  is not random, indeed it has a quasi-periodic form. The magnetic field in these simulations is rapidly oscillating in a reoccurring pattern. Never remaining in a state with a small  $I_S$  for a significant amount of time and failing to converge over long timescales toward a stable steady state.

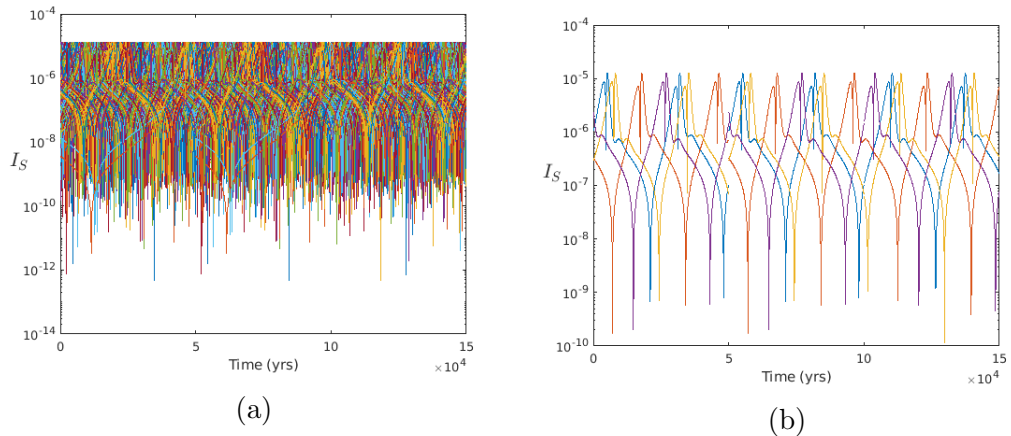


Figure 4.4: Graph showing the evolution of  $I_S$  with time for the suite of mixed symmetry, with (a) all 1000 different random initial conditions shown, (b) just 4 models with initial conditions plotted for clarity.

### 4.4.3 The evolution from a quasi-steady Taylor state

The apparent rarity, or even entire absence, of stable Taylor states for the general mixed symmetry case motivates a more targeted approach than the simulations with random initial conditions used in the previous section. This consists of firstly, actively searching for ‘quasi-steady’ Taylor states, using an optimisation method to hone in on the regions where local minima are, followed by using these found

‘quasi-steady’ Taylor states as initial conditions in dynamical simulations to test their stability.

The calculations of  $I_S$  shown in figure 4.1 reveal many locations where the fields are ‘quasi-steady’, and  $I_S$  takes a small value within the parameter space of varying just two coefficients explicitly. Since a Taylor state being ‘quasi-steady’ is a prerequisite for being a stable steady Taylor state, this highlights a number of fields that are candidates and can be examined further. Dynamical simulations carried out using the method of §4.2.2, evolving from these specifically chosen initial conditions examines the long term stability of these fields. This should allow us to either discover, such stable steady Taylor states, or more definitively rule out their existence.

To improve generality, we wish to expand the domain being surveyed here, therefore this is extended to allow direct variation in more coefficients. The Taylor state construction method here is an extension to the method described in §4.3, where the magnetic field components were as shown in equation (4.9). Here the magnetic field has the constituent parts shown in equation (4.11). The poloidal field is still fixed to that of the stable dipole symmetric solution reported in Li et al. (2018),  $\mathcal{S}_0$ . However, no toroidal coefficients are taken from this solution anymore, importantly removing any favouritism for producing a field similar to that. The toroidal field is constructed by the  $m$  largest scale modes being assigned a randomly chosen value from within the domain  $[-1, 1]$ , and the rest of the toroidal field determined through solving the linear system of Taylor’s constraints.

$$\begin{aligned} \mathbf{B} = & \mathcal{S}_0 + a_1 \mathcal{T}_1 + a_2 \mathcal{T}_2 + \dots + a_m \mathcal{T}_m + a_{m+1}(a_1, a_2, \dots, a_m, \mathcal{S}_0) \mathcal{T}_{m+1} + \dots \\ & + a_n(a_1, a_2, \dots, a_m, \mathcal{S}_0) \mathcal{T}_n. \end{aligned} \quad (4.11)$$

Here, it is the largest scale mode coefficients that are imposed and then the remaining smaller scale modes which are determined through solving Taylor’s constraints. This is the principle we have chosen throughout this chapter, which is directly implemented in the expansion of equation (4.10), and even in the more complex situation of the expansion used in equation (4.9), it is the reason why the the large scale  $\mathcal{T}_1$  and  $\mathcal{T}_2$  are imposed and the smaller scale  $\mathcal{T}_3$  solved for. The reasons for adopting this approach are twofold. Firstly, it broadens the diversity of fields within our search space, as the large scale modes contain the bulk of the magnetic energy in our converged energy spectrum, so independently varying these modes can lead to substantially different fields. Secondly, we did experiment with the reverse approach and encountered numerical solvability difficulties, with the need for inverting pseudo-singular matrices, this is thought to be due to a general issue with the po-

tentially ill-posed nature of attempting to modify a small scale magnetic field into a Taylor state through the addition of purely large scale modes.

The expansion (4.11) allows an  $m$ -dimensional space to be explored, as opposed to the 2-dimensional space considered in §4.3. In addition, a more sophisticated method for searching for minima in instantaneous  $I_V$  is utilised. A neighbourhood algorithm optimisation (Sambridge, 1999) is implemented to more efficiently locate the regions of small  $I_V$  than our uniform grid evaluations described in §4.3. The neighbourhood algorithm works as an optimisation scheme, seeking to minimise  $I_V$ . This method requires varying the spherical harmonic coefficients of  $\mathbf{B}$  subject to satisfying all of Taylor’s constraints. Hence the field remains on the manifold of Taylor states at each point that  $I_V$  is evaluated in pursuit of its minimisation. The algorithm involves a random selection of  $p$  points being chosen, distributed through the  $m$ -dimensional parameter space and then  $I_V$  being evaluated at each location. The domain is then divided up into  $p$  ‘Voronoi’ cells surrounding each point and the  $q$  regions with the smallest values retained to be explored further through repeating the process of evaluations of the objective function at new points obtained by a uniform random walk within each of these cells. This process is then iterated  $x$  times, where  $p$ ,  $q$  and  $x$  are input parameters suitably chosen to balance computational time, global generality of minima, and accuracy of the precise minima locations.

The specific example reported here has a resolution defined by a maximum degree of  $L = 10$ ,  $N = 5$ ; this means there are  $n = 50$  degrees of freedom and  $n - m = 18$  Taylor constraints that need to be satisfied. Hence the coefficients of the  $m = 32$  largest scale modes are independently varied in search of minimising  $I_V$ . The Neighbourhood algorithm parameter values used to explore this 32-dimensional space are:  $p = 20$ ,  $q = 10$ ,  $x = 5$ . This results in a number of different magnetic fields, all of which correspond to local minima of  $I_V$ . The selection of which of these quasi-steady Taylor states are promising enough to test the stability of is chosen to be those that fall below a threshold of  $10^{-8} \text{ yrs}^{-2}$ . This results in 68 magnetic fields, which are used as initial conditions in dynamical simulations.

Significantly we find that none of the quasi-steady Taylor states found are in fact stable. Figure 4.5 shows the entire evolutionary path for a sample of two of these quasi-steady Taylor state magnetic fields. The path consists of diverging from the initial state before eventually converging to what is the known stable steady Taylor state within dipole symmetry identified by Li et al. (2018).

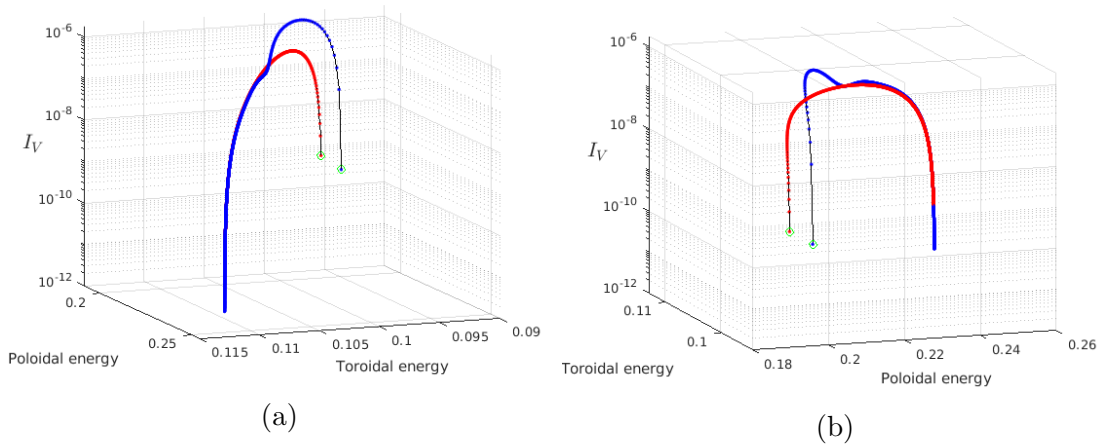


Figure 4.5: The paths taken from two initial magnetic fields (coloured red and blue) that are quasi-steady Taylor states. The fields diverge from the initial states (green circles) before finally converging to the same stable steady Taylor state. (a) and (b) show the same 3D plot viewed from a different angle.

#### 4.4.4 The strength of the known symmetric solutions as attractors

The stable steady Taylor states that we observe are few in number, just a single case per symmetry, polarity and  $\alpha$ -effect (only results with one single choice of  $\alpha$ -effect have been presented thus far, but different  $\alpha$ -effects have also been explored, as discussed in §4.4.5). It can be instructive to examine the attractiveness of these states, for there are two obvious explanations as to why these states are so persistently arrived at: either they are the only stable states or they are so dominantly attractive that they prevent any other state from being found. The analysis of §4.4.1 strongly favours the former explanation, as these fields that have mixed symmetry fail to converge to any stable state, despite the option of collapsing into a specific symmetry class.

Here, we start with initial conditions that are small perturbations from the known stable steady Taylor state solution within dipole symmetry (Li et al., 2018). Perturbations which consist of a magnetic field that is either purely poloidal or purely toroidal and has an opposite symmetry to the unperturbed field will provide zero additional contribution to the Taylor integral. It is therefore guaranteed that the resultant, perturbed magnetic field will also be a Taylor state. Here we make a careful choice of modes in the perturbation such that we can take advantage of this. This allows us to perturb the magnetic field by varying some specific modal coefficients arbitrarily, independent of the rest, which hence can remain fixed. This

is because the dipole symmetric field from the steady Taylor state found from the dynamic code (as in [Li et al. \(2018\)](#)), which is used as the basic state, consists purely of odd poloidal modes and even toroidal modes. Therefore the addition of any odd toroidal modes, (which themselves are of quadruple symmetry), will have zero impact on the Taylor interaction, due to the absence of any interaction with the existing modes. Therefore this allows an entirely free choice of coefficients for these modes while maintaining a Taylor state field. This approach does have the drawback of a lack of true generality, but is a pragmatic approach which allows us to arbitrarily vary these coefficients in a pre-determined fashion, without the existing modes needing to vary. Therefore it provides a fair and transparent way to impose a perturbation of a chosen magnitude. The perturbation magnitude is measured by  $\delta$ , defined as the magnitude of the imposed quadrupole field as a ratio to the original dipole field. The perturbation is achieved through setting all the odd toroidal model coefficients (which are otherwise zero in the stable steady Taylor state from [Li et al. \(2018\)](#)) to take the same non-zero value.

The results of this analysis show that the threshold for a perturbed field returning to the stable state is around  $\delta = 10^{-2} - 10^{-3}$ . For initial conditions with  $\delta > 10^{-2}$  then the field fails to converge, as was seen in §4.4.1. This suggests that the transformation of collapsing to a specific symmetry class is an unfavoured scenario within the dynamo model. Therefore, combined with the absence of any stable Taylor states within the case of mixed symmetry then this suggests that general dynamo models would not be expected to arrive at a stable Taylor state.

#### 4.4.5 The dependence on the choice of $\alpha$ -effect

The arbitrary nature of the way that any  $\alpha$ -effect is chosen can be considered a little less satisfactory than we would desire. It is a valuable approach when studying dynamos within simple and axisymmetric settings, but it remains difficult to rigorously justify its applicability to the real geophysical situation of Earth's core. In order to ensure some generality in our results it is useful to explore varying both the magnitude and the spatial structure of the  $\alpha$ -effect to test the sensitivity with respect to these.

##### Magnitude of $\alpha_0$

The analysis of §4.3 is repeated with a reduced strength of  $\alpha$ -effect from  $\alpha_0 = 18$ , to  $\alpha_0 = 16$  (which remains above the critical value of  $\alpha_0 = 13.1$ ). The equivalent

plot as figure 4.1 is shown in figure 4.6, with the stable solution of Li et al. (2018) at this new value of  $\alpha_0 = 16$  indicated by as the red line.

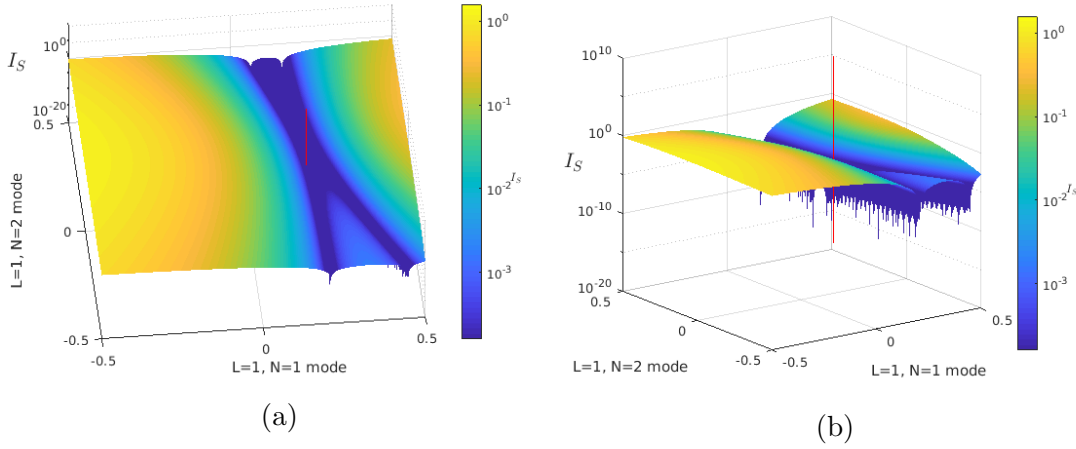


Figure 4.6: Surface plot of  $I_S$  as a function of the  $L = 1, N = 1$  and  $L = 1, N = 2$  coefficients values. The vertical red line corresponds to the coefficient values of the known stable steady solution of Li et al. (2018). The  $\alpha$ -effect form (4.2) is used, with an above critical magnitude of  $\alpha_0 = 16$ . (a) and (b) show the same 3D plot viewed from a different angle.

Similarly, we repeat the dynamical simulations of §4.4.2, now with  $\alpha_0 = 16$  but using the same random mixed symmetry initial conditions as figure 4.4. This time we find that instead of remaining in a periodic state and failing to converge, the fields do appear to converge to a steady state. In fact what we observe is the convergence to the known solutions in dipole and quadrupole symmetry as reported by Li et al. (2018). Therefore we have still failed to find any stable steady Taylor state that has the complexity of a mixed dipole and quadrupole symmetry. The difference for the case of  $\alpha_0 = 16$  is merely that the strength of attraction of these stable points appears stronger and therefore enables convergence from arbitrary initial conditions, unlike for  $\alpha_0 = 18$ , where we found that in order for the system to collapse to a symmetry class and hence find the stable point, the initial condition was required to be sufficiently close.

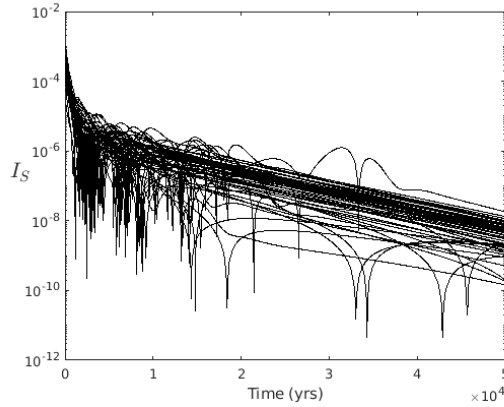


Figure 4.7: Normalised instantaneous rate of change of magnetic field on the core surface,  $I_S$ , with  $\alpha_0 = 16$ , for 60 different random initial conditions of mixed symmetry.

As  $\alpha_0$  is increased further above critical (e.g.  $\alpha_0 = 25$ ), these strongly forced models result in a rapidly growing magnetic field energy. This results in numerical stability difficulties in our simulations, due to the large and rapidly growing magnetic field. This effect may be confined to the axisymmetric problem we are studying, as found by [Fearn and Rahman \(2004\)](#). They report that in the full three-dimensional problem non-linear interaction limits the field strength overcoming this issue.

In summary what we observe is no fundamental change in the conclusions of abundance of ‘quasi-steady’ Taylor states, but a scarcity of stable steady Taylor states (and a complete absence in mixed symmetry). The difference discerned is merely that less strongly driven models allow magnetic fields to more easily collapse into dipole/quadrupole symmetry and hence converge to these specific stable steady states from a wider range of initial conditions.

### Structure of the $\alpha$ -effect

Alternative structures of the  $\alpha$ -effect are also considered and the same simulations beginning with mixed symmetry initial conditions conducted. The forms used are the following

$$\alpha = \alpha_0 \sqrt{\frac{7}{3}} \frac{334}{48} r^3 (1 - r^2)^2 \cos(3\theta),$$

and

$$\alpha = \alpha_0 \cos(\theta),$$

which are normalised by the maximum value such that  $\max|\alpha| = \alpha_0$ . This helps to allow a fair comparison, although note that this does not require the critical value of  $\alpha_0$  to be the same. It has been calculated that the critical value takes the slightly smaller value of  $\alpha_0 = 12.5$  (Li et al., 2018) for the former and  $\alpha_0 = 13.1$  (Fearn and Rahman, 2004) for the latter (the same as for the form of equation (4.2)).

Qualitatively similar results are observed for all  $\alpha$ -effect structures, we observe four types of behaviour dependent of the magnitude of  $\alpha_0$ : at values of  $\alpha_0$  below critical, dynamo action fails and the field decay via magnetic diffusion; slightly above critical our models converge toward one of two stable states, of either dipole or quadrupole symmetry; more strongly forced models have continually and rapidly varying rates of change and fail to converge to a stable state (as shown in figure 4.4); while significantly super-critical values of  $\alpha_0$  lead to a divergent magnetic field rate of change toward very large magnetic field energies.

## 4.5 Comparison to observational models

Earth’s magnetic field is itself not entirely static, but is evolving on a range of timescales. While features such as the longstanding dominance of the axially symmetric dipolar component of the field appear stable, there are many fluctuations in the geomagnetic field.

In order to assess the Earth-like credentials of a Taylor state magnetic field, we need to compare to the secular variation of the Earth’s magnetic field over the same magnetostrophic timescale.

We calculate the CMB averaged rate of change of magnetic field according to the CHAOS-6 model, at epoch 2015, itself based on satellite and ground-based data (Finlay et al., 2016) to be  $2.4 \times 10^{-4} \text{ yrs}^{-2}$ . This is notably larger than many of the results we present. However, this is to be expected, due to short time scale secular variation dominating the observational signal. These fast dynamics are explicitly excluded from our magnetostrophic model that neglects inertia and viscosity, so this value is more representative of the perturbations to a Taylor state, as opposed to the background evolution of the state itself.

Archaeomagnetic data allow us to estimate the Earth’s magnetic field over the long timescales necessary to be compatible with a Taylor state. Using the GGF100k model (Panovska et al., 2018) we can calculate the secular variation of the Earth’s magnetic field throughout the previous 100,000 years, with a yearly temporal

resolution. This allow us to calculate  $\frac{\partial \mathbf{B}}{\partial t}$  and hence the normalised measure of the rate of change of magnetic field on the CMB surface,  $I_S$ , as a function of time. This useful geophysical benchmark, which allows a comparison of the normalised rate of change of our Taylor state magnetic fields is plotted in figure 4.8,

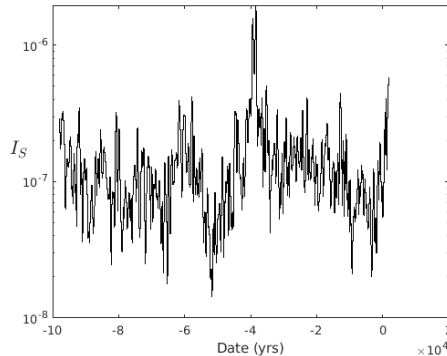


Figure 4.8: Plot of  $I_S$  over the last 100,000 years for CMB field data from the GGF100k model (Panovska et al., 2018).

#### 4.5.1 Comparison to other numerical dynamo simulations

Numerical dynamo simulations also provide a useful source of data for comparison. We use data from simulations run by Julien Aubert, using the dynamo code Aubert et al. (2017) at a range of parameters (shared via personal communication). These results from simulations carried out at  $E = 3 \times 10^{-5}$  and  $E = 3 \times 10^{-10}$  are shown in figure 4.9; we note that they are not sensitive to the choice of parameter values as they are modified along the ‘path’ towards the Earth defined by Aubert et al. (2017), with the position along this path indicated by the parameter  $\epsilon$  and Earth’s core believed to be located at  $\epsilon = 10^{-7}$ .

Our dynamo simulations are all constrained to axisymmetry, due to the current capability of the model. The geomagnetic observational model of GGF100k is truncated at degree 10 as a result of observational limitations and uncertainties. Therefore in figure 4.10 we restrict ourselves to both these limiting factors and make a direct comparison of all three data sets for the axisymmetric component of the magnetic field in degrees up to 10.

Figure 4.10 shows that the range of values of  $I_S$  from observational models, and other numerical geodynamo models that include viscosity and inertia, lie within that of our model. This suggests that arguably, our magnetostrophic dynamo model is consistent with representing the dynamo operating in Earth’s core. However, we do also note, the apparent greater variability in the rate of change of magnetic field

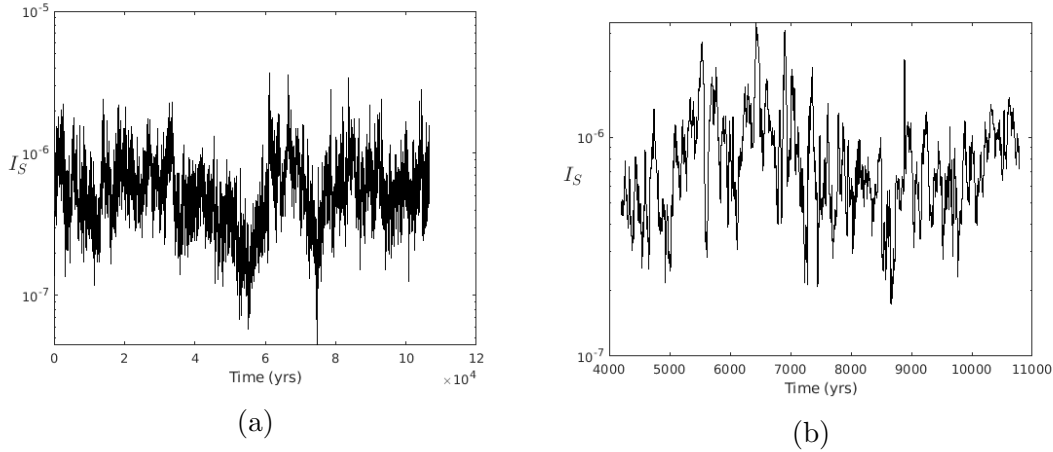


Figure 4.9: Plot of  $I_S$  for core surface field data from Aubert’s simulation (a) at  $\epsilon = 1$  ( $E = 3 \times 10^{-5}$ ), (b) at  $\epsilon = 1 \times 10^{-5}$  ( $E = 3 \times 10^{-10}$ ).

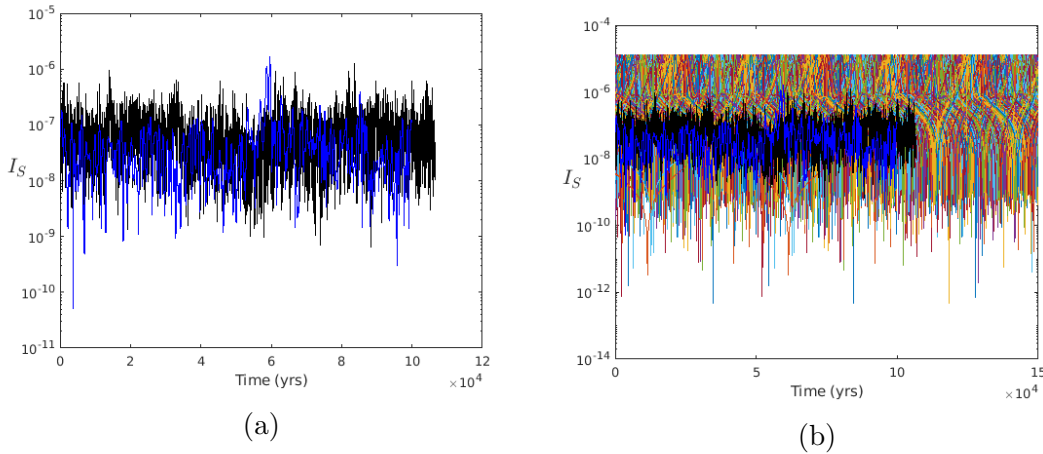


Figure 4.10: Plot of  $I_S$  for the core surface field (a) comparing the axisymmetric, degree 10 truncated data from Aubert’s simulation at  $\epsilon = 1$  (black) with the GGF100k data (blue) and in (b) with our simulation results (§4.4.2) too.

in the magnetostrophic system. The significance of this, and potential reasons for it, are discussed in more detail in the following section.

## 4.6 Discussion

It has been previously shown that there is a large space of magnetic fields that exactly satisfy Taylor’s constraint (§6.4, Livermore et al. (2009)). However, these theoretically derived snapshots are free from physical considerations and can be inconsistent with features of Earth’s magnetic field and geodynamo production mechanism. A magnetic field can be made to satisfy all criteria at a snapshot in time but the

broader question of dynamical self-consistency is more challenging. Will the flows driven by this field, in turn modify the field into an unphysical state, irreconcilable with geomagnetic observations? Here we have addressed this question in our study of the dynamics of Taylor states.

Firstly, we have been able to show that there exists a large space of Taylor states with a rate of change of the core surface field  $I_S$  that is comparable to models derived from geomagnetic observations at the Earth's CMB. The approximate value of  $10^{-7} \text{ yrs}^{-2}$  shown in figure 4.8 can be easily achieved as an instantaneous rate of change as illustrated in figure 4.1.

Secondly, we find that stable steady Taylor states are very rare. Within specific imposed symmetries of either dipole or quadrupole, only a single stable state is found. While in the more general and physically relevant situation, without any symmetrical restrictions then our extensive search for any stable states is fruitless. This suggests that it may be the case that no stable steady Taylor states with a mixed symmetry exist.

Of course despite using a wide range of initial conditions, across a range of spatial scales, we can not rule out the possibility that some stable Taylor states do exist, but that they are merely not sufficiently strong attractors to be arrived at. Also, we emphasise that all our calculations are restricted to axisymmetry, the full three-dimensional setting should also be considered, to investigate whether it yields different results.

If however, this absence of any stable steady Taylor states is confirmed it poses serious challenges for magnetostrophic dynamo models that seek to realistically replicate the evolution of the geomagnetic field. These idealised models may be hampered by often resulting in a larger rate of change of magnetic field than that which is observed for the Earth. This contrasts to traditional dynamo models that include inertial and viscous effects, which are able to produce magnetic fields that remain consistent with geomagnetic observations, as shown in figure 4.10.

The more extreme rate of field changes experienced in our simplified models, with both periods of relatively large  $I_S$  and brief periods of very small  $I_S$  (quasi-steady points), could be due to the complex impact of the combination of effects excluded. Inertia often acts as a restoring force, acting on short timescales and causing a rapid response to perturbations in the system. For example, it permits torsional waves, as discussed in §2.7, which act to re-establish the unperturbed state. In the absence of this correction mechanism, deviations from the long term equilibrium state do not result in a large rate of change  $\mathbf{B}$ , but rather, may be ex-

pected to persist, with the perturbations then only slowly suppressed on the longer magnetostrophic timescale. Viscosity causes diffusion of all pronounced features in the fluid, this diffusive effect acts to damp out extreme characteristics and potentially hinder substantial variation. Therefore inviscid models such as ours, might be expected to contain faster and more extreme variations. The mean field  $\alpha$ -effect used to provide the driving force for our axisymmetric dynamos, acts as a non-ideal proxy for buoyancy. It results in a linear interaction and a non-adaptive buoyancy force. Solving the full temperature equation equation (1.11) within a coupled system would facilitate more complex non-linear interactions with direct system feedback. Alternatively, as a more direct and simple extension to our model, buoyancy nonlinearities can also be introduced through  $\alpha$ -quenching. Where the value of  $\alpha$  is no longer fixed but allowed to evolve subject to the magnetic feedback leading to deformation of the turbulence (Rüdiger and Kichatinov, 1993). The addition of a quenching of the  $\alpha$ -effect, is of course a non-ideal way of truly representing this physical phenomenon, as the actual form may be more sophisticated than the chosen model. However, the inclusion of a simple algebraic form, such as  $\alpha = \frac{\alpha_0}{1+B^2/B_0^2}$  of Moss et al. (2008), where  $B_0$  is the equipartition field strength, would allow an initial study into any stabilising effect.

The stability of mean field dynamos has been previously examined within finite viscosity models. Fearn and Rahman (2004) study the  $\alpha^2$ -dynamo model at (relatively large) finite Ekman numbers of  $3.5 - 4 \times 10^{-4}$  and compare the behaviour within a three-dimensional non-axisymmetric nonlinear system and the two-dimensional axisymmetry case. They report very different behaviour in these two situations, in the axisymmetric case the magnetic energy grows quickly as the forcing  $\alpha_0$  is increased (for values above critical). This agrees with our findings in §4.4.5 that axisymmetric and strongly forced models result in very strong magnetic fields that become increasingly computationally expensive and less physically relevant. Whereas the non-linear interaction between the field and the flow driven by the Lorentz force in the three-dimensional case more representative of the geodynamo, results in an instability that constrains the strength of the magnetic field generated. Therefore caution is required when interpreting axisymmetric studies such as ours in the context of the three-dimensional geomagnetic field.

The variability of stability as a function of Ekman number has been studied by Hollerbach and Ierley (1991), who have investigated the asymptotically small limit of viscosity in an  $\alpha^2$ -dynamo model. For all  $\alpha$ -effects considered their solutions do approach a Taylor state in this limit. However, the manner of the transition from the viscous to inviscid regime does vary. The formal limit  $E \rightarrow 0$  is seen to not always be well behaved, sometimes requiring a discontinuous jump. The subsequent

inviscid equilibration does however result in a stable field that is either steady or oscillatory.

There have been many suggestions of a marked difference in the fluid behaviour in magnetostrophic and finitely viscous models (McLean et al., 1999). While not definitively proven, the plausible intuition remains that the dynamo is particularly unstable as  $E \rightarrow 0$  (Zhang and Gubbins, 2000), as in the absence of viscous damping to suppress evolution stable states are less likely to be sustained. Instability can arise due to dynamo action being extremely sensitive to the vigour of convection by which it is driven (the difference between the Rayleigh number and its critical value). Zhang and Gubbins (2000) showed that at small Ekman numbers then the critical Rayleigh number is increasingly sensitive to the poloidal magnetic field. Therefore small fluctuations in the magnetic field will directly lead to rapid variations in the strength of convection and significantly alter the progression of the dynamo. The nature of the Earth's core being at an unattainable value of  $E = 10^{-15}$  therefore makes it very challenging to accurately model the stability of the geodynamo. While magnetostrophic models (at  $E = 0$ ) may be over-sensitive to instabilities, all present finite viscosity ( $E > 10^{-9}$ ) models have the opposing problem of inherently being more stable than the geodynamo itself.



# Chapter 5

## Stratified layer at the top of Earth's core

### 5.1 Stratification in outermost part of core

The question of whether or not the fluid at the top of Earth's liquid outer core is stratified, either compositionally or thermally, has long been debated (Waler, 1980; Braginsky, 1967, 1987; Hardy and Wong, 2019; Gubbins, 2007). In this chapter we discuss the range of evidence on this topic. It is useful for us to explore this in detail before proceeding with constructing a representative model of Earth's core in Chapter 6.

Seismic body wave measurements have provided a key strand of evidence for the non-uniform nature of Earth's outer core. Any perturbation in the estimated velocity of detected waves is suggestive of a different density and/or elasticity. It has been noted that within the region immediately beneath the CMB wave velocities appear smaller than in the rest of the core, indicative of a layer compositionally distinct from the bulk.

These observations rely on a specific type of waves, known as SmKS waves which propagate as a S wave in the mantle and as a P wave in the liquid core. The discontinuity at the CMB, which has a density jump of  $4.3 \times 10^3 \text{ kg m}^{-3}$  causes this SmKS wave to undergo  $m - 1$  reflections at the underside of the CMB (as many as five reflections have been observed) as shown in figure 5.1. The significance of this is that it means the majority of the travel time of this wave is spent in the outermost part of the core and so the SmKS wave allows investigation of this layer

to determine stratification.

A large number of studies have observed this deviation in the travel times of SmKS waves, which pass through this layer several times, as they undergo multiple reflections at the CMB, with waves that undergo more reflections spending more time closer to the CMB, as illustrated in figure 5.1.

Many independent analyses of the travel times of various SmKS waves have led to estimates of a stratified layer at the top of the outer core, in which wave velocities are lower, of thickness approximately 200 km (Helfrich and Kaneshima, 2013; Lay and Young, 1990) to 300 km (Helfrich and Kaneshima, 2010), with some are as large as 800 km (Kaneshima, 2018; Souriau and Poupinet, 1991).

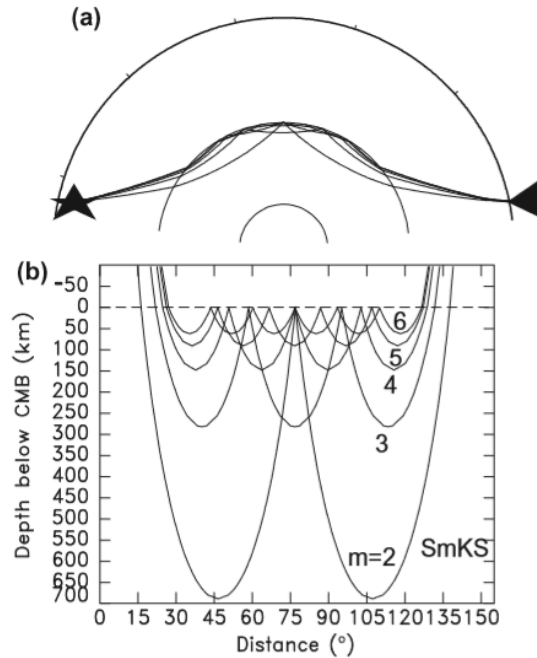


Figure 5.1: (a) Ray paths for SmKS ( $2 \leq m \leq 6$ ) for a source (star) 550 km deep to a station (triangle) at 155. (b) Core legs of ray path. As multiples in core increase, bottoming depth in core decreases. S6KS bottoms at 60km below the CMB, whereas S2KS bottoms 700 km below the CMB (Helfrich and Kaneshima, 2013) .

However, as the large discrepancy in estimated layer depths suggests, this evidence is far from conclusive. There remains uncertainty due to poor knowledge of the properties of liquid iron alloys at the extreme pressures and temperatures that exist in the Earth's core. Also, while a perturbation in velocity is expected within a layer of differing composition, the sign of the observed change is counter-intuitive. The velocity measured is lower than the rest of the core, which is the opposite to what we might expect if the density is smaller, since wave velocity is inversely proportional to the square root of density. This is of course problematic

and not well understood.

It is possible that the elastic properties of liquid mixtures can behave non-intuitively on account of mixing non-ideality. [Helffrich \(2012\)](#) finds that under certain conditions this can result in scenarios where wave speeds in liquids decrease as more of a ‘faster’ component is added. Theoretically this means that the assumption of a linear variation of wave speed with concentration is generally invalid, but the high temperature, high pressure, conditions in Earth’s core would be expected to inhibit any non-ideal mixing. [Brodholt and Badro \(2017\)](#) estimate the composition required to explain seismic observations at the top of the core. When considering the conditions present at the CMB, they find that increasing the concentration of any light elements always increases velocity and so a low-velocity and low-density layer cannot be made by simply increasing light element concentration. While a low-velocity and low-density layer could exist at the top of Earth’s core, this would require a delicate combination of an increase in the concentration of some light elements and a relative decrease in others.

The difficulty in explaining the conclusions drawn from seismological observations, may lead one to question their validity. There are inherent difficulties in inverting seismic wave travel times to determine wave velocities within this remote and relatively shallow region. In fact some argue that the velocities estimated agree with the well mixed model of PREM to within the observational uncertainties. [Alexandrakis and Eaton \(2010\)](#) claim that there is insufficient evidence to suggest that an anomalous layer exists at the top of the core. Also, the latest results for the elastic parameters of the outer core from [Irving et al. \(2018\)](#), predict a steeper wave velocity gradient with depth in the core, which enables SmKS wave travel times to be explained without requiring an anomalously slow layer at the top of the core. Hence, while the majority of current seismic evidence is in favour of this stratified layer, unequivocal evidence does not exist.

### 5.1.1 Formation

Various mechanisms have been suggested to explain why the upper reaches of the core could have become stably stratified, either compositionally or thermally. A buoyant compositional layer could form through the accumulation of light elements underneath the CMB. There are many possible theories for how a higher proportion of lighter elements could end up in this region. Light material could be diffused inwards across the CMB or created due to chemical reaction with the mantle ([Jean-](#)

loz, 1990; Buffett and Seagle, 2010). Alternatively light elements could enter from below by the process of barodiffusion (the tendency of light elements to diffuse along a pressure gradient) after being either expelled outwards from the freezing inner core (Braginsky, 2006; Bouffard et al., 2019), or precipitated out of the bulk of the outer core mixture (Gubbins and Davies, 2013). However, barodiffusion alone can not be solely responsible as this would result in a high-velocity, low-density layer, rather than the low-velocity, low-density layer observed. Additionally, due to inadequate knowledge of the early Earth, we can not rule out the possibility of inheritance. Perhaps the stratified layer is a remnant of the early Earth, as a result of incomplete mixing in the core following an impactor. This possibility was recently explored in depth by Landeau et al. (2016). A compositionally stratified layer would be stable to convection penetrating from fluid below (Buffett and Seagle, 2010) and would grow at the rate determined by the ratio of the net supply of light elements and any entrainment from the bulk.

Lastly, thermal heterogeneity can arise even in the absence of chemical or boundary effects. If current estimates of the thermal conductivity of iron (which are significantly larger than previously thought) are correct (Pozzo et al., 2012), then this results in an adiabatic heat flux at the CMB which is higher than most estimates based on mantle convection models. This creates sub-adiabatic conditions at the top of the core, meaning a thermally stratified layer must exist. The complex interaction of both thermal and chemical effects may be important in the formation of this layer, as highlighted by Davies et al. (2015), and incorporated in the recent thermo-chemical model by Nakagawa (2018).

## 5.2 The effect of a stratified layer on the observed geomagnetic field

In this section we consider the effect that the presence of a stratified layer at the top of the core may have on the observed geomagnetic field. There are two distinct key effects: the impact as a passive, diffusive filter of the observed surface magnetic field, and the active role of modifying the boundary effects for the dynamo region.

A stratified layer at the top of the core may affect the magnetic field signal we observe as it would provide a physical separation between the region in which the dynamo action produces the field and the location at which observational data is known (the CMB). This layer would place the convective region further from the

surface and act as a diffusive spatial filter of the magnetic field signal, enhancing the ratio of the dipole component to smaller-scale components in the surface magnetic field. This means that, although the dominantly dipolar nature of Earth's field is clearly intrinsic to the dynamo mechanism, a stratified layer would magnify its observed preeminence.

In terms of using observations of the changing internal geomagnetic field as a window on the dynamics within the core, the existence of a stratified layer is crucial because motion confined to the stratified layer such as waves may have a pronounced geomagnetic signature, which may be falsely interpreted as emanating from the large-scale dynamo process ongoing beneath.

This is important for modelling core dynamics because observational measurements of the Earth's magnetic field are downward continued to the CMB, and this is interpreted as the magnetic field at the outer edge of the convective region generating the dynamo action. However, the presence of a stratified layer below the CMB means this may differ from the field in the convective region, raising the question of whether the effects of any CMB heterogeneity, whether topographical, electromagnetic or thermal, would directly translate through the stratified layer, or be damped? Such a layer may disconnect the Ekman boundary layer from the free-stream flow, leading to a partial or even full suppression of the boundary-driven zonal flow, due to a competition between stratification and boundary forcing that results from heterogeneous outer boundary conditions (Cox et al., 2019).

### 5.2.1 Compatibility of a stratified layer with geomagnetic simulations and observations

A key approach to understanding the observational signature of a stratified layer is by numerical simulation of a stratified geodynamo model (Nakagawa, 2011). Models of outer core dynamics have demonstrated that dynamo action can be sensitive to variations in the assumed background state of a fully convective outer core, and that the presence of stably stratified layers can significantly alter the dynamics and morphology of the resultant magnetic field (Glane and Buffett, 2018; Christensen, 2018; Olson et al., 2018). Hence comparisons between the magnetic fields from stratified models with the geomagnetic field can be used to infer compatibility with the presence of a stratified layer. This has been used to constrain the possible thickness of a stratified layer such that it is consistent with geomagnetic observations. Yan

and Stanley (2018) find that unstratified dynamo simulations significantly underpredict the octupolar component of the geomagnetic field. Their model endorses the presence of a thin stably stratified layer, as the resultant magnetic field can be rendered Earth-like by the inclusion of 60-130 km layer. However, the results are rather sensitive to both the strength of stratification and layer depth, with a thicker layer of 350 km resulting in an incompatible octupole field. Similarly Olson et al. (2017) find that stratified model results compare favorably with the time-averaged geomagnetic field for partial stratification in a thin layer of less than 400 km, but unfavorably for stratification in a thick 1000 km layer beneath the CMB.

Additionally, in terms of dynamics, a stratified layer at the top of the liquid core behaves differently; it supports distinct waves that in principle are observationally visible. One such class are magnetostrophic (MAC) waves, which arise from the interplay between magnetic, buoyancy (Archimedean) and Coriolis forces, whose equilibrium forms the dominant balance in Earth's core. These waves typically have a timescale of  $10^4 - 10^5$  years in the absence of a stratified layer. However, due to the dynamics within stratified fluids, principally the suppressed radial motion, a different suite of waves are supported, which means that if a stably stratified layer exists at the top of the outer core it would introduce MAC waves of much shorter timescales (Braginsky, 1993). Buffett (2014) modelled these waves and appears to confirm Braginsky's idea by finding MAC waves with a period of 60 years. This is consistent with observations of secular variation in the geomagnetic field that have identified periodic fluctuations on a period of 60 years (Roberts et al., 2007). This adds to the weight of evidence that the top of the fluid core is stably stratified and reveals an effect that this has on the magnetic field. The model of Buffett et al. (2016) suggests that MAC waves underneath the CMB are also able to account for a significant part of the fluctuations in length of day (LOD) (Gross, 2001; Holme and De Viron, 2005) through explaining the dipole variation, but are contingent on the existence of a stratified layer at the top of the core with a thickness of at least 100 km.

However, despite the evidence for the presence of this stratified layer outlined above, there is still no consensus on its existence. Not all stratified dynamo model results champion this scenario for the Earth. It has been found that the inclusion of a thin stable layer in numerical models can act to destabilise the dynamo, through generating a thermal wind which creates a different differential rotation pattern in the core (Stanley and Mohammadi, 2008), also the magnetic field structure is seen to differ due to the suppression of non-axisymmetric magnetic field components (Christensen and Wicht, 2008). This apparent contradiction, with many distinctive features of the observed geomagnetic field not reproduced in stratified

models, remains significant and troublesome to resolve. Geomagnetic observations find strong local variations in magnetic field strength, called reverse flux patches, where the magnetic field in a small region has opposite polarity to the dominant polarity in that hemisphere. These regions grow or shrink and move location with time. This secular variation can only be explained by radial flows close beneath the CMB, which are accelerated locally or by very strong poloidal field gradients (Gubbins, 2007). However, radial flows are not expected to exist in stratified layers, so it is difficult to explain the geomagnetic observations if a stratified layer does exist at the top of the core. Strongly stratified dynamo models result in magnetic fields without any such reverse flux patches (Mound et al., 2019; Christensen and Wicht, 2008). Gubbins (2007) shows that the toroidal flux expulsion associated with the observed secular variation of flux patches requires vertical flow within 100 km of the core surface in the absence of steep poloidal field gradients immediately beneath the CMB, for which no convincing justification has been made. This suggests an upper limit on the thickness of this layer, at least in the regions where reverse flux patches exist.

Overall, observational geomagnetism has offered equivocal evidence for stratified layers. Time dependent observational models can be explained by simple core flow structures on the core-mantle boundary (CMB) which have either no layer (Holme, 2015; Amit, 2014) (upwelling at the CMB is permitted), or a strongly stratified layer (in which all radial motion is suppressed) (Lesur et al., 2015). Lesur et al. (2015) examined whether it is possible to produce the observed secular variation, from a large scale purely toroidal flow, permissible within a stratified layer. They found that in this idealised case of pure toroidal flow and no diffusion it is not possible to fit the CHAMP satellite data, but including a small amount of poloidal flow allows models that accurately describe secular variation observations. In reality, within Earth's core, although stratification may be strong, it would not entirely prevent all poloidal flow, so it is not possible to conclude that secular variation observations violate the hypothesis that the outermost part of the core is stably stratified.

The existence of this stratified layer remains very much still an open question, as reconciling geomagnetic observations with seismological evidence has proved extremely challenging. One alternative hypothesis is the possibility of a non-global stratified layer, which instead of spanning the whole CMB, leaves space for regions of active radial flows (Mound et al., 2019). While more research is required, this plausibility of a stratified layer being present at the top of Earth's core motivates the work of Chapter 6, where we examine how the magnetic field may be expected to differ within such a layer.



## Chapter 6

# Constraints on the magnetic field within a stratified outer core

### 6.1 Introduction

Mounting evidence from both seismology and numerical experiments on core composition suggests the existence of a layer of stably stratified fluid at the top of Earth's outer core (as summarised in the previous chapter). In such a layer, radial fluid motion is suppressed and importantly this provides a condition on the flow, which in turn limits the space of possible magnetic fields. In this chapter we consider how this can be combined with the existing constraints on the magnetic field structure for dynamo action within a magnetostrophic force balance.

The previously derived (2.7) Taylor constraint

$$T(s, t) \equiv \int_{C(s)} ((\nabla \times \mathbf{B}) \times \mathbf{B})_{\phi} s d\phi dz = 0, \quad (6.1)$$

applies in the general case for fluids independent of stratification. It was first shown by Malkus (1979) how this can be refined within a stratified layer of constant depth, which in the limit of zero radial flow leads to a more strict constraint. This constraint now applies on every axisymmetric ring coaxial with the rotation axis that lies within the layer (see figure 6.1b) and is known as the *Malkus constraint*

$$M(s, z, t) \equiv \int_0^{2\pi} ((\nabla \times \mathbf{B}) \times \mathbf{B})_{\phi} d\phi = 0,$$

for any  $s$  and  $z$  within the layer; thus for the stratified case a single Taylor constraint

on a cylinder transforms into an infinite number of Malkus constraints. A full derivation of this constraint is given in the following section §6.2. Magnetic fields that satisfy the Taylor or Malkus constraints respectively are termed Taylor or Malkus states.

In this chapter we consider from a theoretical standpoint the structure of the geomagnetic field within any such strongly stratified layer and we explore the use of both the Taylor and Malkus constraints as a tool for probing instantaneous structures of the magnetic field throughout Earth's core. This method ignores any dynamics and asks simply whether we can find a set of magnetic fields which satisfy the necessary constraints.

Our task is a challenging one: even finding magnetic fields that exactly satisfy the comparatively simple case of Taylor's constraint has proven to be difficult in the 55 years since the seminal paper of Taylor (1963), although notable progress has been made in axisymmetry (Hollerbach and Ierley, 1991; Soward and Jones, 1983) and in 3D (Jault and Cardin, 1999) subject to imposing a specific symmetry. Recently, significant progress has been made in this regard by presenting a more general understanding of the mathematical structure of Taylor's constraint in three dimensions (Livermore et al., 2008). This method was implemented by Livermore et al. (2009) to construct simple, large scale magnetic fields compatible with geomagnetic observations. It is this which provides the foundation for the work presented here.

While exploring the theoretical implications of the Malkus constraints, we will aim to address the following objectives:

1. Do exact or approximate Malkus states exist? It is not *a priori* obvious whether or not there are enough degrees of freedom within any magnetic field to satisfy all required constraints.
2. Does any snapshot of the geomagnetic field convey information about whether there is a strongly stratified layer at the top of the core?
3. What might be the present-day internal structure of the geomagnetic field inside a stratified layer?

The remainder of this chapter is structured as follows. In §6.2 we present a new, more general derivation of the condition required to be satisfied with a stratified layer of fluid, which under an idealised limit reduces to what is known as Malkus' constraint. In sections 6.3 to 6.5 we summarise a method for constructing Malkus

states, applying it to a snapshot of the present day field in sections 6.6 and 6.7; we conclude in §6.8.

## 6.2 Derivation of Malkus' constraint

Within stably stratified fluids radial flows are suppressed, hence in the limit of strong stratification radial fluid velocities are negligibly small (Braginsky, 1999; Davies et al., 2015). We proceed within this idealised limit and require that  $u_r = 0$  within a region of stratified fluid that is a volume of revolution: we represent the proposed stratified layer within Earth's core as a spherically symmetric layer of constant depth. We assume further that the system is in magnetostrophic balance; that is, rapidly rotating with negligible inertia and viscosity. The resulting constraint was first derived by Malkus (1979), however, here we present an alternative and more straightforward derivation courtesy of Dominique Jault (personal communication).

We use the condition for incompressible flow that  $\nabla \cdot \mathbf{u} = 0$  and the standard toroidal poloidal decomposition within spherical coordinates  $(r, \theta, \phi)$ . From the condition that there is no spherically-radial component of velocity then  $\mathbf{u}$  must be purely toroidal and hence can be written as

$$\mathbf{u} = \nabla \times (\mathcal{T}(r, \theta, \phi)\hat{\mathbf{r}}) = \frac{1}{r \sin \theta} \frac{\partial \mathcal{T}}{\partial \phi} \hat{\boldsymbol{\theta}} - \frac{1}{r} \frac{\partial \mathcal{T}}{\partial \theta} \hat{\boldsymbol{\phi}}.$$

Therefore the cylindrically-radial velocity, written in spherical coordinates, is

$$u_s = \sin \theta u_r + \cos \theta u_\theta = \frac{\cos \theta}{r \sin \theta} \frac{\partial \mathcal{T}}{\partial \phi}$$

and so

$$\int_0^{2\pi} u_s \, d\phi = \frac{\cos \theta}{r \sin \theta} \int_0^{2\pi} \frac{\partial \mathcal{T}}{\partial \phi} \, d\phi = 0.$$

Now, since  $\hat{\boldsymbol{\phi}} \cdot (\hat{\mathbf{z}} \times \mathbf{u}) = u_s$  then, from the azimuthal component of the magnetostrophic equation (2.2) we have

$$2u_s = -\frac{\partial p'}{\partial \phi} + ((\nabla \times \mathbf{B}) \times \mathbf{B})_\phi.$$

Integrating in  $\phi$  around any circle of constant  $(s, z)$ , as illustrated by the red rings in figure 6.1b, and using the single-valued nature of pressure, gives Malkus' constraint,

$$2 \underbrace{\int_0^{2\pi} u_s \, d\phi}_{=0} = - \underbrace{\int_0^{2\pi} \frac{\partial p'}{\partial \phi} \, d\phi}_{=0} + \int_0^{2\pi} ((\nabla \times \mathbf{B}) \times \mathbf{B})_\phi \, d\phi = 0,$$

or equivalently requiring that the Malkus integral  $M$  is zero:

$$M(s, z, t) \equiv \int_0^{2\pi} ((\nabla \times \mathbf{B}) \times \mathbf{B})_\phi \, d\phi = 0. \quad (6.2)$$

We are also able to generalise this constraint from considering the idealised limit of requiring  $u_r = 0$  within the stratified fluid to the more general situation of permitting  $u_r \neq 0$ , where we express the Malkus integral in terms of the radial flow. Now, the flow  $\mathbf{u}$  is no longer purely toroidal and hence

$$M(s, z, t) = 2 \int_0^{2\pi} u_s \, d\phi = \int_0^{2\pi} 2u_\theta \cos \theta \, d\phi + \int_0^{2\pi} 2u_r \sin \theta \, d\phi. \quad (6.3)$$

We now use the condition for incompressible flow that  $\nabla \cdot \mathbf{u} = 0$ ,

$$\begin{aligned} 0 = \nabla \cdot \mathbf{u} &= \frac{1}{r^2} \frac{\partial(r^2 u_r)}{\partial r} + \frac{1}{r \sin \theta} \frac{\partial(u_\theta \sin \theta)}{\partial \theta} + \frac{1}{r \sin \theta} \frac{\partial u_\phi}{\partial \phi} \\ \Rightarrow \int_0^{2\pi} \left( \frac{\sin \theta}{r} \frac{\partial(r^2 u_r)}{\partial r} + \frac{\partial(u_\theta \sin \theta)}{\partial \theta} \right) \, d\phi &= - \int_0^{2\pi} \frac{\partial u_\phi}{\partial \phi} \, d\phi = 0. \end{aligned}$$

Now integrating over  $[0, \theta]$  we find

$$\begin{aligned} \int_0^{2\pi} u_\theta \, d\phi &= \frac{1}{\sin \theta} \int_0^\theta \frac{\sin \theta'}{r} \int_0^{2\pi} \frac{\partial(r^2 u_r)}{\partial r} \, d\phi \, d\theta' \\ &= - \frac{1}{r \sin \theta} \int_0^\theta \sin \theta' \frac{\partial}{\partial r} \left( r^2 \int_0^{2\pi} u_r \, d\phi \right) \, d\theta' \\ \Rightarrow M &= - \frac{2}{r \tan \theta} \int_0^\theta \frac{\partial}{\partial r} \left( r^2 \int_0^{2\pi} u_r \sin \theta' \, d\phi \right) \, d\theta' + \int_0^{2\pi} 2u_r \sin \theta \, d\phi. \end{aligned}$$

In the above derivation, no assumption has been made about stratification and this equation holds as an identity in the magnetostrophic regime independent of stratification. In the case considered by Malkus,  $M = 0$  is recovered in the limit of  $u_r \rightarrow 0$ .

It is clear that Malkus' constraint is similar to Taylor's constraint except now not only does the azimuthal component of the Lorentz force need to have zero

average over fluid cylinders, it needs to be zero for the infinite set of constant- $z$  slices of these cylinders (here termed *Malkus rings*, see figure 6.1b) that lie within the stratified region. In terms of the flow, the increased restriction of the Malkus constraint arises because it requires zero azimuthally-averaged  $u_s$  at any given value of  $z$ , whereas Taylor’s constraint requires only that the cylindrically averaged  $u_s$  vanishes and allows outward flow at a given height to be compensated by inward flow at another. We note that all Malkus states are Taylor states, but the converse is not true.

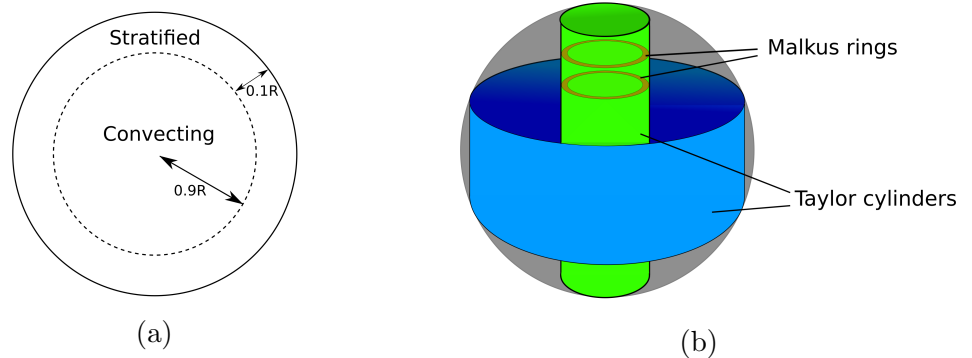


Figure 6.1: (a) Earth-like spherical shell with radius  $r_{SL} = 0.9R$ . A Malkus state defined in a stratified layer surrounds an interior Taylor state. (b) Geometry of constraint surfaces.

### 6.3 Geometry and representation of a stratified magnetostrophic model

The physical motivation for applying Malkus’ constraint arises from seeking to find a realistic model for the magnetic field in the proposed stratified layer within Earth’s outer core. Hence we compute solutions for the magnetic field in the Earth-like configuration illustrated in figure 6.1a, consisting of a spherical region in which Taylor’s constraint applies, representing the inner convective region of Earth’s core, surrounded by a spherical shell in which Malkus’ constraint applies, representing the stratified layer immediately beneath the CMB. Our method allows a free choice of inner radius  $r_{SL}$ ; in order to agree with the bulk of seismic evidence (Helffrich and Kaneshima, 2010, 2013; Lay and Young, 1990), the value  $r_{SL} = 0.9R$  is chosen for the majority of our solutions, where  $R$  is the full radius of the core (3845 km). However due to the uncertainty which exists for the thickness of Earth’s stratified layer (Kaneshima, 2018), we also probe how sensitive our results are to layer thickness, considering  $r_{SL} = 0.5R, 0.85R, 0.95R, 0.99R$  and  $0.999R$  as well. The Earth’s inner core is neglected throughout, since incorporating it would lead to additional intricacy.

cies due to the cylindrical nature of Taylor's constraint which leads to a distinction between regions inside and outside the tangent cylinder (Livermore and Hollerbach, 2012; Livermore et al., 2008; Roberts and Wu, 2020). Since the focus here is on the outermost reaches of the core, we avoid such complications.

The method used to construct the total solution for the magnetic field throughout Earth's core that is consistent with the Taylor and Malkus constraints is sequential. Firstly, we use a regular representation of the form shown in equation (6.6) to construct a Malkus state in the stratified layer. Secondly, we construct a Taylor state which matches to the Malkus state at  $r = r_{SL}$ ; overall the magnetic field is continuous but may have discontinuous derivatives on  $r = r_{SL}$ . We note that any flow driven by this magnetic field through the magnetostrophic balance may also be discontinuous at  $r = r_{SL}$  because in general  $u_r \neq 0$  in the inner region but  $u_r = 0$  is assumed in the stratified region. In a fully consistent model, where all the fluid velocities associated with the magnetic fields are determined, it would be appropriate for one to require that  $u_r = 0$  at the interface and therefore that the radial velocity in the inner region smoothly tends towards zero at the boundary. However, considerations of such dynamics lie outside the scope of the present study focussed only on the magnetic constraints, but imposing continuity of  $u_r$  for example would clearly require additional constraints.

As a pedagogical exercise we also construct some Malkus states within a fully stratified sphere ( $r_{SL} = 0$ ), as detailed in appendix B. Without the complications of matching to a Taylor state, the equations take a simpler form and we present some first examples in appendix B. Dynamically, sustenance of a magnetic field within a fully stratified sphere is ruled out by the theory of Busse (1975), which provides a strictly positive lower bound for the radial flow as a condition on the existence of a dynamo. Nonetheless it can be insightful to first consider the full sphere case, as it facilitates the consideration of fundamental principles of the magnetic field and Malkus constraint structure, and allows direct comparisons to be made with similar full sphere Taylor states.

In what follows we represent a magnetic field by a sum of toroidal and poloidal modes (as introduced in §3.2) with specific coefficients

$$\mathbf{B} = \sum_{l=1}^{L_{max}} \sum_{m=-l}^l \sum_{n=1}^{N_{max}} a_{l,n}^m \mathcal{T}_{l,n}^m + b_{l,n}^m \mathcal{S}_{l,n}^m \quad (6.4)$$

where  $\mathcal{T}_{l,n}^m = \nabla \times (T_{l,n}(r)Y_l^m \hat{\mathbf{r}})$ ,  $\mathcal{S}_{l,n}^m = \nabla \times \nabla \times (S_{l,n}(r)Y_l^m \hat{\mathbf{r}})$ ,  $N_{max}$  is the radial truncation of the poloidal and toroidal field. In the above,  $Y_l^m$  is a spherical harmonic

of degree  $l$  and order  $m$ , normalised to unity by its squared integral over solid angle. Positive or negative values of  $m$  indicate respectively a  $\cos m\phi$  or  $\sin m\phi$  dependence in azimuth. The scalar functions  $T_{l,n}$  and  $S_{l,n}$ ,  $n \geq 1$ , are respectively chosen to be the functions  $\chi_{l,n}$  and  $\psi_{l,n}$  composed of Jacobi polynomials (Li et al., 2010, 2011). They are orthogonal, and obey regularity conditions at the origin and the electrically insulating boundary condition at  $r = R$  (derived in appendix C.4)

$$\frac{d\mathcal{S}_l^m}{dr} + l\mathcal{S}_l^m/R = \mathcal{T}_l^m = 0. \quad (6.5)$$

We note that this description is convenient but incomplete when used within the spherical shell, for which the magnetic field does not need to obey regularity at the origin. For simplicity, we nevertheless use this representation in both layers, although restricting the domain of the radial representation to  $[0, r_{SL}]$  for the inner region. The use of these full sphere, regular radial basis functions throughout, is overly restrictive, since it requires that any Malkus state solved for within the stratified layer is consistent with a possible Malkus state field in the interior region. While, as explained above, the interior fields in our solutions are determined separately, having the additional freedom of only needing to satisfy Taylor's constraint, the field in the stratified layer remains overly-constrained in this process. Therefore it is important to note that it is not possible to rigorously know that we always find the simplest or most extremal field possible after optimising with respect to a quantity of interest (see equation (6.13)).

## 6.4 Discretisation of the constraints

### 6.4.1 The Taylor constraints

Since the Malkus constraint forms a more restrictive constraint which encompasses the Taylor constraint it is useful for us to first summarise the structure of the Taylor constraint in a full sphere. The integral given in equation (6.1), which Taylor's constraint requires to be zero, is known as the Taylor integral. Although applied on an infinite set of surfaces, Livermore et al. (2008) showed that Taylor's constraint reduces to a finite number of constraint equations for a suitably truncated magnetic field expansion

$$\mathcal{S}_l^m(r) = r^{l+1} \sum_{j=0}^{N_{max}} c_j r^{2j} \quad \text{and} \quad \mathcal{T}_l^m(r) = r^{l+1} \sum_{j=0}^{N_{max}} d_j r^{2j}, \quad (6.6)$$

which is an expanded version of (6.4) for some  $c_j$  and  $d_j$ , which are linearly dependent on constants  $a_{l,n}^m$  and  $b_{l,n}^m$ . The Taylor integral itself then collapses to a polynomial of finite degree which depends upon  $s^2$  (Lewis and Bellan, 1990) and the coefficients  $a_{l,n}^m, b_{l,n}^m$ , and takes the form

$$T(s) = s^2 \sqrt{R^2 - s^2} Q_{D_T}(s^2) = 0, \quad (6.7)$$

for some polynomial  $Q_{D_T}$  of maximum degree  $D_T$ .

Taylor's constraint is now equivalent to enforcing that the coefficients of all powers of  $s$  in the polynomial  $Q_{D_T}$  equal zero, as this ensures  $T(s)$  vanishes identically on every geostrophic contour. This translates into  $C_T = L_{max} + 2N_{max} - 2$  conditions after the single degeneracy due to the electrically insulating boundary condition is removed (Livermore et al., 2008), transforming the infinite number of constraints to a finite number of simultaneous, coupled, quadratic, homogeneous equations. This reduction is vital as it gives a procedure for enforcing Taylor's constraint in general, and allows the implementation of a method to construct magnetic fields which exactly satisfy this constraint, known as Taylor states, as demonstrated by Livermore et al. (2009). In the next section we see how, with some relatively simple alterations this procedure can be extended to the construction of exact Malkus states.

### 6.4.2 The Malkus constraints

Along similar lines as we showed for Taylor's constraints, we now outline some general properties of the mathematical structure of Malkus' constraints. On adopting the representation (6.4) the Malkus integral reduces to a multinomial in  $s^2$  and  $z$  (Lewis and Bellan, 1990) and we require

$$M(s, z) = Q_{D_M}(s^2, z) = 0$$

for some finite degree multinomial  $Q_{D_M}$  in  $s$  and  $z$ . Note that the Taylor integral (6.7) is simply a  $z$ -integrated form of  $Q_{D_M}$ . Equating every multinomial term in  $Q_{D_M}(s^2, z)$  to zero results in a finite set of constraints that are nonlinear in the coefficients  $a_{l,n}^m$  and  $b_{l,n}^m$ .

The number of constraints can be quantified for a given truncation following a similar approach as that employed by Livermore et al. (2008) for Taylor's constraint, by tracking the greatest exponent of the dimension of length. Here, we

calculate the maximum possible exponent in dimension of length within the Malkus integral and since each constraint equation arises from ensuring a coefficient of a different exponent vanishes, enumerating all possibilities gives the maximum number of constraints.

There are three possible non-zero interactions whose sum comprises the Malkus integral, toroidal-toroidal, toroidal-poloidal and poloidal-poloidal as defined in equation (6.12). Since the poloidal field definition contains two curls whereas the toroidal field only one, then this extra derivative reduces the maximum exponent by one for interactions involving a poloidal field as opposed to a toroidal one. This means that the maximal case is determined by the toroidal-toroidal interaction,  $[\mathcal{T}_1, \mathcal{T}_2]$ . Since the Malkus integrand is identical to the Taylor integrand, we observe that the maximum radial exponent in the Malkus integrand  $((\nabla \times \mathcal{T}_1) \times \mathcal{T}_2)_\phi$  is  $2L_{max} + 4N_{max} - 1$ , as derived by Livermore et al. (2008). This is then reduced by two due to the property that the interaction of two toroidal harmonics that have identical spherical harmonic degrees and orders is zero (Livermore et al., 2008). This requires that one of the two modes has an  $L_{max}$  of at least one smaller than the other, hence resulting in a maximum possible degree in  $r$  of  $2L_{max} + 4N_{max} - 3$ .

Now under a transform in coordinate systems we note that  $r^n$  in spherical coordinates can be expressed as  $s^j z^k$  in cylindrical coordinates, where  $n = j + k$ . Since only even values of  $j$  are present this results in  $L_{max} + 2N_{max} - 2 = C_T$  non-trivial constraint equations in this dimension. There is no such restriction on  $k$ , which can take all values up to the maximum of  $2L_{max} + 4N_{max} - 3 = 2C_T + 1$ .

Each one of the constraints arises from a coefficient of a term with a different combination of exponents in  $s$  and  $z$ , explicitly, these terms have the following form:

$$\begin{aligned} & (A_{C_T,0}z^0 + A_{C_T,1}z)s^{2C_T} + (A_{C_T-1,0}z^0 + A_{C_T-1,1}z + A_{C_T-1,2}z^2 + A_{C_T-1,3}z^3)s^{2(C_T-1)} \\ & + (A_{C_T-2,0}z^0 + \dots + A_{C_T-2,5}z^5)s^{2(C_T-2)} + \dots \\ & + (A_{1,0} + \dots + A_{1,2C_T-1}z^{2C_T-1})s^2 + (A_{0,0} + \dots + A_{0,2C_T+1}z^{2C_T+1}). \end{aligned} \quad (6.8)$$

Hence from the summation of the total number of these terms for every combination of  $j$  and  $k$ , with  $j$  even, such that  $j + k \leq 2C_T + 1$  we have the following expression for the maximum number of Malkus constraints,

$$C_M = 2 \sum_{n=0}^{C_T} (n+1) = (C_T+1)(C_T+2) = C_T^2 + 3C_T + 2. \quad (6.9)$$

Therefore we find that as expected the Malkus' constraints are more numerous than Taylor's constraints. It is significant to notice that  $C_M \gg C_T$  and in particular for high degree/resolution systems  $C_M \approx C_T^2$ .

In order to satisfy these constraints, the magnetic field has  $2L_{max}N_{max}(L_{max} + 2)$  degrees of freedom (this being the number of unknown spectral coefficients within the truncation of  $(L_{max}, N_{max})$ ). In axisymmetry the number of degrees of freedom reduces to  $2N_{max}L_{max}$ .

If we truncate the magnetic field quasi-uniformly as  $N = \mathcal{O}(L_{max}) \approx \mathcal{O}(N_{max})$ , then we observe that at high  $N$  the number of constraints ( $\mathcal{O}(N^2)$  Malkus constraints;  $\mathcal{O}(N)$  Taylor constraints) is exceeded by the number of degrees of freedom of  $N^3$ . A simple argument based on linear algebra suggests that many solutions (for both Taylor and Malkus states) exist at high  $N$ , however this may be misleading because the constraints are nonlinear and it is not obvious *a priori* whether any solutions exist, or if they do, how numerous they might be. We will discuss this further in the next section, but first we present a simple example, which is insightful for showing the structure of the constraint equations that arise.

Here we consider a simple example of an axisymmetric magnetic field in a full sphere, consisting of four modes: a toroidal  $l = 1, n = 1$  mode, a toroidal  $l = 1, n = 2$  mode, a poloidal  $l = 1, n = 1$  mode and a poloidal  $l = 1, n = 2$  mode, each of which has an unspecified corresponding coefficient  $\alpha_{l,n}$  and  $\beta_{l,n}$  for toroidal and poloidal modes respectively. Through this we demonstrate the form of the linear constraints which arise from Malkus' constraint in this case. It is significant to note the vital role of degeneracy within these constraints in permitting a solution.

Using the formula for  $C_M$  derived above we can calculate that the maximum number of constraints in a system with  $L_{max} = 1, N_{max} = 2$  is  $C_M = 20$ . However, the restriction to axisymmetry means the actual number of constraints here is significantly smaller than this upper bound. Through computing the Malkus integral and enforcing that this is zero for all values of  $s$  and  $z$  by requiring that the coefficients of all powers of  $s$  and  $z$  vanish we obtain a series of simultaneous equations:

$$\left(-\frac{11}{8}\beta_{1,2} + 2\beta_{1,1}\right)\alpha_{1,2} - \frac{253}{140}\left(\frac{77}{69}\beta_{1,2} + \frac{56}{759}\beta_{1,1}\right)\alpha_{1,1} = 0,$$

$$\left(\frac{319}{84}\beta_{1,2} - \frac{10}{3}\beta_{1,1}\right)\alpha_{1,2} - \frac{253}{70}\beta_{1,2}\alpha_{1,1} = 0,$$

$$\left(-\frac{165}{56}\beta_{1,2} + \beta_{1,1}\right)\alpha_{1,2} - \frac{253}{140}\beta_{1,2}\alpha_{1,1} = 0,$$

$$\left(\frac{319}{84}\beta_{1,2} - \frac{10}{3}\beta_{1,1}\right)\alpha_{1,2} - \frac{253}{70}\beta_{1,2}\alpha_{1,1} = 0,$$

$$\left(-\frac{165}{28}\beta_{1,2} + 2\beta_{1,1}\right)\alpha_{1,2} - \frac{253}{70}\beta_{1,2}\alpha_{1,1} = 0,$$

$$\left(-\frac{165}{56}\beta_{1,2} + \beta_{1,1}\right)\alpha_{1,2} - \frac{253}{140}\beta_{1,2}\alpha_{1,1} = 0.$$

The 6 equations here arise from the coefficients of the exponents  $s^4z$ ,  $s^2z$ ,  $s^2z^3$ ,  $s^0z^1$ ,  $s^0z^3$ ,  $s^0z^5$ , the only coefficients that are not trivially zero, due to the interactions of the limited modes present. Although there are 6 equations here, it is clear that there are only two independent conditions:

$$\alpha_{1,1}\beta_{1,2} + \frac{5}{2}\alpha_{1,2}\beta_{1,2} = 0, \quad \text{and} \quad \alpha_{1,2}\beta_{1,1} + \frac{11}{7}\alpha_{1,2}\beta_{1,2} = 0.$$

If both  $\beta_{1,2}$  and  $\alpha_{1,2}$  are nonzero, then these become linear constraints.

Hence, in this case we can see that there are 4 degrees of freedom, 6 constraint equations but only 2 independent constraints. This means that while on first inspection the system appears to be overconstrained with no solution, there are in fact multiple Malkus state solutions, with the solution space being spanned by two degrees of freedom  $(\beta_{1,2}, \alpha_{1,2})$  with the other coefficients determined in terms of these by the relationships:

$$\alpha_{1,1} = -\frac{5}{2}\alpha_{1,2} \quad \text{and} \quad \beta_{1,1} = -\frac{11}{7}\beta_{1,2}.$$

Despite the significant degeneracy in the Malkus constraints, they are notably more restrictive than the Taylor constraints for this truncation of  $L_{max} = 1$ ,  $N_{max} = 2$ , for which the Taylor integral is identically zero and so provides no restriction.

The example highlights that many of the Malkus constraints are linearly

dependent: the constraint degeneracy plays a far more significant role for the Malkus constraints compared with the Taylor constraints, which only have a single weak degeneracy due to the electrically insulating boundary condition (Livermore et al., 2008). While this degeneracy effectively lowers the number of constraints (making it easier to find a solution), due to the complex nature of the nonlinear equations at present we have no predictive theory for the total number of independent constraints.

## 6.5 Existence of Malkus states

In this section we address the question of: when do Malkus states exist? We proceed in two parts. First we give some analytic examples of non-geophysical but simple and exact Malkus states. Second, we show how a Malkus state can be constructed that matches any exterior potential field, thereby markedly extending the class of known Malkus states.

### 6.5.1 Simple analytic states

Simple Malkus states may be constructed by exploiting the analytic form of the integrand defining the Malkus constraint (see theorem 6.5.1) and the symmetries inherent in the spherical harmonics that define our basis representation for the magnetic field. In order of simplicity, we present a list of some simple Malkus states:

- (A) any magnetic field based on a single spherical harmonic because of symmetry in the azimuthal integration
- (B) any axisymmetric purely toroidal or poloidal field since the integrand itself  $((\nabla \times \mathbf{B}) \times \mathbf{B})_\phi$  is zero
- (C) equatorially symmetric purely toroidal or poloidal field comprising either only cosine or only sine dependence in azimuth, as the resultant integrand is anti-symmetric with respect to a rotation of  $\pi$  radians in azimuth and hence vanishes under azimuthal integration over  $[0, 2\pi]$ .

The last example plays an important role in the more general discussion of Malkus states (and see theorem 6.5.1).

### 6.5.2 General Malkus states

We now investigate whether it is possible to find much more general Malkus states; specifically we address whether we can find a Malkus state that matches at the edge of the core any given exterior potential magnetic field

$$\mathbf{B}_{ext} = -\nabla V; \quad V = R \sum_{l=1}^{L_{max}} \sum_{m=0}^l \left(\frac{R}{r}\right)^{l+1} (g_l^m \cos(m\phi) + h_l^m \sin(m\phi)) P_l^m(\cos\theta), \quad (6.10)$$

where  $P_l^m$  is an associated Legendre polynomial and  $g_l^m$  and  $h_l^m$  are the Gauss coefficients.

In the following, we set out one procedure for finding such a Malkus state. Following the method of [Livermore et al. \(2009\)](#) which describes how to find analogous Taylor states, we also choose to completely specify the poloidal field within the core, downwards continuing the exterior potential field inside the core  $r \leq R$  by assuming a profile for each poloidal harmonic of degree  $l$  that minimises the Ohmic dissipation within the modelled core, compatible both with an electrically insulating outer boundary and regularity at the origin ([Backus et al., 1996](#)):

$$(2l + 3)r^{l+1} - (2l + 1)r^{l+3}. \quad (6.11)$$

It is the  $r^{l+1}$  factor here that is crucial for ensuring that for all modes there is a factor of at least  $r^2$ , resulting in regularity at the origin; note that the poloidal scalar differs from the magnetic field components themselves by a similar  $r^2$  factor, which are hence permitted to remain finite and non-zero extending to the origin (see [figure 6.4](#)).

Because the core's toroidal field is hidden from external view, we are now free to choose it without affecting the matching to  $\mathbf{B}_{ext}$ . The question is two fold: whether there are sufficient degrees of freedom in the toroidal field to exceed the number of independent nonlinear constraints, and whether a solution can be found.

These issues are addressed in the following theorem, in which we prove that it is indeed possible to find such a toroidal field that renders any given poloidal field a Malkus state, by identifying a judicious choice of toroidal modes which result in a linear (rather than a non-linear) system whose solution is then straightforward.

**Theorem 6.5.1.** *Any arbitrary, prescribed, polynomial poloidal field can be transformed into a Malkus state through the addition of an appropriate polynomial toroidal*

field.

*Proof.* We prove below that by considering an arbitrary, prescribed, truncated poloidal field, the addition of a specific choice of toroidal modes renders the Malkus constraints linear in the unknown toroidal coefficients. By taking a sufficient number of such modes such that the degrees of freedom exceed the number of constraints, it follows that for the general case (barring specific degenerate cases) by solving the linear system the resultant magnetic field is a Malkus state.

To show this, because the Malkus constraint is quadratic in the magnetic field, we introduce the concept of a magnetic field interaction. In general there are three possible field interactions within the Malkus integral, toroidal-toroidal, poloidal-poloidal and toroidal-poloidal, respectively

$$M = \sum_{l_1, l_2}^{L_{max}} \sum_m^{L_{max}} ([\mathbf{T}_{l_1}^m, \mathbf{T}_{l_2}^m] + [\mathbf{S}_{l_1}^m, \mathbf{S}_{l_2}^m] + [\mathbf{T}_{l_1}^m, \mathbf{S}_{l_2}^m]),$$

where

$$\begin{aligned} [\mathbf{T}_{l_1}^m, \mathbf{T}_{l_2}^m] &= \int_0^{2\pi} \frac{l_1(l_1+1)\mathcal{T}_{l_1}^m\mathcal{T}_{l_2}^m}{r^3 \sin \theta} \left( Y_{l_1}^m \frac{\partial Y_{l_2}^m}{\partial \phi} \right) s \, d\phi + sc, \\ [\mathbf{S}_{l_1}^m, \mathbf{S}_{l_2}^m] &= \int_0^{2\pi} \frac{l_1(l_1+1)\mathcal{S}_{l_1}^m(\frac{d^2}{dr^2} - l_2(l_2+1)/r^2)\mathcal{S}_{l_2}^m}{r^3 \sin \theta} \left( Y_{l_1}^m \frac{\partial Y_{l_2}^m}{\partial \phi} \right) s \, d\phi + sc, \\ [\mathbf{T}_{l_1}^m, \mathbf{S}_{l_2}^m] &= \int_0^{2\pi} \frac{1}{r^3} \left( l_1(l_1+1)\mathcal{T}_{l_1}^m \frac{d\mathcal{S}_{l_2}^m}{dr} Y_{l_1}^m \frac{\partial Y_{l_2}^m}{\partial \theta} - l_2(l_2+1)\mathcal{S}_{l_2}^m \frac{d\mathcal{T}_{l_1}^m}{dr} Y_{l_2}^m \frac{\partial Y_{l_1}^m}{\partial \theta} \right) s \, d\phi, \end{aligned} \quad (6.12)$$

where  $sc$  is the symmetric counterpart given by interchanging the vector harmonics and hence the positions of  $l_1$  and  $l_2$  (Livermore et al., 2008). Note that there is no poloidal-toroidal interaction since the curl of a poloidal vector is toroidal and  $(\mathcal{T}_1 \times \mathcal{T}_2)_\phi = 0$ , for any two toroidal vectors  $\mathcal{T}_1$  and  $\mathcal{T}_2$ .

For the situation we consider of a given poloidal field, then the only non-linearity within the unspecified coefficients arises from the toroidal-toroidal interactions, which results in quadratic dependence, just as for the general case with unprescribed poloidal field. However, by restricting attention to toroidal fields that result in no toroidal-toroidal interaction, the unknown toroidal coefficients appear only in a linear form through the toroidal-poloidal interactions. Axisymmetric modes are the simplest set of toroidal modes which are non-self-interacting (that is, no modes interact with any other modes in the set), however there are too few of them (within the truncation) to solve the resulting linear system which is over-constrained (see

figure 6.2). This is not surprising, since perfect axisymmetry vastly reduces the ability of a magnetic field to satisfy the Malkus constraint, no longer can there be any cancellation within the integral over  $\phi$ . The Malkus integral (6.2) is only zero when the integrand itself vanishes.

Therefore we require additional non-axisymmetric toroidal modes, which we choose such that the total set of toroidal modes remains non-self-interacting. This is achieved by exploiting the previously noted observations that any single harmonic is a Malkus state and that the set of equatorially symmetric toroidal modes  $T_l^l$  is a Malkus state (and therefore has no self-interaction). Owing additionally to azimuthal symmetry, the modes

$$T_1^0, T_2^0, \dots, T_1^{-1}, T_1^1, T_2^{-2}, T_2^2, \dots,$$

that is, the modes  $T_l^m$  with  $m = 0$  or  $m = \pm l$ , have no self-interactions. Each harmonic mode may be expanded in radial modes up to the truncation  $N_{max}$ . The non-interacting nature of the modes may be confirmed from equation (6.12).

The addition of these nonaxisymmetric modes increases the number of degrees of freedom from the axisymmetric case by a factor of three such that it is now larger than the number of constraints (which are now all linear). This can be shown in general since for a toroidal field truncated at  $L_1, N_1$  and a poloidal field truncated at  $L_2, N_2$  the number of Taylor constraints is equal to half of the maximum degree of the polynomial in  $s$ , (i.e.  $C_T = \frac{1}{2}(L_1 + L_2 + 2N_1 + 2N_2) - 2$ ) (Livermore et al., 2008) and the maximum number of Malkus constraints we have shown is given in terms of  $C_T$  by equation (6.9). This results in a situation where if the poloidal field is fixed at a chosen resolution then for a toroidal field truncated quasi-uniformly as  $N = \mathcal{O}(L_{max}) \approx \mathcal{O}(N_{max})$ , the number of Malkus constraints scales as  $\frac{9}{4}N^2$ , which grows slower than the number of degrees of freedom for the non-axisymmetric linear system which scales as  $3N^2$ . Hence it is guaranteed that at a sufficiently large resolution toroidal field representation then there will be more degrees of freedom than constraints.

Therefore, barring degenerate cases, Malkus states exist. Compared with the case of a purely axisymmetric toroidal field, the number (but not the specific form) of linear constraints remains unaltered by the addition of these extra non-axisymmetric modes.

It is worth noting that the depth of the stratified layer does not enter into above derivation. The magnetic field solution in fact satisfies the Malkus constraints everywhere within its region of definition: in our case, this is the full sphere  $0 \leq$

$r \leq R$ . □

We do note the lack of full generality in the above deviation, as it is based upon a polynomial representation, which is sufficient for our purposes here. However, we know that any continuous function defined on a closed interval can be uniformly approximated as closely as desired by a polynomial function, and hence it can be extended to include an arbitrary magnetic field structure by expressing the relevant scalars in a polynomial basis of suitably large truncation.

Figure 6.2 illustrates what we have proven: the existence of solutions of this special class of Malkus states. It provides a specific example of the number of constraints given  $\mathbf{B}_{ext}$  of degree 13 and demonstrates three important things. Firstly, that due to degeneracy the independent linear constraints (red triangles) are much fewer than the full set of linear constraints (red squares). Secondly, that the number of degrees of freedom exceed the number of independent constraints at  $L_{max} = N_{max} \geq 10$  if we consider our preferred non-axisymmetric toroidal basis (described in the proof of theorem 6.5.1, blue circles); in particular if we adopt a toroidal field of the same degree as the poloidal field  $L_{max} = N_{max} = 13$  then we find an infinite set of Malkus states. Thirdly, a laterally complex toroidal field is required to find a Malkus state. Here this is demonstrated by the fact that any attempt to find a Malkus state by adding to the poloidal field an axisymmetric toroidal field will fail, because the number of degrees of freedom (blue stars) is always exceeded by the number of independent constraints.

Having found a Malkus state defined within the stratified layer, we then need to match to a Taylor state in the region beneath. One way of proceeding is to simply extend the polynomial description (already known) of the Malkus state beneath the stratified layer (where the solution also satisfies Taylor constraint); however this effectively imposes additional constraints on the inner region and is overly restrictive. Instead, we apply a similar procedure as for the Malkus states to the inner solution: we use the same poloidal profile and expand the unknown toroidal field in the same way. Because the Taylor constraints are also now linear, this allows for an inner Taylor state to be found. This procedure can be applied to find a Malkus/Taylor state defined by any depth of stratification.

Even within these geomagnetically consistent Malkus states, there are nevertheless multiple degrees of freedom remaining. This raises the question of which of the multiple possible solutions are most realistic for the Earth, and motivates us to incorporate additional conditions to distinguish ‘Earth-like’ solutions.

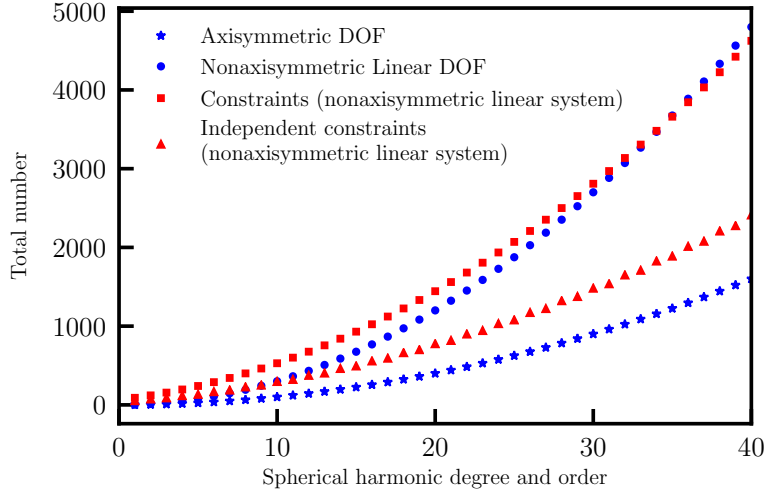


Figure 6.2: This graph compares the number of constraints to degrees of freedom (DOF) as a function of toroidal field spherical harmonic resolution with  $L_{max} = N_{max}$ , given a fixed poloidal field of  $L_{max} = 13$ . This illustrates that for the non-axisymmetric linear system, the number of degrees of freedom (blue circles) exceeds the number of independent constraints (red triangles) for a toroidal field of resolution  $L_{max} = N_{max} \geq 10$ .

We determine specific solutions through choosing the toroidal field  $\mathbf{T}$  that minimises either its Ohmic dissipation or its energy, respectively

$$Q = \frac{\eta}{\mu_0} \int_V (\nabla \times \mathbf{T})^2 dV, \quad \mathcal{E} = \frac{1}{2\mu_0} \int_V \mathbf{T}^2 dV, \quad (6.13)$$

where  $\eta \approx 1 \text{ m}^2\text{s}^{-1}$  is magnetic diffusivity and  $\mu_0 = 4\pi \times 10^{-7} \text{ NA}^{-2}$  is the permeability of free space. Both of these target functions are quadratic in the magnetic field, and so seeking a minimal value subject to the now linear constraints is straightforward. In our sequential method to find a matched Malkus-Taylor state, we first optimise the Malkus state, and then subsequently find an optimal matching Taylor state.

Of the dissipation mechanisms in the core: Ohmic, thermal and viscous, the Ohmic losses are believed to dominate. On these grounds, the most efficient arrangement of the geomagnetic field would be such that Ohmic dissipation  $Q$  is minimised. It is worth noting that in general this procedure is not guaranteed to provide the Malkus state field with least dissipation, but only an approximation to it, since we effectively separately, rather than jointly, optimise for the poloidal and toroidal components. However, we will present our solutions of finding a Malkus state with minimum toroidal field energy, this is particularly useful in allowing us to determine the weakest toroidal field which is required in order to transform the imposed poloidal field into a Malkus state. Therefore providing the geophysically

interesting quantity of a lower bound on toroidal field strength.

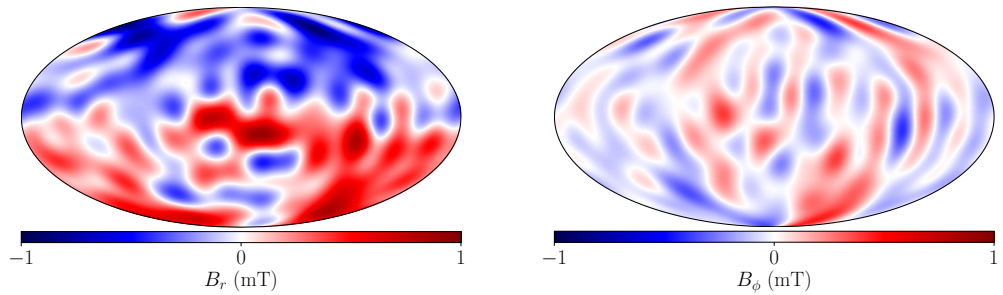
## 6.6 Earth-like Malkus states

We now present Malkus states found using the method explained above with minimal toroidal energy, applied to two external field models. First, we use the CHAOS-6 model (Finlay et al., 2016) at epoch 2015 evaluated to degree 13, the maximum obtainable from geomagnetic observations without significant interference due to crust magnetism (Kono, 2015). Second, we use the time-averaged field over the last 10000 years from the CALS10k.2 model (Constable et al., 2016), which although defined to degree 10, has power concentrated mostly at degrees 1–4 because of strong regularisation of sparsely-observed ancient magnetic field structures. Recalling that the magnetostrophic state that we seek is defined over millennial timescales, this longer average provides on the one hand a better approximation to the background state, but on the other a much lower resolution.

The geometry assumed here is as illustrated in figure 6.1a, with a Malkus state in the stratified layer in the region  $0.9R < r \leq R$ , matching to an inner Taylor state. The strength of the externally-invisible but important toroidal field will be shown by contour plots of its azimuthal component. We note that the radial component of the magnetic field is defined everywhere by the imposed poloidal field of equation (6.11).

### 6.6.1 Magnetic field at 2015

We begin by showing in figure 6.3 both the radial and azimuthal structure,  $B_r$  and  $B_\phi$ , of the poloidal CHAOS-6 model at epoch 2015 on the CMB,  $r = R$ . Of note is that at the truncation to degree 13, the azimuthal component is about half as strong as the radial component.



(a)  $B_r$  at the CMB, (max value = 0.91 mT). (b)  $B_\phi$  at the CMB, (max value = 0.46 mT).

Figure 6.3: Magnetic field at the CMB based on the poloidal field fit to CHAOS-6 at epoch 2015. Visualised using the Mollweide projection and centred on the Greenwich meridian.

Figure 6.4 summarises the strength of the toroidal field in our solutions as a function of radius, this being the minimum energy toroidal field necessary to construct a Malkus state. Different toroidal truncations  $L_{max} = N_{max}$  are shown to demonstrate convergence. The toroidal field is required to be four orders of magnitude stronger in the stratified layer in order to satisfy the more restrictive Malkus constraints, compared with the inner region in which the weaker Taylor constraint applies, and adopts a profile that is converged by degree 13. The strong toroidal field throughout the stratified layer occurs despite the electrically insulating boundary condition (6.4) at the outer boundary that requires the toroidal field to vanish. Within the stratified layer, the azimuthal toroidal field strength attains a maximum rms value of 2.5 mT at a radius of about  $0.98R$  or a depth of about 70 km, about double the poloidal component of azimuthal field value observed at the CMB, and exceeding the locally imposed azimuthal poloidal magnetic field of rms 0.28 mT at this radius. Within the convective region, small oscillations in the toroidal component of  $B_\phi^{\text{rms}}$  as a function of radius are noticeable in figure 6.4. It is not obvious as to the exact cause of these and whether they are due to a limitation of the model or a physical phenomenon, as we find that the amplitude of period of these variations appear to be independent of both radial resolution and stratified layer thickness. However, we do not dwell on this, as we re-emphasise that the toroidal field in this region is not an estimate for the geomagnetic field, but rather that the very small magnitude of this lower bound merely demonstrates the lack of restrictiveness of our model within this region.

Figure 6.5 shows  $B_\phi$  for both the total field and the toroidal component in isolation, using a toroidal truncation of 13 (corresponding to the blue line in fig-

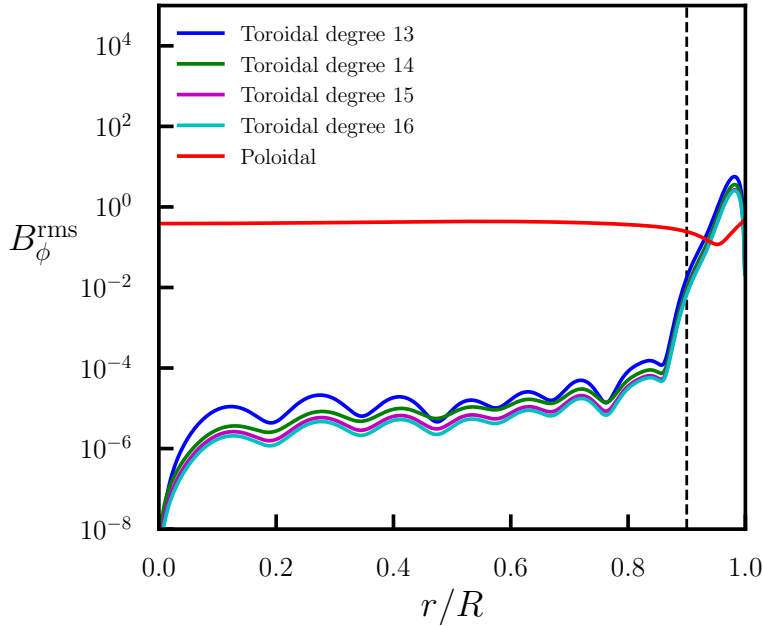
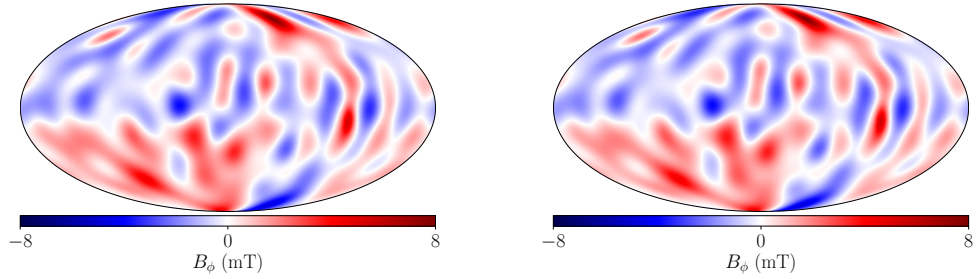


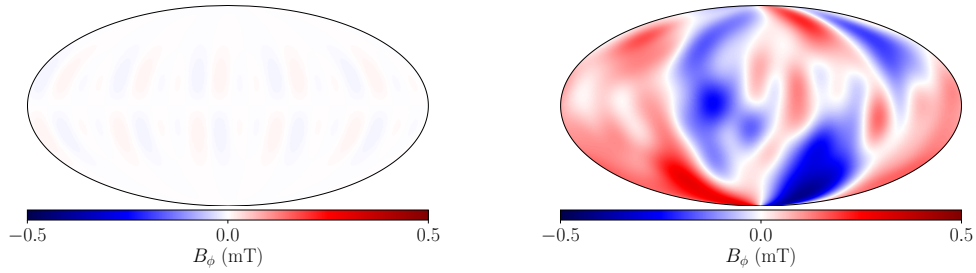
Figure 6.4: The root mean squared azimuthal field strength (defined over solid angle)  $B_{\phi}^{\text{rms}} = \sqrt{\int_0^{2\pi} \int_0^{\pi} B_{\phi}^2 \sin \theta \, d\theta \, d\phi}$ , as a function of radius, comparing the strengths of the poloidal field (red) and toroidal field (blue, green, magenta and cyan) for toroidal fields with maximum spherical harmonic degree, order and radial resolution, 13–16 respectively. The poloidal field is the degree 13 field of minimum Ohmic dissipation compatible with the CHAOS-6 model at epoch 2015 (Finlay et al., 2016).

ure 6.4.) The top row shows the structure at the radius of maximum rms toroidal field ( $r = 0.98R$ ), demonstrating that the additive toroidal field component (of maximum 8 mT) dominates the total azimuthal field. The bottom row shows a comparable figure at  $r = 0.7R$ , in the inner region where only Taylor’s constraint applies. Plotted on the same scale, the required additive toroidal component is tiny compared with the imposed poloidal field. This results in a maximum value of the toroidal magnetic field within the outer layer which is about 100 times larger compared to that in the inner region. This highlights again that the Malkus constraint is much more restrictive than the Taylor constraint.

For comparison, figure 6.6 shows an equivalent solution to figure 6.5(a,b) but in the absence of stratification (where the magnetic field satisfies only Taylor’s constraint). Despite the imposed poloidal field being the same, the toroidal contribution to the azimuthal field is very weak here (note the colourbar range is reduced from that of figure 6.5(a,b) from 8 to 0.04 mT) and it is of very large scale. This further highlights the weakness of the Taylor constraints compared with the Malkus constraints.



(a) Toroidal field  $B_\phi$  at  $r = 0.98R$ , (max value = 7.74 mT, RMS = 2.50 mT). (b) Total field  $B_\phi$  at  $r = 0.98R$ , (max value = 7.80 mT, RMS = 2.53 mT).

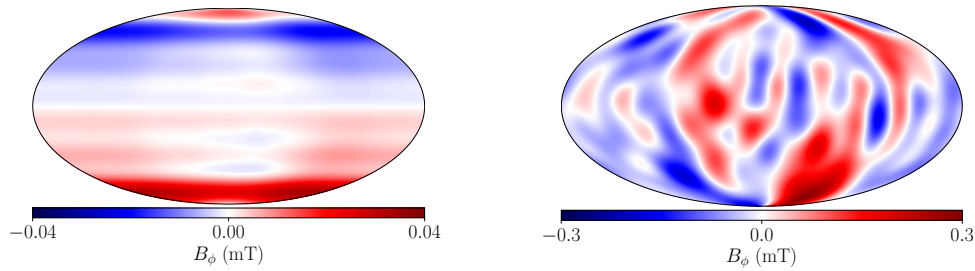


(c) Toroidal field  $B_\phi$  at  $r = 0.7R$ , (max value = 0.012 mT) (d) Total field  $B_\phi$  at  $r = 0.7R$ , (max value = 0.41 mT)

Figure 6.5: Minimal toroidal-energy solution (a,c) shown by the azimuthal component, of a Malkus state ( $0.9R < r \leq R$ ) and Taylor state  $r \leq 0.9R$ , compared with the total azimuthal component (b,d). Figures (a,b) show the field at a radius of  $r = 0.98R$ , close to where the maximum rms azimuthal toroidal field occurs, while (c,d) show the inner region at  $r = 0.7R$ .

## 6.6.2 Time averaged field over the past ten millenia

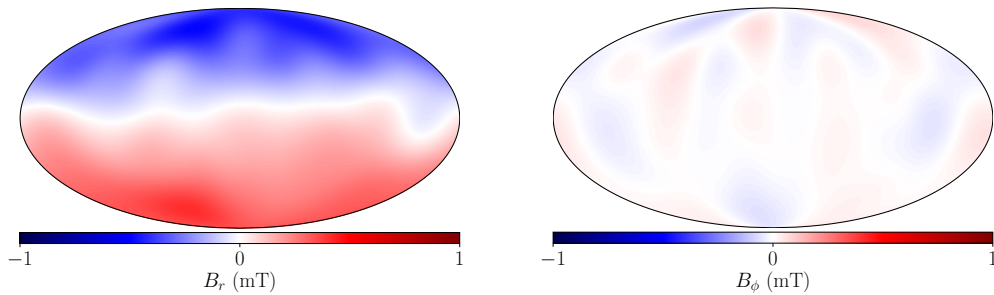
Here we show results for a poloidal field that is derived from the 10000-year time averaged field from the CALS10k.2 model (Constable et al., 2016), which is as shown in figure 6.7. The model is only available up to spherical harmonic degree 10, hence we adopt a truncation of  $L_{max} = N_{max} = 10$  for the toroidal field. Due to the absence of small-scale features in the field (caused by regularisation) the maximum value of  $B_r$  is reduced to about 1/2 of the comparable value from the degree-13 CHAOS-6 model from epoch 2015, and similarly the azimuthal field to about 1/6 of its value. We note that over a long enough time span, Earth's magnetic field is generally assumed to average to an axial dipole: a field configuration that is both a Malkus state and one in which the azimuthal component vanishes. Thus a small azimuthal component is consistent with such an assumption.



(a) Toroidal field  $B_\phi$  at  $r = 0.98R$ ,  
(max value = 0.034 mT)

(b) Total field  $B_\phi$  at  $r = 0.98R$ ,  
(max value = 0.29 mT)

Figure 6.6: Azimuthal field for an unstratified comparative case, for which the magnetic field satisfies only Taylor's constraint.



(a)  $B_r$ , max value = 0.50 mT.

(b)  $B_\phi$ , max value = 0.085 mT.

Figure 6.7: Magnetic field at the CMB based on the 10000-year time average field from CALS10k.2

Contours of the azimuthal field within the stratified layer (at  $r = 0.97R$ ) are shown in figure 6.8, which is approximately the radius at which the maximum rms azimuthal toroidal field occurs. As before, the toroidal field dominates the azimuthal component whose maximum value (1.66 mT) is about 20 times that on the CMB (0.085 mT) and 4 orders of magnitude larger than in the interior core. Although this value is less than the 8 mT found in the 2015 example above, this is consistent with the overall reduction in structure of the imposed poloidal field.

## 6.7 Discussion

Having presented our results, we now begin our discussion by addressing in turn the three objectives listed at the beginning of the chapter.

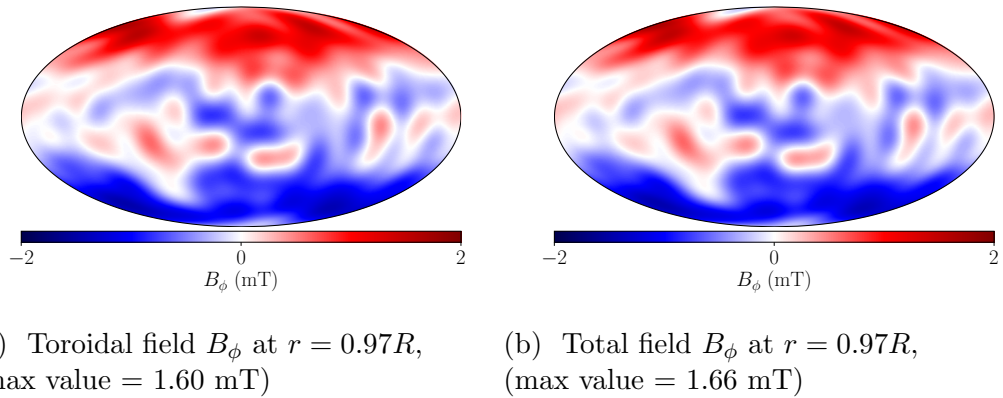


Figure 6.8: The azimuthal component of the Malkus state magnetic field within the stratified layer at a radius of  $r = 0.97R$ , approximately the radius of maximum rms azimuthal toroidal field.

### 6.7.1 Do Malkus states exist?

We have shown that many exact Malkus states exist, both by imposing specific symmetries and by constructing states with a given poloidal field by solving linearly for a suitable toroidal field. We note that even within our linearised framework that ignores a significant part of the toroidal field, there are many such solutions. Owing to the nonlinearity and the difficulty in enumerating the number of independent Malkus constraints, we have no way of quantifying the space of solutions, but it is surely large.

Moreover, the abundance of exact Malkus states also implies the existence of a plenitude of approximate Malkus states. These may indeed be more relevant for the Earth, where some of our idealised assumptions, for example an exact magnetostrophic force balance or zero radial flow, are relaxed.

### 6.7.2 Can we tell from a snapshot of the geomagnetic field if a stratified layer exists?

We have shown in this work that any exterior potential field can be matched to a Malkus state. In fact our result is much stronger (see theorem 6.5.1), namely that we can fit a potential field to either a Taylor state (no stratification assumed), or a Malkus state (defined within a stratified layer of arbitrary depth). Thus if the core is in an exact magnetostrophic balance, then using only considerations of Malkus constraints means that instantaneous knowledge of the geomagnetic field outside the core cannot discriminate between the existence, or not, of a stratified layer.

However, incorporating considerations of the time-dependence of the geomagnetic field, from either a theoretical or observational perspective, may indeed provide additional information. For example, one might consider the evolution of a dynamo-generated time-dependent Malkus state, that satisfies all relevant constraints as time progresses. It is possible that examples of exterior fields are realised by the Earth that cannot match a time-dependent Malkus state. Furthermore, geomagnetic secular variation may provide an avenue to discriminate between observational signatures that are, or are not, compatible with a stratified layer: it may be that dynamics that are guided by stratification (such as waves) provide convincing evidence for such a layer, in a similar vein to the evidence from torsional waves (e.g. [Gillet et al., 2010](#)) which suggests that Earth’s core is close to a Taylor state. Unfortunately a rigorous examination of the dynamics (and perturbations) of Malkus states is out of the scope of this work.

### 6.7.3 What might be the present-day internal structure of the geomagnetic field inside a stratified layer?

Estimating the magnetic field strength inside the core is challenging, because observations made on Earth’s surface, using a potential-field extrapolation, only constrain the poloidal magnetic structure down to the CMB and not beneath. Furthermore, even this structure is visible only to about spherical harmonic degree 13.

By constructing a Malkus state with minimal azimuthal field, we have estimated that for the modern (epoch 2015) field then within the stratified layer (at radius  $r = 0.98R$  or a depth of about 70 km) a maximum azimuthal component of around 8 mT is found. This value is consistent with other estimates of internal field strength that range between 1 – 100 mT ([Zhang and Fearn, 1993](#); [Sreenivasan and Narasimhan, 2017](#); [Gillet et al., 2010](#); [Hori et al., 2015](#); [Shimizu et al., 1998](#); [Buffett, 2010](#); [Gubbins, 2007](#)), relying on studies of numerical models, waves, electric field measurements, tides and reversed flux patches, which indicates that the assumptions underpinning our model are consistent with other approaches. Nevertheless, the strong toroidal field of 8 mT, about 8 times stronger than the observed radial field of 1 mT on the CMB, has significant implications for dynamics within the core. One important example is the speed of Magneto-Coriolis waves, which depends upon the average squared azimuthal field strength, as shown explicitly by [Hori et al. \(2015\)](#). Thus a stratified layer could support fast waves, for example the equatorial waves suggested by [Finlay and Jackson \(2003\)](#), driven in part by the stratification itself but possibly also by the stronger required magnetic field ([Hori et al., 2018](#)).

A key second result is that the azimuthal component of our solution within the inner unstratified region is about 100 times weaker than within the stratified layer. This demonstrates the extent to which Malkus’ constraint is far more restrictive than Taylor’s constraint, and requires a more complex and stronger magnetic field. If the Earth has a stratified layer, this suggests that the magnetic field within the layer would likely be quite different from that of the bulk of the core. This has profound implications on what can be inferred about deep-core dynamics such as large-scale flows (e.g. [Holme, 2015](#)), since any inferences are based only on the magnetic field at the edge of the core, at the top of the layer. Indeed, if the magnetic field has a two layer structure, then the dynamics that it drives will also likely be different within each layer. The deeper dynamics would then be effectively screened from observation by the change in magnetic structure demanded by the stratified layer. Inverting this logic suggests that if deep core structures can be inferred by surface observations, that there can be no stratified layer. Relevant evidence for this line of argument comes from the close correspondence between changes in the length of day and the angular momentum carried by core flows, particularly between 1970-2000 (e.g. [Barrois et al., 2017](#)), although the link is not so well defined in the last few decades during the satellite era.

#### 6.7.4 Limitations and robustness

Our model does not produce a formal lower bound on the azimuthal component of a magnetic field that satisfies both the Malkus and Taylor constraints in their relevant regions along with matching conditions at the CMB. Instead, our results give only an upper bound on the lower bound (e.g. [Jackson et al., 2011](#)) because we have made a variety of simplifying assumptions, the most notable of which are (i) we have restricted ourselves to a subspace of Malkus states for which the constraints are linear (ii) we have imposed the entire poloidal profile and (iii) we have used a regular basis set for all magnetic fields even within the stratified layer when this is not strictly necessary. However, we show for the example considered in [appendix B](#) that in this case assumption (i) does not have a significant impact and our estimate is close to the full nonlinear lower bound. Also with regard to assumption (ii), we have experimented with some slightly different poloidal profiles, with the result being only small (less than 10%) variations in our azimuthal field estimates, indicating some generality of our results. It may be that the other assumptions also do not cause our azimuthal field estimates to deviate significantly from the actual lower bound.

There remains much uncertainty over the depth of any stably stratified

layer at the top of the Earth’s core (Hardy and Wong, 2019). Hence it is natural to consider how our results may change if the layer were to be of a different thickness to the 10% of core radius used, as such we also calculated minimum toroidal-energy solutions matched to CHAOS-6 in epoch 2015 for a range of layer thicknesses. We find very little dependence of the field strengths internal to the layer on the depth of the layer itself, with our root mean square azimuthal field taking peak values of 1.9, 2.7, 2.5, 2.4 and 2.1 mT for thicknesses of 1%, 5%, 10%, 15% and 50% respectively. However for extremely thin layers such as a layer depth of 0.1%, the resulting peak is only of magnitude  $B_\phi = 0.12$  mT and actually occurs beneath the stratified layer. This much smaller value is due to the immediate proximity of the boundary at which the toroidal field must vanish.

The resolution of poloidal field also impacts significantly our optimal solutions. This has already been identified in the comparison between the degree-13 2015 model, and the degree-10 10,000-yr time-averaged model, that respectively resulted in rms azimuthal field estimates of 2.5 and 1.2 mT. We can further test the effect of resolution by considering maximum poloidal degrees of 6 and 10 for the 2015 model to compare with our solution at degree 13. We find that our estimates for the root mean square azimuthal field (taken over their peak spherical surface) were 1.6 and 2.2 mT respectively. In all these calculations, the spherical harmonic degree representing the toroidal field was taken high enough to ensure convergence. Thus stronger toroidal fields are apparently needed to convert more complex poloidal fields into a Malkus state. This has important implications for the Earth, for which we only know the degree of the poloidal field to about 13 due to crustal magnetism. Our estimates of the azimuthal field strength would likely increase if a full representation of the poloidal field were known.

### 6.7.5 Ohmic dissipation

Our method can be readily amended to minimise the toroidal Ohmic dissipation, rather than the toroidal energy. In so doing, we provide a new estimate of the lower bound of Ohmic dissipation within the core. Such lower bounds are useful geophysically as they are linked to the rate of entropy increase within the core, which has direct implications for: core evolution, the sustainability of the geodynamo, the age of the inner core and the heat flow into the mantle (Jackson et al., 2011).

The poloidal field with maximum spherical harmonic degree 13 that we use, based on CHAOS-6 (Finlay et al., 2016) and the minimum Ohmic dissipation radial profile (Backus et al., 1996) has by itself an Ohmic dissipation of 0.2 GW.

[Jackson and Livermore \(2009\)](#) showed that by adding additional constraints for the magnetic field, a formal lower bound on the dissipation could be raised to 10 GW, and even higher to 100 GW with the addition of further assumptions about the geomagnetic spectrum. This latter bound is close to typical estimates of 1 - 15 TW ([Jackson and Livermore, 2009](#); [Jackson et al., 2011](#)).

The addition of extra conditions derived from the assumed dynamical balance, namely Taylor constraints, were considered by [Jackson et al. \(2011\)](#) by adopting a very specific magnetic field representation. These constraints alone raised their estimate of the lower bound from 0.2 to 10 GW, that is, by a factor of 50. In view of the much stronger Malkus constraints (compared to the Taylor constraints), we briefly investigate their impact here.

We follow our methodology and find an additive toroidal field of minimal dissipation (rather than energy) that renders the total field a Malkus state. The dissipation is altered from 0.2 to 0.7 GW. That this increase is rather small (only a small factor of about 3) is rather disappointing, but is not in contradiction to our other results. It is generally true that the Malkus constraints are more restrictive than the Taylor constraint, but this comparison can only be made when the same representation is used for both. The method of [Jackson et al. \(2011\)](#) assumed a highly restrictive form, so that in fact their Taylor states were apparently actually more tightly constrained than our Malkus states and thus produced a higher estimate of the lower bound. Despite our low estimate here, additional considerations of the Malkus constraints may increase the highest estimates of [Jackson and Livermore \(2009\)](#) well into the geophysically interesting regime.

## 6.8 Conclusion

In this study we have shown how to construct magnetic fields that are consistent with a strongly stratified layer and the exact magnetostrophic balance thought to exist within Earth's core. We have found that these *Malkus states* are abundant, so much so that one can always be found that matches any exterior potential field (for example as derived from observational geomagnetic data).

However, despite this, the Malkus constraints derived here are proven to be significantly more restrictive than the equivalent conditions within an unstratified fluid, those of the well known Taylor constraints. The structure of magnetic fields that satisfy the Malkus constraints gives insight into the nature of the Earth's

magnetic field immediately beneath the CMB, where a layer of stratified fluid may be present. We find that the increased restrictions in the constraints requires an enhanced magnetic field within the layer. We estimate that for the present-day, the toroidal field within the stratified layer is about 8 mT. This suggests that the stratified layer may be distinct from the inner convective part of the core, characterised not only by suppressed radial flow but by a strong magnetic field, and may support different dynamics to those of the bulk of the core.

# Chapter 7

## Conclusions and future work

### 7.1 Summary

In this thesis the geodynamo and Earth's magnetic field have been investigated through focussing on the limit of negligibly small inertial and viscous forces. This magnetostrophic regime is of great interest due to its proximity to the force balance within Earth's core, but despite this, little is known about the 'Taylor state' magnetic fields that exist within this idealised model. Throughout this thesis the properties of the magnetic fields that arise within this regime, the fluid dynamics required to sustain them and the magnetic field evolution have been studied. This has always been conducted in the context of enhancing knowledge of the Earth's core. Therefore Earth-like conditions have been imposed wherever possible, from ensuring consistency with geomagnetic observations at the CMB, to stipulating constraints on fluid motion within a stratified layer.

In chapter 3 a new and completely general methodology to calculate the instantaneous fluid flow generated by any given Taylor state magnetic field has been developed. This is the first generally correct method, as the previous method of [Taylor \(1963\)](#) has been shown to fail in many circumstances, particularly for many geophysically relevant choices of boundary conditions within a fully three-dimensional domain. This correct analytical formulation of the geostrophic flow reveals key properties of the flow, specifically the presence, or otherwise, of any singularities: it has been proven that in 3D, in contrast to previous suggestions ([Roberts and Wu, 2014](#)), a regular initial magnetic field will drive a regular flow (theorem [3.13.1](#)).

The evolution of Taylor state magnetic fields is considered in chapter 4. It

is shown that there exist many Taylor states that have a rate of change comparable to the slowly evolving geomagnetic field that is observed. However, it is also established that Taylor states that are stable are very rare, with our model unable to find a single stable Taylor state with the general mixed symmetry situation applicable to the Earth.

In chapters 5 and 6 the possibility that a layer of stratified fluid may exist at the top of Earth's core has been discussed and the implications that this may have, have been considered. The concept of a Malkus state magnetic field has been introduced, as a direct extension of the previously known idea of a Taylor state, within stratified fluids. It has been shown that Malkus states do exist, with the first example of such fields given. A general methodology for constructing Malkus states is outlined along with a theoretical analysis of the restrictiveness of the Malkus constraints. This leads to a proof that in many general situations such states are numerous (theorem 6.5.1).

Through analysing Malkus states compatible with geomagnetic observations, the impact that a stratified layer may have on the core field is deduced. Interesting features that are revealed include the requirement of a strong azimuthal magnetic field immediately beneath the CMB. The toroidal magnetic field within the stratified layer is as much as 100 times stronger compared to that in the convective core, taking a maximum value of 8 mT at a core depth of 70 km. The dynamical regime of such a layer, modulated by suppressed radial motion but also a locally enhanced magnetic field, may therefore be quite distinct from that of any interior dynamo.

## 7.2 Further extensions

The research carried out in the thesis could be extended by future studies in many ways, we outline some of the most promising avenues here.

The Malkus states we computed in chapter 6, which match to exterior potential fields, provide a plausible background state at the top of the core. It is worth noting though, that we have investigated only static Malkus states without consideration of dynamics: we do not require the magnetic field to be either steady or stable, both of which would apply additional important conditions. An obvious extension to this work then is to investigate the fluid flows which are generated by the Lorentz force associated with these magnetic fields. This would then allow

a consideration of how such flows would modify the field through the induction equation. These dynamics are however still relatively poorly known even for the much simpler problem of Taylor states. We have made progress in this regard with the work in chapter 3, which now allows a full calculation of the flow driven by a Taylor state and the work in chapter 4 which analyses the rate of change of these fields. This provides a general way to discover steady and stable Taylor states comparable with geomagnetic observations through the use of the time-stepping scheme of [Li et al. \(2018\)](#).

There is much similarity between the two cases of Taylor and Malkus state dynamics. In both cases, the magnetostrophic equation (2.2) fails to provide a complete solution for the entire flow. A component that is vital for satisfying the constraint remains arbitrary and must be determined separately. In the unstratified situation, this takes the form of an azimuthally directed and solely cylindrically radially dependent geostrophic flow  $u_g(s)\hat{\phi}$ , which plays the important role of maintaining a Taylor state, and can be determined through enforcing that the time derivative of the Taylor constraint is satisfied. For the situation of a stratified fluid then the requirement of the time derivative of the Malkus constraint being zero should also inform one about the component of the flow unspecified by the magnetostrophic equation. One might expect that instead of being a  $z$ -invariant geostrophic flow, it should describe the flow on ‘Malkus rings’ of constant  $z$  values (illustrated in figure 6.1b), but it also seems intuitive to believe that the flow of adjacent rings would be not be entirely independent, but related to each other. Formalising the detail of this into a rigorous theoretical description is a pre-requisite for enabling the development of a code to dynamically simulate the regime of Malkus states, that is, maintaining an exact magnetostrophic balance while incorporating a stratified layer and ensuring all constraints are maintained.

Within rapidly rotating unstratified systems, invariance in the vertical direction is maintained by inertial waves. Any perturbation is distributed along the axis of energy propagation of these inertial waves maintaining the  $z$ -invariance of the Taylor-Proudman theorem. In the (theoretical) case of infinitely strong stratification, which is the situation for the Malkus constraint, then it is gravity waves that dominate, maintaining the layered stratification through horizontal energy propagation. In the more realistic scenario of rapid rotation and finite stratification (finite radial flow), both these features are present. Now a perturbation in  $\mathbf{B}$  at a point would lead to inertial-gravity waves enforcing invariance in an inclined direction. This may make the constraint geometry more complex, no longer taking the simple form of a right cylinder, as in the unstratified case, or a horizontal ring, as for the infinitely stratified case.

Simulations of the full dynamo equations (including finite viscous and inertial forces) can be utilised to investigate the behaviour within a stratified layer. We have conducted some preliminary calculations using the XSHELLS dynamo code (Schaeffer, 2013; Schaeffer et al., 2017), with the following approach. The poloidal field is fixed from the observational geomagnetic field model Chaos-6 (Finlay et al., 2016), and the radial profile of minimum ohmic dissipation (6.11) (Backus et al., 1996), similar to in Chapter 6. Electric currents are then generated from the poloidal field, which provide a force to generate flow that will generate toroidal and poloidal field. However, the poloidal field at the core surface is held constant in order to maintain the observational field. Stratification is enforced through a stably stratified temperature field, which provides a restoring force to any deviations. The temperature field is then uniform throughout the bulk of the core and has a linear gradient imposed within the outer 10% of the domain. This system is initially transient, but evolves to a steady state, which is what is of interest to analyse.

Here the Taylor or Malkus constraints are not enforced, as both viscous and stratification effects remain finite. It would then be of interest to compare the resultant fields of  $\mathbf{B}$  and  $\mathbf{u}$  to a Malkus state, within the stratified region. This can give some insight into the importance of the terms that are neglected a priori in other idealised models, and provide some physical intuition on the magnetic field and the fluid behaviour within a finitely stratified layer beneath the CMB.

Viscous, thermal and magnetic diffusivities are all set to unity:  $\nu = 1$ ,  $\kappa = 1$ ,  $\eta = 1$ . Therefore Prandtl number  $P_r = 1$  and magnetic Prandtl number  $P_m = 1$ . This aids numerical simplicity and efficiency, they are achievable conditions that are approximately Earth-like. The radial flow is examined as a function of three dimensionless parameters: the Ekman number, the Rayleigh number and the ratio of the buoyancy frequency to the Coriolis frequency within the stratified region  $N_0$ , which is defined as

$$N_0^2 = \frac{N^2}{\Omega^2} = \frac{E^2 R_a}{P_r} \frac{\partial T}{\partial r},$$

where the buoyancy frequency for Earth is estimated to be approximately  $N = 2 \times 10^{-4} \text{ s}^{-1}$  (Christensen, 2018; Helffrich and Kaneshima, 2010). Therefore, since  $\Omega_0 = 7.272 \times 10^{-5} \text{ s}^{-1}$ , it is believed that for Earth,  $N_0 \approx 2.75$ .

The initial simulation reveal some qualitative features. The fluid flows in the steady final state field are shown in figures 7.1 and 7.2, from these we firstly note the expected columnar structures observed for rapidly rotating convection, particularly prominent in the azimuthal flow (figure 7.1), but also notable in the radial flows (figure 7.2). This becomes increasingly apparent as the ratio of Ekman

number to Rayleigh number is reduced and the Coriolis force becomes dominant over radial buoyant convection.

Secondly, focusing on the stratified region ( $r = 0.9 - 1$ ), then it is clear how the radial flow is vastly smaller than it is in the bulk of the core ( $r = 0 - 0.9$ ), with this effect considerable for values of  $N_0 > 1$ . It is this feature that is important, when assessing the validity of the assumption necessary for the Malkus constraint that  $u_r = 0$ , within the layer. A more complete systematic and quantitative study using this model's setup would provide a firmer basis for the parameter space in which the Malkus constraint is applicable.

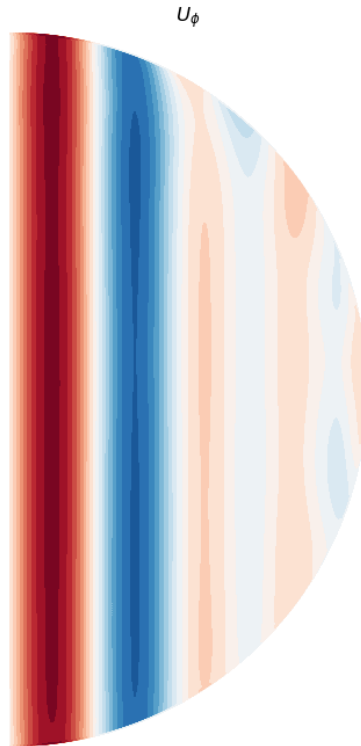


Figure 7.1:  $u_\phi$ ,  $E = 10^{-6}$ ,  $R_a = 10^8$ ,  $N_0 = 0.0707$

The work of Chapter 4 can also be built on with a full investigation of the impact of viscosity on the stability of the Taylor state magnetic fields. A dynamo simulation code such as XSHELLS (Schaeffer, 2013) could be used to further investigate the evolution from a Taylor state magnetic field. This would provide a direct comparison with the magnetostrophic dynamo simulations we have conducted, one would expect the results from these approaches to converge as the Ekman and Rossby numbers tend to zero. Also this would explicitly test the stability of Taylor states to the perturbation of including small viscous effects, a question that is vitally

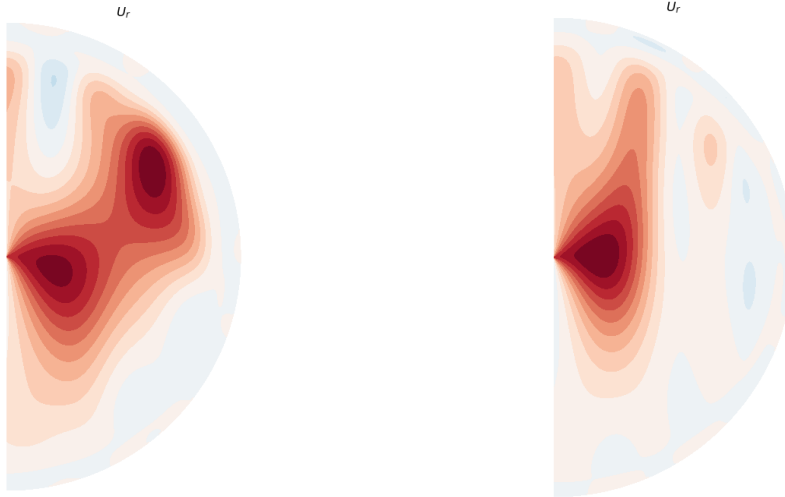
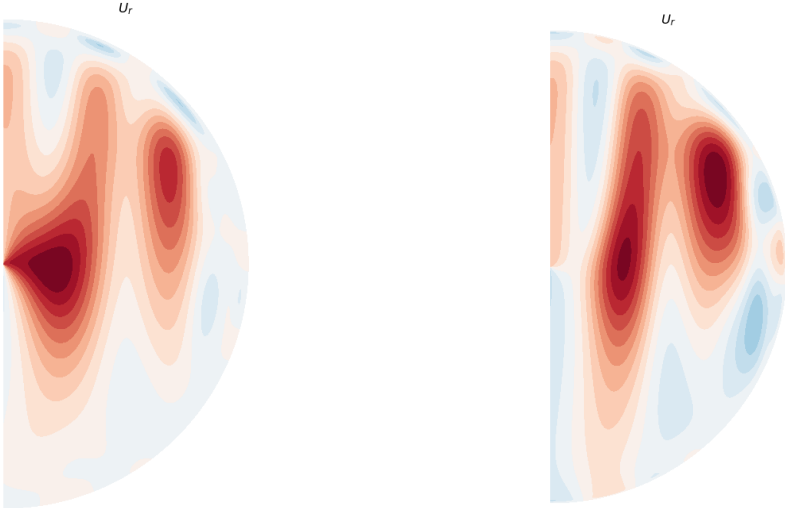
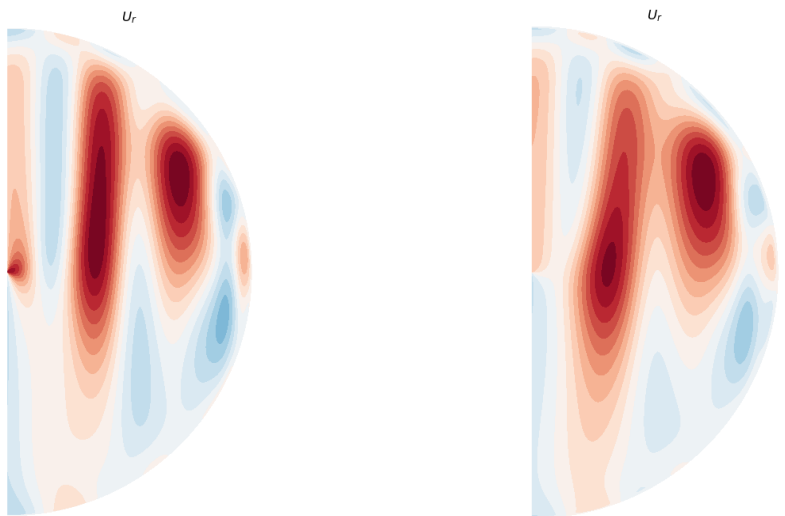
(a)  $u_r$ ,  $E = 10^{-3}$ ,  $R_a = 10^5$ ,  $N_0 = 7.07$ (b)  $u_r$ ,  $E = 10^{-4}$ ,  $R_a = 10^7$ ,  $N_0 = 7.07$ (c)  $u_r$ ,  $E = 10^{-4}$ ,  $R_a = 10^6$ ,  $N_0 = 2.236$ (d)  $u_r$ ,  $E = 10^{-5}$ ,  $R_a = 10^7$ ,  $N_0 = 0.2236$ (e)  $u_r$ ,  $E = 10^{-6}$ ,  $R_a = 10^8$ ,  $N_0 = 0.0707$ (f)  $u_r$ ,  $E = 10^{-6}$ ,  $R_a = 10^9$ ,  $N_0 = 0.2236$ 

Figure 7.2: Radial flow contours of the steady state, with a thermally stratified layer in the region ( $r = 0.9 - 1$ )

important for the physical situation of the dynamo within Earth’s core.

The well established test used to determine whether the appropriate magnetostrophic force balance is achieved within numerical dynamo simulations is ‘Taylorisation’, which represents a normalised measure of the magnitude of the Taylor integral equation (6.1) and hence the departure from the geophysically relevant, magnetostrophic regime (e.g. [Takahashi et al., 2005](#)). This would be an important metric for consideration here, measuring how rapidly it may grow, whether this growth is unstable or stable and oscillatory, and how it may depend on the value of the Ekman number.

When considering a stratified fluid then we propose an analogous quantity to Taylorisation, termed ‘Malkusisation’ defined in the same way, in terms of the Malkus integral:

$$\text{Malkusisation} = \frac{|\int_0^{2\pi} ([\nabla \times \mathbf{B}] \times \mathbf{B})_\phi d\phi|}{\int_0^{2\pi} |([\nabla \times \mathbf{B}] \times \mathbf{B})_\phi| d\phi}$$

This quantity is expected to be very small within a stratified layer adjacent to a magnetostrophic dynamo, provided stratification is sufficiently strong. The recently developed dynamo simulations of [Olson et al. \(2018\)](#); [Christensen \(2018\)](#); [Gastine et al. \(2020\)](#), which incorporate the presence of a stratified layer, can utilise the computation of this quantity to access the simulation regime. Additionally, magnetic fields from these dynamo simulations could be incorporated into our modelling of Chapter 6 through providing a poloidal field to a resolution beyond the degree 13 exterior potential field. It would be interesting to discover how these may change the resultant bound on the required toroidal field and how this value compares to both that within the simulation and indeed the existing estimates for the Earth.

It may be interesting for future work to investigate how waves thought to exist within such a stratified layer (e.g. [Buffett, 2014](#)) may behave when considered as perturbations from such a background state, and whether they remain compatible with the observed secular variation in the geomagnetic field. Similarly, combining our analysis with constraints on  $B_s$  from torsional wave models ([Gillet et al., 2010](#)) may be insightful, and would combine aspects of both long and short-term dynamics.

Finally, we note that the appropriate description of a stratified layer may in fact need to be more complex than a single uniform layer that we assume. Numerical simulations of core flow with heterogeneous CMB heat flux by [Mound et al. \(2019\)](#) find that localised subadiabatic regions that are stratified are possible amid the

remaining actively convecting liquid. If indeed local rather than global stratification is the more appropriate model for the Earth's outermost core then the condition of requiring an exact Malkus state would not apply, and the constraints on the magnetic field would be weakened by the existence of regions of non-zero radial flow. This is also supported by the recent study by [Chi-Durán et al. \(2020\)](#), who suggest non-uniform layer thickness. Their analysis of secular acceleration data from the Chaos-6 model finds evidence for waves within equatorial and high-latitude regions that are compatible with a stratified fluid.

## Appendix A

# Derivation of an alternative form of the Taylor constraint

It is possible to derive an expression for the Taylor constraint, which instead of being in the standard form of a single integral term comprises contributions from two distinct terms (Braginsky, 1970). This form proves to be particularly useful for highlighting the significance of incorporating the boundary conditions correctly when solving for the geostrophic flow, as described in Chapter 3. This is as a result of enabling the contributions of the interior domain and the boundary conditions to be separated and clearly identified.

The Lorentz force is given by  $\mathbf{F} = q(\mathbf{E} + \mathbf{v} \times \mathbf{B})$ , so considering a continuous charge distribution we have  $d\mathbf{F} = dq(\mathbf{E} + \mathbf{v} \times \mathbf{B})$  over a volume  $dV$  and therefore the force per unit volume

$$\mathbf{f} = \frac{d\mathbf{F}}{dV} = \rho(\mathbf{E} + \mathbf{v} \times \mathbf{B}) = \mathbf{J} \times \mathbf{B} = \frac{1}{\mu_0}(\nabla \times \mathbf{B}) \times \mathbf{B},$$

in the absence of an electric field, where  $\rho$  is the charge density and  $\mathbf{J} = \rho\mathbf{v}$  is the current density. From Gauss' magnetism law  $\nabla \cdot \mathbf{B} = 0 \Rightarrow (\nabla \cdot \mathbf{B})\mathbf{B} = 0$ , therefore we can add a term of this form to  $\mathbf{f}$  without changing its value. We write

$$\mathbf{f} = \frac{1}{\mu_0} ((\nabla \cdot \mathbf{B})\mathbf{B} - \mathbf{B} \times (\nabla \times \mathbf{B})),$$

and using the vector identity

$$\mathbf{B} \times (\nabla \times \mathbf{B}) = \frac{1}{2}\nabla(\mathbf{B} \cdot \mathbf{B}) - (\mathbf{B} \cdot \nabla)\mathbf{B},$$

we can write

$$\mathbf{f} = \frac{1}{\mu_0} \left( (\nabla \cdot \mathbf{B})\mathbf{B} + (\mathbf{B} \cdot \nabla)\mathbf{B} - \frac{1}{2}\nabla(\mathbf{B} \cdot \mathbf{B}) \right) = \frac{1}{\mu_0} \left( \nabla \cdot \underbrace{\left( B_i B_j - \frac{1}{2}\delta_{ij} B^2 \right)}_{\equiv \mu_0 M_{ij}} \right) \equiv \nabla \cdot \underline{\mathbf{M}}.$$

Substituting this into the Taylor constraint equation (2.6) gives

$$\int_{C(s)} (\nabla \cdot \underline{\mathbf{M}})_\phi \, s d\phi dz = 0 \quad \Rightarrow \quad \int_{C(s)} (\nabla \cdot \underline{\mathbf{M}})_\phi \, d\phi dz = 0. \quad (\text{A.1})$$

Now expanding the integrand and using the symmetry of  $\underline{\mathbf{M}}$  gives

$$(\nabla \cdot \underline{\mathbf{M}})_\phi = \frac{\partial M_{s\phi}}{\partial s} + \frac{1}{s} \frac{\partial M_{\phi\phi}}{\partial \phi} + \frac{\partial M_{z\phi}}{\partial z} + \frac{1}{s} (M_{s\phi} + M_{\phi s}) = \frac{\partial M_{s\phi}}{\partial s} + \frac{2}{s} M_{s\phi} + \frac{1}{s} \frac{\partial M_{\phi\phi}}{\partial \phi} + \frac{\partial M_{z\phi}}{\partial z},$$

and by the chain rule we know that

$$\frac{1}{s^2} \frac{\partial (s^2 M_{s\phi})}{\partial s} = \frac{1}{s^2} (2s) M_{s\phi} + \frac{\partial M_{s\phi}}{\partial s} = \frac{2}{s} M_{s\phi} + \frac{\partial M_{s\phi}}{\partial s}.$$

Substituting this into equation (A.1) gives

$$\int_{C(s)} \frac{1}{s^3} \frac{\partial (s^2 B_\phi B_s)}{\partial s} + \frac{1}{2s^2} \frac{\partial B_\phi^2}{\partial \phi} + \frac{1}{s} \frac{\partial (B_\phi B_z)}{\partial z} \, d\phi dz = 0$$

and

$$\int_{-z_1}^{z_1} \int_0^{2\pi} \frac{\partial B_\phi^2}{\partial \phi} \, d\phi dz = \int_{-z_1}^{z_1} [B_\phi^2]_0^{2\pi} \, dz = 0,$$

where  $z_1 = \sqrt{r_0^2 - s^2}$  and  $r_0$  is the radius of the sphere. Hence

$$\int_{-z_1}^{z_1} \int_0^{2\pi} \frac{1}{s^3} \frac{\partial (s^2 B_\phi B_s)}{\partial s} + \frac{1}{s} \frac{\partial (B_\phi B_z)}{\partial z} \, d\phi dz = 0,$$

and by the Leibniz integral rule

$$\int_{-z_1}^{z_1} \frac{\partial}{\partial s} (s^2 B_s B_\phi) \, dz = \frac{\partial}{\partial s} \int_{-z_1}^{z_1} (s^2 B_s B_\phi) \, dz - s^2 (B_\phi B_s)|_{z_1} \frac{\partial z_1}{\partial s} - s^2 (B_\phi B_s)|_{-z_1} \frac{\partial z_1}{\partial s}.$$

Therefore

$$\begin{aligned} & \frac{1}{s^3} \int_0^{2\pi} \left( -s^2 (B_\phi B_s)|_{z_1} \frac{\partial z_1}{\partial s} - s^2 (B_\phi B_s)|_{-z_1} \frac{\partial z_1}{\partial s} + \frac{\partial}{\partial s} \int_{-z_1}^{z_1} (s^2 B_s B_\phi) \, dz \right) \, d\phi \\ & + \frac{1}{s} \int_0^{2\pi} [B_\phi B_z]_{-z_1}^{z_1} \, d\phi = 0, \end{aligned}$$

and since

$$\frac{\partial z_1}{\partial s} = -\frac{s}{z_1},$$

substituting this in yields

$$\begin{aligned} & \frac{1}{s} \frac{\partial}{\partial s} \left( s^2 \int_{-z_1}^{z_1} \int_0^{2\pi} B_\phi B_s \, d\phi dz \right) \\ & + s \int_0^{2\pi} B_\phi \left( \frac{s}{z_1} B_s \Big|_{z_1} + B_z \Big|_{z_1} + \frac{s}{z_1} B_s \Big|_{-z_1} - B_z \Big|_{-z_1} \right) d\phi = 0. \end{aligned}$$

The radial unit normal vector is  $\hat{\mathbf{n}} = \frac{1}{r_0}(s, 0, z)$  and therefore  $B_r = \mathbf{B} \cdot \hat{\mathbf{n}} = \frac{s}{r_0} B_s + \frac{z}{r_0} B_z$  which means that  $r_0 B_r \Big|_{z_1} = s B_s \Big|_{z_1} + z_1 B_z \Big|_{z_1}$  and  $r_0 B_r \Big|_{-z_1} = s B_s \Big|_{-z_1} + z_1 B_z \Big|_{-z_1}$ .

Hence

$$\frac{1}{s} \frac{\partial}{\partial s} \left( s^2 \int_{-z_1}^{z_1} \int_0^{2\pi} B_\phi B_s \, d\phi dz \right) + \frac{r_0 s}{z_1} \int_0^{2\pi} B_\phi B_r \Big|_{z_1} + B_\phi B_r \Big|_{-z_1} \, d\phi = 0$$

or

$$\frac{1}{s} \frac{\partial}{\partial s} \left( s^2 \int_{C(s)} B_\phi B_s \, d\phi dz \right) + \frac{r_0 s}{z_1} \oint_{N+S} B_\phi B_r \, d\phi = 0,$$

where  $N$  and  $S$  are the circles where  $C(s)$  meets the spherical caps that close off the volume that  $C(s)$  contains, at its northern and southern ends respectively.

Therefore we arrive at the condition (3.12) that for a sphere of radius  $r_0 = 1$ , Taylor's constraint is equivalent to

$$\frac{1}{s} \frac{\partial}{\partial s} \left( s^2 \int_{C(s)} B_\phi B_s \, d\phi dz \right) + \frac{s}{\sqrt{1-s^2}} \oint_{N+S} B_\phi B_r \, d\phi = 0, \quad (\text{A.2})$$

where the first term is the contribution from the domain's interior and the second term is the contribution from the boundary conditions.



## Appendix B

# Solution of a full sphere low-resolution Malkus state

We present a simple non-trivial solution of a Malkus state, without making any simplifying assumptions as to the form of the toroidal field. Here we consider a full sphere magnetic field truncated at  $L_{max} = 3$ ,  $N_{max} = 3$ , and impose a minimum Ohmic dissipation poloidal profile that matches the CHAOS-6 model (to degree 3) at the CMB ( $r = R$ ). We seek a toroidal field using all spherical harmonic modes within the truncation  $L_{max} = 3$ ,  $N_{max} = 3$  (described by 45 degrees of freedom) that when added to this poloidal field satisfies the Malkus constraints. Of the 72 nonlinear constraint equations, only 42 are independent. Thus the number of degrees of freedom exceed the number of independent constraints, although since the constraints are nonlinear it is not immediate that a solution exists. However, using the computer algebra software Maple, we find the solution that minimises toroidal field strength as well as satisfying all the constraints, which is visualised in figure B.1. We cannot generalise this procedure to higher resolutions because of the numerical difficulty in finding optimal solutions in such a nonlinear problem.

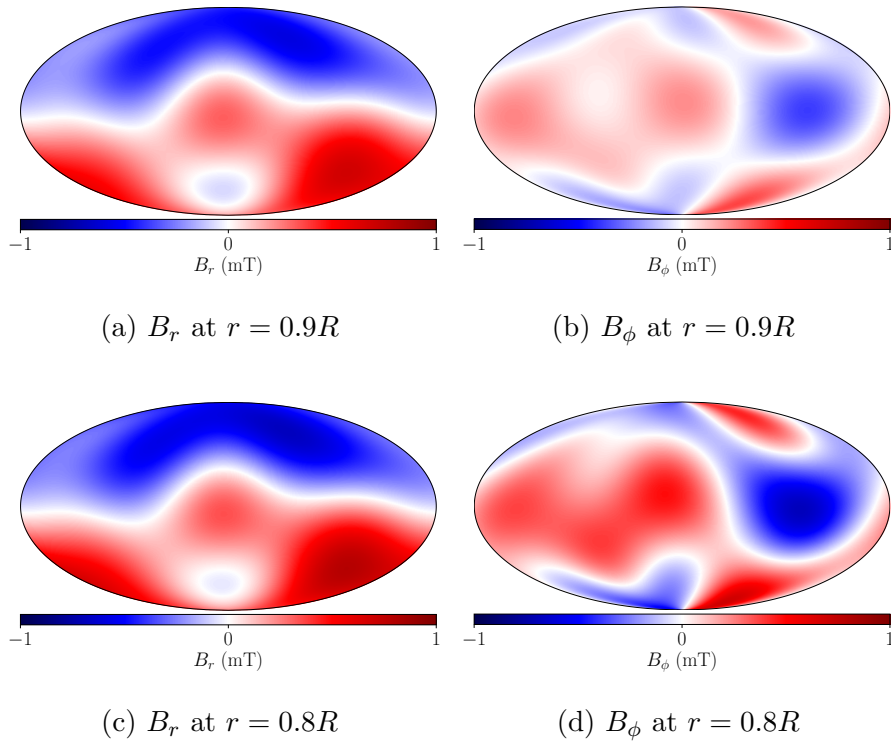


Figure B.1: Fully nonlinear Malkus state with  $L_{max} = 3$ ,  $N_{max} = 3$  with minimal toroidal field.

For comparison (see figure B.2) we also compute the solution using the method described in §6.5, which owing to the specific choice of toroidal spherical harmonic modes results in a linear system. The solutions are qualitatively and quantitatively similar, with rms values of  $B_\phi$  of 0.21 and 0.23 mT for the non-linear and linear solutions respectively, suggesting that the optimised linear solutions we have found are close to those optimal solution based on the full non-linear system.

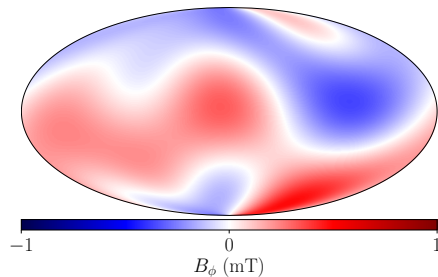


Figure B.2: Linear Malkus state with minimal toroidal field, showing  $B_\phi$  at  $r = 0.9R$ , using the method outlined in §6.5 and used for the Earth-like solutions.

# Appendix C

## Basic theory

### C.1 Toroidal and poloidal functions

The magnetic field and fluid velocity representations defined in §3.2, which are used throughout this thesis and widely within the geodynamo community, result in an expansion in terms of toroidal, poloidal and spherical harmonics functions. Here we highlight some interesting properties of these functions.

The toroidal component of magnetic field in spherical coordinates is

$$\nabla \times (Y_l^m(\theta, \phi) \mathcal{T}_l^m(r) \hat{\mathbf{r}}) = 0 \hat{\mathbf{r}} + \frac{\mathcal{T}_l^m(r)}{r \sin \theta} \frac{\partial Y_l^m(\theta, \phi)}{\partial \phi} \hat{\boldsymbol{\theta}} - \frac{\mathcal{T}_l^m(r)}{r} \frac{\partial Y_l^m(\theta, \phi)}{\partial \theta} \hat{\boldsymbol{\phi}}, \quad (\text{C.1})$$

While the poloidal component, when written out explicitly, similarly becomes

$$\begin{aligned} & \nabla \times \nabla \times (Y_l^m(\theta, \phi) \mathcal{S}_l^m(r) \hat{\mathbf{r}}) \\ &= \frac{L^2 \mathcal{S}_l^m(r) Y_l^m(\theta, \phi)}{r^2} \hat{\mathbf{r}} + \frac{1}{r} \frac{\partial Y_l^m(\theta, \phi)}{\partial \theta} \frac{\partial \mathcal{S}_l^m(r)}{\partial r} \hat{\boldsymbol{\theta}} + \frac{1}{r \sin \theta} \frac{\partial Y_l^m(\theta, \phi)}{\partial \phi} \frac{\partial \mathcal{S}_l^m(r)}{\partial r} \hat{\boldsymbol{\phi}}, \end{aligned} \quad (\text{C.2})$$

where the result derived in appendix C.6 has been used to expand the double curl and express this in terms of the angular momentum operator  $L$ . Applying this

operator, using the result  $L^2 f = l(l+1)f$  derived in appendix C.5, gives

$$\begin{aligned} & \nabla \times \nabla \times (Y_l^m(\theta, \phi) \mathcal{S}_l^m(r) \hat{\mathbf{r}}) \\ &= \frac{l(l+1) \mathcal{S}_l^m(r) Y_l^m(\theta, \phi)}{r^2} \hat{\mathbf{r}} + \frac{1}{r} \frac{\partial Y_l^m(\theta, \phi)}{\partial \theta} \frac{\partial \mathcal{S}_l^m(r)}{\partial r} \hat{\boldsymbol{\theta}} + \frac{1}{r \sin \theta} \frac{\partial Y_l^m(\theta, \phi)}{\partial \phi} \frac{\partial \mathcal{S}_l^m(r)}{\partial r} \hat{\boldsymbol{\phi}}. \end{aligned} \quad (\text{C.3})$$

Toroidal vectors have no radial component, as seen by equation (C.1), so they are confined to spherical surfaces of constant radius. This allows us to relate the radial component of the magnetic field and the poloidal function.

$$(B_l^m)_r = \frac{l(l+1)}{r^2} \mathcal{S}_l^m(r) Y_l^m(\theta, \phi) \Rightarrow \mathcal{S}_l^m(r) = \frac{r^2}{l(l+1)} \oint (B_l^m)_r Y_l^m(\theta, \phi) d\Omega,$$

where the integral is over all solid angles  $d\Omega = \sin \theta d\theta d\phi$ .

Taking the curl of equation (3.4) interchanges toroidal and poloidal vectors. Since the curl of the toroidal vector is obviously poloidal and by the vector identity  $\nabla \times \nabla \times \mathbf{A} = \nabla(\nabla \cdot \mathbf{A}) - \nabla^2 \mathbf{A}$  we have

$$\nabla \times \nabla \times \nabla \times (\mathcal{S} \hat{\mathbf{r}}) = -\nabla^2 \nabla \times (\mathcal{S} \hat{\mathbf{r}}). \quad (\text{C.4})$$

This allows us to directly relate the radial component of the curl of the magnetic field and the toroidal function.

$$((\nabla \times \mathbf{B})_l^m)_r = \frac{l(l+1)}{r^2} \mathcal{T}_l^m(r) Y_l^m(\theta, \phi) \Rightarrow \mathcal{T}_l^m(r) = \frac{r^2}{l(l+1)} \oint ((\nabla \times \mathbf{B}_l^m)_r) Y_l^m(\theta, \phi) d\Omega$$

The rate of change of the toroidal and poloidal scalars are similarly related to the magnetic induction by

$$\frac{\partial \mathcal{T}_l^m(r)}{\partial t} = \frac{r^2}{l(l+1)} \oint \left( \nabla \times \frac{\partial B_l^m}{\partial t} \right)_r Y_l^m(\theta, \phi) d\Omega, \quad (\text{C.5})$$

$$\frac{\partial \mathcal{S}_l^m(r)}{\partial t} = \frac{r^2}{l(l+1)} \oint \frac{\partial (B_l^m)_r}{\partial t} Y_l^m(\theta, \phi) d\Omega, \quad (\text{C.6})$$

## C.2 Solving Laplace's equation

Laplace's equation

$$\frac{1}{r^2} \frac{\partial}{\partial r} \left( r^2 \frac{\partial V}{\partial r} \right) + \frac{1}{r^2 \sin \theta} \frac{\partial}{\partial \theta} \left( \sin \theta \frac{\partial V}{\partial \theta} \right) + \frac{1}{r^2 (\sin \theta)^2} \frac{\partial^2 V}{\partial \phi^2} = 0, \quad (\text{C.7})$$

describes the potential field  $V$  within an electrical insulator (e.g. the mantle). This partial differential equation can be solved analytically in spherical coordinates using the method of separation of variables, by using the substitution

$$V(r, \theta, \phi) = R(r)\Theta(\theta)\Phi(\phi).$$

After dividing equation (C.7) by  $R\Theta\Phi$  and collecting terms dependent of each variable we have

$$\left( \frac{r^2 (\sin \theta)^2}{R} \frac{d^2 R}{dr^2} + \frac{2r (\sin \theta)^2}{R} \frac{d}{dr} \right) + \left( \frac{1}{\Phi} \frac{d^2 \Phi}{d\phi^2} \right) + \left( \frac{\cos \theta \sin \theta}{\Theta} \frac{d\Theta}{d\theta} + \frac{(\sin \theta)^2}{\Theta} \frac{d^2 \Theta}{d\theta^2} \right) = 0. \quad (\text{C.8})$$

Since the second bracket is the only term dependent on  $\phi$ , this must be equal to a constant, allowing us to solve for  $\Phi$

$$\frac{1}{\Phi} \frac{d^2 \Phi}{d\phi^2} = -m^2 \Rightarrow \Phi(\phi) = A_m e^{im\phi}.$$

Substituting this back into equation (C.8) and dividing by  $(\sin \theta)^2$  now gives us an equation in the two remaining unknowns.

$$\left( \frac{r^2}{R} \frac{d^2 R}{dr^2} + \frac{2r}{R} \frac{d}{dr} \right) + \frac{1}{(\sin \theta)^2} \left( \frac{\cos \theta \sin \theta}{\Theta} \frac{d\Theta}{d\theta} + \frac{(\sin \theta)^2}{\Theta} \frac{d^2 \Theta}{d\theta^2} - m^2 \right) = 0. \quad (\text{C.9})$$

Now the first bracket is the only term dependent on  $r$  and hence must be equal to a constant and  $R$  can be similarly solved for

$$\frac{r^2}{R} \frac{d^2 R}{dr^2} + \frac{2r}{R} \frac{d}{dr} = l(l+1).$$

This is a standard Euler ordinary differential equation, which can be solved through the substitution  $R = r^c$  leading to  $c = l, -l - 1$  and

$$R(r) = A_l r^l + C_l r^{-l-1},$$

where  $A_l$  and  $C_l$  are constant coefficients. Substituting this back into equation (C.9) we now have the ordinary differential equation in  $\Theta$

$$\frac{d^2\Theta}{d\theta^2} + \frac{\cos\theta}{\sin\theta} \frac{d\Theta}{d\theta} + \left( l(l+1) - \frac{m^2}{(\sin\theta)^2} \right) \Theta = 0,$$

which we can write in the form of the general Legendre equation

$$\begin{aligned} & \frac{1}{(\sin\theta)^2} \frac{d}{d\theta} \left( (1 - (\cos\theta)^2) \frac{d\Theta}{d\theta} \right) + \left( l(l+1) - \frac{m^2}{1 - (\cos\theta)^2} \right) \Theta \\ &= \frac{d}{dx} \left( (1 - x^2) \frac{d\Theta}{dx} \right) + \left( l(l+1) - \frac{m^2}{1 - x^2} \right) \Theta = 0, \end{aligned}$$

where  $x = \cos\theta$  and  $|m| = 0, \dots, l$ . The solutions of which are the associated Legendre polynomials  $P_l^m(\cos\theta)$ . Therefore, in terms of these, the complete solution is

$$V = \sum_{l=0}^{\infty} \sum_{m=-l}^l (A_l r^l + C_l r^{-l-1}) P_l^m(\cos\theta) e^{-im\phi},$$

or in terms of spherical harmonics

$$V = \sum_{l=0}^{\infty} \sum_{m=-l}^l (A_l r^l + C_l r^{-l-1}) Y_l^m(\theta, \phi).$$

### C.3 Spherical Harmonics

The associated Legendre functions are orthogonal functions  $P_l^m$  defined on the domain  $[-1, 1]$  as

$$P_l^m(x) = \frac{(-1)^m}{2^l l!} (1 - x^2)^{\frac{m}{2}} \frac{d^{l+m}}{dx^{l+m}} (x^2 - 1)^l$$

From the definition of spherical coordinates it is obvious that we can express any axisymmetric function, which has no dependence on  $\phi$ , in terms of the associated Legendre functions by mapping  $\theta$  into the  $[-1, 1]$  domain using  $\cos\theta$ .

The set of sine and cosine functions also form a set of orthogonal functions. Therefore, in order to provide orthogonality for non-axisymmetric functions, the associated Legendre functions for the  $\theta$  dependence are combined with the sine and cosine functions for the  $\phi$  dependent part, resulting in the formal definition of a spherical harmonic of degree  $l$  and order  $m$  of

$$Y_l^m(\theta, \phi) = P_l^m(\cos\theta) \begin{cases} \sin(m\phi) \\ \cos(m\phi) \end{cases}. \quad (\text{C.10})$$

These spherical harmonics are a complete set of orthogonal functions on a sphere, and thus can be used to represent functions defined on the surface of a sphere.

### C.3.1 Equatorial symmetry

A scalar  $s$  is equatorially symmetric if  $s(r, \pi - \theta, \phi) = s(r, \theta, \phi)$ , and equatorially antisymmetric if  $s(r, \pi - \theta, \phi) = -s(r, \theta, \phi)$ .

A vector  $\mathbf{v}$  is equatorially symmetric if  $\mathbf{v}(r, \pi - \theta, \phi) = [v_r, -v_\theta, v_\phi](r, \theta, \phi)$ , and equatorially antisymmetric if  $\mathbf{v}(r, \pi - \theta, \phi) = [-v_r, v_\theta, -v_\phi](r, \theta, \phi)$ .

Spherical harmonics have the symmetrical property that

$$Y_l^m(\pi - \theta, \phi) = (-1)^{(l-m)} Y_l^m(\theta, \phi).$$

Since each curl operation switches the equatorial symmetry then  $\mathcal{T}_l^m$  is anti-symmetric to its  $Y_l^m$  whereas  $\mathcal{S}_l^m$  is symmetric to its  $Y_l^m$ . This means that  $\mathcal{T}_l^m$  is equatorially symmetric when  $l - m$  is odd and equatorially antisymmetric when  $l - m$  is even, while  $\mathcal{S}_l^m$  is equatorially symmetric when  $l - m$  is even and equatorially antisymmetric when  $l - m$  is odd.

### C.3.2 Rotational symmetry

From equation (C.10) and the knowledge that  $\sin \phi$  is antisymmetric and  $\cos \phi$  is symmetric, we find that

$$Y_l^{ms}(\pi - \theta, -\phi) = (-1)^{(l-m+1)} Y_l^{ms}(\theta, \phi),$$

and

$$Y_l^{mc}(\pi - \theta, -\phi) = (-1)^{(l-m)} Y_l^{mc}(\theta, \phi),$$

where the superscripts  $s$  and  $c$  refer to the individual sine and cosine components. Since curl operations leave the rotational symmetry unchanged then  $\mathcal{T}_l^m$  and  $\mathcal{S}_l^m$  have the same symmetry as their  $Y_l^m$ . So  $\mathcal{T}_l^{ms}$  and  $\mathcal{S}_l^{ms}$  are rotationally symmetric when  $l - m$  is odd and rotationally antisymmetric when  $l - m$  is even, while  $\mathcal{T}_l^{mc}$  and  $\mathcal{S}_l^{mc}$  are rotationally symmetric when  $l - m$  is even and rotationally antisymmetric when  $l - m$  is odd.

## C.4 Boundary conditions

At the exterior of the outer core is a boundary with the electrically insulating mantle, known as the core-mantle boundary (CMB). Certain quantities including the magnetic field  $\mathbf{B}$  must remain continuous across any surface. This includes surfaces across which conductivity is discontinuous, which is the case for the CMB. Therefore we need to apply the magnetic field boundary conditions across a perfectly insulating surface

$$[\mathbf{B}] = \hat{\mathbf{n}} \cdot \mathbf{J} = 0, \quad \text{at } r = 1,$$

where  $\hat{\mathbf{n}}$  is the unit normal vector to the surface and the notation  $[\mathbf{B}]$  means the jump of the field  $\mathbf{B}$  across the boundary surface. From the continuity of  $\mathbf{B}$  it is clear that there must be zero jump in all components at the boundary, as well as zero jump in the gradient of any components normal to the boundary

$$[\mathcal{T}_l^m] = 0, \quad [\mathcal{S}_l^m] = 0, \quad \left[ \frac{d\mathcal{S}_l^m}{dr} \right] = 0, \quad \text{at } r = 1, \quad (\text{C.11})$$

where, since for a quantity to be continuous over the boundary then all its spherical harmonic components must also be continuous, we have extended the condition of continuity down to individual components.

If conductivity is zero then by Ampère's law  $\nabla \times \mathbf{B} = 0$ , so the magnetic field in an electrical insulator can be written as a potential  $\mathbf{B} = -\nabla V$  where  $V$  is a scalar function and  $\nabla^2 V = \nabla \cdot \mathbf{B} = 0$ .

By using the result of equation (C.4) we have that

$$\nabla \times \mathbf{B} = \nabla \times \nabla \times (\mathcal{T}\hat{\mathbf{r}}) + \nabla \times (-\nabla^2 \mathcal{S}\hat{\mathbf{r}}),$$

and hence, in an insulator

$$\nabla \times \mathbf{B} = 0 \quad \Rightarrow \quad \mathcal{T} = 0, \quad \nabla^2 \mathcal{S} = 0. \quad (\text{C.12})$$

From equation (C.11) we require  $\mathcal{T}_l^m$  to be continuous at the boundary  $r = 1$  and we have seen that in an insulator  $\mathcal{T} = 0 \Rightarrow \mathcal{T}_l^m = 0$  therefore this must be the case at the boundary and provides the boundary condition for the toroidal component of the magnetic field.

Deriving the poloidal condition requires a little more effort, but can be

done as follows. As a vector identity the poloidal component can be expressed as

$$\nabla \times \nabla \times (\mathcal{S}\hat{\mathbf{r}}) = \nabla (\nabla \cdot \mathcal{S}\hat{\mathbf{r}}) - \hat{\mathbf{r}}\nabla^2 \mathcal{S}.$$

Therefore, due to equation (C.12), the total magnetic field in an insulator can be written as

$$\mathbf{B} = \nabla \times (\mathcal{T}\hat{\mathbf{r}}) + \nabla \times \nabla \times (\mathcal{S}\hat{\mathbf{r}}) = \nabla (\nabla \cdot \mathcal{S}\hat{\mathbf{r}}),$$

and hence

$$V = -\nabla \cdot \mathcal{S}\hat{\mathbf{r}}.$$

As derived in appendix C.2, the general solution of Laplace's equation  $\nabla^2 V = 0$  in spherical coordinates is

$$V = \sum_{l=0}^{\infty} \sum_{m=0}^l (A_l^m r^l + C_l^m r^{-l-1}) Y_l^m(\theta, \phi),$$

where  $A_l^m$  and  $C_l^m$  are constant coefficients and for our problem of the insulator surrounding a conducting sphere we require that  $\mathbf{B} \rightarrow 0$  as  $r \rightarrow \infty$  and hence  $A_l^m = 0$ . Therefore

$$V = \sum_{l=0}^{\infty} \sum_{m=0}^l C_l^m r^{-l-1} Y_l^m(\theta, \phi),$$

and

$$\mathcal{S} = - \int V dr = \sum_{l=0}^{\infty} \sum_{m=0}^l C_l^m \frac{r^{-l}}{l} Y_l^m(\theta, \phi).$$

This means that within the external insulator

$$\mathcal{S}_l^m(r) = C_l^m \frac{r^{-l}}{l}.$$

Returning to the continuity conditions (C.11), for the poloidal component we require  $\mathcal{S}_l^m$  and  $\frac{d\mathcal{S}_l^m}{dr}$  to be continuous at CMB boundary. This provides the external boundary conditions for the core that must be satisfied at  $r = 1$ ,

$$\mathcal{S}_l^m = \frac{C_l^m}{l},$$

and

$$\frac{d\mathcal{S}_l^m}{dr} = -C_l^m.$$

Both these conditions are in terms of the unknown scalar  $C_l^m$ , so we combine them to eliminate  $C_l^m$  and give one condition. The complete boundary conditions for the

magnetic field on the core-mantle boundary of Earth are

$$\frac{d\mathcal{S}_l^m}{dr} + l\mathcal{S}_l^m = 0, \quad \mathcal{T}_l^m = 0, \quad \text{at } r = 1 \quad (\text{C.13})$$

## C.5 Angular momentum

Angular momentum is defined classically as  $\mathbf{L} = \mathbf{r} \times \mathbf{p}$ , for position vector  $\mathbf{r}$  and linear momentum  $\mathbf{p}$ . The result of applying the angular momentum operator  $L^2$  to a function  $f$  can be derived through a simple quantum mechanical calculation. Working in units where the reduced Plank constant  $\hbar = 1$ , the one dimensional linear momentum operator  $\hat{p} = -i\frac{\partial}{\partial x}$ , where  $i = \sqrt{-1}$  is the unit imaginary number. The three Cartesian components of angular momentum are

$$L_x = yp_z - zp_y, \quad L_y = zp_x - xp_z, \quad L_z = xp_y - yp_x,$$

with commutators

$$\begin{aligned} [L_x, L_y] &= - \left( \left( y \frac{\partial}{\partial z} - z \frac{\partial}{\partial y} \right) \left( z \frac{\partial}{\partial x} - x \frac{\partial}{\partial z} \right) - \left( z \frac{\partial}{\partial x} - x \frac{\partial}{\partial z} \right) \left( y \frac{\partial}{\partial z} - z \frac{\partial}{\partial y} \right) \right) \\ &= -y \frac{\partial}{\partial x} + x \frac{\partial}{\partial y} = iL_z, \end{aligned}$$

$$\begin{aligned} [L_y, L_z] &= - \left( \left( z \frac{\partial}{\partial x} - x \frac{\partial}{\partial z} \right) \left( x \frac{\partial}{\partial y} - y \frac{\partial}{\partial x} \right) - \left( x \frac{\partial}{\partial y} - y \frac{\partial}{\partial x} \right) \left( z \frac{\partial}{\partial x} - x \frac{\partial}{\partial z} \right) \right) \\ &= -z \frac{\partial}{\partial y} + y \frac{\partial}{\partial z} = iL_x, \end{aligned}$$

$$\begin{aligned} [L_z, L_x] &= - \left( \left( x \frac{\partial}{\partial y} - y \frac{\partial}{\partial x} \right) \left( y \frac{\partial}{\partial z} - z \frac{\partial}{\partial y} \right) - \left( y \frac{\partial}{\partial z} - z \frac{\partial}{\partial y} \right) \left( x \frac{\partial}{\partial y} - y \frac{\partial}{\partial x} \right) \right) \\ &= -x \frac{\partial}{\partial z} + z \frac{\partial}{\partial x} = iL_y, \end{aligned}$$

and

$$[L^2, L_z] = [L_x^2, L_z] + [L_y^2, L_z] + \underbrace{[L_z^2, L_z]}_{=0}.$$

Now using the identity  $[AB, C] = A[B, C] + [A, C]B$  and  $[A, B] = -[B, A]$  we have

$$[L_x^2, L_z] = L_x(-iL_y) + (-iL_y)L_x = -i(L_xL_y + L_yL_x),$$

and

$$[L_y^2, L_z] = L_y(iL_x) + (iL_x)L_y = i(L_xL_y + L_yL_x),$$

$\Rightarrow [L^2, L_z] = 0$ . This means that  $L^2$  and  $L_z$  commute, and therefore  $L^2$  has simultaneous eigenfunctions with  $L_z$ . This means we can define  $L^2f = \lambda f$  and  $L_zf = mf$  where  $f$  is a joint eigenfunction of  $L^2$  and  $L_z$ , with respective eigenvalues  $\lambda$  and  $m$ .

Using Dirac notation (Dirac, 1939), with raising and lowering operators defined as  $L_+ = L_x + iL_y$  and  $L_- = L_x - iL_y$  respectively,

$$\underbrace{\langle \lambda, m | L^2 - L_z^2 | \lambda, m \rangle}_{\lambda - m^2} = \underbrace{\langle \lambda, m | L_x^2 | \lambda, m \rangle}_{\geq 0} + \underbrace{\langle \lambda, m | L_y^2 | \lambda, m \rangle}_{\geq 0},$$

$\Rightarrow \lambda \geq m^2$ . This means that there must exist an upper state such that  $L_+ |\lambda, m_{max}\rangle = 0$ , with  $m_{max} = l$ , for a positive integer  $l$ . Therefore  $L_-L_+ |\lambda, m_{max}\rangle = 0$ . We also know that  $L_-L_+ = (L_x - iL_y)(L_x + iL_y) = L_x^2 + L_y^2 + i[L_x, L_y] = L^2 - L_z^2 - L_z$ .

Combining these results gives

$$(L^2 - L_z^2 - L_z) |\lambda, l\rangle = \lambda - l^2 - l = 0 \Rightarrow \lambda = l(l + 1).$$

Therefore we arrive at the final result for the  $L^2$  operator

$$L^2f = l(l + 1)f, \tag{C.14}$$

where importantly for us, the spherical harmonics (C.10) are eigenfunctions of  $L^2$  and  $L_z$ , with eigenvalues  $l(l + 1)$  and  $m$  respectively.

## C.6 Vector calculus

The double curl of a radial vector can be expanded through some vector calculus manipulations.

The standard vector identity allows us to write

$$\nabla \times \nabla \times A\hat{\mathbf{r}} = \nabla(\nabla \cdot A\hat{\mathbf{r}}) - \nabla^2(A\hat{\mathbf{r}}) \tag{C.15}$$

for any scalar  $A$ , and the first term on the right hand when expanded is

$$\nabla(\nabla \cdot A\hat{\mathbf{r}}) = \frac{1}{r^2} \frac{\partial}{\partial r} \left( r^2 \frac{\partial A}{\partial r} \right) \hat{\mathbf{r}} + \frac{1}{r} \frac{\partial}{\partial \theta} \frac{\partial A}{\partial r} \hat{\boldsymbol{\theta}} + \frac{1}{r \sin \theta} \frac{\partial}{\partial \phi} \left( \frac{\partial A}{\partial r} \right) \hat{\boldsymbol{\phi}}$$

Defining the angular momentum operator

$$L^2 = - \left( \frac{1}{\sin \theta} \frac{\partial}{\partial \theta} \left( \sin \theta \frac{\partial}{\partial \theta} \right) + \frac{1}{(\sin \theta)^2} \frac{\partial^2}{\partial \phi^2} \right),$$

allows us to write the Laplacian operator in terms of this as

$$\nabla^2 = \frac{1}{r^2} \frac{\partial}{\partial r} \left( r^2 \frac{\partial}{\partial r} \right) + \frac{1}{r^2 \sin \theta} \frac{\partial}{\partial \theta} \left( \sin \theta \frac{\partial}{\partial \theta} \right) + \frac{1}{r^2 (\sin \theta)^2} \frac{\partial^2}{\partial \phi^2} = \frac{1}{r^2} \frac{\partial}{\partial r} \left( r^2 \frac{\partial}{\partial r} \right) - \frac{L^2}{r^2}.$$

Therefore the second term on the right hand side of equation (C.15) can be written as

$$\nabla^2(A\hat{\mathbf{r}}) = \left( \frac{1}{r^2} \frac{\partial}{\partial r} \left( r^2 \frac{\partial A}{\partial r} \right) - \frac{L^2 A}{r^2} \right) \hat{\mathbf{r}}.$$

Substituting these expansions back into equation (C.15), results in the following form, which proves useful when expanding a poloidal field

$$\nabla \times \nabla \times A\hat{\mathbf{r}} = \frac{L^2 A}{r^2} \hat{\mathbf{r}} + \frac{1}{r} \frac{\partial}{\partial \theta} \frac{\partial A}{\partial r} \hat{\boldsymbol{\theta}} + \frac{1}{r \sin \theta} \frac{\partial}{\partial \phi} \left( \frac{\partial A}{\partial r} \right) \hat{\boldsymbol{\phi}}.$$

# References

Citing pages are listed after each entry.

- Abdel-Aziz, M. and Jones, C. 1988.  $\alpha\omega$ -dynamos and Taylor's constraint. *Geophysical & Astrophysical Fluid Dynamics*. **44**(1-4), pp. 117–139. Cited on pp. [29](#) and [49](#).
- Alexandrakis, C. and Eaton, D. 2010. Precise seismic-wave velocity atop Earth's core: No evidence for outer-core stratification. *Physics of the Earth and Planetary Interiors*. **180**(1-2), pp. 59–65. Cited on p. [101](#).
- Amit, H. 2014. Can downwelling at the top of the Earth's core be detected in the geomagnetic secular variation? *Physics of the Earth and Planetary Interiors*. **229** (C), pp. 110–121. Cited on p. [105](#).
- Aubert, J. 2012. Flow throughout the Earth's core inverted from geomagnetic observations and numerical dynamo models. *Geophysical Journal International*. **192**(2), pp. 537–556. Cited on p. [17](#).
- Aubert, J. 2014. Earth's core internal dynamics 1840–2010 imaged by inverse geodynamo modelling. *Geophysical Journal International*. **197**(3), pp. 1321–1334. Cited on p. [17](#).
- Aubert, J. 2019. Approaching Earth's core conditions in high-resolution geodynamo simulations. *Geophysical Journal International*. Cited on p. [16](#).
- Aubert, J. 2020. Recent geomagnetic variations and the force balance in Earth's core. *Geophysical Journal International*. **221**(1), pp. 378–393. Cited on p. [71](#).
- Aubert, J. and Finlay, C. 2019. Geomagnetic jerks and rapid hydromagnetic waves focusing at Earth's core surface. *Nature Geoscience*. **12**(5), pp. 393. Cited on p. [16](#).

- Aubert, J. and Fournier, A. 2011. Inferring internal properties of Earth's core dynamics and their evolution from surface observations and a numerical geodynamo model. *Nonlinear Processes in Geophysics*. **18**(5), pp. 657–674. Cited on p. 17.
- Aubert, J., Aurnou, J., and Wicht, J. 2008. The magnetic structure of convection-driven numerical dynamos. *Geophysical Journal International*. **172**(3), pp. 945–956. Cited on p. 15.
- Aubert, J., Gastine, T., and Fournier, A. 2017. Spherical convective dynamos in the rapidly rotating asymptotic regime. *Journal of Fluid Mechanics*. **813**, pp. 558–593. Cited on pp. 26 and 93.
- Aurnou, J. and King, E. 2017. The cross-over to magnetostrophic convection in planetary dynamo systems. *Proceedings of the Royal Society of London A: Mathematical, Physical and Engineering Sciences*. **473**(2199), pp. 20160731. Cited on p. 22.
- Aurnou, J., Calkins, M., Cheng, J., Julien, K., King, E., Nieves, D., Soderlund, K., and Stellmach, S. 2015. Rotating convective turbulence in Earth and planetary cores. *Physics of the Earth and Planetary Interiors*. **246**, pp. 52–71. Cited on pp. ix and 25.
- Backus, G., Parker, R., and Constable, C. 1996. *Foundations of Geomagnetism*. CUP. Cited on pp. 55, 119, 132, and 138.
- Barrois, O., Gillet, N., and Aubert, J. 2017. Contributions to the geomagnetic secular variation from a reanalysis of core surface dynamics. *Geophysical Journal International*. **211**(1), pp. 50–68. Cited on p. 131.
- Bergman, M. I. 1993. Magnetic Rossby waves in a stably stratified layer near the surface of the earth's outer core. *Geophysical & Astrophysical Fluid Dynamics*. **68**(1-4), pp. 151–176. Cited on p. 3.
- Bloxham, J., Zatman, S., and Dumberry, M. 2002. The origin of geomagnetic jerks. *Nature*. **420**(6911), pp. 65–68. Cited on p. 30.
- Bouffard, M., Choblet, G., Labrosse, S., and Wicht, J. 2019. Chemical convection and stratification in the Earth's outer core. *Frontiers in Earth Science*. **7**, pp. 99. Cited on p. 102.
- Boyd, J. 2001. *Chebyshev and Fourier Spectral Methods*. Dover. Cited on pp. 43 and 67.
- Braginsky, S. 1967. Magnetic waves in the Earth's core. *Geomagnetism and Aeronomy*. **7**, pp. 851–859. Cited on p. 99.

- Braginsky, S. 1970. Torsional magnetohydrodynamic vibrations in the Earth's core and variations in the length of day. *Geomagnetism and Aeronomy*. **10**, pp. 1–10. Cited on pp. [26](#), [40](#), [44](#), and [143](#).
- Braginsky, S. 1975. Nearly axially symmetric model of the hydrodynamic dynamo of the Earth. I. *Geomagnetism and Aeronomy*. **15**, pp. 122–128. Cited on p. [40](#).
- Braginsky, S. 1979. Magnetic waves in the core of the Earth. II. *Geophysical & Astrophysical Fluid Dynamics*. **14**(1), pp. 189–208. Cited on p. [31](#).
- Braginsky, S. 1984. Short-period geomagnetic secular variation. *Geophysical & Astrophysical Fluid Dynamics*. **30**(1-2), pp. 1–78. Cited on p. [3](#).
- Braginsky, S. 1987. Waves in a stably stratified layer on the surface of the terrestrial core. *Geomagnetism and Aeronomy*. **27**, pp. 410–414. Cited on pp. [3](#) and [99](#).
- Braginsky, S. 1993. MAC-oscillations of the hidden ocean of the core. *Journal of geomagnetism and geoelectricity*. **45**(11-12), pp. 1517–1538. Cited on p. [104](#).
- Braginsky, S. 1999. Dynamics of the stably stratified ocean at the top of the core. *Physics of the earth and planetary interiors*. **111**(1), pp. 21–34. Cited on p. [109](#).
- Braginsky, S. 2006. Formation of the stratified ocean of the core. *Earth and Planetary Science Letters*. **243**(3-4), pp. 650–656. Cited on p. [102](#).
- Brodholt, J. and Badro, J. 2017. Composition of the low seismic velocity E' layer at the top of Earth's core. *Geophysical Research Letters*. **44**(16), pp. 8303–8310. Cited on p. [101](#).
- Buffett, B. 2010. Tidal dissipation and the strength of the Earth's internal magnetic field. *Nature*. **468**(7326), pp. 952–954. Cited on p. [130](#).
- Buffett, B. 2014. Geomagnetic fluctuations reveal stable stratification at the top of the Earth's core. *Nature*. **507**(7493), pp. 484–487. Cited on pp. [104](#) and [141](#).
- Buffett, B. and Mound, J. 2005. A Green's function for the excitation of torsional oscillations in the Earth's core. *Journal of Geophysical Research: Solid Earth*. **110**(B8). Cited on p. [32](#).
- Buffett, B. and Seagle, C. 2010. Stratification of the top of the core due to chemical interactions with the mantle. *Journal of Geophysical Research: Solid Earth*. **115**(B4). Cited on p. [102](#).
- Buffett, B., Mound, J., and Jackson, A. 2009. Inversion of torsional oscillations for the structure and dynamics of Earth's core. *Geophysical Journal International*. **177**(3), pp. 878–890. Cited on p. [32](#).

- Buffett, B., Knezek, N., and Holme, R. 2016. Evidence for MAC waves at the top of Earth's core and implications for variations in length of day. *Geophysical Journal International*. **204**(3), pp. 1789–1800. Cited on p. [104](#).
- Bullard, E. The stability of a homopolar dynamo. In *Mathematical Proceedings of the Cambridge Philosophical Society*, volume 51, pp. 744–760. Cambridge University Press, 1955. Cited on p. [11](#).
- Bullard, E. and Gellman, H. 1954. Homogeneous dynamos and terrestrial magnetism. *Philosophical Transactions of the Royal Society of London. Series A, Mathematical and Physical Sciences*. **247**(928), pp. 213–278. Cited on p. [6](#).
- Busse, F. 1975. A necessary condition for the Geodynamo. *Journal of Geophysical Research*. **80**(2), pp. 278–280. Cited on pp. [6](#) and [112](#).
- Chi-Durán, R., Avery, M., Knezek, N., and Buffett, B. 2020. Decomposition of geomagnetic secular acceleration into traveling waves using complex empirical orthogonal functions. *Geophysical Research Letters*. **47**(17). Cited on p. [142](#).
- Christensen, U. 2018. Geodynamo models with a stable layer and heterogeneous heat flow at the top of the core. *Geophysical Journal International*. **215**(2), pp. 1338–1351. Cited on pp. [103](#), [138](#), and [141](#).
- Christensen, U. and Wicht, J. 2008. Models of magnetic field generation in partly stable planetary cores: Applications to Mercury and Saturn. *Icarus*. **196**(1), pp. 16–34. Cited on pp. [104](#) and [105](#).
- Christensen, U. and Wicht, J. Numerical dynamo simulations. In Schubert, G., editor, *Treatise on Geophysics, Vol. 8*, pp. 245–277. Elsevier, Amsterdam, 2015. Cited on p. [16](#).
- Christensen, U., Holzwarth, V., and Reiners, A. 2009. Energy flux determines magnetic field strength of planets and stars. *Nature*. **457**(7226), pp. 167. Cited on p. [16](#).
- Christensen, U., Aubert, J., and Hulot, G. 2010. Conditions for Earth-like geodynamo models. *Earth and Planetary Science Letters*. **296**(3-4), pp. 487–496. Cited on p. [16](#).
- Constable, C. 2000. On rates of occurrence of geomagnetic reversals. *Physics of the Earth and Planetary Interiors*. **118**(3-4), pp. 181–193. Cited on p. [30](#).
- Constable, C., Korte, M., and Panovska, S. 2016. Persistent high paleosecular variation activity in southern hemisphere for at least 10 000 years. *Earth and Planetary Science Letters*. **453**, pp. 78–86. Cited on pp. [11](#), [124](#), and [127](#).

- Cowling, T. 1933. The magnetic field of sunspots. *Monthly Notices of the Royal Astronomical Society*. **94**, pp. 39–48. Cited on pp. [4](#), [27](#), and [29](#).
- Cox, G., Davies, C., Livermore, P., and Singleton, J. 2019. Penetration of boundary-driven flows into a rotating spherical thermally stratified fluid. *Journal of Fluid Mechanics*. **864**, pp. 519–553. Cited on p. [103](#).
- Davies, C. and Constable, C. 2020. Rapid geomagnetic changes inferred from Earth observations and numerical simulations. *Nature communications*. **11**(1), pp. 1–10. Cited on p. [71](#).
- Davies, C., Pozzo, M., Gubbins, D., and Alfè, D. 2015. Constraints from material properties on the dynamics and evolution of Earth’s core. *Nature Geoscience*. **8** (9), pp. 678–685. Cited on pp. [49](#), [102](#), and [109](#).
- Desjardins, B. and Dormy, E. Introduction to self-excited dynamo action. In Dormy, E. and Soward, A., editors, *Mathematical Aspects of Natural Dynamos*, pp. 1–58. Academic Press, 2007. Cited on p. [12](#).
- Dirac, P. A new notation for quantum mechanics. In *Mathematical Proceedings of the Cambridge Philosophical Society*, volume 35, pp. 416–418. Cambridge University Press, 1939. Cited on p. [157](#).
- Dziewonski, A. and Anderson, D. 1981. Preliminary reference Earth model. *Physics of the Earth and Planetary Interiors*. **25**, pp. 297–356. Cited on p. [2](#).
- Evans, L. 2010. *Partial Differential Equations*. American Mathematical Society. Cited on p. [47](#).
- Fearn, D. 1998. Hydromagnetic flow in planetary cores. *Reports on Progress in Physics*. **61**, pp. 175–235. Cited on p. [49](#).
- Fearn, D. and Proctor, M. 1987. Dynamically consistent magnetic fields produced by differential rotation. *Journal of Fluid Mechanics*. **178**, pp. 521–534. Cited on pp. [43](#), [65](#), and [67](#).
- Fearn, D. and Proctor, M. 1992. Magnetostrophic balance in non-axisymmetric, non-standard dynamo models. *Geophysical & Astrophysical Fluid Dynamics*. **67** (1-4), pp. 117–128. Cited on p. [40](#).
- Fearn, D. and Rahman, M. 2004. Evolution of non-linear  $\alpha^2$ -dynamos and Taylor’s constraint. *Geophysical & Astrophysical Fluid Dynamics*. **98**(5), pp. 385–406. Cited on pp. [27](#), [73](#), [91](#), [92](#), and [96](#).

- Fearn, D. and Roberts, P. The geodynamo. In Dormy, E. and Soward, A., editors, *Mathematical Aspects of Natural Dynamos*, pp. 201–256. Academic Press, 2007. Cited on p. [22](#).
- Finlay, C. and Jackson, A. 2003. Equatorially Dominated Magnetic Field Change at the Surface of Earth’s Core. *Science*. **300**(5628), pp. 2084–2086. Cited on p. [130](#).
- Finlay, C., Olsen, N., Kotsiaros, S., Gillet, N., and Toffner-Clausen, L. 2016. Recent geomagnetic secular variation from *Swarm* and ground observatories as estimated in the CHAOS-6 geomagnetic field model. *Earth Planets Space*. **68**(1), pp. 1–18. Cited on pp. [ix](#), [xii](#), [7](#), [8](#), [10](#), [92](#), [124](#), [126](#), [132](#), and [138](#).
- Folgerhaiter, G. 1899. Sur les variations seculaires de l’inclinaison magnetique dans antiquité. *Journal de Physique*. **8**, pp. 5–16. Cited on p. [6](#).
- Fournier, A., Eymin, C., Alboussière, T., and Tangborn, A. 2007. A case for variational geomagnetic data assimilation: insights from a one-dimensional, nonlinear, and sparsely observed mhd system. *Nonlinear Processes in Geophysics*. **14**(2). Cited on p. [17](#).
- Gastine, T., Aubert, J., and Fournier, A. 2020. Dynamo-based limit to the extent of a stable layer atop Earth’s core. *Geophysical Journal International*. **222**(2), pp. 1433–1448. Cited on p. [141](#).
- Gillet, N., Jault, D., Canet, E., and Fournier, A. 2010. Fast torsional waves and strong magnetic field within the Earth’s core. *Nature*. **465**(7294), pp. 74–77. Cited on pp. [16](#), [32](#), [49](#), [130](#), and [141](#).
- Glane, S. and Buffett, B. 2018. Enhanced core-mantle coupling due to stratification at the top of the core. *Frontiers in Earth Science*. **6**, pp. 171. Cited on p. [103](#).
- Glatzmaier, G. and Roberts, P. 1995. A three-dimensional convective dynamo solution with rotating and finitely conducting inner core and mantle. *Physics of the Earth and Planetary Interiors*. **91**(1-3), pp. 63–75. Cited on pp. [4](#) and [15](#).
- Gross, R. 2001. A combined length-of-day series spanning 1832–1997: Lunar97. *Physics of the Earth and Planetary Interiors*. **123**(1), pp. 65–76. Cited on p. [104](#).
- Gubbins, D. 2007. Geomagnetic constraints on stratification at the top of Earth’s core. *Earth, planets and space*. **59**(7), pp. 661–664. Cited on pp. [99](#), [105](#), and [130](#).
- Gubbins, D. and Davies, C. 2013. The stratified layer at the core–mantle boundary caused by barodiffusion of oxygen, sulphur and silicon. *Physics of the Earth and Planetary Interiors*. **215**, pp. 21–28. Cited on p. [102](#).

- Gubbins, D. and Roberts, N. 1983. Use of the frozen flux approximation in the interpretation of archaeomagnetic and palaeomagnetic data. *Geophysical Journal International*. **73**(3), pp. 675–687. Cited on p. [58](#).
- Gubbins, D. and Roberts, P. Magnetohydrodynamics of the Earth’s core. In Jacobs, J., editor, *Geomagnetism Vol. 2*, pp. 1–183. Academic Press, 1987. Cited on pp. [13](#), [21](#), and [56](#).
- Gubbins, D., Alfe, D., Masters, G., Price, G., and Gillan, M. 2003. Can the Earth’s dynamo run on heat alone? *Geophysical Journal International*. **155**, pp. 609–622. Cited on p. [5](#).
- Gutenberg, B. 1912. Über die Konstitution des Erdinnern, erschlossen aus Erdbebenbeobachtungen. *Nachrichten von der Gesellschaft der Wissenschaften zu Göttingen, Mathematisch-Physikalische Klasse*. **14**, pp. 1217–1218. Cited on p. [2](#).
- Hardy, C. and Wong, J. 2019. Stably stratified layers within Earth’s core. *Astronomy & Geophysics*. **60**(3), pp. 3–30. Cited on pp. [ii](#), [99](#), and [132](#).
- Hardy, C., Livermore, P., Niesen, J., Luo, J., and Li, K. 2018. Determination of the instantaneous geostrophic flow within the three-dimensional magnetostrophic regime. *Proceedings of the Royal Society of London A: Mathematical, Physical and Engineering Sciences*. **474**(2218), pp. 20180412. Cited on p. [ii](#).
- Hardy, C., Livermore, P., and Niesen, J. 2020. Enhanced magnetic fields within a stratified layer. *Geophysical Journal International*. **222**(3), pp. 1686–1703. Cited on p. [ii](#).
- Helfrich, G. 2012. How light element addition can lower core liquid wave speeds. *Geophysical Journal International*. pp. 1065–1070. Cited on p. [101](#).
- Helfrich, G. and Kaneshima, S. 2010. Outer-core compositional stratification from observed core wave speed profiles. *Nature*. **468**(7325), pp. 807–810. Cited on pp. [100](#), [111](#), and [138](#).
- Helfrich, G. and Kaneshima, S. 2013. Causes and consequences of outer core stratification. *Physics of the Earth and Planetary Interiors*. **223**, pp. 2–7. Cited on pp. [xii](#), [100](#), and [111](#).
- Hollerbach, R. 1996. On the theory of the geodynamo. *Physics of the Earth and Planetary Interiors*. **98**, pp. 163–185. Cited on p. [69](#).
- Hollerbach, R. 2000. A spectral solution of the magneto-convection equations in spherical geometry. *International journal for numerical methods in fluids*. **32**(7), pp. 773–797. Cited on p. [15](#).

- Hollerbach, R. 2003. The range of timescales on which the geodynamo operates. *Earth's core: dynamics, structure, rotation*. **31**, pp. 181–192. Cited on p. [30](#).
- Hollerbach, R. and Ierley, G. 1991. A modal  $\alpha^2$ -dynamo in the limit of asymptotically small viscosity. *Geophysical & Astrophysical Fluid Dynamics*. **56**, pp. 133–158. Cited on pp. [27](#), [29](#), [74](#), [96](#), and [108](#).
- Holme, R. Large-scale flow in the core. In Schubert, G., editor, *Treatise on Geophysics, Vol. 8*, pp. 91–113. Elsevier, Amsterdam, 2015. Cited on pp. [x](#), [63](#), [64](#), [68](#), [105](#), and [131](#).
- Holme, R. and De Viron, O. 2005. Geomagnetic jerks and a high-resolution length-of-day profile for core studies. *Geophysical Journal International*. **160**(2), pp. 435–439. Cited on p. [104](#).
- Hori, K., Jones, C., and Teed, R. 2015. Slow magnetic Rossby waves in the Earth's core. *Geophysical Research Letters*. **42**(16), pp. 6622–6629. Cited on p. [130](#).
- Hori, K., Teed, R., and Jones, C. 2018. The dynamics of magnetic Rossby waves in spherical dynamo simulations: A signature of strong-field dynamos? *Physics of the Earth and Planetary Interiors*. **276**, pp. 68–85. Cited on p. [130](#).
- Irving, J., Cottaar, S., and Lekić, V. 2018. Seismically determined elastic parameters for Earth's outer core. *Science advances*. **4**(6), pp. eaar2538. Cited on p. [101](#).
- Jackson, A. 1997. Time-dependency of tangentially geostrophic core surface motions. *Physics of the earth and planetary interiors*. **103**(3-4), pp. 293–311. Cited on p. [32](#).
- Jackson, A. and Finlay, C. Geomagnetic secular variation and its applications to the core. In Schubert, G., editor, *Treatise on Geophysics, Vol. 5*, pp. 147–193. Elsevier, Amsterdam, 2007. Cited on p. [30](#).
- Jackson, A. and Livermore, P. 2009. On Ohmic heating in the Earth's core I: nutation constraints. *Geophysical Journal International*. **179**(2), pp. 923–928. Cited on p. [133](#).
- Jackson, A., Jonkers, A., and Walker, M. 2000. Four centuries of geomagnetic secular variation from historical records. *Philosophical Transactions of the Royal Society of London A: Mathematical, Physical and Engineering Sciences*. **358**(1768), pp. 957–990. Cited on p. [7](#).
- Jackson, A., Livermore, P., and Ierley, G. 2011. On Ohmic heating in the Earth's core II: Poloidal magnetic fields obeying Taylor's constraint. *Physics of the Earth and Planetary Interiors*. **187**(3-4), pp. 322–327. Cited on pp. [131](#), [132](#), and [133](#).

- Jault, D. 1995. Model Z by computation and Taylor's condition. *Geophysical & Astrophysical Fluid Dynamics*. **79**(1), pp. 99–124. Cited on pp. [26](#), [43](#), and [65](#).
- Jault, D. Electromagnetic and topographic coupling. In Jones, C. A., Soward, M. A., and Zhang, K., editors, *Earth's Core and Lower Mantle*. Taylor and Francis, 2003. Cited on pp. [40](#), [54](#), [57](#), and [68](#).
- Jault, D. 2008. Axial invariance of rapidly varying diffusionless motions in the Earth's core interior. *Physics of the Earth and Planetary Interiors*. **166**(1-2), pp. 67–76. Cited on p. [26](#).
- Jault, D. and Cardin, P. 1999. On dynamic geodynamo models with imposed velocity as energy source. *Physics of the Earth and Planetary Interiors*. **111**, pp. 75–81. Cited on p. [108](#).
- Jault, D. and L egaut, G. 2005. Alfv en waves within the Earth's core. *Fluid Dynamics and Dynamos in Astrophysics and Geophysics*. pp. 277–293. Cited on p. [62](#).
- Jault, D., Gire, C., and Le Mou el, J. 1988. Westward drift, core motions and exchanges of angular momentum between core and mantle. *Nature*. **333**(6171), pp. 353–356. Cited on p. [30](#).
- Jeanloz, R. 1990. The nature of the Earth's core. *Annual Review of Earth and Planetary Sciences*. **18**(1), pp. 357–386. Cited on p. [101](#).
- Johnson, C. and Constable, C. 1997. The time-averaged geomagnetic field: global and regional biases for 0–5 Ma. *Geophysical Journal International*. **131**(3), pp. 643–666. Cited on p. [58](#).
- Jones, C. Thermal and Compositional Convection in the Outer Core. In Schubert, G., editor, *Treatise on Geophysics, Vol. 8*, pp. 131–185. Elsevier, Amsterdam, 2007. Cited on p. [5](#).
- Kageyama, A. and Sato, T. 1995. Computer simulation of a magnetohydrodynamic dynamo. II. *Physics of Plasmas*. **2**(5), pp. 1421. Cited on p. [15](#).
- Kaneshima, S. 2018. Array analyses of SmKS waves and the stratification of earth's outermost core. *Physics of the Earth and Planetary Interiors*. **276**, pp. 234–246. Cited on pp. [100](#) and [111](#).
- Kind, R. and Li, X. Deep Earth Structure - The Earth's Cores. In Schubert, G., editor, *Treatise on Geophysics, Vol. 1*, pp. 655–682. Elsevier, Amsterdam, 2015. Cited on p. [3](#).

- Kono, M. Geomagnetism - an introduction and overview. In Schubert, G., editor, *Treatise on Geophysics, Vol. 5*, pp. 1–30. Elsevier, Amsterdam, 2015. Cited on pp. [ix](#), [7](#), [8](#), [9](#), and [124](#).
- Krause, F. and Rädler, K.-H. 1980. *Mean field MHD and dynamo theory*. Oxford, Pergamon Press, 1 edition. Cited on p. [29](#).
- Landeau, M., Olson, P., Deguen, R., and Hirsh, B. 2016. Core merging and stratification following giant impact. *Nature Geoscience*. **9**(10), pp. 786. Cited on p. [102](#).
- Larmor, J. 1919. How could a rotating body such as the Sun become a magnet. *British Association for the Advancement of Science*. **87**, pp. 159–160. Cited on p. [4](#).
- Lay, T. and Young, C. 1990. The stably-stratified outermost core revisited. *Geophysical Research Letters*. **17**(11), pp. 2001–2004. Cited on pp. [100](#) and [111](#).
- Lehmann, I. 1936. Inner Earth. *Bureau Central Séismologique International Strasbourg: Publications du Bureau Central Scientifiques*. **14**, pp. 87–115. Cited on p. [2](#).
- Lesur, V., Whaler, K., and Wardinski, I. 2015. Are geomagnetic data consistent with stably stratified flow at the core–mantle boundary? *Geophysical Journal International*. **201**(2), pp. 929–946. Cited on p. [105](#).
- Lewis, H. and Bellan, P. 1990. Physical constraints on the coefficients of Fourier expansions in cylindrical coordinates. *Journal of Mathematical Physics*. **31**(11), pp. 2592–2596. Cited on pp. [64](#), [69](#), and [114](#).
- Li, K. 2012. *Numerical approaches to the geodynamo problem*. PhD thesis, ETH Zurich. Cited on p. [76](#).
- Li, K., Livermore, P., and Jackson, A. 2010. An optimal Galerkin scheme to solve the kinematic dynamo eigenvalue problem in a full sphere. *Journal of computational physics*. **229**(23), pp. 8666–8683. Cited on pp. [35](#) and [113](#).
- Li, K., Jackson, A., and Livermore, P. 2011. Variational data assimilation for the initial value dynamo problem. *Physical Review E*. **84**(5), pp. 056321. Cited on pp. [35](#) and [113](#).
- Li, K., Jackson, A., and Livermore, P. 2018. Taylor state dynamos found by optimal control: axisymmetric examples. *Journal of Fluid Mechanics*. **853**, pp. 647–697. Cited on pp. [xi](#), [25](#), [26](#), [29](#), [36](#), [37](#), [39](#), [42](#), [43](#), [52](#), [66](#), [67](#), [70](#), [73](#), [74](#), [78](#), [79](#), [80](#), [81](#), [83](#), [86](#), [87](#), [88](#), [89](#), [90](#), [92](#), and [137](#).

- Livermore, P. and Hollerbach, R. 2012. Successive elimination of shear layers by a hierarchy of constraints in inviscid spherical-shell flows. *Journal of Mathematical Physics*. **53**(7), pp. 073104. Cited on pp. [70](#) and [112](#).
- Livermore, P., Jones, C., and Worland, S. 2007. Spectral radial basis functions for full sphere computations. *Journal of Computational Physics*. **227**(2), pp. 1209–1224. Cited on p. [76](#).
- Livermore, P., Ierley, G., and Jackson, A. 2008. The structure of Taylor’s constraint in three dimensions. *Proceedings of the Royal Society of London A: Mathematical, Physical and Engineering Sciences*. **464**(2100), pp. 3149–3174. Cited on pp. [ix](#), [24](#), [32](#), [37](#), [72](#), [108](#), [112](#), [113](#), [114](#), [115](#), [118](#), [120](#), and [121](#).
- Livermore, P., Ierley, G., and Jackson, A. 2009. The construction of exact Taylor states. I: The full sphere. *Geophysical Journal International*. **179**(2), pp. 923–928. Cited on pp. [37](#), [72](#), [94](#), [108](#), [114](#), and [119](#).
- Livermore, P., Ierley, G., and Jackson, A. 2011. The evolution of a magnetic field subject to Taylor’s constraint: a projection operator applied to free decay. *Geophysical Journal International*. **187**, pp. 690–704. Cited on pp. [38](#), [39](#), [70](#), and [77](#).
- Livermore, P., Bailey, L., and Hollerbach, R. Mar. 2016. A comparison of no-slip, stress-free and inviscid models of rapidly rotating fluid in a spherical shell. *Scientific Reports*. **6**(22812), pp. 1–11. Cited on pp. [27](#) and [69](#).
- Livermore, P., Finlay, C., and Bayliff, M. 2020. Recent north magnetic pole acceleration towards Siberia caused by flux lobe elongation. *Nature Geoscience*. **13**(5), pp. 387–391. Cited on p. [30](#).
- Maffei, S. and Jackson, A. 2016. Propagation and reflection of diffusionless torsional waves in a sphere. *Geophysical Journal International*. **204**(3), pp. 1477–1489. Cited on p. [66](#).
- Malkus, W. 1979. Dynamo macrodynamics in rotating stratified fluids. *Physics of the Earth and Planetary Interiors*. **20**(2-4), pp. 181–184. Cited on pp. [19](#), [107](#), and [109](#).
- Maus, S., Gordon, D., and Fairhead, D. 1997. Curie-temperature depth estimation using a self-similar magnetization model. *Geophysical Journal International*. **129**(1), pp. 163–168. Cited on p. [4](#).

- 
- McLean, D., Fearn, D., and Hollerbach, R. 1999. Magnetic stability under the magnetostrophic approximation. *Physics of the earth and planetary interiors*. **111**(1-2), pp. 123–139. Cited on p. [97](#).
- Mercanton, P.-L. 1926. Inversion de l'inclinaison magnetique terrestre aux ages geologiques. *Journal of Geophysical Research*. **31**(4), pp. 187–190. Cited on p. [7](#).
- Moss, D., Sokoloff, D., Usoskin, I., and Tutubalin, V. 2008. Solar grand minima and random fluctuations in dynamo parameters. *Solar Physics*. **250**(2), pp. 221. Cited on p. [96](#).
- Mound, J., Davies, C., Rost, S., and Aurnou, J. 2019. Regional stratification at the top of Earth's core due to core-mantle boundary heat flux variations. *Nature Geoscience*. Cited on pp. [105](#) and [141](#).
- Nakagawa, T. 2011. Effect of a stably stratified layer near the outer boundary in numerical simulations of a magnetohydrodynamic dynamo in a rotating spherical shell and its implications for Earth's core. *Physics of the Earth and Planetary Interiors*. **187**(3-4), pp. 342–352. Cited on p. [103](#).
- Nakagawa, T. 2018. On the thermo-chemical origin of the stratified region at the top of the earth's core. *Physics of the Earth and Planetary Interiors*. **276**, pp. 172–181. Cited on p. [102](#).
- Nimmo, F. Thermal and compositional evolution of the core. In Schubert, G., editor, *Treatise on Geophysics, Vol. 9*, pp. 217–241. Elsevier, Amsterdam, 2007. Cited on p. [5](#).
- Oldham, R. 1906. The constitution of the interior of the Earth, as revealed by earthquakes. *Quarterly Journal of the Geological Society*. **62**(1-4), pp. 456–475. Cited on p. [2](#).
- Olson, P., Landeau, M., and Reynolds, E. 2017. Dynamo tests for stratification below the core-mantle boundary. *Physics of the Earth and Planetary Interiors*. **271**, pp. 1–18. Cited on p. [104](#).
- Olson, P., Landeau, M., and Reynolds, E. 2018. Outer core stratification from the high latitude structure of the geomagnetic field. *Frontiers in Earth Science*. **6**, pp. 140. Cited on pp. [103](#) and [141](#).
- Panovska, S., Finlay, C., Donadini, F., and Hirt, A. 2012. Spline analysis of holocene sediment magnetic records: uncertainty estimates for field modeling. *Journal of Geophysical Research: Solid Earth*. **117**(B2). Cited on p. [11](#).

- Panovska, S., Constable, C., and Korte, M. 2018. Extending global continuous geomagnetic field reconstructions on timescales beyond human civilization. *Geochemistry, Geophysics, Geosystems*. **19**(12), pp. 4757–4772. Cited on pp. [xi](#), [92](#), and [93](#).
- Panovska, S., Korte, M., and Constable, C. 2019. One hundred thousand years of geomagnetic field evolution. *Reviews of Geophysics*. **57**(4), pp. 1289–1337. Cited on p. [11](#).
- Parker, E. 1955. Hydromagnetic Dynamo Models. *The Astrophysical Journal*. **122**, pp. 293–314. Cited on p. [27](#).
- Pozzo, M., Davies, C., Gubbins, D., and Alfè, D. 2012. Thermal and electrical conductivity of iron at Earth’s core conditions. *Nature*. **485**, pp. 355–358. Cited on p. [102](#).
- Proctor, M. 2004. An extension of the toroidal theorem. *Geophysical & Astrophysical Fluid Dynamics*. **98**(3), pp. 235–240. Cited on p. [6](#).
- Roberts, P. 1972. Kinematic dynamo models. *Philosophical Transactions of the Royal Society of London. Series A, Mathematical and Physical Sciences*. **272** (1230), pp. 663–698. Cited on pp. [29](#) and [74](#).
- Roberts, P. and Aurnou, J. 2011. On the theory of core-mantle coupling. *Geophys. Astrophys. Fl. Dyn.* **106**(2), pp. 157–230. Cited on pp. [15](#), [40](#), [62](#), and [68](#).
- Roberts, P. and King, E. 2013. On the genesis of the Earth’s magnetism. *Reports on Progress in Physics*. **76**(9), pp. 096801. Cited on pp. [34](#), [62](#), and [69](#).
- Roberts, P. and Wu, C. 2014. On the modified Taylor constraint. *Geophysical & Astrophysical Fluid Dynamics*. **108**(6), pp. 696–715. Cited on pp. [26](#), [62](#), [65](#), [66](#), [67](#), and [135](#).
- Roberts, P. and Wu, C. 2018. On magnetostrophic mean-field solutions of the geodynamo equations. part 2. *Journal of Plasma Physics*. **84**(4). Cited on pp. [25](#), [66](#), and [67](#).
- Roberts, P. and Wu, C. 2020. On magnetostrophic dynamos in annular cores. *Geophysical & Astrophysical Fluid Dynamics*. pp. 1–53. Cited on pp. [70](#) and [112](#).
- Roberts, P., Yu, Z., and Russell, C. 2007. On the 60-year signal from the core. *Geophysical and Astrophysical Fluid Dynamics*. **101**(1), pp. 11–35. Cited on p. [104](#).

- Rüdiger, G. and Kichatinov, L. 1993. Alpha-effect and alpha-quenching. *Astronomy and Astrophysics*. **269**, pp. 581–588. Cited on p. [96](#).
- Sambridge, M. 1999. Geophysical inversion with a neighbourhood algorithm — I. searching a parameter space. *Geophysical Journal International*. **138**(2), pp. 479–494. Cited on p. [87](#).
- Schaeffer, N. 2013. Efficient spherical harmonic transforms aimed at pseudospectral numerical simulations. *Geochemistry, Geophysics, Geosystems*. **14**(3), pp. 751–758. Cited on pp. [15](#), [138](#), and [139](#).
- Schaeffer, N., Jault, D., Cardin, P., and Drouard, M. 2012. On the reflection of Alfvén waves and its implication for Earth’s core modelling. *Geophysical Journal International*. **191**(2), pp. 508–516. Cited on p. [66](#).
- Schaeffer, N., Jault, D., Nataf, H.-C., and Fournier, A. 2017. Turbulent geodynamo simulations: a leap towards Earth’s core. *Geophysical Journal International*. **211**(1), pp. 1–29. Cited on pp. [ix](#), [16](#), [26](#), [71](#), and [138](#).
- Shimizu, H., Koyama, T., and Utada, H. 1998. An observational constraint on the strength of the toroidal magnetic field at the CMB by time variation of submarine cable voltages. *Geophysical research letters*. **25**(21), pp. 4023–4026. Cited on p. [130](#).
- Souriau, A. Deep Earth’s structure - the Earth’s cores. In Schubert, G., editor, *Treatise on Geophysics, Vol. 1*, pp. 655–693. Elsevier, Amsterdam, 2007. Cited on pp. [ix](#) and [3](#).
- Souriau, A. and Poupinet, G. 1991. A study of the outermost liquid core using differential travel times of the SKS, SKKS and S3KS phases. *Physics of the Earth and Planetary Interiors*. **68**(1-2), pp. 183–199. Cited on p. [100](#).
- Soward, A. and Jones, C. 1983.  $\alpha^2$ -Dynamo and Taylor’s Constraint. *Geophysical & Astrophysical Fluid Dynamics*. **27**, pp. 87–122. Cited on pp. [27](#), [29](#), and [108](#).
- Sprain, C., Biggin, A., Davies, C., Bono, R., and Meduri, D. 2019. An assessment of long duration geodynamo simulations using new paleomagnetic modeling criteria (qpm). *Earth and Planetary Science Letters*. **526**, pp. 115758. Cited on p. [16](#).
- Sreenivasan, B. and Narasimhan, G. 2017. Damping of magnetohydrodynamic waves in a rotating fluid. *Journal of Fluid Mechanics*. **828**, pp. 867–905. Cited on p. [130](#).

- Stanley, S. and Mohammadi, A. 2008. Effects of an outer thin stably stratified layer on planetary dynamos. *Physics of the Earth and Planetary Interiors*. **168**(3-4), pp. 179–190. Cited on p. [104](#).
- Steenbeck, M., Krause, F., and Rädler, K.-H. 1966. Berechnung der mittleren Lorentz-Feldstärke für ein elektrisch leitendes Medium in turbulenter, durch Coriolis-Kräfte beeinflusster Bewegung. *Zeitschrift für Naturforschung A*. **21**(4), pp. 369–376. Cited on p. [28](#).
- Szegö, G. 1939. Orthogonal polynomials, American Mathematical Society colloquium publications. *American Mathematical Society*. Cited on p. [35](#).
- Takahashi, F., Matsushima, M., and Honkura, Y. 2005. Simulations of a Quasi-Taylor State Geomagnetic Field Including Polarity Reversals on the Earth Simulator. *Science*. **309**, pp. 459–461. Cited on p. [141](#).
- Tarduno, J. A., Cottrell, R. D., Davis, W. J., Nimmo, F., and Bono, R. K. 2015. A hadean to paleoarchean geodynamo recorded by single zircon crystals. *Science*. **349**(6247), pp. 521–524. Cited on pp. [4](#) and [71](#).
- Taylor, J. 1963. The magneto-hydrodynamics of a rotating fluid and the Earth’s dynamo problem. *Proceedings of the Royal Society of London A: Mathematical, Physical and Engineering Sciences*. **274**(1357), pp. 274–283. Cited on pp. [iv](#), [18](#), [22](#), [24](#), [31](#), [33](#), [34](#), [39](#), [45](#), [68](#), [108](#), and [135](#).
- Tilgner, A. and Busse, F. 1997. Finite-amplitude convection in rotating spherical fluid shells. *Journal of Fluid Mechanics*. **332**, pp. 359–376. Cited on p. [15](#).
- Vallis, G. 2017. *Atmospheric and oceanic fluid dynamics*. Cambridge University Press. Cited on p. [5](#).
- Whaler, K. 1980. Does the whole of the Earth’s core convect? *Nature*. **287**(5782), pp. 528. Cited on p. [99](#).
- Wicht, J. and Christensen, U. 2010. Torsional oscillations in dynamo simulations. *Geophysical Journal International*. **181**, pp. 1367–1380. Cited on p. [16](#).
- Wicht, J. and Sanchez, S. 2019. Advances in geodynamo modelling. *Geophysical & Astrophysical Fluid Dynamics*. **113**(1-2), pp. 2–50. Cited on p. [16](#).
- Wu, C. and Roberts, P. 2015. On magnetostrophic mean-field solutions of the geodynamo equations. *Geophysical & Astrophysical Fluid Dynamics*. **109**(1), pp. 84–110. Cited on pp. [25](#), [26](#), [29](#), [39](#), [40](#), [41](#), [42](#), [43](#), [44](#), [65](#), [70](#), [73](#), [74](#), and [78](#).

- Yan, C. and Stanley, S. 2018. Sensitivity of the geomagnetic octupole to a stably stratified layer in the Earth's core. *Geophysical Research Letters*. **45**(20), pp. 11–005. Cited on p. [103](#).
- Zhang, K. and Fearn, D. 1993. How strong is the invisible component of the magnetic field in the Earth's core. *Geophysical Research Letters*. **20**(19), pp. 2083–2086. Cited on p. [130](#).
- Zhang, K. and Gubbins, D. 2000. Is the geodynamo process intrinsically unstable? *Geophysical Journal International*. **140**(1), pp. F1–F4. Cited on pp. [71](#) and [97](#).